MODELLING OF TURBULENT SWIRLING FLOWS

by

Lee Nicholas Jones

Submitted in accordance with the requirements for the degree of

Doctor of Philosophy

The University of Leeds

School of Mechanical Engineering

December 2004

ABSTRACT

This thesis investigates the predictability of non-reacting and reacting anisotropic, turbulent, swirling flows using popular turbulence models with a robust numerical procedure.

The performance of these turbulence models is assessed and compared against experimental data for anisotropic, turbulent swirling flow in a cylindrical pipe and non-reacting and reacting combustion chambers. The transport equations for the $k-\epsilon$ and $k-\omega$ two-equation turbulence models are presented along with the LRR and SSG second-moment closure models for isothermal and variable density flows. The effect of anisotropy in the Reynolds stress dissipation rate tensor is accounted for by the inclusion of an algebraic model for the dissipation anisotropy tensor dependent on the mean strain and vorticity of the flow.

The implementation of the SMART and CUBISTA boundedness preserving, high order accurate convective discretisation schemes is shown to yield superior predictive accuracy compared to previous methods such as Upwinding. The PISO and SIMPLE solution algorithms are employed to provide a robust calculation procedure.

The second moment closure models are found to provide increased predictive accuracy compared to those of the two-equation models. Mean flow properties are predicted well, capturing the effects of the swirl in the experimental flow field. The LRR model shows a premature decay of swirl downstream compared to the more accurate predictions of the other models. The effect of dissipation anisotropy on the SSG model shows an over-prediction of the turbulent properties in the upstream region followed by premature decay downstream. In the near field of the non-reacting combustion chamber flow, the anisotropic dissipation model corrects the SSG model over-prediction of the velocities at the central axis.

A combined CMC-flamelet combustion model is employed alongside the anisotropic dissipation Reynolds stress model to predict the flow field and combustion related properties of the TECFLAM swirl burner. The species mass fractions are conditioned on the mixture fraction to provide an accurate model for the determination

of the probability density functions governing the reactions within the turbulent flamelet.

The turbulence model shows an ability to provide accurate predictions for the aerodynamic properties of the flow whilst providing accurate determination of combustion related phenomena alongside the combustion model. A limitation of the flamelet assumption was identified with the over-prediction of CO due to the larger lengthscales of the oxidation reactions present in such flows.

PUBLICATIONS

L.N. Jones, P.H. Gaskell, H.M. Thompson, X.J. Gu and D.R. Emerson
"Anisotropic, isothermal, turbulent swirling flow in a complex combustor geometry."
Accepted for publication in: International Journal for Numerical Methods in Fluids.

CONFERENCES

L.N. Jones, P.H. Gaskell, H.M. Thompson, X.J. Gu and D.R. Emerson
"Highly anisotropic, isothermal, turbulent swirling flow in a complex combustor geometry." *in*: Proceedings of the ICFD Conference on Numerical Methods for Fluid Dynamics, Oxford, 2004.

ACKNOWLEDGEMENTS

Thanks must go to my family and friends for supporting me thoughout the course of my studies. Special thanks must go to Grace for looking after me, and Steve and Scott when we all needed a little cheering up. I am grateful to the room 344 posse, especially Mathieu and Yun Hon, for providing some light entertainment when it was much needed.

Finally, I am grateful for the help of my supervisors: Prof. P.H. Gaskell, Dr. H.M. Thompson and Dr. X.J. Gu.

Contents

List of Figures

List of Tables

NOMENCLATURE

Most of the symbols used in this thesis have different meanings in different chapters while others are only relevant to short sections of text. Below are listed those symbols which have a general meaning, however specific definitions will depend on the context.

a_{ij}	Reynolds stress anisotropy tensor
$a_{N,S,E,W,P}$	Discretisation equation coefficients
C_{IF}	Convective influx
d_{ij}	Dissipation rate anisotropy tensor
$D_{n,s,e,w}$	Diffusive mass fluxes through control volume faces
$F_{n,s,e,w}$	Convective mass fluxes through control volume faces
k	Turbulent kinetic energy
$\mathcal{L}$	Markstein length
Pe	Peclet number
P	Mean pressure
p'	Fluctuating pressure
$p(\cdot)$	pdf of variable $(\cdot)$
$p(x, y)$	Joint pdf of general variables x and y
$\bar{q}_l$	Mean volumetric heat release rate
Re	Reynolds number
s	Flame stretch rate
$\overline{S}_{ij}$	Mean strain rate tensor
T	Temperature
u^+	Friction velocity
u_l	Laminar burning velocity
U, V, W, U_i	Mean velocity components
$\tilde{u}$, $\tilde{v}$, $\tilde{w}$, $\tilde{u}_i$	Favre mean velocity components

u', v', w', u_i'	Fluctuating velocity components
u'', v'', w'', u_i''	Favre fluctuating velocity components
$\overline{u^2}$, $\overline{v^2}$, $\overline{w^2}$	Normal Reynolds stresses
$\tilde{u^2}$, $\tilde{v^2}$, $\tilde{w^2}$	Favre averaged normal stresses
$\overline{uv}$, $\overline{vw}$, $\overline{uw}$	Reynolds shear stresses
$\widetilde{uv}$, $\widetilde{vw}$, $\widetilde{uw}$	Favre averaged shear stresses
$\overline{W}_{ij}$	Mean vorticity tensor
W_X	Volumetric rate of formation of species X
x, y, z	Cartesian coordinates
x, r, ϕ	Cylindrical coordinates
y^+	Normalised distance from a wall
$\overline{(\cdot)}$	Reynolds averaged quantity
$\widetilde{(\cdot)}$	Density weighted (Favre) averaged quantity
$\langle \cdot \vert z \rangle$	Expectation value of $(\cdot)$ conditional on z

Greek letters

μ	Dynamic viscosity
ν	Kinematic viscosity
ν_T	Turbulent viscosity
ρ	Density
σ_{ij}	Viscous stress tensor
ξ	Mixture fraction
λ	Taylor microscale
θ	Reaction progress variable
ϵ	Dissipation rate of turbulent kinetic energy
ϵ_{ij}	Dissipation rate tensor
χ	Scalar dissipation rate
Π_{ij}	Stress redistribution tensor
δ_l	Laminar flame thickness
τ_{ij}	Reynolds stress tensor
τ_w	Wall shear stress
ϕ	General scalar
κ	Von Karman constant
ω	The rate of dissipation of turbulence energy

Abbreviations

ASM	Algebraic stress model
CBC	Convection boundedness criterion
CMC	Conditional moment closure
CCCT	Curvature compensated convective transport
CFD	Computational fluid dynamics
FV	Finite volume
LES	Large eddy simulation
NVD	Normalised variable diagram
pdf	Probability density function
QUICK	Quadratic upstream interpolation for convective kinematics
RANS	Reynolds averaged Navier-Stokes
SOUS	Second order upwind scheme
SST	Shear stress transport
TV	Total variation
TVD	Total variation diminishing

Chapter 1

Introduction

Contents

1.1 General background

Swirling flows arise in many areas of engineering and in the natural world. Examples of natural phenomena include flows such as tornadoes, hurricanes and whirlpools, whilst engineering flows include vortex shedding at wing-tips (Gursul, 2004), cyclonic separators (Hoekstra *et al.*, 1999), jet propulsion engines and combustion chambers (Gupta *et al.*, 1984). A thorough understanding of swirling flow facilitates the prediction of many of the above examples, an important one being the prediction of gas motion inside combustion chambers.

With the advent of modern computers, the ability to predict fluid flows by computational means has become commonplace, with many researchers exploiting the current increase in computing power and memory storage to study more complex flows, for example the Direct Numerical Simulation (see below) of swirling flow inside the cylinder of an internal combustion engine (Jakirlic *et al.*, 2001).

Computational methods have been employed to predict swirl at the inlet of a combustion chamber (see Shih *et al.*, 1997; Hogg and Leschziner, 1989; Chen and Lin, 1999). The amount of swirl incorporated at the jet can be used to control the combustion characteristics in the following manner for liquid fuel diffusion flames. The fuel is first atomised into droplets and sprayed into the swirling airflow as shown in figure 1.1. The main swirl-induced recirculation provides a flow of hot reaction prod-

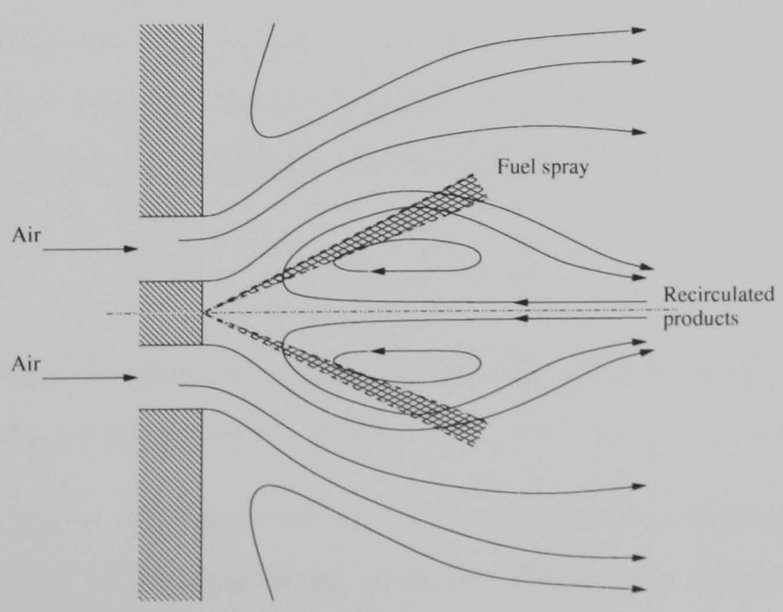

FIGURE 1.1: Inlet region of a swirling jet for a liquid fuel burner.

ucts to the flame, passing through the fuel spray, aiding fuel/air mixing, maintaining reaction upon reaching the flame. By adjusting the swirl velocity, stabilisation of the flame can be achieved by matching the flame front speed to the speed of the recirculated products. If the flame speed is greater than the speed of the fuel/air stream, extinction occurs due to an eventual lack of fuel. When the fuel/air stream speed is greater than the flame speed the flame is lifted from the jet, causing blow-off (Gupta *et al.*, 1984).

1.2 Characterisation of swirling flow

Swirling flow is characterised by the presence of a tangential velocity component. Experimentally, this tangential component is often created using rotating guiding vanes (Kitoh, 1991; Al-Masseeh, 1991), the angle and speed of which may be adjusted to increase or decrease the swirl. This flow is then passed to the area of interest, either through a narrow aperture into stagnant surroundings to create a swirling jet, or into a chamber.

The swirling flow created by the generator can be cast as two types according to the radial distribution of their tangential velocities. The *free vortex* can be described by the swirling jet flow ejected from a nozzle into stagnant fluid. When the jet emerges from the nozzle, the tendency for a body to continue in a straight line, causes the jet to spread radially outwards, producing a conical shape as distance is increased from the nozzle. The tangential velocity decreases with radius due to the dissipation of the kinetic energy of the jet into the stationary fluid. The decrease is described by an inverse law,

$$W = \frac{C}{r}, \tag{1.1}$$

where C represents the maximum tangential velocity and r the radial distance from the centre of the jet (Gupta *et al.*, 1984).

The *forced vortex*, or *solid body rotation*, can be described by the generation of swirl via wall friction in an axially rotating cylinder. The velocity obtained at the wall decays radially towards the axis of the cylinder, where it vanishes in an axisymmetric

flow, and is governed by

$$W = C_\Omega r \tag{1.2}$$

where C_Ω is the angular velocity at the pipe wall.

In reality, the axial vortex core of the free vortex must have a small forced vortex about the axis where equation (1.1) does not hold. Firstly an undefined tangential velocity would otherwise appear at zero radius, and secondly the sign of the tangential velocity must change at the axis of symmetry that can only be described by forced vortex flow. The radial position of the largest value of tangential velocity can be used to differentiate between the two vortex types. The free vortex has its maximum velocity close to the central axis, while the forced vortex maximum is near the radial extremities, away from the axis. A combination of the two types of vortex leads to the Rankine vortex, where the inner part is governed by forced vortex motion and the outer by the free vortex type.

The presence of a jet entering a flow causes flow recirculations to be produced in a similar way to the classical sudden expansion problem. The addition of swirl to such a flow modifies the flow field in such a way that additional recirculation is produced. The most important of such recirculations in the combustion application is the toroidal recirculation zone that extends axially along a cylinder, as studied by Young *et al.* (1999). Figures 1.2 and 1.3 show flow streamlines when an annular inlet produces a jet into a cylindrical chamber, the first without swirl, the second with a swirl number of 0.3 [see equation (4.6)]. These figures illustrate the additional

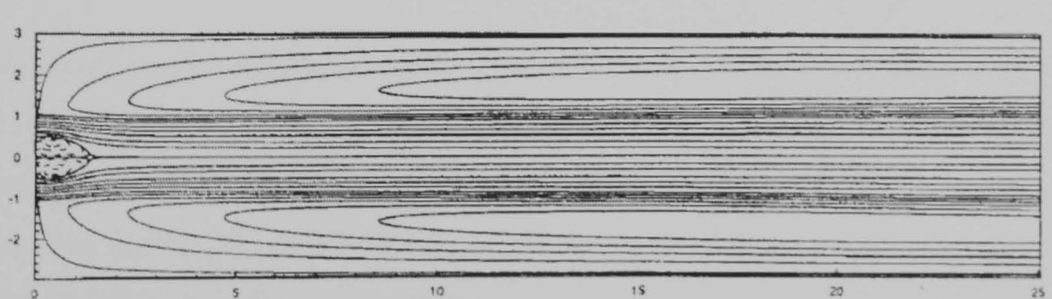

FIGURE 1.2: Annular flow without swirl; Young *et al.* (1999).

recirculations set about by swirl in a laminar flow. Many applications involving swirl are inherently turbulent, such as turbomachinery (Gupta *et al.*, 1984), and so the turbulence interaction with swirl needs to be investigated.

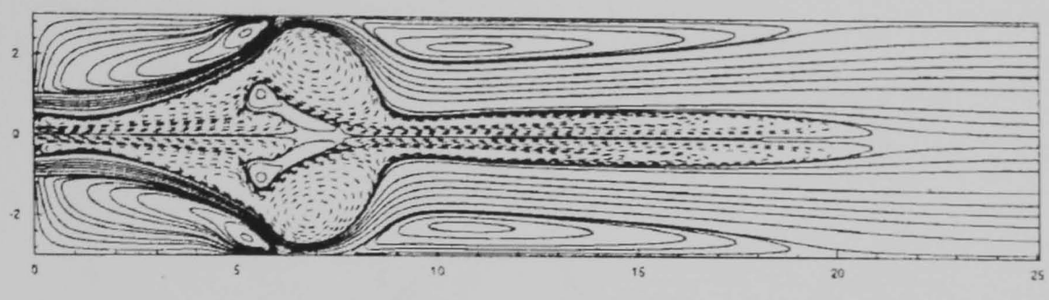

FIGURE 1.3: Annular flow with $S = 0.3$; Young *et al.* (1999).

1.3 Turbulence and swirling flow

Turbulence is characterised by an instability in a fluid, that causes rapid fluctuations in velocity about its mean value. The early work of Reynolds (1895) was instrumental in its understanding, from which the Reynolds decomposition of flow variables into their mean and fluctuating components arises.

Turbulent flows have characteristic structures present within them. The largest are the turbulent eddies that draw energy from the mean flow. Kolmogorov (1941) was the first to describe the so-called energy cascade from the large turbulent eddies to their smaller counterparts. The turbulent energy is eventually dissipated into heat by viscous action.

The fluctuating velocity components in turbulent flows give rise to Reynolds' concept of turbulent stresses, known as Reynolds stresses. These stresses are able to generate secondary flows such as secondary flows in non-circular ducts (Speziale, 1996), features which do not arise in laminar flow.

Turbulence is often produced in wall bounded or shear flows due to the speed of the flow inducing shear leading to vortex roll up and shedding. Swirl introduces a tangential component to the strain as opposed to the usual axial and radial components, thus making the strain field more complex, and the production of turbulence more difficult to predict. To understand how swirl effects the turbulence, it is instructive to compare the rotation vector of the whole flow, Ω, to the local vorticity of a small fluid element, ω, (Hanjalic and Jakirlic, 2002).

When the local vorticity, is aligned with the rotation of the bulk flow, as in figure 1.4(a) for a rotating pipe flow, less turbulence is produced as the local shear upon

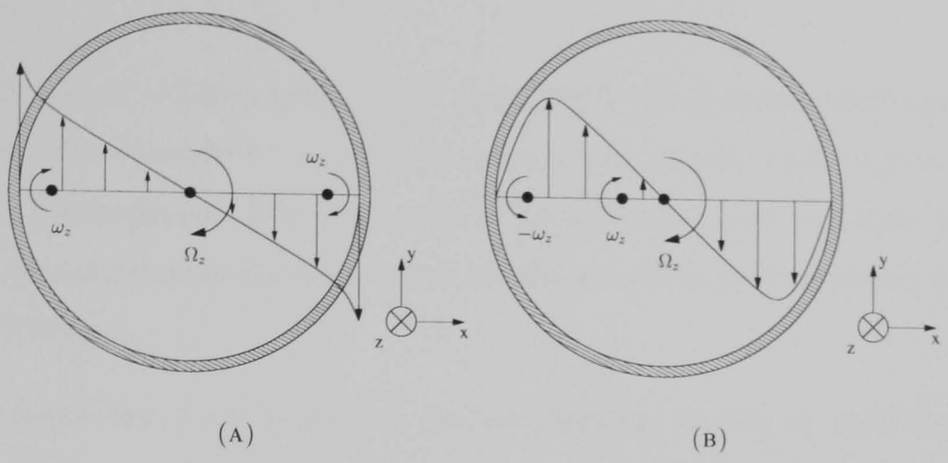

(A) (B)

FIGURE 1.4: Effect of swirl on turbulence for: (a) swirl in a rotating pipe, (b) swirl in a stationary pipe.

a fluid element is reduced. For certain rotation speeds, the flow may even become laminar if the turbulent dissipation outweighs its production. For swirling flow in a pipe with stationary walls, the reverse radial gradient of the tangential velocity causes the local vorticity, ω, to have an opposing sign to that of Ω. This increases the turbulence production due to the increase in shear in the $r-\theta$ plane. At the core of the vortex, both the local and bulk rotation are aligned, again causing reduced production of turbulence and even laminarisation.

To predict the turbulent contribution to swirling flows, it is necessary to solve the time-dependent Navier-Stokes equations on a numerical mesh whose grid spacing is of the size of the smallest turbulent motions (the Kolmogorov scale). Unfortunately, due to their small size, prohibitively large numbers of computational nodes need to be used. This leads to the use of turbulence models to provide turbulence information by modelling the effect of the Reynolds stresses on the mean flow field.

The two most popular models providing ease of use and reasonable predictive power are those of the two equation $k-\epsilon$ and $k-\omega$ models (Launder and Sharma, 1974; Wilcox, 1994). These models have been tested on separating and swirling flows with variants such as the *Shear Stress Transport* (SST) model of Menter (1994) by various authors (Yaras and Grosvenor, 2003; Chen and Lin, 1999; Jakirlic *et al.*, 2001). However, these types of models are unable to capture free vortex motion, exhibiting a characteristic premature return to solid body rotation axially along a

pipe.

Researchers such as Chien (1982), Shih *et al.* (1997) and Speziale (1987) attempted to improve the standard $k - \epsilon$ model by accounting for stress anisotropies by using nonlinear combinations of the mean rate of strain tensor. However, these types of models did not improve the accuracy of prediction significantly as shown by Yuan and So (1998).

Improvements have been made over the two equation models in predicting other flows, such as square duct flows (see Speziale, 1996), using the differential stress transport, or Reynolds stress, model. The increased predictive power, despite the additional computational cost, promotes their use in swirling flow.

The main area of research has been into the model for the redistribution of turbulent stress by pressure fluctuations - also known as the pressure-strain correlation. Among the first models produced were those of Rotta (1951), followed by Hanjalic and Launder (1972) and Launder *et al.* (1975) with the now ubiquitous LRR (named after the authors) model, all using the stress anisotropy tensor to account for features such as return to isotropy of initially strained turbulence.

Work by Lumley (1978) presented an improved model by showing a need to apply physical constraints on the modelling assumptions using the concept of realisability. More recent research has been performed by Speziale *et al.* (1991) and Fu, Launder and Tselepidakis (1987), where the coefficients of the mean velocity gradients are represented as nonlinear functions of the anisotropy tensor. Modern models include the two-component limit model of Craft and Launder (2001), and that of Jovanovic *et al.* (2003), at walls or free surfaces. For these models the incorporation of the two-component nature of the turbulence, where the wall-normal Reynolds stress is reduced and the tangential components enhanced, is used to provide more accurate prediction of flow physics in these areas.

Research on the validity of the assumption of dissipation isotropy has also been undertaken by authors such as Speziale and Gatski (1997), Hallback *et al.* (1990) and Jakirlic and Hanjalic (2002). This is due to the inability of the pressure-strain models to capture all the features of turbulent flows. Although no validation has

explicitly been carried out, to the author's knowledge, on swirling flow. computations have been performed by So *et al.* (1999) for buoyant shear flows, indicating that additional modelling still needs to be done in this area.

Reynolds stress models show improved performance over the two equation models for flows such as the turbulent swirling free jet studied by Younis *et al.* (1996) using the SSG model (Speziale *et al.*, 1991). This model was also used successfully to predict free vortex flow in a cylinder by Chen and Lin (1999) where the developed version of the LRR model by Fu, Launder and Leschziner (1987) gave poor predictions. More advanced models such as that of Craft and Launder (2001) are, as yet, untested for such flows, so it is not known if any improvement in prediction will be achieved.

1.4 Swirling flows and combustion

As mentioned above, one of the primary uses for swirling flow is the stabilisation of flame and mixing of fuel with oxidant in combustors. These effects control the chemistry of the reactions present in a flame, and hence the proper application of swirl in a combustor can lead to greater efficiency. Using turbulence models, the effect of swirl on a flow can be predicted well, however prediction of the combustion process is also required.

A consequence of the heat release due to combustion is the appearance of fluctuating and variable density. This complicates the normally constant density turbulence models with additional density based correlations that require further modelling assumptions to be made. To remove the appearance of the fluctuating density, Favre - or density weighted - averaging is commonly employed (Jones, 1979). However, modelling the density weighted terms leads to additional problems and so it is common to use turbulence models developed for constant density.

To model turbulent combustion, the chemical reaction is decoupled from the aerodynamic effects and modelled. One of the simplest models is to assume that all reaction occurs in a negligibly thin flame sheet, on one side of which is unburnt reactants, the other side burnt products (see figure 1.5). This forms the basis of the G

equation of Libby and Williams (1990) for premixed combustion where the G isoline separates the reactants and products. However, the laminar burning velocity is still required by this equation, and its use is confined to constant density flows (Libby and Williams, 1994), an unrealistic simplification for reactions with significant heat release.

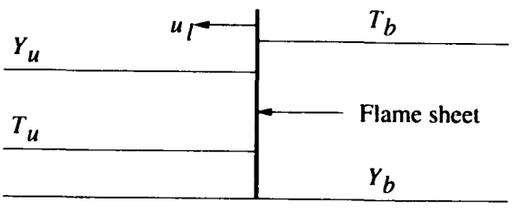

FIGURE 1.5: The flame sheet model of combustion.

A more widely known model for premixed turbulent combustion is the BML model of Libby and Bray (1977). A scalar, in the form of the reaction progress variable, defines areas of pre- and post-reaction. A joint probability density function is used to describe the properties of the flow in the combustion region between these two states. By using assumed pdf techniques (whereby the pdf is approximated by a beta function), expressions for the multiple fluctuating velocity and reactedness correlations brought about by Favre averaging are solved. This model has been successful in predicting the counter gradient diffusion phenomena of turbulent flames (Libby and Bray, 1981).

Flamelet models for turbulent combustion also incorporate assumed pdfs to calculate fluctuating density, and other variables, as functions of mixture fraction. Bray and Peters (1994) present a model utilising the G equation, where the burning velocity is specified via the stretched laminar burning velocity and Markstein lengths. Both first and second moment equations of G are utilised where the pdf of G is used in the BML model to find mean reactedness, mass fractions and other scalar quantities.

Other groups, such as that at Leeds, have produced their own versions of the flamelet model for premixed and diffusion flames (Bradley, Gaskell and Gu, 1998*a*,*b*). Here, an assumed pdf incorporating reactedness and mixture fraction and the pdf of stretch rate are used to find the unknown chemically related variables (Gu, 1993). Previously computed chemistry data for laminar flamelets is used in the manner of a flame library, which is then integrated with the pdf over stretch rate and mixture

fraction to provide details of the turbulent diffusion flame. Particular emphasis on this model involves the prediction of the correct behaviour of turbulent burning velocities at positive and negative stretch rates of the flame due to aerodynamic strain and flame curvature (Bradley, 2002).

In an effort to improve the modelling for turbulent diffusion flames, Klimenko and Bilger (1999) have developed the conditional moment closure equations, whereby the joint velocity-scalar pdf is conditioned on a particular value of the scalar (usually mixture fraction). From this, the conditional first and second moment equations for mass fraction result, leading to an improved prediction over assumed pdf beta function methods.

Bradley *et al.* (2002) combined the flamelet model with the conditional moment closure equations in an attempt to provide a better evaluation of the pdf of reactedness. This study was performed using the second moment CMC equations after earlier attempts (Bradley, Gaskell and Gu, 1998*a*) to use the first moment equations resulted in poor prediction of lift off height for jet flames. These second moment equations were shown to improve the prediction of mass fractions in the highly stretched jet flames.

1.5 Outline of present work

The main thrust of this work is the evaluation of modern Reynolds stress turbulence models for the simulation of isothermal and reacting swirling, turbulent flows. Research by Speziale *et al.* (1991) has highlighted the need for a new approach to Reynolds stress modelling due to inherent deficiencies in the general model for the pressure-strain term. Indeed, Jakirlic *et al.* (2002) states that the addition of nonlinear terms affords little improvement for swirling flows. Thus the improvement of existing terms such as that of the dissipation rate tensor has been undertaken.

Chapter 2 provides a brief review of the need for turbulence models, their history, and the current state of their development. Two equation models, namely the standard $k - \epsilon$ and $k - \omega$ models, and full differential stress models of Launder *et al.*

(1975) and Speziale *et al.* (1991) are introduced as a tool for predicting isothermal swirling flows. As swirl induces large stress anisotropy, it is not inconceivable that the same applies to the dissipation of turbulence (Jakirlic and Hanjalic, 2002). The model presented is one based on that of Speziale and Gatski (1997), using an algebraic approach as opposed to a full differential model. These models are then converted for use in variable density flows by Favre averaging.

The numerical procedures undertaken are then presented in Chapter 3. Here, the finite volume method is used to integrate the governing differential equations. Particular emphasis is given to the discretisation of the troublesome convective terms. Two schemes are finally recommended because of their high order interpolative accuracy whilst maintaining boundedness; CUBISTA (Alves *et al.*, 2003) and SMART (Gaskell and Lau, 1988). Solution algorithms are then presented in the form of SIMPLE (Patankar, 1980) and PISO (Issa, 1985).

Two swirling, isothermal test cases are then considered in Chapter 4, namely the free vortex type flow studied experimentally by Kitoh (1991) and the combustion chamber flow studied by Al-Masseeh (1991). The two equation models are used for both flows, as are the Reynolds stress models and the benefits of accounting for dissipation anisotropy are discussed.

Chapters 5 and 6 describe the combustion model used and its application to the TECFLAM research flame. An introduction to the forerunners of the flamelet-CMC combustion model, the laminar flamelet and Conditional Moment Closure models, is presented. The flamelet-CMC model is then addressed, with special emphasis on the coupling with the turbulent dissipation rate and its effect on combustion. Results for the TECFLAM flame are presented showing the model capability to predict the axial recirculation and heat release rate.

Chapter 7 discusses conclusions and offers suggestions for possible future work.

Chapter 2

Turbulence Modelling

Contents

2.1 Introduction

This chapter introduces the continuous equations and models that describe turbulent isothermal and variable density swirling fluid flows.

A flow may be accelerated from laminar conditions to a transitional state by an increase in velocity. Transitional flow is inherently unstable, and the instabilities present introduce new flow features - or 'structures'. The increased shear in the flow leads to a rolling up in the shear layer and the creation of vortices. A well known example of this is the Kelvin-Helmholtz instability, where vortices are formed in the shear layer of a wall bounded flow (Acheson, 1998).

If the flow is accelerated beyond the transitional regime the flow becomes fully turbulent. The increased shear and strain of the flow increases the instability and more vortices are produced. The smaller vortices 'feed' from the mean flow, squashing and stretching and ultimately increasing in energy and size. These large vortices are effectively inviscid in nature, for instance vortices in the atmosphere or in the ocean, and have long lifetimes. Smaller vortices are created due to the fluctuation in vorticity around their larger neighbours. These smaller versions are, however, susceptible to the action of viscosity, and the turbulent energy is dissipated into heat by the action of viscosity.

The study and prediction of turbulent flow remains an active field of research. Reynolds (1895) chose to represent turbulence as consisting of a mean and fluctuating part. This method, called Reynolds Decomposition, is used with statistical averaging methods to predict the mean quantities of the flow, such as velocity and pressure.

Turbulence is present in many engineering applications, such as the flow over the wing of an aircraft (Rhie and Chow, 1983) or combustion in the cylinder of an internal combustion engine (Jakirlic *et al.*, 2000). Its effects can be either a help, assisting the mixing of fuel and oxidant in a combustion chamber, or a hindrance, when turbulence reduces the efficiency of an aeroplane wing leading to a sudden loss of lift. Such effects make the effective prediction of turbulent flows of great interest.

In the following sections, the equations governing fluid flow are presented. However, as explained, these equations are unable, in their compact form, to predict the high Reynolds number flows of interest here and mathematical models are required. Several types of model are shown, such as the two-equation $k - \epsilon$ (Launder and Sharma, 1974) and $k - \omega$ (Wilcox, 1994) models. Higher order Reynolds stress equations, and associated models, are also discussed. Finally, models are presented incorporating the effect of variable density, facilitating their use in flows with heat release, such as combustion.

2.2 The Navier-Stokes Equations

The Navier-Stokes equations were developed independently by Stokes (1845) and Navier (1821) and represent the general behaviour of a fluid. The equation for the conservation of mass of a fluid element in the steady-state, known as the *Continuity Equation*, is expressed as,

$$\nabla \cdot (\rho \mathbf{u}) = 0, \tag{2.1}$$

where ρ is the density of the fluid and $\mathbf{u}$ its velocity.

The equation for conservation of momentum in an incompressible fluid in the steady state is,

$$(\rho \mathbf{u} \cdot \nabla)\mathbf{u} = -\nabla p + \rho \mathbf{g} + \nabla \sigma \tag{2.2}$$

where σ is the viscous stress tensor (see below), $\mathbf{g}$ is representative of a body force (such as the vectorial acceleration due to the Earth's gravitational field) and p the pressure field within the fluid.

Equations (2.1) and (2.2) can be re-expressed in Cartesian tensor form, adopting the Einstein summation convention. Using this notation, u_j represents a vector, with individual components (for $j = 1, \ldots 3$),

$$u_1 = u, \quad u_2 = v, \quad u_3 = w. \tag{2.3}$$

A repeated index, denotes a summation (or contraction of the tensor into a scalar).

$$\frac{\partial u_j}{\partial x_j} = \sum_{j=1}^{3} \frac{\partial u_j}{\partial x_j} \equiv \frac{\partial u}{\partial x} + \frac{\partial v}{\partial y} + \frac{\partial w}{\partial z}. \tag{2.4}$$

Equation (2.4) can clearly be seen to denote the divergence of the velocity vector, $\nabla \cdot \mathbf{u}$. From this point onwards, the summation convention is adopted for ease of representation.

Re-expressing (2.1) and (2.2) in tensorial form gives,

$$\frac{\partial}{\partial x_j}(\rho u_j) = 0, \tag{2.5}$$

$$\frac{\partial}{\partial x_j}(\rho u_j u_i) = -\frac{\partial p}{\partial x_i} + \frac{\partial \sigma_{ij}}{\partial x_j}. \tag{2.6}$$

where

$$\sigma_{ij} = \mu\left(\frac{\partial u_i}{\partial x_j} + \frac{\partial u_j}{\partial x_i}\right) - \frac{2}{3}\mu\frac{\partial u_k}{\partial x_k}\delta_{ij} \tag{2.7}$$

is the viscous stress tensor, with (2.5) - (2.6) referred to as the steady-state *Navier-Stokes* equations.

2.3 Treatment of turbulence

Isothermal, turbulent motion is characterised by the apparent random motion of velocity and pressure about a mean value at a point in a fluid. The nature of the fluctuations are such that even though the mean values of pressure and velocity are steady, turbulent flows are inherently time-dependent. The velocity at a point in a stable, steady-state laminar flow will always be at a constant value, but as the flow becomes more unstable (usually due to an increase in Reynolds number) a transition to turbulent motion occurs. In pipe flow, this transition takes place at Reynolds numbers of around two thousand (Acheson, 1998). In turbulent flow, the smallest scale of motion is that of the Kolmogorov length scale, η. This is the size of the

smallest turbulent eddies in a flow and is dependent on the flow properties.

$$\eta = \frac{l_0}{R_t^{3/4}}. \tag{2.8}$$

where l_0 is the lengthscale of the large turbulent eddies and

$$R_t = \frac{k_0^{1/2} l_0}{\nu_0} \tag{2.9}$$

is the turbulent Reynolds number with k_0 and ν_0 representative values of turbulent kinetic energy and kinematic viscosity, respectively. Due to the small size of the Kolmogorov eddies [$\eta = 0.36mm$ for uniform shear (Champagne *et al.*, 1970)], it is difficult to simulate them numerically. However, with the continual increase in computing power, it is becoming increasingly feasible to simulate these small eddies directly via the Navier-Stokes equations using *Direct Numerical Simulation* (DNS). This method discretises the Navier-Stokes equations on a computational grid, where the spacing between grid nodes is of the order of the Kolmogorov length scale, so that the entire range of length scales is resolved. With the size of the largest eddies representative of the size of the computational domain, a measure of the nodes needed to resolve the Kolmogorov scales is given by the ratio (Libby and Williams, 1994)

$$\frac{l_0}{\eta} = R_t^{3/4} \quad . \tag{2.10}$$

In three-dimensional flows, the number of nodes required for DNS increases as $(l_0/\eta)^3$ and hence $R_t^{9/4}$. DNS is therefore limited in its application to only low Reynolds number simulations, such as transitional flow to mildly turbulent: Le *et al.* (1997) performed a study over a backward facing step at a Reynolds number of 5100. Sandham (2002) states that the increase in computational nodes needed with a doubling of Reynolds number is between 2.2 to 2.5. Despite the low Reynolds number applications, DNS is useful for improving the predictions of turbulence models (Mansour *et al.*, 1989). It also facilitates the prediction of flow quantities that are difficult to measure experimentally, such as the strain rate tensor. For turbulent flows of engineering interest, however, this computational cost is too great at present, and other methods must be used.

Large Eddy Simulation (LES) has emerged as a method which has far less computational cost than DNS. LES splits the turbulent length scales, so that the large scales are resolved directly as in DNS, while the smaller scales are filtered, using a filter function, and modelled. The advantage of LES over DNS is that higher Reynolds numbers may be simulated as the nodal resolution required is much lower. However, LES still requires a large computational investment for industrial applications.

2.3.1 Reynolds averaging

The approach used in the present work makes use of the *Reynolds Averaged Navier-Stokes* (RANS) equations. Instead of directly simulating the time-dependent, fluctuating velocity, the RANS equations consider the mean value of the velocity. Reynolds decomposition expresses the flow variables as the sum of a mean and fluctuating (turbulent) part,

$$\begin{aligned} u_i &= U_i + u_i' \\ p &= P + p', \end{aligned} \tag{2.11}$$

where the mean flow quantity is denoted by uppercase letters, and the fluctuating quantity by lowercase primed letters. The RANS equations are derived on a statistical basis where *ensemble averaging* can be used to describe the properties of the ensemble (or mean properties of the flow), by averaging over N experiments.

$$U_i = \lim_{N\to\infty} \frac{1}{N} \sum_{m=1}^{N} u_i^m \tag{2.12}$$

The process of averaging leads intuitively to the following relations,

$$\begin{aligned} \overline{u_i'} &= 0 \\ \overline{p'} &= 0 \\ \overline{U_i u_j'} &= 0 \\ \overline{u_i u_j} &= U_i U_j + \overline{u_i' u_j'}. \end{aligned} \tag{2.13}$$

From the above relations, the equations of motion for the mean flow quantities can be obtained by inserting (2.11) into equations (2.5) and (2.6) followed by averaging, to give,

$$\frac{\partial}{\partial x_j}(\rho U_j) = 0 \tag{2.14}$$

$$\frac{\partial}{\partial x_j}(\rho U_j U_i) = -\frac{\partial P}{\partial x_i} + \frac{\partial}{\partial x_j}(\overline{\sigma}_{ij} - \tau'_{ij}) \quad . \tag{2.15}$$

Equation (2.14) is the mean flow continuity equation and (2.15) is the mean flow momentum equation where

$$\tau'_{ij} = \overline{\rho u'_i u'_j} \tag{2.16}$$

are the turbulent stresses known as the *Reynolds Stresses*, formed by the action of the fluctuating velocity components. The above relations constitute the RANS equations for turbulent flow.

The introduction of averaging to yield equations for the mean flow introduces new unknowns, τ'_{ij}. In order to solve turbulent flows with the RANS equations, new equations for τ'_{ij} must be developed. These may be calculated by obtaining a transport equation governing the motion of the fluctuating velocities. By subtracting equation (2.15) from (2.6) gives,

$$\frac{\partial}{\partial x_j}(\rho U_j u'_i) = -\frac{\partial}{\partial x_j}(\rho u'_j u'_i) - \frac{\partial}{\partial x_j}(\rho u'_j U_i) - \frac{\partial p'}{\partial x_i} + \mu \nabla^2 u'_i + \frac{\partial \tau'_{ij}}{\partial x_j} \tag{2.17}$$

which, after rearrangement using (2.5), leads to,

$$U_j \frac{\partial u'_i}{\partial x_j} = -u'_j \frac{\partial u'_i}{\partial x_j} - u'_j \frac{\partial U_i}{\partial x_j} - \frac{1}{\rho}\frac{\partial p'}{\partial x_i} + \nu \nabla^2 u'_i + \frac{1}{\rho}\frac{\partial \tau'_{ij}}{\partial x_j} \tag{2.18}$$

However, this does not help to close equation (2.15) in the steady-state, as the turbulent fluctuations are a temporal phenomena and have no steady-state counterpart. Also, the presence of unknown Reynolds stresses is still not solved.

By using the notation that equation (2.18) can be written as $\mathcal{N} u'_i = 0$, where $\mathcal{N}$ is

the operator,

$$U_j\frac{\partial}{\partial x_j}+u'_j\frac{\partial}{\partial x_j}+u'_j\frac{\partial U_j}{\partial x_j}+\frac{1}{\rho}\frac{\partial p'}{\partial x_i}-\nu\nabla^2-\frac{1}{\rho}\frac{\partial \tau'_{ij}}{\partial x_j} \quad , \tag{2.19}$$

a transport equation for the Reynolds stresses can be found. The statistical second moment is constructed as

$$\overline{u'_i\mathcal{N}u'_j+u'_j\mathcal{N}u'_i}=0 \tag{2.20}$$

which leads to the *Reynolds Stress Transport Equation* in its standard form

$$U_k\frac{\partial \tau'_{ij}}{\partial x_k}=-\tau'_{ik}\frac{\partial U_j}{\partial x_k}-\tau'_{jk}\frac{\partial U_i}{\partial x_k}+\Pi_{ij}-\epsilon_{ij}-\frac{\partial}{\partial x_k}C_{ijk}+\nu\nabla^2\tau'_{ij} \tag{2.21}$$

where

$$\Pi_{ij} = \overline{\frac{p'}{\rho}\left[\frac{\partial u'_j}{\partial x_i}+\frac{\partial u'_i}{\partial x_j}\right]} \quad \text{is the stress redistribution term} \tag{2.22}$$

$$\epsilon_{ij} = 2\nu\left(\overline{\frac{\partial u'_i}{\partial x_k}\frac{\partial u'_j}{\partial x_k}}\right) \quad \text{is the viscous destruction term} \tag{2.23}$$

and

$$C_{ijk} = \overline{u'_iu'_ju'_k}+\frac{1}{\rho}\overline{p'u'_i}\delta_{jk} + \frac{1}{\rho}\overline{p'u'_j}\delta_{ik} \quad \text{are the diffusive transport terms.} \tag{2.24}$$

One may think that it is now possible to close equation (2.15), and hence all of the equations, as the Reynolds stresses are now provided for. Upon closer inspection of equation (2.21), however, it can be seen that (2.22), (2.23) and (2.24) are not closed due to the appearance of the unknown fluctuating velocities. One can go further to derive higher statistical moments to close the equations, but terms created therein contain variables that are, again, not defined. This phenomena is known as the *closure problem*, whereby the introduction of transport equations for lower order statistical correlations, leads to unknown higher order correlations, and a closed set of equations can not be obtained. Therefore, to close the RANS equations, approximations, or *models* are required based on physical assumptions, leading to an area that has become a research topic in its own right, namely *turbulence modelling*.

2.4 Turbulence modelling

The purpose of turbulence modelling is to provide the extra terms required to close the RANS equations. Some of the most popular models are described below.

2.4.1 Zero and one equation models

Early models closed the RANS equations by modelling the Reynolds stresses in an algebraic fashion, such that estimated quantities of the mean flow were used to approximate τ'_{ij}. The most well known models use the *Boussinesq Eddy Viscosity* hypothesis, $\tau'_{ij} = -2\nu_T \overline{S}_{ij}$, or in its updated form

$$\tau'_{ij} = -2\nu_T \overline{S}_{ij} + \frac{2}{3} k \delta_{ij} \tag{2.25}$$

where ν_T is termed the turbulent, or *Eddy Viscosity* and $\overline{S}_{ij}$ is the strain rate tensor

$$\overline{S}_{ij} = \frac{1}{2}\left(\frac{\partial U_i}{\partial x_j} + \frac{\partial U_j}{\partial x_i}\right) \quad . \tag{2.26}$$

Boussinesq made this approximation in analogy to the viscous stress tensor in the momentum equation, $\sigma_{ij} = 2\nu S_{ij}$. After substituting (2.25) into the RANS equations, the only term to be modelled is the eddy viscosity itself. Of all the algebraic (or *zero* equation models), Prandtl's mixing length hypothesis is the most well known.

The eddy viscosity, defined as the ratio of a turbulent length scale, l_0, to a turbulent time scale, t_0, of the largest eddies,

$$\nu_T = \frac{l_0^2}{t_0} \tag{2.27}$$

was refined by Prandtl (1925) when he suggested that the eddy viscosity could be represented by the mean velocity gradient

$$\nu_T = l_0^2 \left|\frac{\mathrm{d}U}{\mathrm{d}y}\right| \tag{2.28}$$

where the mixing length is defined as

$$l_0 = \kappa y \tag{2.29}$$

with κ the Von Kármán constant and y the normal distance from a wall. In (2.28), the time scale is implied through the mean velocity gradient leaving only the length scale to be determined in order to complete the model. Equation (2.29) is commonly used to provide this quantity in the case of boundary layer flows (Launder and Spalding, 1972) with $\kappa = 0.4$.

Prandtl's mixing length model, has been used successfully to provide predictions for free shear flows such as far wakes, mixing layers and jets (Wilcox, 1994). However, despite this, the model has some serious limitations. Firstly it cannot be applied to recirculating flows due to the uni-directional formulation of the eddy viscosity. Also, the transport of the turbulent quantities is not considered, meaning upstream and downstream conditions have no effect on the turbulence. The empirical nature of the model means that it is difficult to use for flows other than shear layers it was designed for. Variations of Prandtl's algebraic model are provided by Smith and Cebeci (1967) and Baldwin and Lomax (1978), where different formulations of the eddy viscosity are applied for different distances from a solid wall. Although these models are an improvement over Prandtl's original model and have been used to predict boundary layer and channel flows well (Wilcox, 1994), they still suffer from the same limitations.

The next method of closing the RANS equations is the implementation of so called *one equation* turbulence models. Instead of just using algebraic methods to close the equations, a transport equation for the turbulent kinetic energy, k, is derived to provide the value of the turbulent timescale of the large eddies. By contracting equation (2.21), the transport equation for k is,

$$U_k \frac{\partial k}{\partial x_k} = -\tau'_{ik} \frac{\partial U_i}{\partial x_k} - \epsilon - \frac{\partial}{\partial x_k} \left(\frac{1}{2} \overline{u'_i u'_i u'_k} + \frac{1}{\rho} \overline{p' u'_i} \delta_{ik} \right) + \nu \nabla^2 k \tag{2.30}$$

where $k = \frac{1}{2}\tau'_{ii}$. The third term on the right hand side of (2.30) represents the turbulent diffusion of k and needs to be modelled. This is done using the gradient

diffusion method,

$$\frac{1}{2}\overline{u_i' u_i' u_k'} + \frac{1}{\rho}\overline{p' u_i'} = -\frac{\nu_T}{\sigma_k}\frac{\partial k}{\partial x_k} \tag{2.31}$$

where σ_k is the effective Prandtl number for the diffusion of k. The dissipation rate of kinetic energy, ϵ, also needs to be modelled due to an inability to quantify it in terms of known flow parameters. ϵ is governed by the larger scales in the turbulence and so its formulation is given in terms of k and the large eddy length scale, l_0. By dimensional analysis

$$\epsilon = C_D \frac{k^{3/2}}{l_0} \tag{2.32}$$

is the modelled form of ϵ, and C_D is an empirical constant. The value of C_D is found by examining simple turbulent flows experimentally and fitting numerical predictions to them. Launder and Spalding (1972) found a value of C_D to be 0.08 for near wall flow. The velocity scale of the large turbulent eddies is deemed, by dimensional considerations, to vary as $\sqrt{k}$, thus the eddy viscosity is given as

$$\nu_T = \sqrt{k}\, l_0 \,, \tag{2.33}$$

and so the RANS equations are closed upon specifying the length scale, l_0. This is usually done empirically using experimental data, or, for shear flows, the mixing length of Prandtl can be used.

Other popular one equation models include that of Spalart and Allmaras (1992), which provides a transport equation for the eddy viscosity. One equation models, in general, perform better than zero equation models due to a transport equation that provides knowledge about a turbulent quantity of the flow, namely the turbulent timescale, t_0. Despite the potential for better predictive capability of the one equation models over their zero equation counterparts, for simple shear flows the zero equation models perform equally well (Murty, 2002) leading to the conclusion that use of one equation models is only worthwhile for more complex flows, or where turbulence information (such as k) is needed.

The limitations of one equation models are based on the empirical specification of the length scale. The latter is *not* a feature of turbulent flows that extends

over all applications, but is a property of the local conditions of the flow, such as boundary proximity etc. This means that without knowledge of flow history, it is very difficult to specify a length scale for the entire flow domain leading to inaccuracies in predictions.

2.4.2 Two equation models

Two equation models represent improvements over one equation models by providing a transport equation for both the time *and* length scales of turbulent motion. Most formulations of the transport equation for the length scale do not feature the length scale explicitly. Kolmogorov (1942) first introduced an equation for the length scale using $\sqrt{k}/l_0$ (the frequency of dissipation of energy), but ϵ, the dissipation rate, is by far the most common choice for modern two equation models. The general transport equation for the length scale can be expressed as the transport of a general quantity $z = k^m l_0^n$ where m and n are constants,

$$U_k \frac{\partial z}{\partial x_k} = \frac{\partial}{\partial x_k}\left(\frac{\nu_T}{\sigma_z}\frac{\partial z}{\partial x_k}\right) - C_{z1}\frac{z}{k}\tau'_{ik}\frac{\partial U_i}{\partial x_k} - C_{z2}z\frac{k}{\nu_T} + S_z \tag{2.34}$$

where σ_z, C_{z1} and C_{z2} are closure coefficients and S_z is a general source term. From this equation the length scale is extracted from k and z.

The k-ϵ model

The k-ϵ model uses a transport equation for the turbulent dissipation rate, ϵ, as a method of determining the turbulent length scale. The form of the model was originally prescribed by Jones and Launder (1972), but then re-tuned by Launder and Sharma (1974) to yield its now 'standard' representation as given below. The time scale is described according to the previous transport equation for k (2.30). An equation for ϵ can be determined by taking

$$2\nu\overline{\frac{\partial u'_i}{\partial x_j}\frac{\partial}{\partial x_j}(\mathcal{N}u'_i)} = 0 \tag{2.35}$$

which eventually leads to

$$
\begin{aligned}
U_i \frac{\partial \epsilon}{\partial x_i} \quad = \quad & -2\nu \overline{\frac{\partial u_j'}{\partial x_i} \frac{\partial u_j'}{\partial x_k}} \frac{\partial U_i}{\partial x_k} - 2\nu \overline{\frac{\partial u_i'}{\partial x_j} \frac{\partial u_k'}{\partial x_j}} \frac{\partial U_i}{\partial x_k} \\
& -2\nu \overline{\frac{\partial u_i'}{\partial x_k} \frac{\partial u_i'}{\partial x_m} \frac{\partial u_k'}{\partial x_m}} - 2\nu \overline{u_k' \frac{\partial u_i'}{\partial x_j}} \frac{\partial^2 U_i}{\partial x_k \partial x_j} \\
& -2\nu \frac{\partial}{\partial x_k} \left(\overline{\frac{\partial p'}{\partial x_m} \frac{\partial u_k}{\partial x_m}} \right) - \nu \frac{\partial}{\partial x_k} \left(\overline{u_k' \frac{\partial u_i'}{\partial x_m} \frac{\partial u_i'}{\partial x_m}} \right) \\
& -2\nu^2 \overline{\frac{\partial^2 u_i'}{\partial x_k \partial x_m} \frac{\partial^2 u_i'}{\partial x_k \partial x_m}} + \nu \nabla^2 \epsilon \quad . \qquad (2.36)
\end{aligned}
$$

The first four terms of (2.36), relate to the production of dissipation P_ϵ, the next two to turbulent diffusion of dissipation, D_ϵ and the penultimate term to the destruction of dissipation. All of these terms require modelling in some form due to the inherent inability to resolve the higher correlations present.

Firstly, Jones and Launder (1972) used dimensional considerations to provide an expression for the eddy viscosity

$$\nu_T = C_\mu \frac{k^2}{\epsilon} \qquad (2.37)$$

where C_μ is an empirical coefficient found by fitting with experiments. The diffusion term in equation (2.36) is modelled in a similar fashion to that in the k equation (2.31) by using gradient diffusion,

$$D_\epsilon = \frac{\partial}{\partial x_k} \left(\frac{\nu_T}{\sigma_\epsilon} \frac{\partial \epsilon}{\partial x_k} \right) \qquad (2.38)$$

where σ_ϵ, the Schmidt number, has a similar meaning as in (2.31). The production term is modelled by assuming production of turbulent dissipation to be proportional to production of turbulent kinetic energy due to energy conservation,

$$P_\epsilon = C_{\epsilon 1} \frac{\epsilon}{k} P \qquad (2.39)$$

where $C_{\epsilon 1}$ is an empirical coefficient and P is the production of turbulent kinetic energy from (2.30),

$$P = -\tau_{ik}' \frac{\partial U_i}{\partial x_k} \quad . \qquad (2.40)$$

Coefficient	Value
$C_{\epsilon 1}$	1.44
$C_{\epsilon 2}$	1.92
C_{μ}	0.09
σ_k	1.0
σ_{ϵ}	1.3

TABLE 2.1: Values of coefficients used in $k-\epsilon$ model, Launder and Sharma (1974)

The next term to be modelled is the destruction of dissipation term. As for the destructive term in the k equation (2.30), the destruction of dissipation is governed by the large scales of the flow, the length and time scales. By dimensional analysis

$$\phi_{\epsilon} = C_{\epsilon 2}\frac{\epsilon^2}{k} \tag{2.41}$$

with $C_{\epsilon 2}$ a dimensionless, empirical constant.

Including the above expressions and after employing the eddy viscosity hypothesis (2.25), the final form of the modelled equation for the dissipation rate is

$$\begin{aligned} U_i\frac{\partial \epsilon}{\partial x_i} &= \frac{\partial}{\partial x_k}\left(\frac{\nu_T}{\sigma_{\epsilon}}\frac{\partial \epsilon}{\partial x_k}\right) + \nu\nabla^2\epsilon \\ &+ C_{\epsilon 1}\frac{\epsilon}{k}\nu_T\left(\frac{\partial U_i}{\partial x_k} + \frac{\partial U_k}{\partial x_i}\right)\frac{\partial U_i}{\partial x_k} - C_{\epsilon 2}\frac{\epsilon^2}{k} \quad . \end{aligned} \tag{2.42}$$

The closure coefficients reported by Launder and Sharma (1974) are given in table 2.1.

To complete the closure, wall functions (see Chapter 3) must be used to extend the model for application at walls. This is due to the destruction of dissipation term in equation (2.42). At a wall, ϵ is finite whilst k must reduce to zero due to the no-slip condition. This means that $C_{\epsilon 2}(\epsilon^2/k)$ represents a singularity (Gatski and Rumsey, 2002).

The k-ω model

In this two equation model, ω, instead of ϵ is used to provide the length scale. ω is a measure of the inverse time scale of the dissipation of turbulence energy, or, as it is

Coefficient	Value
α	$\frac{5}{9}$
β	$\frac{3}{40}$
β^*	0.09
σ_ω	2
σ^*_ω	2

TABLE 2.2: Values of coefficients used in $k-\omega$ model, Wilcox (1994)

more commonly referred to, the rate of dissipation per unit turbulent kinetic energy. Wilcox (1994) completed the modern formulation of the model after earlier work by Kolmogorov (1942) and Saffman (1970). In Wilcox's model, the eddy viscosity is represented as the ratio of turbulent kinetic energy to ω,

$$\nu_T = \frac{k}{\omega}, \tag{2.43}$$

and the transport equation for ω as

$$U_j \frac{\partial \omega}{\partial x_j} = \alpha \frac{\omega}{k} \tau'_{ij} \frac{\partial U_i}{\partial x_j} - \beta \omega^2 + \frac{\partial}{\partial x_j} \left[\left(\nu + \frac{\nu_T}{\sigma_\omega} \right) \frac{\partial \omega}{\partial x_j} \right]. \tag{2.44}$$

The first term on the right hand side of (2.44) represents the production of ω, while the second represents its turbulent destruction, with gradient diffusion employed for the turbulent diffusion term. The equation for the transport of turbulent kinetic energy is slightly modified from that used in the $k-\epsilon$ model,

$$U_j \frac{\partial k}{\partial x_j} = \tau'_{ij} \frac{\partial U_i}{\partial x_j} - \beta^* k \omega + \frac{\partial}{\partial x_j} \left[\left(\nu + \frac{\nu_T}{\sigma^*_\omega} \frac{\partial k}{\partial x_j} \right) \right] \tag{2.45}$$

where the dissipation rate, ϵ, is given by

$$\epsilon = \beta^* \omega k. \tag{2.46}$$

The closure coefficients given by Wilcox (1994) are shown in table 2.2.

The advantage that the $k-\omega$ model has over the $k-\epsilon$ model is its ability to be integrated to the wall. This allows better resolution of the viscous sublayer (see Chapter 3), especially for flows where the mean flow penetrates this layer and the local turbulent Reynolds number is low. These factors enable the model to cope

better for transitional regions of the flow. This also means that wall functions (see later) are not necessarily needed, as opposed to the use of the $k-\epsilon$ model where it is compulsory in its standard form. However, low-Reynolds number versions of the $k-\epsilon$ model, integrated through the viscous sublayer, have been developed (see Yaras and Grosvenor, 2003) as is discussed next.

Discussion of two equation models

The main disadvantage of two equation modelling is the use of the eddy viscosity hypothesis since models which employ this term to represent the Reynolds stresses cannot account for complex flows where the turbulence is highly anisotropic. The eddy viscosity hypothesis will always produce isotropic turbulence for the normal stresses (the diagonal component of the Reynolds stress tensor). Speziale (1996) noted that without a method of determining the anisotropic nature of the Reynolds stresses, it is impossible to predict secondary motions due to differences in the Reynolds stresses, such as flows in square ducts. Researchers studying swirling flows (Chen and Lin, 1999; Wall and Taulbee, 1995) have shown the inability of these models to capture the mean flow, often showing behaviour such as premature development of solid body rotation. These researchers have also shown that flows with high streamline curvature are also poorly represented by these models due to their inability to capture the shear stresses correctly.

Yaras and Grosvenor (2003) used low Reynolds number versions of two equation models to solve axisymmetric, separating and swirling flow problems. In their study the two-layer $k-\epsilon$ model of Rodi (1988), the $k-\omega$ model of Wilcox (1994), the Shear Stress Transport (SST) model of Menter (1994), the nonlinear $k-\epsilon$ model of Chien (1982) and the eddy viscosity transport model of Spalart and Allmaras (1992) were compared. All of the models incorporated a streamline curvature correction term to account for areas of high streamline curvature where standard eddy viscosity models are inaccurate.

The advantage these latter models possess over the standard $k-\epsilon$ model, is that integration of the transport equations through the viscous sublayer is achievable.

This removes the requirement of wall functions to approximate the flow in this region of the boundary layer. Models such as the SST model and Rodi's two-layer model, split the flow domain into two distinct regions and model each separately: the SST model uses the $k-\omega$ model in near wall regions and the $k-\epsilon$ model far from the walls.

Yaras and Grosvenor found that the velocity profiles for a separating flow were predicted well. However the coefficients of pressure and friction were not resolved for the separation region. The model of Chien, did not reproduce separation whilst Rodi's model did not produce the velocity reversal at this point. For the swirling flow case, all models showed poor agreement with experiment, and in particular predicted a premature solid body rotation. The authors reported that the $k-\omega$ model was impossible to converge for this flow whilst giving meaningful results. Addition of curvature correction did not improve results, with the SST model giving the least acceptable results for tangential velocity.

Speziale (1996) recommended that two equation models with an anisotropic representation of the turbulence using a non-linear formulation are the minimum required to close the RANS equations. Non-linear eddy viscosity models employ an expansion of the strain rate tensor in (2.25) to include non-linear combinations of S_{ij}. In these models the Reynolds stresses are given by an algebraic formulation, and not a transport equation. This immediately shows that these types of closures cannot account for history effects of the turbulence in the flow. Despite the promise of more accurate prediction of flows using non-linear, two equation models (such as that of Speziale (1987)), their formulation tends to be ad hoc, with extra terms added to account for previous model failings.

A nonlinear $k-\epsilon$ model was proposed by Shih *et al.* (1997) and tested against data for an axially rotating pipe and swirling flow in a combustor. The Reynolds stresses were modelled by cubic terms in the mean velocity gradients, with additional rotational terms. For both flow cases, the model agreed better with the experimental data compared to the standard $k-\epsilon$ model.

Wall and Taulbee (1995) developed an improved algebraic stress model (ASM).

The algebraic equation set was improved so as to be applicable over a large range of turbulence anisotropies compared to standard algebraic models which are only applicable for constant anisotropy. Additional rotation-dependent terms were also added. The nonlinear solution to these equation sets was implemented as a two-equation model to predict the flow in a swirling jet. The results for the new model were in reasonable agreement with experimental data, and bettered those of the older ASM and the standard $k - \epsilon$ models. However, the results of the second moment closure of Launder *et al.* (1975) showed better predictions than any of the other models when compared with experiment. Wall and Taulbee (1995) attributed this to the inability of the algebraic models to take into account the history of the turbulence.

Yuan and So (1998) used two-equation models and a low Reynolds number second moment closure to study swirling and rotating flows. Two low Reynolds number, two-equation models were modified by using the anisotropic stress representation of Speziale (1987) and the anisotropic dissipation rate model of Speziale and Gatski (1997) to account for turbulence anisotropy. The models were tested on two swirling flows in straight pipes with different inlet conditions. For both flows, the anisotropic two-equation models performed poorly in comparison to the experimental data for the mean velocity profiles. Along the axis of the pipe, a solid body rotation is predicted prematurely by the two equation models, with the dip in velocity close to the axis grossly under-predicted. Only the second moment closure model predicted adequate results.

As alluded to above, two-equation models are inadequate for solving flows with high streamline curvature and anisotropy, such as is present in swirling flows, despite some successes (Shih *et al.*, 1997). The natural extension to modelling turbulence is to look at the higher correlations of turbulence, such as the Reynolds stresses, and how they are transported. This leads to the modelling of the Reynolds stress transport equation (2.21) itself.

2.5 Second moment closures

Second moment closures use the transport equation for the Reynolds stresses (2.21) to determine turbulent motion. As mentioned previously, terms (2.22), (2.23) and (2.24) lead to an open set of equations and models need to be developed for accurate prediction using mean flow quantities. The first closure for this equation was made by Rotta (1951), where the pressure redistribution term (2.22) was modelled in the absence of mean flow gradients (known as the return to isotropy model). Subsequent additions to the closure of the Reynolds stress equations were made by Daly and Harlow (1970) and Hanjalic and Launder (1972), where the latter made adequate predictions of thin shear flows using a simplified set of equations for the Reynolds stresses.

The model of Launder *et al.* (1975) (LRR) proved to be a major improvement to Reynolds stress modelling. The work made significant steps in improving the pressure redistribution term (also known as the pressure-strain correlation), by expressing the coefficients of the rapid term (that depending on the mean velocity gradients) with the anisotropy of the Reynolds stresses. This, coupled with the inclusion of an estimate for near wall turbulence, led to the use of this model for more complex flows such as an axisymmetric pipe contraction (Launder *et al.*, 1975).

Further improvements to the model were made by Gibson and Launder (1978), where the near wall terms were modified to enhance the prediction of pressure 'echo' effects - the reflection of pressure fluctuations at the wall. Lumley (1978) described the need for nonlinear modelling of the pressure-strain correlation by expressing the coefficients of the mean velocity gradients in terms of a nonlinear function of the anisotropy tensor. Another important addition was that of the realisability condition. This condition identifies that all non-negative quantities, such as turbulent kinetic energy, must remain so. Lumley developed a coordinate invariant formulation for the constraints allowing them to be applied to any general curvilinear coordinate system.

Speziale *et al.* (1991) created a new pressure-strain model by developing a general formulation from which a hierarchy of models can be taken. By examining homo-

geneous turbulence, and using a tensor invariant formulation, they created a model that is quadratic in the Reynolds stress anisotropy for the rapid term (discussed below). This led to an improvement over the LRR model which only expressed the rapid term using linear anisotropic coefficients for the mean velocity gradients. Another advantage of the model is the ability to predict flows well without the need for wall 'echo' terms as used in the LRR model. The model was tested against the LRR and FLT model (Fu, Launder and Tselepidakis, 1987) for rotating shear flow, where it outperformed both when compared against LES data for the decay of turbulent kinetic energy.

An interesting note was made by Speziale *et al.* (1991) concerning the nature of the general hierarchy of pressure-strain models. The general model formed by the authors, which constitutes all forms of the pressure-strain terms, inherently cannot capture all the features of plane homogeneous flow. It was argued that adding more complex terms to the model that are nonlinear in the anisotropy tensor would not overcome this problem but only potentially increase the accuracy of an inadequate formulation.

For swirling and rotating flows many forms of second moment closure have been used. Liu *et al.* (1998) showed that the second moment closure of Launder *et al.* (1975) performed better than the standard $k-\epsilon$, and Renormalisation Group (RNG) $k-\epsilon$ model in a typical combustor geometry. For the two equation models, the tangential velocity predicted showed a premature solid body rotation, where the free vortex type flow decayed into the forced vortex type too early along the length of the pipe. Sharif and Wong (1995) compared a nonlinear $k-\epsilon$ model with an algebraic stress model and full second moment closure (Gibson and Launder, 1978) for swirling flow in a combustor. The algebraic and second moment closures predicted the experimental data well for the mean flow quantities with little difference between them. The nonlinear $k-\epsilon$ model gave poor results in comparison, suffering from the previous faults of two equation models. The turbulent quantities were not predicted well for any of the models, showing that improvement in the modelling of these quantities is needed for swirling and rotating flow.

Chen and Lin (1999) studied two swirling flows using the SSG model of Speziale *et al.*

(1991) and the 'Isotropisation of Production' model of Fu, Launder and Leschziner (1987), a development of the LRR model of Launder *et al.* (1975). For the strongly swirling case (swirl number 2.25) both second moment closures predicted results in agreement with the experiments, in contrast to the $k-\epsilon$ model. However, for less strongly swirling flow (swirl number 0.85), there was a marked difference between them. The SSG model was closer in agreement with the experiments than the model by Fu *et al.* This was attributed to the additional quadratic terms in the pressure-strain correlation (missing in the linear pressure-strain term of Fu *et al*). The extra terms in the SSG model were able to capture the small shear stresses more accurately, with the model of Fu *et al* overestimating them due to a lack of sink terms in its formulation.

Younis *et al.* (1996) compared the use of three different pressure-strain models on free turbulent jets with and without swirl. The models used were the SSG model of Speziale *et al.* (1991) and the two forms of the LRR model given by Launder *et al.* (1975). For the axisymmetric and plane jets the findings of the different models were of comparable accuracy with experiment. For the swirling jet, however, the SSG model was able to predict the turbulent quantities with a greater accuracy than those predicted by the two LRR variants. This was due to the extra terms in the SSG model which were able to partly counteract the effect of some of the standard terms (such as the erroneous large negative $\overline{uw}$ shear stress predicted by all models near the jet centreline).

Even though Speziale *et al.* (1991) developed a pressure-strain correlation that is quadratic in the stress anisotropy tensor and hinted that higher nonlinearities may not be beneficial, some authors developed cubic models. The model by Fu, Launder and Tselepidakis (1987) represents the pressure-strain correlation with cubic terms in the anisotropy tensor to try to capture the effect of high strain which could be used in flows with high streamline curvature. Speziale *et al.* (2000) argued, however, that cubic terms show little advantage over the quadratic models. This, unfortunately, has not been demonstrated in the literature to the author's knowledge for swirling flows.

2.5.1 Stress redistribution term modelling

Launder, Reece and Rodi model

One of the most widely used Reynolds stress closures is that of Launder *et al.* (1975) (hereafter denoted as LRR). The main thrust of their work was to develop a successful model for the pressure-strain correlation (2.22). The representation of this term takes the form of Chou (1945), whereby a Poisson equation for the fluctuating pressure is obtained by taking the divergence of equation (2.18) (note that from this point onwards the prime notation for fluctuating quantities has been dropped),

$$\frac{\partial^2 p}{\partial x_l^2} = -\frac{\partial^2}{\partial x_l \partial x_m}\left(\rho u_l u_m - \rho\overline{u_l u_m}\right) - 2\rho\frac{\partial U_l}{\partial x_m}\frac{\partial u_m}{\partial x_l}. \tag{2.47}$$

This can then be integrated using Green's functions to give p at position $\mathbf{x}$

$$\frac{p}{\rho} = \frac{1}{4\pi}\int_V \left(\frac{\partial^2}{\partial x_l' \partial x_m'}\left(u_l' u_m' - \overline{u_l' u_m'}\right) + 2\frac{\partial U_l'}{\partial x_m'}\frac{\partial u_m'}{\partial x_l'}\right)\frac{\mathrm{d}V}{|\mathbf{x}' - \mathbf{x}|} \tag{2.48}$$

where the primed variables are denoted as being at the location $\mathbf{x}'$. If equation (2.48) is multiplied by $(\partial u_i/\partial x_j + \partial u_j/\partial x_i)$ and then ensemble averaging is used, an exact equation for Π_{ij} (2.22) is obtained.

$$\begin{aligned}\overline{\frac{p}{\rho}\left(\frac{\partial u_i}{\partial x_j} + \frac{\partial u_j}{\partial x_i}\right)} = \frac{1}{4\pi}\int_V \Bigg[& \underbrace{\overline{\left(\frac{\partial^2 (u_l u_m)}{\partial x_l \partial x_m}\right)'\left(\frac{\partial u_i}{\partial x_j} + \frac{\partial u_j}{\partial x_i}\right)}}_{\phi_{ij,1}} \\ & + \underbrace{2\left(\frac{\partial U_l}{\partial x_m}\right)'\overline{\left(\frac{\partial u_m}{\partial x_l}\right)'\left(\frac{\partial u_i}{\partial x_j} + \frac{\partial u_j}{\partial x_i}\right)}}_{\phi_{ij,2}}\Bigg]\frac{\mathrm{d}V}{|\mathbf{x}' - \mathbf{x}|} \\ & + \underbrace{\frac{1}{4\pi}\int_A \left[\frac{1}{r}\frac{\partial}{\partial n'}\overline{p'\left(\frac{\partial u_i}{\partial x_j} + \frac{\partial u_j}{\partial x_i}\right)} - \overline{p'\left(\frac{\partial u_i}{\partial x_j} + \frac{\partial u_j}{\partial x_i}\right)}\frac{\partial}{\partial n'}\left(\frac{1}{r}\right)\right]\mathrm{d}A}_{\phi_{ij}^w}\end{aligned} \tag{2.49}$$

The meanings of the above terms are provided by Hanjalic and Jakirlic (2002). $\phi_{ij,1}$ represents the return to isotropy of non-isotropic Reynolds stresses in the absence of mean strain, body force and wall effects. The pressure fluctuations force the Reynolds stresses into a more isotropic state. This term is more commonly known

as the 'slow term'. $\phi_{ij,2}$ is the isotropisation of the production of the Reynolds stresses by the mean strain rate. The pressure fluctuations effect the dominant stress component by feeding it into the weaker components, returning the turbulence to a more isotropic state. The pressure fluctuations also slow the feeding of turbulence production into the dominant stress component. This term is more commonly known as the 'rapid term'. ϕ_{ij}^{w} represents $\phi_{ij,1}$ and $\phi_{ij,2}$ in the region of a solid wall. Here, the boundary acts so as to impede the isotropisation of turbulence by the pressure fluctuations (known as the blocking effect; Hanjalic and Jakirlic (2002)) increasing turbulence anisotropy. However, the pressure fluctuations are reflected from the wall surface, increasing the isotropisation of the turbulence. Despite this, the blocking effect is the larger of the two, leading to strong Reynolds stress anisotropy in the near wall region.

To close the $\phi_{ij,1}$ term, Launder *et al.* (1975) used the model of Rotta (1951),

$$\phi_{ij,1} = -C_1 \frac{\epsilon}{k} \left(\overline{u_i u_j} - \frac{2}{3} \delta_{ij} k \right) \tag{2.50}$$

where C_1 is an empirical constant. It can be seen that this model is negatively proportional to the anisotropy tensor,

$$a_{ij} = \frac{\tau_{ij}}{2k} - \frac{1}{3} \delta_{ij} \tag{2.51}$$

having the effect of increasing the isotropy of the turbulence by a measure of its anisotropy. The rapid term of the pressure-strain correlation, $\phi_{ij,2}$, is also modelled following an approximation by Rotta (1951),

$$\phi_{ij,2} = \frac{\partial U_l}{\partial x_m} \left(b_{ljmi} + b_{limj} \right) \tag{2.52}$$

Launder *et al.* (1975) expressed the fourth rank tensor, b_{ljmi}, as a linear combination of the Reynolds stresses,

$$\begin{aligned} b_{ljmi} &= \alpha \delta_{lj} \overline{u_m u_i} + \beta (\delta_{ml} \overline{u_i u_j} + \delta_{mj} \overline{u_i u_l} + \delta_{il} \overline{u_m u_j} + \delta_{ij} \overline{u_m u_l}) \\ &+ C_2 \delta_{mi} \overline{u_l u_j} + [\eta \delta_{mi} \delta_{lj} + \nu (\delta_{ml} \delta_{ij} + \delta_{mj} \delta_{il})] k \end{aligned} \tag{2.53}$$

where

$$\begin{aligned}
\alpha &= \frac{1}{11}(4C_2 + 10) \\
\beta &= -\frac{1}{11}(2 + 3C_2) \\
\eta &= -\frac{1}{55}(50C_2 + 4) \\
\nu &= \frac{1}{55}(20C_2 + 6)
\end{aligned} \tag{2.54}$$

and C_2 is an empirical constant. Combining the above equations leads to the model,

$$\begin{aligned}
\phi_{ij,2} = &-\frac{C_2 + 8}{11}\left(P_{ij} - \frac{2}{3}P\delta_{ij}\right) \\
&-\frac{30C_2 - 2}{55}k\left(\frac{\partial U_i}{\partial x_j} + \frac{\partial U_j}{\partial x_i}\right) - \frac{8C_2 - 2}{11}\left(D_{ij} - \frac{2}{3}P\delta_{ij}\right)
\end{aligned} \tag{2.55}$$

where P_{ij} represents the production of turbulence,

$$P_{ij} = -\left(\overline{u_i u_k}\frac{\partial U_j}{\partial x_k} + \overline{u_j u_k}\frac{\partial U_i}{\partial x_k}\right) \tag{2.56}$$

and

$$D_{ij} = -\left(\overline{u_i u_k}\frac{\partial U_k}{\partial x_j} + \overline{u_j u_k}\frac{\partial U_k}{\partial x_i}\right). \tag{2.57}$$

Launder *et al.* (1975) noted that equation (2.52) did not approximate the effect of the mean straining on the pressure-strain term near the wall where high mean velocity gradients vary rapidly. The surface integral term in equation (2.49) becomes very significant if the size of the energetic turbulent eddies is of the order of the distance from the wall, hence the surface integral was re-expressed for a plane wall as,

$$\begin{aligned}
\phi_{ij}^w = \frac{1}{4\pi}\int_V \Bigg[&\overline{\left(\frac{\partial(u_l u_m)}{\partial x_l \partial x_m}\right)'\left(\frac{\partial u_i}{\partial x_j} + \frac{\partial u_j}{\partial x_i}\right)} \\
&+2\left(\frac{\partial U_1}{\partial x_2}\right)'\overline{\left(\frac{\partial u_2}{\partial x_1}\right)'\left(\frac{\partial u_i}{\partial x_j} + \frac{\partial u_j}{\partial x_i}\right)}\Bigg]\left(\frac{1}{|\mathbf{x}' - \mathbf{x}|} + \frac{1}{|\mathbf{x}' - \mathbf{x}^*|}\right) dV
\end{aligned} \tag{2.58}$$

where x_2 is the coordinate normal to the surface, $\mathbf{x}^*$ is the image of point $\mathbf{x}$ behind the wall. This equation was modelled as

$$\phi_{ij}^w = \left[C_1'\frac{\epsilon}{k}\left(\overline{u_i u_j} - \frac{2}{3}\delta_{ij}k\right) + \frac{\partial U_l}{\partial x_m}(c_{ljmi} + c_{limj})\right] f\left(\frac{l}{x_2}\right) \tag{2.59}$$

where c_{ljmi} is expressed in a similar way to b_{ljmi} in terms of the Reynolds stresses,

$$c_{ljmi} = \alpha'\delta_{ij}\overline{u_m u_i} + \beta'(\delta_{ml}\overline{u_i u_j} + \delta_{mj}\overline{u_i u_l} + \delta_{il}\overline{u_m u_j} + \delta_{ij}\overline{u_m u_l})$$
$$+C_2'\delta_{mi}\overline{u_l u_j} + [\eta'\delta_{mi}\delta_{lj} + \nu'(\delta_{ml}\delta_{ij} + \delta_{mj}\delta_{il})]k \qquad (2.60)$$

Equation (2.59) shows that the effect of the wall is dependent on the anisotropy tensor (2.51) which gives a term similar to equation (2.50) but with the *opposite* sign, increasing the turbulence anisotropy. The mean strain is also represented by the second term in (2.59) and contributes to the wall effect.

Launder *et al.* (1975) modelled the effect of the mean straining as

$$\frac{\partial U_l}{\partial x_m}(c_{ljmi} + c_{limj}) = C_2'(P_{ij} - D_{ij}) + \zeta' k\left(\frac{\partial U_i}{\partial x_j} + \frac{\partial U_j}{\partial x_i}\right). \qquad (2.61)$$

The function $f(l/x_2)$ in (2.59) is a wall proximity function that must decrease to zero as the distance from the wall is increased. l is the length scale of the energy containing eddies and is approximated by Launder *et al.* (1975) as the dissipation length scale $k^{\frac{3}{2}}/\epsilon$. The values attributed to C_1' and C_2' are 0.5 and 0.06, respectively, and with a coefficient of 4.0 for the wall proximity function the final model for near wall effects is given as,

$$\phi_{ij}^w = \left[0.125\frac{\epsilon}{k}\left(\overline{u_i u_j} - \frac{2}{3}k\delta_{ij}\right) + 0.015(P_{ij} - D_{ij})\right]\frac{k^{\frac{3}{2}}}{\epsilon x_2}. \qquad (2.62)$$

The rest of the work by Launder *et al.* (1975) is for closing the turbulent diffusion term (2.24) and dissipation rate tensor (2.23). Launder *et al.* (1975) only modelled the turbulent diffusion part of the former, making the assumption that for high Reynolds numbers, diffusion by pressure fluctuations is negligible. Hence, the isotropic model of Daly and Harlow (1970) was used,

$$-\overline{u_i u_j u_k} = c_s\frac{k}{\epsilon}\overline{u_k u_l}\frac{\overline{\partial u_i u_j}}{\partial x_l} \qquad (2.63)$$

where c_s is an empirical constant. Another model was derived by Launder *et al.* (1975), by simplifying the transport equation for the third moments. This was

Coefficient	Value
C_1	1.5
C_2	0.4
C_1'	0.5
C_2'	0.06
C_s	0.25
$C_{\epsilon 1}$	1.44
$C_{\epsilon 2}$	1.90
C_ϵ	0.15

TABLE 2.3: Values of coefficients used in LRR model, Launder *et al.* (1975)

shown, however, to provide little improvement over the Daly and Harlow model.

The dissipation rate tensor, was modelled under the assumption of isotropic dissipation,

$$\epsilon_{ij} = 2\nu \overline{\frac{\partial u_i}{\partial x_j}\frac{\partial u_j}{\partial x_i}} = \frac{2}{3}\delta_{ij}\epsilon \tag{2.64}$$

where ϵ is the dissipation rate. Launder *et al.* (1975) modelled this term from its transport equation (2.36) applied at high Reynolds numbers as,

$$U_i\frac{\partial \epsilon}{\partial x_i} = C_\epsilon \frac{\partial}{\partial x_k}\left(\frac{k}{\epsilon}\overline{u_k u_l}\frac{\partial \epsilon}{\partial x_l}\right) - C_{\epsilon 1}\frac{\epsilon}{k}\overline{u_i u_k}\frac{\partial U_i}{\partial x_k} - C_{\epsilon 2}\frac{\epsilon^2}{k} \quad , \tag{2.65}$$

where C_ϵ, $C_{\epsilon 1}$ and $C_{\epsilon 2}$ are all empirical coefficients. The empirical coefficients used in the model were decided by numerical experiments, and are shown in table 2.3. Test cases used for model calibration included homogeneous shear flow, near wall turbulent flows and decay of grid turbulence (see Launder *et al.*, 1975).

Speziale, Sarkar and Gatski model

A newer method for closure of the Reynolds stress transport equations was proposed by Speziale *et al.* (1991). This model, like the LRR model before it, focuses on the pressure-strain correlation, deriving its form, however, from a coordinate frame invariant methodology, meaning that the physics of the model do not differ under a change of coordinate system. By studying the case of plane homogeneous turbulent flow, a nonlinear form was derived for the rapid pressure-strain correlation term that is quadratic in the anisotropy tensor (unlike the linear LRR model). Using

the above conditions, a simplified model of the general pressure-strain correlation is formed,

$$\begin{aligned}\Pi_{ij} &= c_1\epsilon a_{ij} + c_2\epsilon\left(a_{ik}a_{kj} - \frac{1}{3}a_{mn}a_{mn}\delta_{ij}\right) \\ &+c_3 k\overline{S}_{ij} + c_4 k\left(a_{ik}\overline{S}_{jk} + a_{jk}\overline{S}_{ik} - \frac{2}{3}a_{mn}\overline{S}_{mn}\delta_{ij}\right) \\ &+c_5 k(a_{ik}\overline{W}_{jk} + a_{jk}\overline{W}_{ik}),\end{aligned} \tag{2.66}$$

where the coefficients c_1, c_2, c_3, c_4 and c_5 are all constants, and

$$\overline{S}_{ij} = \frac{1}{2}\left(\frac{\partial U_i}{\partial x_j} + \frac{\partial U_j}{\partial x_i}\right) \tag{2.67}$$

$$\overline{W}_{ij} = \frac{1}{2}\left(\frac{\partial U_i}{\partial x_j} - \frac{\partial U_j}{\partial x_i}\right) \tag{2.68}$$

are the mean strain rate and vorticity tensors, respectively. Calibration of the coefficients from equation (2.66) was performed by considering several constraints (Speziale *et al.*, 1991); namely agreement with,

1. the asymptotic limit of small anisotropy;
2. *Rapid Distortion Theory* (RDT) for initially isotropic, homogeneously strained flows;
3. experimental values of homogeneous shear flow in equilibrium;
4. RDT for rotating shear flows;
5. experiments on the return to isotropy problem of initially anisotropic flow.

Firstly the coefficient of the slow term, c_1 was replaced by,

$$c_1 = -\left(C_1 + C_1^*\frac{P}{\epsilon}\right), \tag{2.69}$$

where C_1 and C_1^* are empirical constants. This representation of c_1 was formulated to take into account areas of the flow where turbulent production, P, is greater than the dissipation rate. The coefficient, c_3, was replaced by terms that include

Coefficient	Value	Constraint
C_1	3.4	5
C_2	4.2	5
C_3	0.8	2
C_4	1.25	3 & 4
C_5	0.40	3 & 4
C_1^*	1.80	3 & 4
C_3^*	1.30	3 & 4

TABLE 2.4: Values of coefficients used in SSG model

the second invariant of the anisotropy tensor,

$$c_3 = C_3 - C_3^* II^{\frac{1}{2}}, \tag{2.70}$$

where C_3 and C_3^* are empirical constants and $II = a_{ij}a_{ij}$ is the second invariant of the anisotropy tensor. These two changes to the model allow the first constraint to be satisfied by making C_1^* and C_3^* vanish in the limit of small anisotropy due to their dependency on the anisotropy tensor.

Table 2.4 shows the values of the empirical coefficients used in the SSG model and the constraint/flow regime that was used for their specification listed on the previous page.

An added advantage of the SSG model over other second moment closures, including the LRR model, is the redundancy of a model for the wall effect term, equation (2.58). It was found that the SSG model performed well without these terms, easing computational cost and obviating the need for additional modelling.

2.5.2 Dissipation term modelling

Established second moment closures such as the LRR and SSG models, as discussed previously, invoke the assumption of local isotropy of dissipation (Kolmogorov, 1941). This assumption is made by considering the energy cascade from large to small eddies. During the transfer of energy from the large energy containing eddies to the small, any directionality is assumed to be scrambled by nonlinear processes, so that at the small dissipative scales at high Reynolds numbers, dissipation is ef-

fectively isotropic. Equation (2.23) could then be written as,

$$\epsilon_{ij} = \frac{2}{3}\epsilon\delta_{ij}, \tag{2.71}$$

where

$$\epsilon = \nu\left(\overline{\frac{\partial u_i \partial u_i}{\partial x_k \partial x_k}}\right) \tag{2.72}$$

is the trace of ϵ_{ij}. This equation is usually modelled in the same manner as its two-equation equivalent, (2.42), but the use of equation (2.40) is now used due to the availability of the Reynolds stresses. Hanjalic and Launder (1972) gave the dissipation rate equation as,

$$U_i\frac{\partial \epsilon}{\partial x_i} = C_\epsilon \frac{\partial}{\partial x_k}\left(\frac{k}{\epsilon}\overline{u_k u_l}\frac{\partial \epsilon}{\partial x_l}\right) - C_{\epsilon 1}\frac{\epsilon}{k}\overline{u_i u_k}\frac{\partial U_i}{\partial x_k} - C_{\epsilon 2}\frac{\epsilon^2}{k} \tag{2.73}$$

with the first term on the right hand side representing turbulent diffusion of dissipation; the second term the production of dissipation and the third term the destruction of dissipation. Equation (2.73) was also used in the LRR model of Launder *et al.* (1975) with the values of the coefficients C_ϵ, $C_{\epsilon 1}$ and $C_{\epsilon 2}$ as given in table 2.3.

The assumption of isotropic dissipation may not be valid in flows where turbulence is not in equilibrium, such as areas close to a solid wall or in regions of high streamline curvature. So *et al.* (1999) states that for homogeneous shear flows, the anisotropy of dissipation can be more than 50% greater than the anisotropy of the Reynolds stresses. Attempts at modelling the anisotropic nature of the turbulent disspation for high Reynolds number flows are limited, with most calculations still using the Kolmogorov assumption, preferring to model any turbulence anisotropy in the pressure-strain term. Low Reynolds number models, however, account for this anisotropy in their formulation (see Hanjalic and Jakirlic, 2002), but impose a greater computational cost by resolving the near wall turbulence. Due to the limitations of modelling the pressure-strain term as stated by Speziale *et al.* (1991), some turbulence modellers are looking at the dissipation rate as an alternative, to improve the accuracy of second moment closures in areas of high dissipation anisotropy.

Current models of anisotropic dissipation rate

Two methods prevail over the representation of turbulence dissipation. The first uses the anisotropy of the Reynolds stresses to give a measure of the anisotropy of the turbulence dissipation. The second represents the anisotropy of dissipation in terms of the mean strain and vorticity.

Hallback *et al.* (1990) gives an expression for the anisotropy of dissipation, d_{ij}, as a series of terms involving the stress anisotropy, a_{ij}. So *et al.* (1999) investigated the use of this model applied to homogeneous buoyant shear flows. It was found that the results for d_{ij} correlated with those for a_{ij} showing that for these types of flow the anisotropy of dissipation has a dependence on a_{ij}. It has been reported, though (So *et al.*, 1999; Hanjalic and Jakirlic, 2002), that the model of Hallback *et al.* (1990) does not perform adequately in near wall regions of the flow. This is a major drawback for wall bounded flows such as cavity flows, where the dimensions of the cavity are such that the wall plays an important part in the development of the flow.

Jakirlic and Hanjalic (2002) developed a new closure of the ϵ_{ij} equation (2.23) based on the viscous terms within a two-point transport equation of the Reynolds stresses. It is shown that the dissipation tensor can be represented in terms of the homogeneous dissipation tensor and the viscous diffusion of Reynolds stress tensor. The homogeneous dissipation tensor is then modelled by 'blending' the isotropic, homogeneous dissipation rate with the same term modified by the stress anisotropy tensor. The modelled equation for homogeneous dissipation rate is then modelled on a term by term basis that leads to an extended set of terms over the standard ϵ equation which does not facilitate speed of calculation.

The model was tested on channel flow and axially rotating pipe flow. Although the results compared favourably with corresponding DNS data, the flow in the axially rotating pipe case showed that for rotating flows, agreement was not as good as for non-rotating flows. This was attributed to the inaccuracy of the DNS input data to the model, although the lack of a mean strain term in the model could have added to this problem (as alluded to by the authors themselves). This model was designed for

use in a low Reynolds number formulation of a second moment closure, integrating through the viscous sublayer to the wall. This requires more computational points in the near wall region, leading to greater computational time; a draw back of this model for engineering applications, where a rapid turn around time for acquisition of results is vital.

A model to describe axisymmetric turbulence anisotropy was given by Jovanovic *et al.* (2003). Here the anisotropy of dissipation is expressed as a function of the invariants of stress and dissipation anisotropy and the stress anisotropy itself. Using axisymmetric formulations of turbulent quantities, such as Reynolds stress and production of dissipation, and using the anisotropy invariant map of Lumley (1978), an anisotropic formulation of the turbulence dissipation equation is stated. The model was tested for the case of initially isotropic turbulence in uniform rotation and axisymmetric contraction. The model proved adequate for the early time evolution of the turbulence but overestimated the decay of turbulence over longer time periods. This inability to reproduce the effect of reduced decay of turbulence energy onset by the rotation may be due to the lack of any dedicated rotational terms in the formulation of the model.

Lu and Semiao (2003) proposed a model for the dissipation rate equation for use in second moment closures. Instead of using constant coefficients in equation (2.73), $C_{\epsilon 1}$ was re-defined as a function of the second invariant of stress anisotropy. This was proposed by reasoning that anisotropy in the large scale eddies promotes the transfer of energy in the cascade process to the smaller eddies more readily compared to isotropic turbulence.

The model was incorporated into the SSG model and tested against the standard SSG and LRR models on the experimental test cases of a dump combustor and an annular burner. Both of the cases were swirling flows. It was shown for the weaker swirling flow of the dump combustor, the anisotropic dissipation rate model performed better than the SSG and LRR models alone in predicting the mean flow and Reynolds stress quantities. For the annular case, little improvement was shown when using the new model. This was due to the increased level of anisotropy of the flow compared to the annular case, making the anisotropic terms in the dissipation

rate model more effective. In both cases, the SSG model was proven to give superior prediction against experimental data over the LRR model.

As mentioned earlier, the second type of dissipation rate modelling related the anisotropy of dissipation to the mean strain and vorticity of the flows. One such model was developed by Speziale and Gatski (1997). Here the authors hypothesised that the orientation of the large eddies has little effect on the small eddies due to 'non-linear scrambling' of directional information in the energy cascade, and that mean strains cause the anisotropy at the smaller scales. A model of the exact transport equation for the dissipation rate tensor was presented, but for ease of implementation, a transport equation for the scalar dissipation rate was derived.

Speziale and Gatski (1997) developed an algebraic anisotropic dissipation rate model that was nonlinear in the mean velocity gradients. This was incorporated into the transport equation for the dissipation rate and tested against the 'isotropisation of production' (IP) model of Launder *et al.* (1975) for homogeneous shear flow with and without rotation. The new algebraic model was shown to perform better than the IP model (and standard SSG model), especially for rotating flows when compared against DNS and LES data. For flow in a square duct, the new model improved the standard SSG model by removing extra secondary flows that were not present in the DNS data provided.

Due to its performance in rotating flows (of which swirling flows constitute a special type of rotating flow), the anisotropic dissipation rate model of Speziale and Gatski (1997) was chosen for inclusion in the present work. The model has only two additional closure coefficients over the standard dissipation rate model, despite the extra terms involved. Also, because of the lack of use of anisotropic dissipation rate models for simulating swirling flows, with the exception of Lu and Semiao (2003), the performance of the model by Speziale and Gatski in rotating flow advocates its usage here. The model is discussed in greater detail in the following section

Speziale and Gatski (1997) model

The Speziale and Gatski (1997) model for anisotropy of dissipation, as stated previously, is formulated in terms of the mean strain and vorticity tensors. Firstly the transport equation for the dissipation rate tensor,

$$\frac{\partial \epsilon_{ij}}{\partial t} = -\epsilon_{ik}\frac{\partial U_j}{\partial x_k} - \epsilon_{jk}\frac{\partial U_i}{\partial x_k} + 2(f_{ikjl} + f_{jkil} - f_{lkij})\frac{\partial U_k}{\partial x_l} + N_{ij}, \tag{2.74}$$

needs to be modelled for f_{ijkl} and N_{ij}. f_{ijkl} is modelled by expressing it as a linear expansion with the anisotropy of dissipation tensor, d_{ij}. N_{ij} is modelled using a relaxation model to give the correct return to isotropy in the absence of any mean straining on the flow. These two considerations lead to the modelled equation for transport of the dissipation rate tensor,

$$\begin{aligned}
\frac{\partial \epsilon_{ij}}{\partial t} &= -\epsilon_{ik}\frac{\partial U_j}{\partial x_k} - \epsilon_{jk}\frac{\partial U_i}{\partial x_k} + \frac{16}{15}\epsilon\overline{S}_{ij} \\
&+ \left(\frac{30}{11}\alpha_3 + \frac{20}{11}\right)\epsilon\left(d_{ik}\overline{S}_{jk} + d_{jk}\overline{S}_{ik} - \frac{2}{3}d_{kl}\overline{S}_{kl}\delta_{ij}\right) \\
&- \left(\frac{14}{11}\alpha_3 - \frac{20}{11}\right)\epsilon\left(d_{ik}\overline{W}_{jk} + d_{jk}\overline{W}_{ik}\right) \\
&- \left(\frac{14}{11}\alpha_3 - \frac{16}{33}\right)\epsilon d_{kl}\overline{S}_{kl}\delta_{ij} + \frac{2}{3}\left(C_{\epsilon 1}\frac{\epsilon}{k}P - C_{\epsilon 2}\frac{\epsilon^2}{k}\right)\delta_{ij} \\
&- C_{\epsilon 5}\frac{\epsilon}{k}\left(\epsilon_{ij} - \frac{2}{3}\epsilon\delta_{ij}\right),
\end{aligned} \tag{2.75}$$

where $\overline{S}_{ij}$ and $\overline{W}_{ij}$ are given in (2.67) and (2.68) and

$$d_{ij} = \frac{\epsilon_{ij} - \frac{2}{3}\epsilon\delta_{ij}}{2\epsilon} \tag{2.76}$$

is the anisotropy of dissipation. Despite providing a model for the dissipation rate tensor, the solution of five additional transport equations is required for a three dimensional calculation, potentially increasing the numerical stiffness of an already stiff equation set. For engineering applications, this additional computational cost is disadvantageous. Instead of finding the solution to equation (2.75), an algebraic approximation to it is used, requiring the solution to only a modified transport equation for dissipation rate. By studying local homogeneous, equilibrium flows,

Speziale and Gatski formulated an equation for the anisotropy of dissipation,

$$d_{ij} = -2C_{\mu\epsilon}\left[\frac{k}{\epsilon}\overline{S}_{ij} + \left(\frac{\frac{7}{11}\alpha_3 + \frac{1}{11}}{C_{\epsilon 5} + \frac{P}{\epsilon} - 1}\right)\frac{k^2}{\epsilon^2}\left(\overline{S}_{ik}\overline{W}_{kj} + \overline{S}_{jk}\overline{W}_{ki}\right)\right. \tag{2.77}$$
$$\left. + \left(\frac{\frac{30}{11}\alpha_3 - \frac{2}{11}}{C_{\epsilon 5} + \frac{P}{\epsilon} - 1}\right)\frac{k^2}{\epsilon^2}\left(\overline{S}_{ik}\overline{S}_{kj} - \frac{1}{3}\overline{S}_{kl}\overline{S}_{kl}\delta_{ij}\right)\right]$$

where P is the production of turbulence energy and,

$$C_{\mu\epsilon} = \frac{1}{15(C_{\epsilon 5} + \frac{P}{\epsilon} - 1)}\left[1 + 2\left(\frac{\frac{7}{11}\alpha_3 + \frac{1}{11}}{C_{\epsilon 5} + \frac{P}{\epsilon} - 1}\right)^2\xi^2 - \frac{2}{3}\left(\frac{\frac{15}{11}\alpha_3 - \frac{1}{11}}{C_{\epsilon 5} + \frac{P}{\epsilon} - 1}\right)^2\eta^2\right]^{-1}. \tag{2.78}$$

$$\eta = (\overline{S}_{ij}\overline{S}_{ij})^{1/2}\frac{k}{\epsilon}, \quad \xi = (\overline{W}_{ij}\overline{W}_{ij})^{1/2}\frac{k}{\epsilon}. \tag{2.79}$$

For flows with mild departures from equilibrium, Speziale and Gatski use the model,

$$\frac{P}{\epsilon} = 2C_\mu^*\eta^2 \tag{2.80}$$

with $C_\mu^* \approx 0.094$ for shear flow in equilibrium.

By making use of the transport equation for the dissipation rate tensor (2.75), a transport equation for the dissipation rate is found. The form of the equation is similar to the standard equation (2.73), with the modification of the coefficient $C_{\epsilon 1}$ taking into account the effects of dissipation rate anisotropy,

$$U_i\frac{\partial\epsilon}{\partial x_i} = C_\epsilon\frac{\partial}{\partial x_k}\left(\frac{k}{\epsilon}\overline{u_k u_l}\frac{\partial\epsilon}{\partial x_l}\right) + C_{\epsilon 1}^*\frac{\epsilon}{k}\overline{u_i u_k}\frac{\partial U_i}{\partial x_k} - C_{\epsilon 2}\frac{\epsilon^2}{k}, \tag{2.81}$$

where

$$C_{\epsilon 1}^* = C_{\epsilon 1} + \frac{2(1+\alpha)}{15C_\mu^*}\left[\frac{C_{\epsilon 5} + 2C_\mu^*\eta^2 - 1}{(C_{\epsilon 5} + 2C_\mu^*\eta^2 - 1)^2 - \frac{2}{3}\beta_2^2\eta^2 + 2\beta_1^2\xi^2}\right]. \tag{2.82}$$

and

$$\beta_1 = \frac{7}{11}\alpha_3 + \frac{1}{11}, \quad \beta_2 = \frac{15}{11}\alpha_3 - \frac{1}{11}, \quad \alpha = \frac{3}{4}\left(\frac{14}{11}\alpha_3 - \frac{16}{33}\right). \tag{2.83}$$

The closure coefficients for the anisotropic dissipation rate model are shown in table

Coefficient	Value
C_ϵ	0.15
$C_{\epsilon 1}$	1.0
$C_{\epsilon 2}$	1.83
$C_{\epsilon 5}$	5.80
C_μ^*	0.094
α_3	0.6

TABLE 2.5: Values of coefficients used in the anisotropic dissipation rate model of Speziale and Gatski (1997)

2.5 and were reached subject to the following requirements (Speziale and Gatski, 1997).

1. The value of 0.15 for C_ϵ was set to agree with the Von Karman constant for boundary layers.

2. $C_{\epsilon 1}$ has a value of unity so that the turbulent time scale grows monotonically with time as $t \to \infty$ to agree with the limit of local isotropy.

3. $C_{\epsilon 2}$ was found by analysing the decay of isotropic turbulence to give a value of 1.83.

4. $C_{\epsilon 5}$ was found by studying the decay of initially anisotropic turbulence in the small scales, to an isotropic state.

5. α_3 was found by studying DNS data of homogeneous shear flows.

To complete the closure, equation (2.81) is coupled to the Reynolds stress transport equation (2.21) through (2.76).

2.6 Variable density turbulence models

To predict turbulent flows where temperature variation is significant - such as those involving chemical reaction, combustion or other forms of heat transfer - it is necessary to make allowances for any corresponding variation in fluid density. For heat transfer in liquids, this may not represent a problem if density changes are small,

and conventional modelling may be used. In gasses, however, density change is large and can not be neglected.

If conventional Reynolds decomposition is used for the turbulent density, splitting into its mean and fluctuating components, many terms involving ρ' appear in the turbulence equations (such as Reynolds stress equations). These terms are difficult to model (Libby and Williams, 1994) due to their complexity, and if they are neglected, important physical processes are removed.

The introduction of density weighted averaging by Favre (1971) instead of using conventional averaging provides equations with a more compact set of terms that allow a more simple physical interpretation. They also avoid the evolution of multiple terms involving ρ'. Density weighted, or Favre, averaging is introduced below.

2.6.1 Favre averaging

For variable density flows, Favre averaging provides a more convenient set of equations to solve, similar to those when using ensemble averaging for constant density flows. Using the notation of Jones (1979), Favre decomposition and averaging is defined as,

$$\begin{aligned} u_i = \tilde{u}_i + u_i'', \quad T = \widetilde{T} + T'' \\ \overline{\rho u_i''} = 0, \quad \overline{\rho T''} = 0 \\ \overline{u_i''} \neq 0, \quad \overline{T''} \neq 0, \end{aligned} \tag{2.84}$$

where T is the temperature, tildes represent Favre (density weighted) averaging

$$\tilde{u}_i = \frac{\overline{\rho u_i}}{\overline{\rho}} = \frac{1}{\overline{\rho}} \lim_{N\to\infty} \frac{1}{N} \sum_{m=1}^{N} (\rho u_i)^m \tag{2.85}$$

(in terms of an ensemble of N elements) and primed variables represent their fluctuating (turbulent) component. The above definitions can be used to describe the

relationship between Favre and conventional ensemble averaging thus.

$$\begin{aligned}
\overline{u}_i &= \tilde{u}_i + \overline{u_i''} \\
\overline{\rho u_i' u_j'} &= \overline{\rho u_i'' u_j''} + \frac{\overline{\rho' u_i'}\,\overline{\rho' u_j'}}{\overline{\rho}} \\
\overline{u_i''} &= -\frac{\overline{\rho' u_i'}}{\overline{\rho}} \\
\overline{\rho' u_i''} &= \overline{\rho' u_i'} \quad .
\end{aligned} \tag{2.86}$$

Using equations (2.84) to (2.86), it is possible to express the equations of motion for variable density flows, the steady-state continuity equation of which is,

$$\frac{\partial}{\partial x_j}(\overline{\rho}\tilde{u}_j) = 0, \tag{2.87}$$

with the steady-state momentum equation given by,

$$\frac{\partial}{\partial x_j}(\overline{\rho}\tilde{u}_j\tilde{u}_i) = -\frac{\partial \overline{p}}{\partial x_i} + \frac{\partial}{\partial x_j}(\overline{\sigma}_{ij} - \widetilde{\overline{\rho u_j'' u_i''}}) \tag{2.88}$$

where $\overline{\sigma}_{ij}$ is the mean viscous stress tensor. As with conventional Reynolds averaging, a closure problem exists - the appearance of the $\widetilde{\overline{\rho u_j'' u_i''}}$ term has no explicit definition. Again, various forms of closure are available, from two equation turbulence models to full second-moment (or Reynolds stress) closures. For the variable density flows considered in chapter 6, the Reynolds stress modelling procedure is used as described below.

2.7 Reynolds stress models for variable density flows

From Jones (1979), and equation (2.20), the variable density Reynolds stress equation can be expressed as

$$\overline{\rho}\tilde{u}_k \frac{\partial \widetilde{\overline{u_i'' u_j''}}}{\partial x_k} = -\widetilde{\overline{\rho u_i'' u_k''}}\frac{\partial \tilde{u}_j}{\partial x_k} - \widetilde{\overline{\rho u_j'' u_k''}}\frac{\partial \tilde{u}_i}{\partial x_k}$$

$$
\begin{aligned}
&+ \underbrace{\overline{p'\left(\frac{\partial u_i''}{\partial x_j}+\frac{\partial u_j''}{\partial x_i}\right)}}_{\text{stress-redistribution}} \\
&- \underbrace{\frac{\partial}{\partial x_k}\left(\widetilde{\overline{\rho u_i'' u_j'' u_k''}}+\overline{p'(u_j''\delta_{ik}+u_i''\delta_{jk})}-\overline{u_j''\sigma_{ik}'}-\overline{u_i''\sigma_{jk}'}\right)}_{\text{turbulent diffusion}} \\
&- \underbrace{\left(\overline{\sigma_{ki}'\frac{\partial u_j''}{\partial x_k}}+\overline{\sigma_{kj}'\frac{\partial u_i''}{\partial x_k}}\right)}_{\text{viscous destruction}} \\
&- \left(\overline{u_i''}\frac{\partial \overline{p}}{\partial x_j}+\overline{u_j''}\frac{\partial \overline{p}}{\partial x_i}\right). \qquad (2.89)
\end{aligned}
$$

Equation (2.89) has similar groups of terms to equation (2.21), with the addition of the last term involving $\overline{u_i''}$ - equal to zero in constant density flows. As with its constant density counterpart, this equation can only be solved by modelling all the terms on the right hand side of (2.89) bar the first.

Modelling of the various terms in equation (2.89) is conducted in the same manner as for constant density flows where the density weighting is assumed to include the influence of density variation (see Jones, 1979; Gu, 1993).

2.7.1 Stress redistribution term modelling

The stress redistribution term due to fluctuating pressure (or pressure-strain correlation) may be modelled as for constant density flows. A Poisson equation for fluctuating pressure can be found (see Chou, 1945) which, for variable density, takes the (time dependent) form

$$
\begin{aligned}
\nabla^2 p' &= -\frac{\partial^2}{\partial t \partial x_i}(\overline{\rho}u_i'' + \rho'\tilde{u}_i) + \frac{\partial^2 \sigma_{ij}'}{\partial x_i \partial x_j} \\
&- \frac{\partial^2}{\partial x_i \partial x_j}(\overline{\rho}u_i''u_j'' - \widetilde{\overline{\rho u_i'' u_j''}} + \overline{\rho}u_i''\tilde{u}_j + \overline{\rho}u_j''\tilde{u}_i) \quad , \qquad (2.90)
\end{aligned}
$$

where the gradient operator includes the time derivative. This equation is much more complex than its constant density counterpart (2.47), and is thus less desirable for use in the pressure-strain correlation (2.90)(see Jones, 1979). In an effort to keep the models as simple as possible, variable density versions of the constant density

models are used, thus the pressure-strain term is re-expressed in density weighted form

$$\overline{p'\left(\frac{\partial u_i''}{\partial x_j}+\frac{\partial u_j''}{\partial x_i}\right)}=\overline{\rho}\widetilde{\left[\frac{p'}{\rho}\left(\frac{\partial u_i''}{\partial x_j}+\frac{\partial u_j''}{\partial x_i}\right)\right]}. \tag{2.91}$$

Equation (2.91) is now of the same form as equation (2.22) and similar models may be used.

LRR model in variable density form

The LRR model of Launder *et al.* (1975) can be recast into variable density form for the pressure-strain model. As in constant density flows, the term is split into the 'slow' and 'rapid' terms. The LRR model also accounts for the near wall region, where eddy squashing occurs. Thus the pressure-strain term is expressed as,

$$\overline{\rho}\widetilde{\left[\frac{p'}{\rho}\left(\frac{\partial u_i''}{\partial x_j}+\frac{\partial u_j''}{\partial x_i}\right)\right]}=\phi_{ij,1}+\phi_{ij,2}+\phi_{ij,w} \tag{2.92}$$

where $\phi_{ij,1}$ is the slow term, $\phi_{ij,2}$ is the rapid term and $\phi_{ij,w}$ is the wall-effect term. From Gu (1993), the LRR model is re-written as

$$\phi_{ij,1} = -C_1\frac{\epsilon}{k}\overline{\rho}\left(\widetilde{u_i''u_j''}-\frac{2}{3}\delta_{ij}k\right) \tag{2.93}$$

$$\begin{aligned}\phi_{ij,2} = &-\frac{C_2+8}{11}\left(P_{ij}-\frac{2}{3}P\delta_{ij}\right)\\ &-\frac{30C_2-2}{55}k\left(\frac{\partial\tilde{u}_i}{\partial x_j}+\frac{\partial\tilde{u}_j}{\partial x_i}\right)-\frac{8C_2-2}{11}\left(D_{ij}-\frac{2}{3}P\delta_{ij}\right)\end{aligned} \tag{2.94}$$

$$\phi_{ij}^{w} = \left[0.125\overline{\rho}\frac{\epsilon}{k}\left(\widetilde{u_i''u_j''}-\frac{2}{3}\delta_{ij}k\right)+0.015(P_{ij}-D_{ij})\right]\frac{k^{\frac{3}{2}}}{\epsilon x_2}, \tag{2.95}$$

where

$$P_{ij}=-\overline{\rho}\left(\widetilde{u_iu_k}\frac{\partial\tilde{u}_j}{\partial x_k}+\widetilde{u_ju_k}\frac{\partial\tilde{u}_i}{\partial x_k}\right) \tag{2.96}$$

and

$$D_{ij}=-\overline{\rho}\left(\widetilde{u_iu_k}\frac{\partial\tilde{u}_k}{\partial x_j}+\widetilde{u_ju_k}\frac{\partial\tilde{u}_k}{\partial x_i}\right). \tag{2.97}$$

with P given by the trace of P_{ij}. The closure coefficients for the model are given in table 2.3.

SSG model in variable density form

The SSG model of Speziale *et al.* (1991) can also be used for variable density flows as outlined by Li *et al.* (2003). As mentioned previously, the SSG model does not include a term for the wall effect, ϕ_{ij}^{w}, but relies on its nonlinear formulation to account for this phenomenon.

The slow and rapid terms for the SSG model are written for variable density flows as

$$\phi_{ij,1} = -\epsilon\overline{\rho}\left(C_1 + C_1^*\frac{P}{\epsilon}\right)a_{ij} \tag{2.98}$$

$$\begin{aligned}\phi_{ij,2} = {} & C_2\overline{\rho}\epsilon\left(a_{ik}a_{kj} - \frac{1}{3}a_{mn}a_{mn}\delta_{ij}\right) + \overline{\rho}\left(C_3 + C_3^* II^{\frac{1}{2}}\right)k\widetilde{S}_{ij} \\ & + C_4\overline{\rho}\left(a_{ik}\widetilde{S}_{jk} + a_{jk}\widetilde{S}_{ik} - \frac{2}{3}a_{mn}\widetilde{S}_{mn}\delta_{ij}\right) \\ & + C_5\overline{\rho}k\left(a_{ik}\widetilde{W}_{jk} + a_{jk}\widetilde{W}_{ik}\right),\end{aligned} \tag{2.99}$$

with the mean strain and vorticity tensors given by

$$\widetilde{S}_{ij} = \frac{1}{2}\left(\frac{\partial\tilde{u}_i}{\partial x_j} + \frac{\partial\tilde{u}_j}{\partial x_i}\right) \tag{2.100}$$

$$\widetilde{W}_{ij} = \frac{1}{2}\left(\frac{\partial\tilde{u}_i}{\partial x_j} - \frac{\partial\tilde{u}_j}{\partial x_i}\right) \tag{2.101}$$

and the stress anisotropy tensor by

$$a_{ij} = \frac{\widetilde{\overline{u_i''u_j''}}}{2k} - \frac{1}{3}\delta_{ij}. \tag{2.102}$$

The closure coefficients used for the model are given in table 2.4.

2.7.2 Turbulent diffusion modelling

The turbulent diffusion of the Reynolds stresses in equation (2.89) can be modelled using the gradient diffusion hypothesis of Daly and Harlow (1970). Gu (1993) states that the turbulent diffusion due to pressure fluctuations is small and the main contribution is from the triple correlation term $-\widetilde{\overline{\rho u_i'' u_j'' u_k''}}$. The gradient diffusion

equation (2.63) can be expressed in variable density form to give the entire model for the turbulent diffusion term

$$\frac{\partial}{\partial x_k}\left(\widetilde{\overline{\rho u_i'' u_j'' u_k''}} + \overline{p'(u_j''\delta_{ik} + u_i''\delta_{jk})} - \overline{u_j''\sigma_{ik}'} - \overline{u_i''\sigma_{jk}'}\right) = \frac{\partial}{\partial x_k}\left(C_s \frac{k}{\epsilon}\widetilde{\overline{\rho u_k'' u_l''}}\frac{\partial \widetilde{\overline{u_i'' u_j''}}}{\partial x_l}\right) \tag{2.103}$$

where C_s is the same closure coefficient as given in table 2.3.

2.7.3 Dissipation modelling

Previously, it was shown that two different types of modelling for dissipation of turbulent kinetic energy are available. It is common to invoke the Kolmogorov hypothesis of local isotropy for high Reynolds number flows given as

$$\left(\overline{\sigma_{ki}'\frac{\partial u_j''}{\partial x_k}} + \overline{\sigma_{kj}'\frac{\partial u_i''}{\partial x_k}}\right) = \overline{\rho}\epsilon_{ij} = \frac{2}{3}\overline{\rho}\epsilon\delta_{ij} \tag{2.104}$$

which is then used in equation (2.89). The other way of modelling dissipation is to assume that the non-linear squashing and stretching of turbulent eddies, reducing them in size to smaller and smaller scales, does not produce isotropic dissipation (Speziale and Gatski, 1997).

The anisotropic dissipation model of Speziale and Gatski (1997) is again used for variable density flow. The expression integrated into the Reynolds stress equation (2.89) consists of the isotropic part and the deviatoric part

$$\overline{\rho}\epsilon_{ij} = 2\overline{\rho}\epsilon d_{ij} + \frac{2}{3}\overline{\rho}\epsilon\delta_{ij}. \tag{2.105}$$

The variable density form of the algebraic equation for dissipation anisotropy is identical to the constant density form [due to its algebraic nature and the variation in density incorporated in equation (2.105)] and is represented in equations (2.77) to (2.80). The closure coefficients are given in table 2.5.

The transport equation for the scalar dissipation rate is expressed for variable density

flows (Gu, 1993) as

$$\overline{\rho}\tilde{u}_i\frac{\partial \epsilon}{\partial x_i} = C_\epsilon \frac{\partial}{\partial x_k}\left(\overline{\rho}\frac{k}{\epsilon}\widetilde{u_k''u_l''}\frac{\partial \epsilon}{\partial x_l}\right) - C_{\epsilon 1}^*\overline{\rho}\frac{\epsilon}{k}\widetilde{u_l''u_k''}\frac{\partial \tilde{u}_l}{\partial x_k} - C_{\epsilon 1}\overline{u_i''}\frac{\partial \overline{p}}{\partial x_i} - C_{\epsilon 2}\overline{\rho}\frac{\epsilon^2}{k}, \quad (2.106)$$

where the third term on the right is a consequence of Favre averaging (see Jones, 1979), and not present in constant density flows. The value of the closure coefficient, $C_{\epsilon 1}^*$, is dependent on the use of either an isotropic or anisotropic formulation. For the isotropic model $C_{\epsilon 1}^* = C_{\epsilon 1}$ and equation (2.104) is used in the Reynolds stress equation with the corresponding value of $C_{\epsilon 1}$ for the LRR or SSG models. For anisotropic flows, $C_{\epsilon 1}^*$ is given by equations (2.82) and (2.83).

2.7.4 Fluctuating velocity model

In equations (2.89) and (2.106) the fluctuating velocity, $\overline{u_i''}$, appears which leads to an open set of equations. To model this term, relation (2.86) is used to express $\overline{u_i''}$ in terms of $\overline{\rho' u_i'}$. Jones (1979) models this term using a complex algebraic equation, which itself requires additional modelling. However, Jones reduces this equation to a more simple form,

$$\overline{u_i''} = \frac{1}{C_{\phi 1}}\frac{k}{\epsilon}\widetilde{u_i''u_k''}\frac{\partial \overline{\rho}}{\partial x_k}, \quad (2.107)$$

by making the assumption that density fluctuations and mean pressure gradients are independent. The closure coefficient, $C_{\phi 1}$, is empirical and is given the value 0.22.

2.8 Summary

This chapter has discussed the various equations needed to describe practical engineering fluid flows with turbulence models employed, using approximations based on physical reasoning, to close the RANS equations. A full second moment closure, using either the popular LRR model or the SSG model, is given with a more modern approach to modelling the dissipation rate of turbulent kinetic energy, using anisotropic methods. The Favre averaged equivalents of these models are also

presented to account for fluid flows - such as the combustion problem reported in Chapter 6 - where variation in density is important.

Chapter 3

Numerical Methods

Contents

3.1 Introduction

To find solutions to the equations of motion presented in Chapter 2. it is necessary to generate complimentary discrete equivalents that can be solved efficiently via a computer. Several means exist for discretising such equations. namely the *finite difference* (Book, 1981), *finite element* (Pironeau. 1989) and *finite volume* methods (Patankar, 1980).

The finite difference approximation turns continuous differential equations into a set of discrete difference equations based at nodal points. The nodes are a set of points situated within the calculation domain of the flow field of interest, 'sampling' the characteristics of the flow at that point. The finite difference method approximates variations in flow variables by using Taylor series expansions truncated at a suitable level of accuracy. This method, although conservative on a domain basis. does not guarantee local conservation, in that momentum and mass are not identically conserved in the control volumes surrounding individual nodes Book (1981).

The finite element method divides the calculation domain into a set of contiguous 'elements' where interpolation functions are used to describe the variation of the flow variables over the element. These functions are then assumed to satisfy the governing equations exactly with the presence of a residual which is then minimised using weighting methods. This provides the coefficients used in the interpolation functions and hence a solution. As with the finite difference method. the finite element method is only conservative over the whole calculation domain and not locally - which may lead to unphysical solutions if care is not maintained. The computational difficulty in implementing this technique is also higher than that of the finite difference method. relying mainly on unstructured. triangular or tetrahedral meshes. These types of elements are, however, highly advantageous for use in complex geometries. The method has been applied in many flows such as free surface flows (Walkley *et al.*, 2004), and cavity flows (Fawehinmi *et al.*, 2002).

The finite volume method. like finite differencing, sub divides the calculation domain into a set of control volumes wherein lie the computational nodes. Unlike the previous methods, the equations of motion are integrated over a control volume.

meaning that momentum and mass are conserved locally within it, and also in the calculation domain. The method is also more intuitive and simple to implement.

For these reasons, the finite volume approach is adopted as the discretisation method of choice and is described below in more detail. The basic formulation is presented along with discretisation schemes for the troublesome convection terms. To solve the resulting algebraic equations, the pressure correction method is employed in the form of the PISO (Issa, 1985) and SIMPLE (Patankar and Spalding, 1972) algorithms. Finally, this method is applied to two-dimensional, laminar test cases.

3.2 The Finite Volume Discretisation Method

The finite volume method is used to discretise the governing partial differential equations encountered in this thesis. Some authors such as Patankar (1980); Versteeg and Malalasekera (1996); Ferziger and Peric (2004) give a good general introduction to the method; an outline only is provided below.

The conservative form of the steady state momentum conservation equation (2.2),

$$\underbrace{\nabla \cdot (\rho \mathbf{u}\mathbf{u})}_{\text{convection}} = \underbrace{-\nabla p}_{\text{pressure gradient}} + \underbrace{\nabla \cdot (\mu \nabla \mathbf{u})}_{\text{diffusion}}, \tag{3.1}$$

can be integrated, using Gauss' theorem, over the two dimensional control volume shown in figure 3.1, where P is the central nodal point, E,W,N,S are the surrounding nodes and lower case letters denote control volume faces.

Splitting the integral into convective, diffusive and pressure gradient components, these can be approximated as,

$$\begin{aligned}
\oint_S (\rho \mathbf{u}\mathbf{u}) \cdot \mathbf{n} dS &= (\rho \mathbf{u}u)_e \Delta y_e - (\rho \mathbf{u}u)_w \Delta y_w + (\rho \mathbf{u}v)_n \Delta x_n - (\rho \mathbf{u}v)_s \Delta x_s \\
\oint_S \mu \nabla \mathbf{u} \cdot \mathbf{n} dS &= (\mu \frac{\partial}{\partial x}\mathbf{u})_e \Delta y_e - (\mu \frac{\partial}{\partial x}\mathbf{u})_w \Delta y_w + (\mu \frac{\partial}{\partial y}\mathbf{u})_n \Delta x_n - (\mu \frac{\partial}{\partial y}\mathbf{u})_s \Delta x_s \\
\oint_S p \mathbf{n} dS &= p_e \mathbf{i} \Delta y_e - p_w \mathbf{i} \Delta y_w + p_n \mathbf{j} \Delta x_n - p_s \mathbf{j} \Delta x_s
\end{aligned} \tag{3.2}$$

where it is assumed that variables integrated over the faces of the control volumes

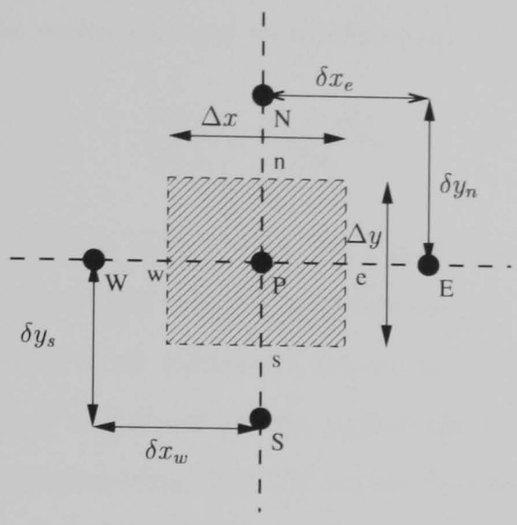

FIGURE 3.1: A control volume in 2D used in the finite volume method.

are constant. Expressing (3.2) in x and y components gives,

x component:

$$(\rho u)_e u_e \Delta y_e - (\rho u)_w u_w \Delta y_w + (\rho v)_n u_n \Delta x_n - (\rho v)_s u_s \Delta x_s =$$
$$\left(\mu \frac{\partial u}{\partial x}\right)_e \Delta y_e - \left(\mu \frac{\partial u}{\partial x}\right)_w \Delta y_w + \left(\mu \frac{\partial u}{\partial y}\right)_n \Delta x_n - \left(\mu \frac{\partial u}{\partial y}\right)_s \Delta x_s -$$
$$[(p\Delta y)_e - (p\Delta y)_w]$$

y component:

$$(\rho u)_e v_e \Delta y_e - (\rho u)_w v_w \Delta y_w + (\rho v)_n v_n \Delta x_n - (\rho v)_s v_s \Delta x_s =$$
$$\left(\mu \frac{\partial v}{\partial x}\right)_e \Delta y_e - \left(\mu \frac{\partial v}{\partial x}\right)_w \Delta y_w + \left(\mu \frac{\partial v}{\partial y}\right)_n \Delta x_n - \left(\mu \frac{\partial v}{\partial y}\right)_s \Delta x_s -$$
$$[(p\Delta x)_n - (p\Delta x)_s]. \tag{3.3}$$

The terms on the left hand side of these equations, preserve the conservation of momentum through the control volume faces due to advection, while the terms on the right hand side conserve momentum due to diffusion effects and pressure gradients, respectively.

The presence of partial derivatives in equations (3.3) means that further discretisation is required before (nonlinear) algebraic equations for the dependent variables can be obtained. One method of removing the partial derivatives is to discretise them using a piecewise linear interpolation scheme. For any scalar variable, ϕ, its gradients at the face of a control volume can be expressed in terms of the difference

between its value at the nodes adjacent to the face, i.e.

$$\left.\frac{\partial \phi}{\partial x}\right|_e = \frac{\phi_E - \phi_P}{\delta x_e}. \tag{3.4}$$

where δx_e is the distance from node P to node E as shown in figure 3.1. All of the diffusion terms in equations (3.3) may be approximated in a similar manner. This method of discretisation is more commonly known as *Central Differencing*, which approximates the gradient as a linear profile, and so the interpolation is first order with a second order truncation term. In CFD circles, it is well known that the order of accuracy of a particular discretisation scheme is given in terms of its leading truncation term, therefore central differencing is said to be second order accurate.

The central differencing method has been successfully used for the discretisation of diffusion terms because no directional information is needed, diffusion being a random motion of particles permeating all directions equally in a uniform medium. The reason for its success numerically is due to its order of accuracy, and demonstrates that when using interpolation formulæ, it is appropriate to use at least an interpolation that is of the same order as the derivative terms in the original continuum equation (see Press *et al.*, 1993).

As mentioned previously, nonlinearities are present in equations (3.3) due to the convective terms. Methods of discretising the convective terms are reviewed below.

3.3 Convective Discretisation Schemes

For the convective terms in the integral equations (3.3), the dependent variable is located at the faces of the control volume. Unfortunately, in the finite volume method, variable values are stored at the centre of control volumes. As such, methods for approximating control volume face fluxes (velocities) in terms of the nodal values are needed.

3.3.1 Central Differencing

Following Patankar (1980) the velocity at the face of a control volume can be expressed using the central difference approximation. At the east face, for example,

$$u_e = \frac{1}{2}(u_E + u_P) \tag{3.5}$$

which assumes that the east face lies midway (denoted by the premultiplying factor of one half) between nodes E and P. Several authors, (Patankar, 1980; Versteeg and Malalasekera, 1996; Ferziger and Peric, 2004) have noted a flaw in the central difference scheme for certain flows.

The ratio of convective flux, F, to diffusive flux, D, in the control volume is known as the *Peclet* number, where

$$F_{e,w} = (\rho u \Delta y)_{e,w} \quad , \quad F_{n,s} = (\rho u \Delta x)_{n,s} \tag{3.6}$$

are the convective fluxes at the faces of the control volume, and

$$D_{e,w} = \left(\frac{\mu \Delta y}{\delta x}\right)_{e,w} \quad , \quad D_{n,s} = \left(\frac{\mu \Delta x}{\delta y}\right)_{n,s} \tag{3.7}$$

are the corresponding diffusive mass fluxes. The Peclet number at the control volume centre for the u-momentum equation is given by

$$Pe = \frac{F}{D} = \frac{\rho u}{\mu / \delta x}. \tag{3.8}$$

Patankar (1980) performed a simple numerical experiment, the outcome of which showed that if $Pe > 2$, the central difference scheme yields unphysical solutions for the discretised equations. Amongst the observed effects was the lack of boundedness of the variables at the control volume faces. That is, in the absence of mass flux sources or sinks, the face values calculated lay outside the upper and lower boundaries of the adjacent nodal values.

The lack of robustness of the central difference scheme for flows with $Pe > 2$, subsequently motivated the search for different methods for obtaining physically

realistic values of the velocities at the control volume faces.

3.3.2 Upwind differencing

One solution to the problems experienced with central differencing is to use *Upwind* differencing (see Ferziger and Peric, 2004). This is a zero order interpolation for the value of the velocity at the node in the *upwind* direction on to the control volume face. The implementation thus requires a knowledge of the direction of the flow *before* discretisation can take place. Taking the left hand side of equations (3.3) for u momentum and expressing it in terms of the mass fluxes F, the convective terms become,

$$F_e u_e - F_w u_w + F_n u_n - F_s u_s. \tag{3.9}$$

To express the face velocities in terms of the nodal values, the direction of the

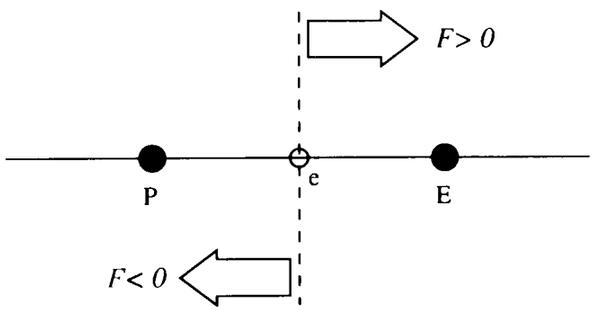

FIGURE 3.2: Use of control volume face mass fluxes in the Upwind scheme.

flow is found by making use of the mass fluxes. Referring to figure 3.2, if F_e is positive(negative), u_e is given by the value of u at node $P(E)$. In summary, this method can be used to express the control volume face values for u velocity as follows.

$$\begin{aligned}
F_e u_e &= max(F_e, 0)u_P - max(-F_e, 0)u_E, \\
F_w u_w &= max(F_w, 0)u_W - max(-F_w, 0)u_P, \\
F_n u_n &= max(F_n, 0)u_P - max(-F_n, 0)u_N, \\
F_s u_s &= max(F_s, 0)u_S - max(-F_s, 0)u_P,
\end{aligned} \tag{3.10}$$

where the $max(x, y)$ function finds the largest of the two values x or y. Incorporating equations (3.10), (3.6), (3.7) and (3.4) into equations (3.3), leads to the following general discretisation equations for u and v momentum,

$$\begin{aligned} a_P u_P &= a_E u_E + a_W u_W + a_N u_N + a_S u_S - [(p\Delta y)_e - (p\Delta y)_w] \\ a_P v_P &= a_E v_E + a_W v_W + a_N v_N + a_S v_S - [(p\Delta x)_n - (p\Delta x)_s] \end{aligned} \tag{3.11}$$

where

$$\begin{aligned} a_E &= max(-F_e, 0) + D_e \quad , \quad a_W = max(F_w, 0) + D_w \\ a_N &= max(-F_n, 0) + D_n \quad , \quad a_S = max(F_s, 0) + D_s \\ a_P &= a_E + a_W + a_N + a_S \end{aligned} \tag{3.12}$$

are the coefficients of the variables at the nodes E, W, N, S and P.

Now that the discretised form of the integral equations (3.3) is complete, it should be a simple matter of moving on to their solution. There are, however, issues with the upwind scheme that require further investigation and discussion.

Limitations of Upwind differencing

Despite overcoming the problems associated with central differencing, the upwind scheme has some serious numerical drawbacks of its own (see Leonard, 1979).

A discretised, one dimensional equation, without source terms, for the transport of a scalar variable, ϕ, may be obtained in a similar manner to that resulting in equations (3.3). Starting with the convection-diffusion equation for ϕ in one dimension (replacing partial with full derivatives),

$$\frac{\mathrm{d}}{\mathrm{d}x}(\rho u \phi) = \frac{\mathrm{d}}{\mathrm{d}x}\left(\mu \frac{\mathrm{d}\phi}{\mathrm{d}x}\right) \tag{3.13}$$

it is possible to form an integral equation by integrating over the one dimensional control volume

$$\int_V \frac{\mathrm{d}}{\mathrm{d}x}(\rho u \phi)\mathrm{d}V = \int_V \frac{\mathrm{d}}{\mathrm{d}x}\left(\mu \frac{\mathrm{d}\phi}{\mathrm{d}x}\right)\mathrm{d}V \quad . \tag{3.14}$$

This reduces to a definite integral over a length $\mathrm{d}x$ from the left side, w, of the control volume to the right hand side, e,

$$\begin{aligned} \int_w^e \mathrm{d}(\rho u\phi) &= \int_w^e \mathrm{d}\left(\mu\frac{\mathrm{d}\phi}{\mathrm{d}x}\right) \\ \Rightarrow\ (\rho u\phi)_e - (\rho u\phi)_w &= \left(\mu\frac{\mathrm{d}\phi}{\mathrm{d}x}\right)_e - \left(\mu\frac{\mathrm{d}\phi}{\mathrm{d}x}\right)_w \\ \Rightarrow\ F_e\phi_e - F_w\phi_w &= \left(\mu\frac{\mathrm{d}\phi}{\mathrm{d}x}\right)_e - \left(\mu\frac{\mathrm{d}\phi}{\mathrm{d}x}\right)_w \quad , \end{aligned} \tag{3.15}$$

where $F_{e,w} = (\rho u)_{e,w}$.

The convective terms in equation (3.15) can be discretised using the upwind and central difference schemes when a positive u velocity is in effect, thus,

Upwind

$$F_e\phi_P - F_w\phi_W = \left(\mu\frac{\mathrm{d}\phi}{\mathrm{d}x}\right)_e - \left(\mu\frac{\mathrm{d}\phi}{\mathrm{d}x}\right)_w \tag{3.16}$$

Central Difference

$$\frac{F_e\phi_E}{2} + \frac{F_e\phi_P}{2} - \frac{F_w\phi_W}{2} - \frac{F_w\phi_P}{2} = \left(\mu\frac{\mathrm{d}\phi}{\mathrm{d}x}\right)_e - \left(\mu\frac{\mathrm{d}\phi}{\mathrm{d}x}\right)_w \tag{3.17}$$

The upwind scheme can be rewritten to look like the left hand side of (3.17) to give,

$$\begin{aligned} \frac{F_e\phi_E}{2} + \frac{F_e\phi_P}{2} - \frac{F_w\phi_W}{2} - \frac{F_w\phi_P}{2} &= \left(\mu\frac{\mathrm{d}\phi}{\mathrm{d}x}\right)_e - \left(\mu\frac{\mathrm{d}\phi}{\mathrm{d}x}\right)_w \\ &+ F_e\left(\frac{\phi_E - \phi_P}{2}\right) + F_w\left(\frac{\phi_W - \phi_P}{2}\right) \end{aligned} \tag{3.18}$$

the final two terms of which can be converted back to their continuous form using the reverse discretisation as per equation (3.4), giving,

$$\begin{aligned} \frac{F_e\phi_E}{2} + \frac{F_e\phi_P}{2} - \frac{F_w\phi_W}{2} - \frac{F_w\phi_P}{2} &= \left(\mu\frac{\mathrm{d}\phi}{\mathrm{d}x}\right)_e - \left(\mu\frac{\mathrm{d}\phi}{\mathrm{d}x}\right)_w \\ &+ \frac{F_e}{2}\left(\frac{\mathrm{d}\phi}{\mathrm{d}x}\right)_e \Delta x - \frac{F_w}{2}\left(\frac{\mathrm{d}\phi}{\mathrm{d}x}\right)_w \Delta x \end{aligned} \tag{3.19}$$

It is now possible to re-express the upwind scheme as a central difference scheme with an effective diffusion term, $\tilde{\mu}$,

$$\frac{F_e\phi_E}{2} + \frac{F_e\phi_P}{2} - \frac{F_w\phi_W}{2} - \frac{F_w\phi_P}{2} = \left(\tilde{\mu}\frac{\mathrm{d}\phi}{\mathrm{d}x}\right)_e - \left(\tilde{\mu}\frac{\mathrm{d}\phi}{\mathrm{d}x}\right)_w . \tag{3.20}$$

where

$$\tilde{\mu}_{e,w} = \mu + \frac{(\rho u)_{e,w}}{2}\Delta x \quad . \tag{3.21}$$

From equation (3.20), the upwind scheme is equivalent to the central difference scheme with the physical diffusion coefficient replaced by (3.21) which is larger than the physical diffusion by $\frac{1}{2}(\rho u)_{e,w}\Delta x$. This suggests that the effect of the zero order interpolation of the upwind scheme introduces additional diffusion in comparison to the first order interpolation of the central difference scheme, an effect that is known as *numerical diffusion* and is characteristic of the upwind scheme (see Leonard, 1979).

Numerical diffusion has a detrimental effect on the accuracy of computed results. Due to the additional diffusion present, sharp gradients in the predicted variable appear smeared, as shown by Leonard (1979) for the convection of a scalar step profile. It is possible to reduce the numerical diffusion by decreasing the mesh size - see equation (3.21) - but this may increase the computational cost beyond the scope of many calculations to reach a desired accuracy.

A partial solution to numerical diffusion and lack of boundedness is to formulate a *hybrid* upwind-central difference scheme (Spalding, 1972). For Peclet numbers of less than two, the central difference scheme is used, but when the flow conditions are such that the Peclet number increases beyond this, upwind differencing is used. Even though this overcomes the problems of the central differencing scheme for high Peclet number flows, its use affords little improvement over the upwind scheme for high speed flows.

An improvement to convective discretisation methods was made by Patankar (1981) in the form of the *Power Law* scheme. This scheme is an improved approximation to the exponential scheme - the discrete version of the exact solution to the convection-diffusion equation (no sources or sinks) in one dimension. The power law scheme enables a higher accuracy approximation of the control volume face values by using a fifth degree polynomial in terms of the Peclet number. It allows a more gradual variation in control volume face values to be predicted for a wider range of Peclet numbers between zero and ten. For Peclet number above ten, the power law scheme

reverts to the upwind scheme.

Although this scheme behaves more like the exponential scheme than the hybrid scheme does, Leonard and Drummond (1995) recently called into question the validity of using any exponential based scheme. They revealed that such schemes approximate the exact exponential solution of the convection-diffusion equation by finding an effective Peclet number that matches the exact solution. They showed that the use of the effective Peclet number led to an additional artificial diffusivity being present in the solution. When the effective Peclet number becomes greater than two, these schemes become equivalent to using the upwind scheme for convection, ignoring the effects of the physical diffusion completely.

Leonard and Drummond also went on to state that these schemes, although suitable for one-dimensional, steady state, source free flows (with constant coefficients in the discretised equations), are not suitable outside these constraints. For example, in two dimensional flows, the cross stream diffusion can be very large if the Peclet number is too large in the cross stream direction. For cases when the flow is oblique to the computational grid, the Peclet number could be too large in both coordinate directions, allowing excessive numerical diffusion in both directions.

Another important point was made regarding the use of exponentially based schemes when used with turbulence equations. In turbulence models that make use of the Bousinesq eddy viscosity hypothesis (see chapter 2), serious problems occur when the artificial Peclet number becomes greater than two. As stated previously, when this happens, physical diffusion is ignored and only the artificial numerical diffusion is present. For eddy viscosity models, such as the $k - \epsilon$ model, this would negate any calculations made to find the eddy viscosity, meaning that solutions would become insensitive to the type of eddy viscosity turbulence model used (Leonard and Drummond, 1995).

These arguments clearly point to a need to increase the accuracy of convective discretisation schemes using higher order interpolations, whilst keeping artificial diffusivity to a minimum. The next section outlines methods that have been developed using these ideas.

3.4 High order convective discretisation schemes

Review

The first step to increase the accuracy of the convective discretisation whilst avoiding the oscillations produced by the central difference scheme, was to introduce a more accurate upwinding method. Warming and Beam (1976) introduced a second order upwind scheme (SOUS) where the value of the convected variable at the control volume face is found by extrapolating the variable gradient found at two upstream nodes. For example

$$\phi_e = \begin{cases} \frac{3}{2}\phi_P - \frac{1}{2}\phi_W & \text{for} \quad u_e > 0 \\ \frac{3}{2}\phi_E - \frac{1}{2}\phi_{EE} & \text{for} \quad u_e < 0 \end{cases} , \tag{3.22}$$

(where the computational stencil is shown later in figure 3.3).

The scheme was tested by Biagioli (1998) using the classical lid driven cavity and sudden expansion problems (see Ghia *et al.*, 1982; Armaly *et al.*, 1983). For the cavity example the second order upwind solution was found to agree with Ghia *et al.* 's solution on a grid of size 80×80 while a hybrid solution could only match it for a grid of size 160×160. The SOUS was capable of reproducing the steep velocity gradients near the lid, despite a more coarse mesh density due to the first order (linear) interpolation providing greater interpolative accuracy. More accurate predictions of reattachment length for the sudden expansion problem were also observed when using the SOUS when comparing against the measurements of Armaly *et al.* (1983).

A third order accurate scheme, QUICK, was introduced by Leonard (1979) and employs an upwind biased quadratic interpolation formula. Leonard showed that this scheme was capable of reproducing sharp gradients, such as convection of a step profile, whilst maintaining convective stability (see later). Despite the ability to predict steep gradients, Leonard himself produced results showing unphysical oscillations in these regions (however much smaller than those produced by a central difference scheme).

Owing to its simplicity of implementation and other schemes' comparative lack of accuracy, the QUICK scheme has enjoyed widespread use and has even been incorporated into several commercial CFD codes such as FLUENT (Fluent Inc.). Due to its significance, and influence on successive schemes, a more complete description of the QUICK scheme is presented later.

A fourth order discretisation scheme was implemented by Lilek and Peric (1995) after integrating the governing equations using Simpson's rule. To maintain the order of approximation of the integral equations, a cubic interpolation scheme, equivalent to a fourth order central difference scheme, was used. For test problems such as the lid driven cavity, the fourth order scheme was shown to achieve grid independence much quicker than the central difference or upwind schemes upon successive grid refinement. Due to the higher numbers of nodes required for interpolation, 15 for any control volume face, the computational cost for the scheme is increased over the central difference scheme.

Unfortunately the above schemes suffer from unbounded (see Gaskell and Lau, 1988) interpolations, so control volume face values may lie outside those of the neighbouring nodal points in the absence of sources or sinks. This property can give rise to unphysical solutions and even computational divergence. There are, however, other schemes that have been developed that counteract this problem.

Total Variation Diminishing (TVD) schemes were first introduced by Harten (1983) for time dependent hyperbolic problems. These schemes dictate that the total variation (TV) of a solution, u, decreases from one time step to the next,

$$\mathrm{TV}(u^{k+1}) \leq \mathrm{TV}(u^{k}) \tag{3.23}$$

where

$$\mathrm{TV}(u) = \sum_{j=-\infty}^{\infty} |u_{j+1} - u_j| \quad . \tag{3.24}$$

Harten also went on to say that these schemes always provide convergent, unique solutions. Many of the schemes derived using this method include flux limiting techniques to stop unbounded solutions from occurring (see Van Leer, 1979; Darwish

and Moukalled, 2003; Sweby, 1984). Despite their ability to capture sharp gradients in variable profiles, TVD schemes are mainly applied to solution of the time dependent Euler equations for compressible, high speed flows, and do not have a steady state counterpart.

For incompressible flows Leonard's QUICK scheme proved very popular due to its ability to resolve steep gradients. However, its ability to predict unbounded solutions was a major drawback. Gaskell and Lau (1988) changed the way that high order discretisation schemes should be conceived by introducing two important methodologies: the Convection Boundedness Criterion (CBC) and Curvature Compensated Convective Transport (CCCT). The CBC was defined using physical principles in order that convective discretisation schemes should remain bounded. CCCT was introduced as a method of providing an explicit curvature correction to the third order QUICK scheme of Leonard, to ensure that the CBC was fulfilled. The specific methods the authors undertook to implement CCCT resulted in the well known SMART algorithm.

The third order accurate SMART scheme was tested against two cases: convection of a top-hat function, and convection of a scalar step, both oblique to the computational mesh. For both test cases, SMART showed superior resolution of the steep gradients compared to lower order interpolative schemes, and matched the results of the QUICK scheme. However, unlike the QUICK scheme, it was able to achieve physical, bounded solutions whilst maintaining good resolution. Gaskell and Lau also included an illustrative tool, the normalised variable diagram (NVD), upon which CCCT schemes such as SMART may be defined complying with the CBC.

Zhu (1991) introduced a scheme based upon a quadratic function in the normalised variable diagram, as opposed to the piecewise linear method proposed by Gaskell and Lau, in an attempt to remove the effect of discontinuities in changing from one linear function to another. Zhu tested his NVD scheme against QUICK and the hybrid scheme but surprisingly not against SMART. For convection of a square step, the scheme outperformed the other schemes in a manner similar to SMART. This scheme however was only second order accurate (as opposed to third order for SMART) due to the second order truncation terms in its formulation.

Seok *et al.* (1995) compared the scheme of Zhu with that of Gaskell and Lau and another high order scheme introduced by the authors. The scheme presented was similar to that of Zhu, being a quadratic function in the normalised variable diagram, but passing through the point $(0.5, 0.75)$ in the NVD with the gradient of the QUICK scheme to ensure third order accuracy. For the convection of a scalar step case, the NVD schemes were virtually identical in capturing the steep gradient without unbounded oscillations.

Song *et al.* (2000) and Alves *et al.* (2003) also added to the list of NVD schemes with the WACEB and CUBISTA variants, respectively. These schemes not only incorporated the CBC to ensure boundedness of any solutions, but also used the TVD constraints to ensure converged solutions. Both schemes have lower interpolative accuracy than the SMART scheme, but when tested for several test cases including convection of a top hat profile, the WACEB scheme was not able to predict the maximum value of the top hat function in the same manner as the SMART scheme, as shown by Gaskell and Lau (1988), and both schemes could not match SMART for convection of a step profile. Despite this, all of the schemes are found to be in close agreement, with only small differences in their predictions.

In this work the SMART scheme of Gaskell and Lau will be used for its higher interpolative accuracy, while the CUBISTA scheme will be used for its TVD convergence properties where SMART experiences convergence difficulties. The following sections describe these schemes in more detail, with an introduction to Leonard's QUICK scheme as an aid to understanding.

QUICK

Leonard (1979) made a significant improvement to convective discretisation with the introduction of his QUICK (Quadratic Upstream Interpolation for Convective Kinematics) scheme. This method extended the interpolation stencil to include the adjacent nodes to the central computational node, plus the far ones, equating to the use of a total of five nodes in 1D (see figure 3.3).

Depending upon the direction of the flow, a quadratic interpolation was imple-

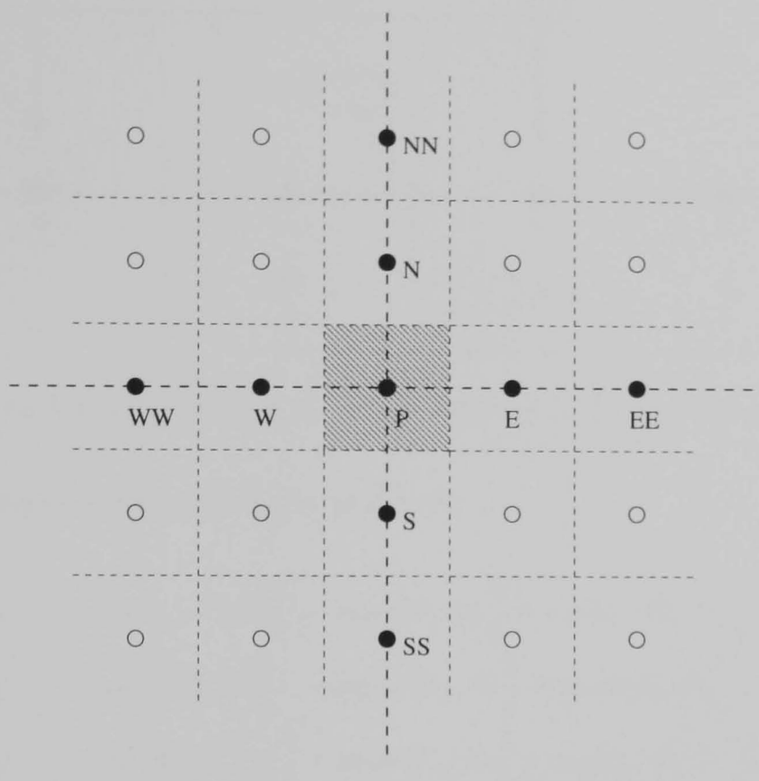

FIGURE 3.3: 2D computational stencil for the QUICK scheme.

mented, weighted in the upstream direction. In the one dimensional example of the advection of a general scalar, ϕ, shown in figure 3.4, the downstream control volume face value is given by

$$\phi_e = \frac{1}{2}(\phi_P + \phi_E) - \frac{1}{8}(\phi_W + \phi_E - 2\phi_P) \tag{3.25}$$

where advection is from left to right ($F > 0$). If advection is in the reverse direction, from right to left ($F < 0$), the interpolation formula for the right control volume face value of ϕ is

$$\phi_e = \frac{1}{2}(\phi_P + \phi_E) - \frac{1}{8}(\phi_{EE} + \phi_P - 2\phi_E) \quad . \tag{3.26}$$

Equations (3.25) and (3.26) can be interpreted as a linear interpolation for ϕ from the neighbouring nodal values plus a correction term that is proportional to the curvature in the variation of ϕ in the upstream direction. Similar expressions exist for the left control volume face value, ϕ_w.

Using the interpolation formulæ(3.25) and (3.26), for u and v velocities, the coeffi-

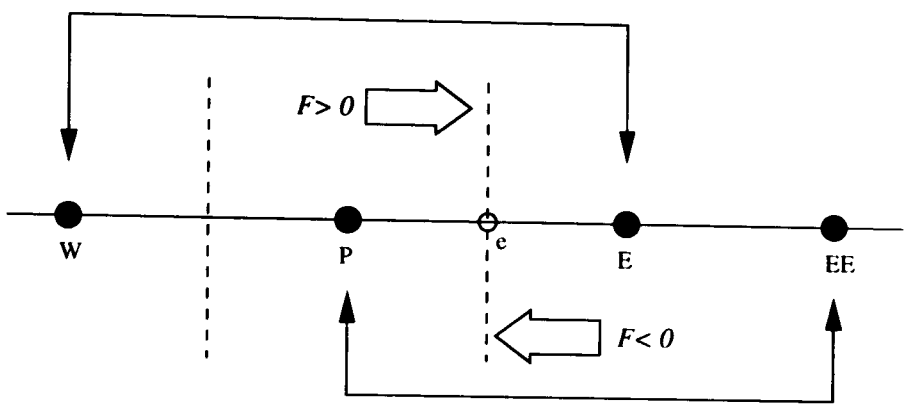

FIGURE 3.4: Illustration of upstream weighting in the QUICK scheme.

cients of the discretisation equations (3.11) are

$$
\begin{aligned}
a_E &= max(-F_e,0)\frac{3}{4} - max(F_e,0)\frac{3}{8} + max(-F_w,0)\frac{1}{8} + D_e \\
a_W &= max(F_w,0)\frac{3}{4} - max(-F_w,0)\frac{3}{8} + max(F_e,0)\frac{1}{8} + D_w \\
a_N &= max(-F_n,0)\frac{3}{4} - max(F_n,0)\frac{3}{8} + max(-F_s,0)\frac{1}{8} + D_n \\
a_S &= max(F_s,0)\frac{3}{4} - max(-F_s,0)\frac{3}{8} + max(F_n,0)\frac{1}{8} + D_s \\
a_{EE} &= -max(-F_e,0)\frac{1}{8} \\
a_{WW} &= -max(F_w,0)\frac{1}{8} \\
a_{NN} &= -max(-F_n,0)\frac{1}{8} \\
a_{SS} &= -max(F_s,0)\frac{1}{8} \\
a_P &= a_E + a_W + a_N + a_S + a_{EE} + a_{WW} + a_{NN} + a_{SS} \quad . \qquad (3.27)
\end{aligned}
$$

As noted previously, the computational stencil is increased compared to the aforementioned upwind or central difference schemes. For two and three dimensions, nine and twelve nodes are required, respectively. At the boundaries of the solution domain, the far node coefficients cannot be prescribed in the usual manner; they lie outside the computational domain. Leonard suggested the use of 'ghost' nodes that mimic real nodes. To overcome this computational problem, the hybrid scheme can be used at domain boundaries, where it is possible to make $Pe < 2$ by adequate mesh refinement, meaning that the central difference part of the hybrid scheme is operational without the instabilities mentioned earlier.

Leonard introduced a new parameter, the *convective sensitivity*, to analyse the sta-

bility of discretisation schemes. Convective sensitivity is defined as the sensitivity of the convective influx to the change in the convected variable ϕ at the central node, P.

$$\frac{\partial C_{IF}}{\partial \phi_P} \begin{cases} < 0 & \text{stable,} \\ = 0 & \text{neutral,} \\ > 0 & \text{unstable} \end{cases} \tag{3.28}$$

The convective sensitivity of the QUICK scheme was shown by Leonard to be unconditionally stable in the simple case of uniform, uni-directional convection of a scalar variable.

The present author has generalised this analysis further here showing that

$$\frac{\partial C_{IF}}{\partial \phi_P} = \begin{cases} -\frac{1}{16\Delta x_P}(12u_e - 6u_w) & \text{if } u_e > 0 \text{ and } u_w > 0 \\ \frac{1}{16\Delta x_P}(6|u_e| + 6u_w) & \text{if } u_e < 0 \text{ and } u_w > 0 \\ -\frac{1}{16\Delta x_P}(12u_e + 12|u_w|) & \text{if } u_e > 0 \text{ and } u_w < 0 \\ \frac{1}{16\Delta x_P}(6|u_e| - 12|u_w|) & \text{if } u_e < 0 \text{ and } u_w < 0 \end{cases}, \tag{3.29}$$

from which the following conclusions can be drawn. Firstly, when fluid is convergent upon a control volume cell (when $u_e < 0$ and $u_w > 0$), convective instability is *always* present. Conversely, when fluid is divergent from a control volume cell (when $u_e > 0$ and $u_w < 0$), convective stability persists. In practice, this may be applicable to only small parts of the flow field, but large instabilities are capable of causing divergent behaviour in a numerical calculation through propagation of unphysical solutions. In the remaining cases of equation (3.29), where the flow is aligned in a single direction, neutral sensitivity is achieved when one of the control volume face velocities is twice the value of the other. For example, when the flow is aligned from left to right, neutral sensitivity occurs when $u_w = 2u_e$. As can be seen from equation (3.29), when the value of u_w exceeds twice the value of u_e convective instability occurs. This effect is reproducible in more realistic flow regimes where impingements or shocks occur, leading to steep velocity gradients over the width of a control volume.

Leonard (1979) tested the QUICK scheme for several ideal flow problems, such as the convection of a scalar square step profile. From these results it was shown that in regions of high gradients for the convected variable, oscillatory behaviour

was observed but the gradient was captured more accurately than with methods such as the central difference or upwind schemes. The nature of the oscillations showed the convected variable exceeding its physically bounding values. The above reasoning would explain this behaviour in the convection of a step profile where one control volume face value of the convected variable is more than double that at the opposing face. This is obviously an undesirable feature of the scheme, leading to physically unrealistic solutions. More recent convective discretisation schemes have been formulated to overcome this problem and are presented below.

3.4.1 The Convection Boundedness Criterion

To counteract the appearance of unphysical oscillations and lack of boundedness in convective discretisation schemes, Gaskell and Lau (1988) proposed the SMART (Sharp and Monotonic Algorithm for Realistic Transport by Convection) scheme. In their analysis, it was noted that the QUICK scheme (and other higher order schemes) does not always achieve interpolative boundedness due to the parabolic interpolation profile adopted.

For the one dimensional control volume shown in figure 3.2, interpolative boundedness at the east face for the convected variable ϕ is satisfied when its value lies between the values at the adjacent nodes when sources are not present. To illustrate interpolative boundedness the normalised variable diagram is used, where the normalised convected variable at a position k between nodes W and E is defined as

$$\hat{\phi}_k = \frac{\phi_k - \phi_W}{\phi_E - \phi_W}. \tag{3.30}$$

Figure 3.5 shows the normalised variable diagram for the normalised variable $\hat{\phi}_e$ at the right face of the control volume against the nodal value at the control volume centre, $\hat{\phi}_P$. In normalised variable notation, interpolative boundedness for $\hat{\phi}_e$ is given by

$$\begin{aligned} \hat{\phi}_e &\in (\hat{\phi}_P, 1] \quad \text{when} \quad \hat{\phi}_P \in (-\infty, 1] \\ \hat{\phi}_e &\in [1, \hat{\phi}_P) \quad \text{when} \quad \hat{\phi}_P \in [1, \infty) \end{aligned} \tag{3.31}$$

The condition of interpolative boundedness is not, however, sufficient to satisfy computational boundedness. When source terms are present, the relations for interpolative boundedness (3.31), need to be modified to create a more general, sufficient definition,

$$\begin{aligned} 1 < \hat{\phi}_e \leqslant \hat{\phi}_P \quad \text{and} \quad 0 \leqslant \hat{\phi}_w < \hat{\phi}_e \quad \text{if} \quad \hat{S} > 0, \quad \hat{\phi}_P > 1 \\ 0 \leqslant \hat{\phi}_w \leqslant \hat{\phi}_P < \hat{\phi}_e \leqslant 1 \quad \text{if} \quad \hat{S} \geqslant 0, \quad 0 \leqslant \hat{\phi}_P \leqslant 1 \\ \hat{\phi}_P \leqslant \hat{\phi}_e < \hat{\phi}_w < 0 \quad \text{if} \quad \hat{S} < 0, \quad \hat{\phi}_P < 0 \end{aligned} \tag{3.32}$$

where $\hat{S}$ is a normalised source term. From equations (3.32), a *Convection Boundedness Criterion* (CBC) can be formulated (Gaskell and Lau, 1988). The CBC is shown in figure 3.5, as the shaded area that lies between $(0,0)$ and $(1,1)$ bounded from below by the line $\hat{\phi}_e = \hat{\phi}_P$ and from above by the line $\hat{\phi}_e = 1$. When $\hat{\phi}_P \notin [0,1]$, $\hat{\phi}_e$ is equal to $\hat{\phi}_P$, as shown by the line. Gaskell and Lau showed that any convective

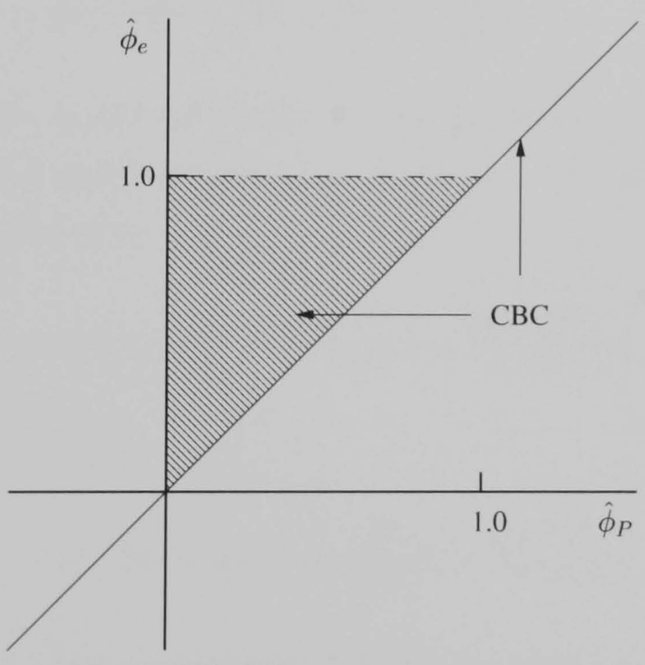

FIGURE 3.5: Normalised variable diagram for ϕ at the east face of the control volume; Gaskell and Lau (1988).

scheme that adheres to the CBC, and falls within the shaded area of figure 3.5, will produce bounded, monotonic interpolations of control volume face variables.

3.4.2 Curvature Compensated Convective Transport

To define their higher order convection scheme, Gaskell and Lau (1988) introduced the novel method of *curvature compensation.* Taking Taylor series expansions of the convected variable, ϕ, about the central node, P and the E and W nodes, ignoring higher order derivatives gives,

$$\begin{aligned}
\phi_E &= \phi_e + \frac{\Delta x}{2}\frac{\partial}{\partial x}\phi_e + \frac{\Delta x^2}{8}\frac{\partial^2}{\partial x^2}\phi_e + \frac{\Delta x^3}{48}\frac{\partial^3}{\partial x^3}\phi_e + \ldots \\
\phi_P &= \phi_e - \frac{\Delta x}{2}\frac{\partial}{\partial x}\phi_e + \frac{\Delta x^2}{8}\frac{\partial^2}{\partial x^2}\phi_e - \frac{\Delta x^3}{48}\frac{\partial^3}{\partial x^3}\phi_e + \ldots \\
\phi_W &= \phi_e - \frac{3\Delta x}{2}\frac{\partial}{\partial x}\phi_e + \frac{9\Delta x^2}{8}\frac{\partial^2}{\partial x^2}\phi_e - \frac{9\Delta x^3}{16}\frac{\partial^3}{\partial x^3}\phi_e + \ldots
\end{aligned} \tag{3.33}$$

from which it is possible to create an expression for the convected variable at the right hand control volume face, ϕ_e,

$$\phi_e = \frac{3}{4}\phi_P + \frac{3}{8}\phi_E - \frac{1}{8}\phi_W - \frac{\Delta x^3}{16}\frac{\partial^3}{\partial x^3}\phi_e \quad . \tag{3.34}$$

By discretising the double differential of ϕ with respect to x, a curvature term (representative of a double derivative) is produced, a measure of which may be deduced by equations (3.33),

$$\phi_E - 2\phi_P + \phi_W = \Delta x^2\frac{\partial^2}{\partial x^2}\phi_e + \frac{\Delta x^3}{2}\frac{\partial^3}{\partial x^3}\phi_e \quad . \tag{3.35}$$

Rearranging this term gives

$$\phi_E - 2\phi_P + \phi_W - \Delta x^2\frac{\partial^2}{\partial x^2}\phi_e = \frac{\Delta x^3}{2}\frac{\partial^3}{\partial x^3}\phi_e \tag{3.36}$$

which can then be added to expression (3.34) for the control volume face value.

$$\begin{aligned}
\phi_e &= \frac{3}{4}\phi_P + \frac{3}{8}\phi_E - \frac{1}{8}\phi_W - \frac{\Delta x^3}{16}\frac{\partial^3}{\partial x^3}\phi_e + \alpha\frac{\Delta x^3}{2}\frac{\partial^3}{\partial x^3}\phi_e - \alpha\frac{\Delta x^3}{2}\frac{\partial^3}{\partial x^3}\phi_e \\
&= \left(\frac{3}{4} + 2\alpha\right)\phi_P + \left(\frac{3}{8} - \alpha\right)\phi_E - \left(\frac{1}{8} + \alpha\right)\phi_W \\
&+ \quad \text{Higher derivative terms.}
\end{aligned} \tag{3.37}$$

Equation (3.37) can be seen as adding a second order curvature correction to the already third order interpolation for the control volume face value, ϕ_e. The α variable is used to dynamically adjust the amount of compensation required to attain bounded, high order interpolations and is typically given by the interpolation scheme used. The piecewise NVD formulations of Gaskell and Lau's SMART scheme and the CUBISTA scheme of Alves *et al.* are used to provide values of α in the present work, and are outlined below.

3.4.3 SMART

To fulfill the CBC, Gaskell and Lau formulated the well known SMART algorithm, which at the time represented a major step forward. At first glance, the interpolation (3.37) has the same form as the QUICK scheme with each coefficient containing a weighted (by α) upstream curvature component. To maintain the third order truncation characteristics, α is kept to a minimum, while maintaining boundedness.

The SMART algorithm is shown diagrammatically in figure 3.6. For $\hat{\phi}_P \notin [0,1]$ the normalised face value, $\hat{\phi}_e$ is equal to $\hat{\phi}_P$ in agreement with the CBC. When $\hat{\phi}_P \in$

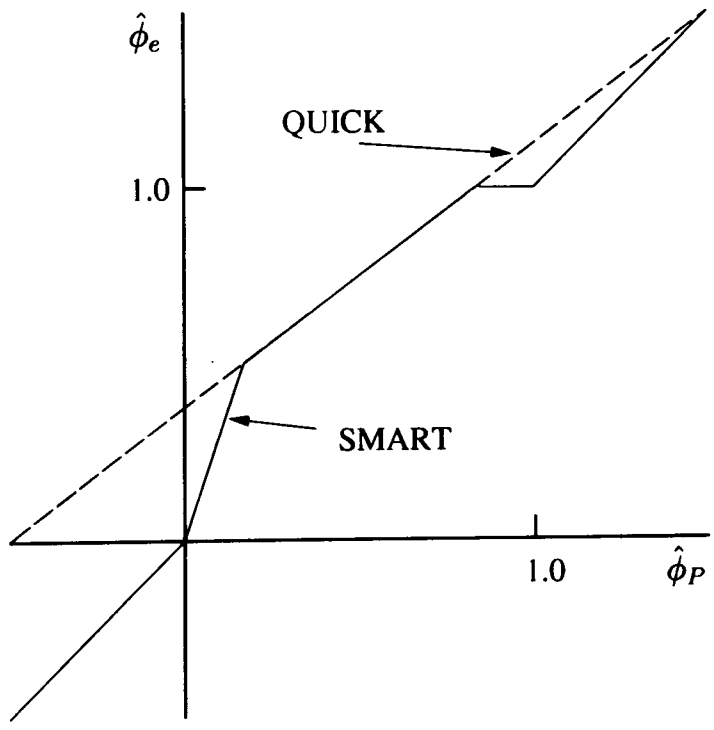

FIGURE 3.6: Normalised variable diagram for the SMART algorithm.

$(\frac{5}{6}, 1]$, to maintain boundedness, $\hat{\phi}_e$ must not be greater than one (as shown by the horizontal line). In the region $\hat{\phi}_P \in [0, \frac{1}{6}]$, $\hat{\phi}_e$ is approximated by the line from $(0,0)$

to $(\frac{1}{6}, \frac{1}{2})$ to prevent lack of boundedness due to undershoots in the interpolation. The remainder of the region lies on the $\alpha = 0$ line, which is identical to the QUICK algorithm with its third order truncation error.

Determination of α yields the amount of curvature compensation required to achieve monotonically varying, bounded interpolations. From equation (3.37), α is given by,

$$\alpha = \frac{\hat{\phi}_e - \frac{3}{8}(2\hat{\phi}_P + 1)}{(2\hat{\phi}_P - 1)}. \tag{3.38}$$

From this equation, and the piecewise linear function shown in the normalised variable diagram (figure 3.6), the following values of α are obtained.

$$\hat{\phi}_e = \begin{cases} \hat{\phi}_P \quad \text{and} \quad \alpha \in (-\frac{1}{8}, \frac{3}{8}) & \text{if} \quad \hat{\phi}_P \notin [0,1] \\ 3\hat{\phi}_P \quad \text{and} \quad \alpha \in (0, \frac{3}{8}] & \text{if} \quad \hat{\phi}_P \in [0, \frac{1}{6}) \\ 1 \quad \text{and} \quad \alpha \in [-\frac{1}{8}, 0) & \text{if} \quad \hat{\phi}_P \in (\frac{5}{6}, 1] \\ \frac{3}{8}(2\hat{\phi}_P + 1) \quad \text{and} \quad \alpha = 0 & \text{if} \quad \hat{\phi}_P \in [\frac{1}{6}, \frac{5}{6}] \end{cases} \tag{3.39}$$

The SMART scheme was implemented and tested by its authors against several idealised flow cases. The two test cases were pure convection of a step profile for differing angles of obliqueness to the computational mesh and pure convection of a top hat function. The SMART algorithm showed important improvements over the QUICK scheme for both test cases. Whilst still being able to capture the steep gradients associated with the step and top hat functions to an equivalent degree of accuracy, SMART did not produce the same under and overshoots in the vicinity of those steep gradients as the QUICK scheme. Computationally, SMART was found to be only slightly more costly than QUICK, with the same mesh density. However, when the mesh was varied so that the upwind, QUICK and SMART schemes all achieved the same accuracy of solution, it was found that SMART was the least costly by the ratio $1{:}1.3{:}1.3 \times 10^3$ (SMART:QUICK:upwind).

3.4.4 CUBISTA

Despite the high accuracy (formally third order truncation error in the smooth flow region) and boundedness of the SMART scheme, the CBC does not always guarantee a converged solution. Gaskell and Lau attempted to remove this problem by under-relaxation of the α parameter for each iteration. Alves *et al.* (2003) noted that the CBC constraints in the normalised variable diagram were not sufficient for convergence, and that only the more severe TVD constraints were able to ensure convergence.

In normalised variable notation, the TVD constraints are given by

$$\begin{aligned} \hat{\phi}_P \leqslant \hat{\phi}_e \leqslant (2-C)\hat{\phi}_P \quad &\text{if} \quad \hat{\phi}_P \leqslant \frac{1}{2} \\ \hat{\phi}_P \leqslant \hat{\phi}_e \leqslant 1 - C(1-\hat{\phi}_P) \quad &\text{if} \quad \hat{\phi}_P > \frac{1}{2}, \end{aligned} \tag{3.40}$$

as shown in figure 3.7. Instead of only the TVD constraints being used for the new convection scheme several others were considered. In the smooth region of the NVD diagram (for instance when $\hat{\phi}_P \in [\frac{1}{6}, \frac{5}{6}]$ in the SMART scheme), the QUICK scheme was used. Using similar reasoning to that of Gaskell and Lau, the QUICK scheme behaves monotonically and is bounded in this region and is also capable of high accuracy due to the third order truncation error. In figure 3.7, the TVD constraints require the gradient of the line in the region $\hat{\phi}_P \approx 0$ to be given by $2 - C$ where C is the Courant number for unsteady flows. In the region where $\hat{\phi}_P \approx 1$, the gradient of the line is equal to C. In these regions, the lines from $(0,0)$ and $(1,1)$ with the corresponding gradients, are joined to the QUICK line. In reality C was treated as a parameter and not a real Courant number due to the implicit time marching algorithm used by Alves *et al.* (2003). The value given for this parameter was 0.25 and obtained by numerical experiments to provide convergent results for all the test cases that the authors considered. This value of C is used to provide a balance between good resolution of steep gradients (when C is small - approximating the SMART scheme), but also to obtain convergent solutions (when C has a higher value).

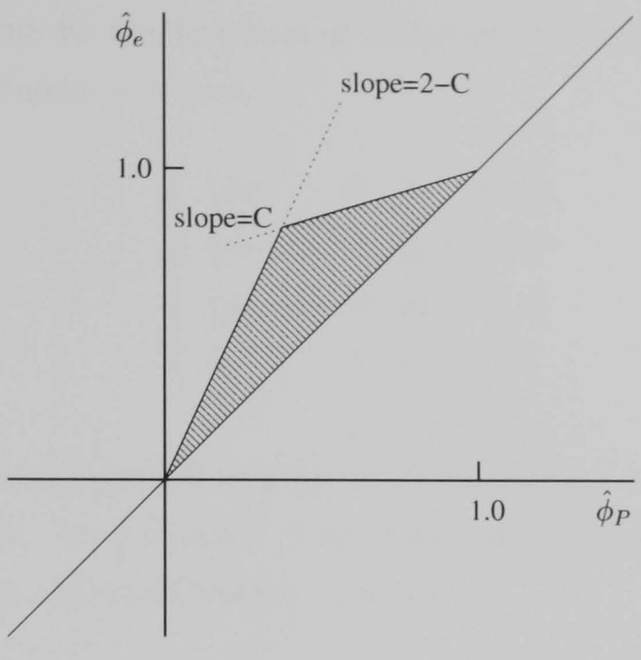

FIGURE 3.7: TVD constraints represented in the Normalised Variable Diagram.

When $\hat{\phi}_P$ approaches unity, it is seen from the normalised variable diagram (figure 3.6) that the QUICK scheme does not obey the CBC (i.e. the line extends beyond $\hat{\phi}_e = 1$). As mentioned previously, this has the effect of causing overshoots in the interpolation of the face variable, ϕ_e. The equation of the QUICK interpolation over a local coordinate ζ may be given as

$$\phi(\zeta) = \phi_P + \frac{\phi_E - \phi_W}{2}\zeta + \frac{\phi_E + \phi_W - 2\phi_P}{2}\zeta^2 \tag{3.41}$$

where: $\phi_P = \phi(0)$, $\phi_E = \phi(1)$ and $\phi_W = \phi(-1)$. Alves *et al* noted that the location at which the overshoot occurred is given by the turning point of the interpolation curve of (3.41) as $\zeta \to 1$, leading to

$$\frac{\phi_P - \phi_W}{\phi_E - \phi_W} \equiv \hat{\phi}_P \geqslant \frac{3}{4}. \tag{3.42}$$

To avoid overshoots as $\hat{\phi}_P \approx 1$, at the point $\hat{\phi}_P = \frac{3}{4}$ a line must be drawn from the QUICK line to the point $(1, 1)$ in the normalised variable diagram. The slope of this line is equivalent to the parameter $C = 0.25$, verifying the results of the numerical experiments undertaken by the authors.

From the above considerations, the CUBISTA (Convergent and Universally Bounded

Interpolation Scheme for the Treatment of Advection) can be defined on the normalised variable diagram as follows,

$$\hat{\phi}_e = \begin{cases} \frac{7}{4}\hat{\phi}_P & \text{if } \hat{\phi}_P \in (0, \frac{3}{8}) \\ \frac{3}{4}\hat{\phi}_P + \frac{3}{8} & \text{if } \hat{\phi}_P \in [\frac{3}{8}, \frac{3}{4}] \\ \frac{1}{4}\hat{\phi}_P + \frac{3}{4} & \text{if } \hat{\phi}_P \in (\frac{3}{4}, 1) \\ \hat{\phi}_P & \text{if } \hat{\phi}_P \notin [0, 1] \end{cases} \tag{3.43}$$

This scheme can be implemented using the CCCT methodology requiring calculation of the α parameter. From equation (3.38), values of α may be obtained for the piecewise linear function for CUBISTA in the NVD.

$$\alpha \begin{cases} \in (0, \frac{3}{8}) & \text{if } \hat{\phi}_P \in (0, \frac{3}{8}) \\ = 0 & \text{if } \hat{\phi}_P \in [\frac{3}{8}, \frac{3}{4}] \\ \in (0, -\frac{1}{8}) & \text{if } \hat{\phi}_P \in (\frac{3}{4}, 1) \\ \in (-\frac{1}{8}, \frac{3}{8}) & \text{if } \hat{\phi}_P \notin [0, 1] \end{cases} \tag{3.44}$$

Both the SMART and CUBISTA schemes can be implemented into the discretised momentum equations using the same method as that for the QUICK scheme, but replacing equation (3.25) by equation (3.37).

3.4.5 Convective sensitivity of SMART and CUBISTA

Previously, it was shown that the QUICK scheme had undesirable oscillations in the solution when predicting steep gradients. The generalised 1D convective sensitivity analysis proved that when $2u_e < u_w$ during positive flow from left to right through the control volume, QUICK is unstable. Despite the improved physical basis of SMART and CUBISTA through the use of the CBC and CCCT methodology, the convective sensitivity of SMART has only briefly been mentioned by Gaskell and Lau (1988) and not at all by Alves *et al.* (2003).

Using the interpolation formula for CCCT in (3.37), a similar convective sensitivity

analysis to that of QUICK is possible,

$$\frac{\partial C_{IF}}{\partial \phi_P} = \begin{cases} -\frac{1}{16\Delta x_P}([12+32\alpha_e]u_e - [6-16\alpha_w]u_w) & \text{if } u_e > 0 \text{ and } u_w > 0 \\ \frac{1}{16\Delta x_P}([6-16\alpha_e]|u_e| + [6-16\alpha_w]u_w) & \text{if } u_e < 0 \text{ and } u_w > 0 \\ -\frac{1}{16\Delta x_P}([12+32\alpha_e]u_e + [12+32\alpha_w]|u_w|) & \text{if } u_e > 0 \text{ and } u_w < 0 \\ \frac{1}{16\Delta x_P}([6-16\alpha_e]|u_e| - [12+32\alpha_w]|u_w|) & \text{if } u_e < 0 \text{ and } u_w < 0 \end{cases} \tag{3.45}$$

The stability equations in (3.45) show a dependence upon the curvature correction parameter, α, at the corresponding control volume faces. From (3.39) and (3.44) the value of α varies between $-\frac{1}{8}$ and $\frac{3}{8}$ which can then be inserted into (3.45) to give an overall picture of sensitivity of SMART and CUBISTA.

For the first condition in (3.45) when face velocities are positive, the largest value of convective sensitivity is given when both $\alpha_e = \alpha_w = -\frac{1}{8}$, leading to,

$$\begin{aligned} &\text{stable} \quad \text{if} \quad u_e > u_w \\ &\text{neutral} \quad \text{if} \quad u_e = u_w \\ &\text{unstable} \quad \text{if} \quad u_e < u_w \quad . \end{aligned} \tag{3.46}$$

The smallest value of convective sensitivity occurs when $\alpha_e = \alpha_w = \frac{3}{8}$, which gives stability as $\partial C_{IF}/\partial \phi_P \propto -24u_e$.

The next condition is for flow convergent on the control volume ($u_e < 0$,$u_w > 0$). In this case, the largest value of convective sensitivity is when $\alpha_e = \alpha_w = -\frac{1}{8}$, giving

$$\frac{\partial C_{IF}}{\partial \phi_P} \propto 8|u_e| + 8u_w, \tag{3.47}$$

and instability. When the smallest value of sensitivity occurs ($\alpha_e = \alpha_w = \frac{3}{8}$) neutral sensitivity persists. This result compares more favourably than the result of the QUICK scheme, where instability is *always* present. For flow divergent from a control volume it is clear to see that stability is always present, as for the QUICK scheme, independent of values of α.

When the face velocities are negative, the opposite happens to when they are posi-

tive. The largest value of convective sensitivity is when $\alpha_e = \alpha_w = -\frac{1}{8}$, giving

$$\begin{aligned} \text{stable} \quad &\text{if} \quad |u_w| > |u_e| \\ \text{neutral} \quad &\text{if} \quad |u_w| = |u_e| \\ \text{unstable} \quad &\text{if} \quad |u_w| < |u_e| \quad . \end{aligned} \tag{3.48}$$

When $\alpha_e = \alpha_w = \frac{3}{8}$, a stable condition persists with the smallest value given by

$$\partial C_{IF}/\partial \phi_P \propto -24|u_w| \quad . \tag{3.49}$$

The above analysis shows that the SMART and CUBISTA schemes have more favourable stability characteristics compared to the QUICK scheme, especially when flow is convergent upon a control volume.

3.5 Solution of the Discretised Equations

Now that the momentum equations have been discretised using the above convective approximations, it is appropriate to discuss methods for their solution. There is, however, a varying physical quantity that appears in these equations but lacks a method for its determination, namely pressure. The lack of an explicit equation for the pressure means that it must be determined indirectly. The main pressure algorithms in use in the CFD community are related to the SIMPLE (Semi IMplicit Pressure Linked Equations) method of Patankar and Spalding (1972), such as the SIMPLER (Patankar, 1980), SIMPLEC (Van Doormaal and Raithby, 1984) and the well known PISO method (Issa, 1985).

3.5.1 The SIMPLE Procedure

Patankar and Spalding (1972) introduced the SIMPLE algorithm as a way of incorporating the effects of pressure into the solution for the momentum equations. This was done indirectly by the use of the continuity equation (2.1). This equation can

be integrated over a control volume in the same way as the momentum equations,

$$\oint_S \rho u \cdot \mathbf{n} dS = [(\rho u)_e - (\rho u)_w]\Delta y + [(\rho v)_n - (\rho v)_s]\Delta x. \tag{3.50}$$

If the equation for a face velocity could be given as (see section 3.5.3)

$$a_e u_e^* = H_e^* - (P_E - P_P)\Delta y \tag{3.51}$$

then it may be used in equation (3.50). In an iterative procedure, the velocity $\mathbf{u}^*$ may not satisfy the continuity condition, and so a correction must be added,

$$\mathbf{u} = \mathbf{u}^* + \mathbf{u}' \rightarrow \mathbf{u}' = \mathbf{u} - \mathbf{u}^*. \tag{3.52}$$

From this an expression for the correction may be obtained (assuming coefficients remain constant)

$$\begin{aligned} u_e' &= \tfrac{1}{a_e}\left[H_e - H_e^* - (P_E - P_E^* - P_P + P_P^*)\Delta y\right] \\ &= \tfrac{1}{a_e}\left[H_e' - (P_E' - P_P')\Delta y\right] \end{aligned} \tag{3.53}$$

where P' is the correction to the pressure to maintain continuity. Patankar (1980) neglected the H_e' term in equation (3.53) because as the calculation converges $\mathbf{u}^* \rightarrow \mathbf{u}$ and so $H_e' \rightarrow 0$. This leaves the correction in a simplified manner as

$$u_e' = -\frac{1}{a_e}(P_E' - P_P')\Delta y \tag{3.54}$$

Inserting this equation, using (3.52), into the integrated continuity equation (3.50) gives a discretisation equation for the pressure correction,

$$A_P P_P' = A_E P_E' + A_W P_W' + A_N P_N' + A_S P_S' + b \tag{3.55}$$

where

$$A_E = \frac{\rho_e \Delta y^2}{a_e} \quad , \quad A_W = \frac{\rho_w \Delta y^2}{a_w}$$
$$A_N = \frac{\rho_n \Delta x^2}{a_n} \quad , \quad A_S = \frac{\rho_s \Delta x^2}{a_s}$$

$$b = (\rho_w u_w^* - \rho_e u_e^*)\Delta y \quad + \quad (\rho_s u_s^* - \rho_n u_n^*)\Delta x. \tag{3.56}$$

To update the pressure field, all that is then needed is to add the correction for the pressure to the current value of the pressure at the nodal point. It is then possible to update the velocity through equation (3.54).

As the SIMPLE algorithm is iterative and the variables are calculated in a segregated manner, the order of calculation needs to be determined. Patankar proposed the following algorithm,

1. guess an initial pressure field,
2. solve the momentum discretisation equations to find u^* and v^*,
3. solve the discretised equation for the pressure correction, P' (3.55),
4. correct the velocity fields from the pressure corrections (3.54) (3.52),
5. correct the pressure field,
6. repeat from step 2.

The SIMPLE algorithm has been the mainstay of the control volume method since its introduction, and is now routinely used in flow situations ranging from laminar to turbulent and viscoelastic flows. Reports, however (Patankar, 1981), (Patankar, 1981) have stated that the convergence rates of SIMPLE are not always favourable. The removal of the H' term from equation (3.53) to (3.54) leads to the over prediction of the pressure correction, slowing convergence rates. By performing under-relaxation for the pressure correction (discussed later), a fraction of the correction is used to update the pressure field. While this helps to stabilise the algorithm, this also leads to slower convergence rates if excessive under-relaxation is required.

3.5.2 PISO

Issa (1985) first introduced the PISO (Pressure-Implicit with Splitting of Operators) algorithm for the improvement of convergence rates for time dependent calculations.

Instead of just using a single pressure correction, as in the SIMPLE algorithm, a second corrector step is added. For time dependent calculations, the PISO algorithm obviates the need for iteration in the calculation, unlike the SIMPLE method. As PISO is stable for large time-steps due to its pseudo- implicit formulation, the author also advocated its use for steady state calculations. It is possible, however, to formulate a steady state version of the algorithm, as used in the course of the present work.

The first step in the PISO algorithm is to calculate a velocity field, $\mathbf{u}^*$, from the previous iterate value of the pressure field, P^k. As with the SIMPLE algorithm, in general, this velocity field will not satisfy the continuity equation. The discretised momentum equation is given as

$$a_P u_P^* = H_P^* - (P_e^k - P_w^k)\Delta y, \tag{3.57}$$

which is known as the predictor step in the PISO algorithm. The next step is to define a velocity field, u^{**}, that satisfies the continuity condition by determining an updated pressure field, P^*.

$$a_P u_P^{**} = H_P^* - (P_e^* - P_w^*)\Delta y \tag{3.58}$$

Note that in equation (3.58), the updated velocity field at the central node is calculated explicitly from its neighbouring nodal values. Subtracting equation (3.57) from (3.58) gives

$$a_P(u_P^{**} - u_P^*) = -(P_e^* - P_e^k - P_w^* + P_w^k)\Delta y \tag{3.59}$$

where the updated pressure is not known. The velocity field satisfies continuity, and so equation (3.50) may be used to obtain an equation for the updated pressure, P^*. If the equation for the updated velocities at control volume faces is written as

$$a_e(u_e^{**} - u_e^*) = -(P_E^* - P_E^k - P_P^* + P_P^k)\Delta y \tag{3.60}$$

then inserting this into equation (3.50), for u^{**}, gives an equation for the updated

pressure, via,

$$\rho\frac{\Delta y^2}{a_w}(P_P^* - P_P^k) + \rho\frac{\Delta y^2}{a_e}(P_P^* - P_P^k) + \rho\frac{\Delta x^2}{a_s}(P_P^* - P_P^k) + \rho\frac{\Delta x^2}{a_n}(P_P^* - P_P^k) =$$
$$\rho\frac{\Delta y^2}{a_e}(P_E^* - P_E^k) + \rho\frac{\Delta y^2}{a_w}(P_W^* - P_W^k) + \rho\frac{\Delta x^2}{a_n}(P_N^* - P_N^k) + \rho\frac{\Delta x^2}{a_s}(P_S^* - P_S^k) +$$
$$\rho(u_w^* - u_e^*)\Delta y + \rho(u_s^* - u_n^*)\Delta x, \tag{3.61}$$

which is identical to relations (3.55) and (3.56) for the SIMPLE algorithm.

Instead of restarting the algorithm from this point, in PISO a second correction step is initiated. The equation for the velocity field, u^{***}, updated via the new pressure field, P^* is given by,

$$a_P u_P^{***} = H_P^{**} - (P_e^{**} - P_w^{**})\Delta y, \tag{3.62}$$

where the velocity field is, once again, solenoidal. To solve this equation, the updated pressure, P^* needs to be calculated. By subtracting equation (3.58) from (3.62) an expression for u^{***} is obtained in terms of the previous and updated pressures.

$$a_P(u_P^{***} - u_P^{**}) = H_P^{**} - H_P^* - (P_e^{**} - P_e^* - P_w^{**} + P_w^*)\Delta y \quad . \tag{3.63}$$

If the velocity at the control volume faces can be expressed as

$$a_e(u_e^{***} - u_e^{**}) = H_e^{**} - H_e^* - (P_E^{**} - P_E^* - P_P^{**} + P_P^*)\Delta y, \tag{3.64}$$

upon substitution into the incompressibility condition (3.50) for u^{***}, the following equation for pressure is obtained,

$$\rho\frac{\Delta y^2}{a_w}(P_P^{**} - P_P^*) + \rho\frac{\Delta y^2}{a_e}(P_P^{**} - P_P^*) + \rho\frac{\Delta x^2}{a_s}(P_P^{**} - P_P^*) + \rho\frac{\Delta x^2}{a_n}(P_P^{**} - P_P^*) =$$
$$\rho\frac{\Delta y^2}{a_e}(P_E^{**} - P_E^*) + \rho\frac{\Delta y^2}{a_w}(P_W^{**} - P_W^*) + \rho\frac{\Delta x^2}{a_n}(P_N^{**} - P_N^*) + \rho\frac{\Delta x^2}{a_s}(P_S^{**} - P_S^*) +$$
$$\rho\frac{\Delta y}{a_w}(H_w^{**} - H_w^*) - \rho\frac{\Delta y}{a_e}(H_e^{**} - H_e^*) + \rho\frac{\Delta x}{a_s}(H_s^{**} - H_s^*) - \rho\frac{\Delta y}{a_n}(H_n^{**} - H_n^*)$$
$$\rho(u_w^* - u_e^*)\Delta y + \rho(u_s^* - u_n^*)\Delta x. \tag{3.65}$$

It is this pressure field that is then used to update the velocity field in equation (3.63), and to complete the correction process.

It has been reported (see Kobayashi and Pereira, 1991) that the PISO scheme greatly

reduces the number of iterations required to obtain a converged solution, and that despite the increased computational cost of a single PISO iteration, the total CPU time was reduced by 15 percent compared to the SIMPLE procedure. Barton (1998) noted that although the SIMPLE scheme used less computational time per iteration, the accuracy of the results obtained with PISO were greater than with SIMPLE for Crank-Nicolson time stepping procedures. Comparisons of the PISO and SIMPLE algorithms for some benchmark laminar flow cases is provided later.

3.5.3 Momentum interpolation

The full solution for the pressure still needs the calculation of the cell face velocities in equations (3.51), (3.60) and (3.64). These equations are required in order to use the discretised form of the continuity equation (3.50), to obtain the pressure field or a correction to it.

The most straightforward method of approximating the control volume face velocities would be to use linear interpolation. From equation (3.50) the u-velocity face difference using linear interpolation is

$$\begin{aligned} u_e - u_w &= \frac{u_E+u_P}{2} - \frac{u_P+u_W}{2} \\ &= \frac{u_E-u_W}{2}, \end{aligned} \tag{3.66}$$

from which, it can be seen that the velocity difference is based upon alternate nodal points. This means that the continuity equation is solved using a grid that has half the nodal density as that for the momentum equation, reducing resolution. Also as the alternate nodes are used, *two* independent grids are present, capable of solving the continuity equation for *two* different velocity fields (and hence pressure correction fields). This gives rise to the well known pressure or velocity chequerboard effect as outlined by Patankar (1980), where two independent solution fields are present on adjacent grid nodes, like the black and white squares on a chess board.

The staggered grid approach

Harlow and Welch (1965) introduced a novel way of dealing with this problem, later adopted by researchers such as Patankar and Spalding (1972). Instead of using just one set of control volumes to discretise the continuous solution over the computational domain, a new set of control volumes was introduced. These control volumes were staggered in such a way that the dependent variable in one set of control volumes lay on the face of another set. To be more specific, the nodal points of the velocity control volumes lie on the faces of the pressure control volumes (as shown in figure 3.8). This has the immediate effect of supplying the face velocities needed to solve the pressure equation, but also the pressure gradient required to solve the momentum equations. The use of a staggered grid provides a strong coupling between the pressure and the velocity.

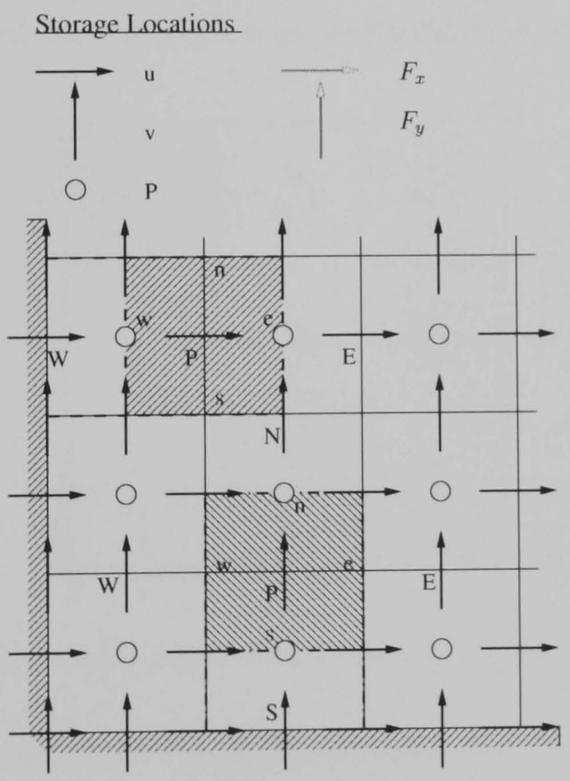

FIGURE 3.8: Staggered control volume arrangement on a structured grid.

There are, however, some disadvantages to using the staggered grid method. The main disadvantage is its geometric complexity, leading to inflexibility. For simple geometries, the staggered grid is trivial to implement. For complex geometries, where unstructured meshes may be implemented to approximate curved regions, the

creation of a staggered grid is much more difficult. Also, the use of more advanced solution techniques, such as the Multigrid method, or Parallelisation of code is more difficult when using a staggered grid arrangement (Lien and Leschziner, 1994).

The collocated grid approach

The alternative to the staggered grid approach is to place all flow variables at the cell centre, known as the *collocated* grid approach as shown in figure 3.9. To calculate the velocity of the fluid, the momentum equations are also calculated at the cell centre as in equations (3.11) and (3.12). However, a method is still required to obtain the velocities at the control volume faces to enable the use of the continuity constraint. The method of solving this problem requires a special interpolation of the velocity component from the cell centre to the face, and is known as *momentum interpolation.* Different forms of momentum interpolation have been proposed in the

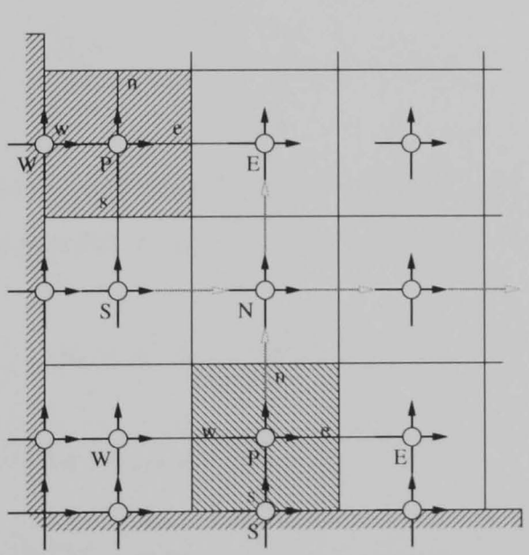

FIGURE 3.9: Collocated control volume arrangement. See figure 3.8 for key to symbols.

literature (see Majumdar, 1988; Papageorgakopoulos *et al.*, 2000), but it is the well-known, and well validated (Lilek and Peric, 1995; Biagioli, 1998; Bradley, Gaskell, Gu, Lawes and Scott, 1998), pressure weighted interpolation method of Rhie and Chow (1983) that is used here. The equation for u-velocity at two adjacent nodal points can be written as,

$$a_P u_P|_P = \sum_{nb} a_{nb} u_{nb}|_P - (P_x)|_P$$

$$a_P u_P|_E = \sum_{nb} a_{nb} u_{nb}|_E - (P_x)|_E \tag{3.67}$$

where nb denotes the neighbouring nodal values to the central node and P_x denotes the gradient of P in the x direction. The equation for the value at the east control volume face is

$$a_e u_e = \sum_{nb} a_{nb} u_{nb}|_e - (P_x)|_e. \tag{3.68}$$

To approximate the first term on the right hand side of (3.68), linear interpolation of the same terms in (3.67) is performed, thus

$$\sum_{nb} a_{nb} u_{nb}|_e = \left[\overline{\sum_{nb} a_{nb} u_{nb}}\right]\Bigg|_e, \tag{3.69}$$

where the overbar denotes linear interpolation. However, this interpolated result can be expressed in terms of the other interpolated terms in (3.67)

$$\left[\overline{\sum_{nb} a_{nb} u_{nb}}\right]\Bigg|_e = \overline{a_e u_e} + \overline{(P_x)|_e}. \tag{3.70}$$

By using (3.70) instead of (3.69) in (3.68), and using $\overline{a_e}$ to approximate the unknown face coefficient a_e, it is possible to obtain Rhie and Chow's interpolation,

$$u_e = \overline{u_e} + \frac{1}{\overline{a_e}}\left[\overline{(P_x)|_e} - (P_x)|_e\right] \tag{3.71}$$

where the pressure gradient terms are given by

$$\begin{aligned} \overline{(P_x)|_e} &= f(P_x)|_E + (1-f)(P_x)|_P \\ (P_x)|_e &= (P_E - P_P)\Delta y, \end{aligned} \tag{3.72}$$

and f is the interpolation factor dependent on the cell face position, varying from zero to unity.

3.5.4 Relaxation

As mentioned previously, under-relaxation can be used in the solution procedure to provide stability to the numerical scheme by limiting the change in the calculated variables from one computational iteration to the next. By rearranging equation (3.11) for u velocity at the central node P,

$$u_P = \frac{1}{a_P}\left(\sum_{nb} a_{nb}u_{nb} - (p_e - p_w)\Delta y\right) \tag{3.73}$$

it is possible to add and subtract the previous value of u_P from the left hand side of (3.73). This gives an equation that shows the present value of velocity in terms of its old value, plus the change, thus

$$u_P = u_P^* + \underbrace{\left[\frac{1}{a_P}\left(\sum_{nb} a_{nb}u_{nb} - (p_e - p_w)\Delta y\right) - u_P^*\right]}_{\text{Change in } u_P \text{ since previous iteration}} \tag{3.74}$$

where u_P^* is the value from the previous iterate. To provide under-relaxation, a fraction of the change may be added to the previous iterate value by the inclusion of an under-relaxation factor, α,

$$u_P = u_P^* + \alpha\left[\frac{1}{a_P}\left(\sum_{nb} a_{nb}u_{nb} - (p_e - p_w)\Delta y\right) - u_P^*\right] \tag{3.75}$$

where values of α vary from zero to one. This has the effect of slowing down convergence, but brings additional stability by limiting the effect of large destabilising oscillations in the solution from one iteration to the next.

Pressure can also be under-relaxed by the use of a similar factor when updating the pressure field. When using either the SIMPLE or PISO algorithms, the pressure correction is added to the pressure, thus updating it. From equations (3.55) and (3.65), a pressure correction can be obtained and added to the pressure,

$$P = P^* + \alpha P' \tag{3.76}$$

where the under-relaxation method is used to limit the change in pressure from one

iteration to the next.

3.6 Boundary Conditions

For any numerical simulation of fluid flow, it is necessary to impose boundary conditions to limit its size. CFD boundary conditions typically consist of wall, inlet, outlet and symmetry conditions.

Wall boundary conditions

Typically, for laminar flow, the no-slip boundary condition is specified for all velocity components, i.e.

$$u_i \to 0 \quad \text{as} \quad n \to 0 \tag{3.77}$$

where n is the normal distance from a stationary wall (Versteeg and Malalasekera, 1996). For turbulent flow this condition still holds for the mean and turbulent velocities, but additional modelling is needed in the vicinity of the wall.

For wall bounded flow, four distinct regions exist (Versteeg and Malalasekera, 1996; Wilcox, 1994). The first region, called the viscous sub-layer, is a very thin layer adjacent to the wall where viscous shear forces dominate the flow, independent of the main flow. The next layer is that of the buffer zone, which rapidly attenuates turbulence from the layers above, to a state where viscous effects dominate. The third layer is the inner region where turbulence is dominant, but the proximity to the wall dictates that the size of the energy containing eddies are of the order of the distance from the wall. The final layer is the outer region, where the size of the turbulent eddies are of the order of the boundary layer thickness.

In the viscous sublayer it is assumed (see Versteeg and Malalasekera, 1996) that the shear forces are equal to the wall shear stress, meaning that the velocity in the direction of the stress is proportional to it, i.e. $U \propto \tau_w$. Non-dimensional parameters

for velocity and wall-normal distance (u^+ and y^+, respectively) may be defined as

$$u^+ = \frac{U}{u_\tau} \quad \text{and} \quad y^+ = \frac{\rho u_\tau y}{\mu}, \tag{3.78}$$

where $u_\tau = (\tau_w/\rho)^{\frac{1}{2}}$ is the friction velocity. In this region ($y^+ < 5$) it is found that $u^+ = y^+$ (i.e. the velocity varies linearly with distance from the wall).

Another commonly used name for the inner layer is the 'log layer' extending from $30 < y^+ < 500$. It's name is derived from the relationship between u^+ and y^+, where the velocity varies logarithmically with the wall distance. Launder and Spalding (1972) express this relationship as

$$u^+ = \frac{1}{\kappa} \ln(E^* y^+), \tag{3.79}$$

where $\kappa = 0.4$ is the Von Karman constant and the value of E^* is given by the physical properties of the wall. Launder and Spalding (1972) give the value of this parameter to be $E^* = 9.0$, but this has been updated to $E^* = 9.8$ for smooth walls Versteeg and Malalasekera (1996).

To resolve the flow accurately in these layers, without modelling, many computational nodes must be inserted. Unfortunately, this greatly increases the computational cost, putting it out of the range of efficient engineering use. The models above, however, show an idealised case of wall bounded shear flow that can be applied to a variety of flows, dependent upon wall flow behaviour. The work of Lien and Leschziner (1994) gives a recent treatment of these near wall models - or wall functions - for use with two equation and second moment turbulent closures and is used here.

To define the wall function, it is common to begin the analysis with the shear force at the wall. This can be written in terms of the wall shear stress as

$$F_s = \tau_w A_S, \tag{3.80}$$

where A_S is the area of the south control volume face adjacent to the wall as shown in figure 3.10. The wall shear stress is given by Versteeg and Malalasekera (1996)

as

$$\tau_w = \frac{\rho C_\mu^{\frac{1}{4}} k_p^{\frac{1}{2}} U_p}{u^+} = \frac{\rho C_\mu^{\frac{1}{4}} k_p^{\frac{1}{2}} \kappa U_p}{\ln\left(E^* \frac{y_P k_P^{1/2}}{\nu}\right)} \tag{3.81}$$

where y_P and k_P are the distance from the wall to the node P and the turbulent kinetic energy at that node, respectively.

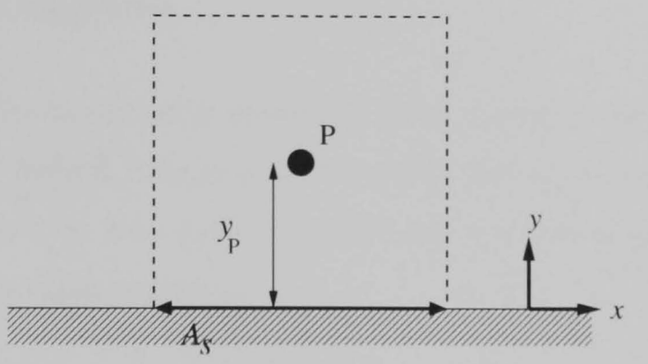

FIGURE 3.10: Control volume adjacent to the wall boundary.

To include the wall function in the momentum equation, the discretisation coefficient at the wall, a_S, is set to zero and the source term of the equation set to include the shear force, giving

$$S_C + S_P U_P = S_C - \frac{\rho C_\mu^{\frac{1}{4}} k_p^{\frac{1}{2}} \kappa U_p}{\ln\left(E^* \frac{y_P k_P^{1/2}}{\nu}\right)} A_S \quad . \tag{3.82}$$

To complete this model, the value of k_p is required. When in the log layer, k is determined by the balance of production and dissipation. The mean production term of k is given by Lien and Leschziner (1994) as

$$P_k = \frac{\ln(y_p/l)}{\rho \kappa y_p k_p^{\frac{1}{2}}} \tau_w^2 \tag{3.83}$$

and the mean turbulent energy dissipation rate as

$$\epsilon = \frac{\rho k_p^{3/2}}{y_p} \left(\frac{2\nu}{l k_p^{1/2}} + \frac{\ln(y_p/l)}{C_l} \right) \tag{3.84}$$

where l is the mixing length and $C_l = 2.55$ is an empirical closure coefficient. To define the Reynolds stresses at the near wall node, it is possible to use the solution

of the k equation instead of defining wall functions for each stress individually as shown by Lien and Leschziner (1994). The approximations used for the stresses are,

$$\overline{u^2} = 1.098k_p, \quad \overline{v^2} = 0.247k_p, \quad \overline{uv} = -0.255k_p \quad . \tag{3.85}$$

Outlet boundary condition

The outlet boundary condition is prescribed using a zero gradient assumption. If the computational domain is large enough that the flow at the outlet is considered to be fully developed, the velocity at the outlet may be taken to be that at the node adjacent to the boundary, implying

$$\frac{\mathrm{d}U}{\mathrm{d}x} = 0, \tag{3.86}$$

for horizontal flow through a vertical outlet boundary. This condition can be extended to any general scalar variable, ϕ.

Symmetry boundary condition

The symmetry condition is very similar to that of the outlet boundary condition. If a boundary is such that it acts as a line of symmetry for the flow then there must be zero gradient of any flow variable across it. For a boundary in the vertical plane

$$\frac{\mathrm{d}U}{\mathrm{d}y} = 0, \tag{3.87}$$

while for an axis of symmetry in axisymmetric flow,

$$\frac{\mathrm{d}U}{\mathrm{d}r} = 0, \tag{3.88}$$

where the axis of symmetry is in the z direction.

3.7 2D Test Cases

Two laminar flow test cases are now investigated, namely the backward facing step and the classical lid driven square cavity. Both provide stern challenges for numerical convection schemes, with high streamline curvature oblique to the computational grid. They also provide a simple introduction to the type of geometries studied later, and a feel for how well the underpinning numerical methods perform.

3.7.1 Lid driven cavity flow

This test case is based on the one studied by Ghia *et al.* (1982), whose results are widely quoted in the literature as a bench-mark solution (see Seok *et al.*, 1995; Deng *et al.*, 1994; Biagioli, 1998). The computational domain is shown in figure 3.11, with the Reynolds number of the flow given by

$$Re = \frac{\rho U_{\text{lid}} L}{\mu} \quad . \tag{3.89}$$

To obtain the Reynolds numbers for comparison with the work of Ghia *et al.* , U_{lid}, L and μ were all set to unity so that density, ρ, corresponded to the required value. Non-slip boundary conditions at the cavity walls were also implemented.

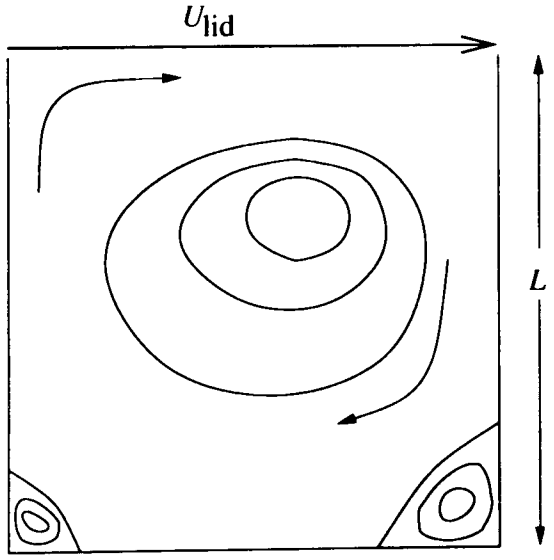

FIGURE 3.11: Flow schematic for the 2-D lid driven cavity case.

Uniform grids of size 16×16, 32×32, 64×64 and 128×128 were used in the

computations, with $Re = 100, 400$. Four convection schemes, Upwind, QUICK, CUBISTA and SMART, were tested as well as the SIMPLE and PISO solution algorithms. Results for the $Re = 100$ case are shown in figures 3.12 to 3.15 together with the benchmark solution of Ghia *et al.* computed using a 129×129 grid.

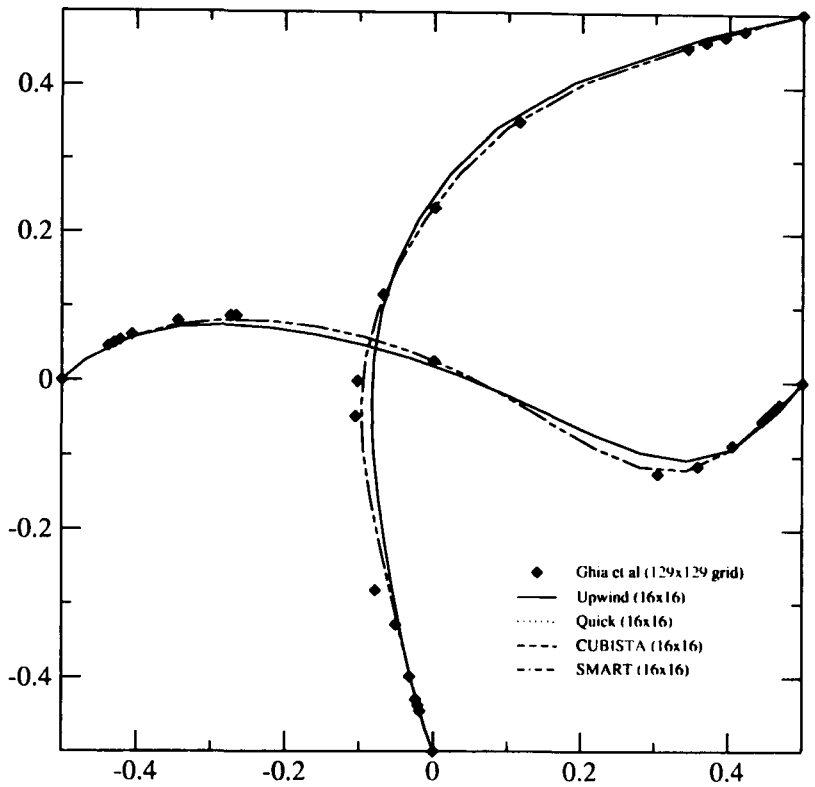

FIGURE 3.12: Results for different discretisation schemes on a 16 × 16 grid; $Re = 100$.

From these figures it can be seen that at this Reynolds number the higher order schemes - QUICK, CUBISTA and SMART - all behave in an identical manner as shown by all the lines converging onto the non- upwind line (solid). The reason for this is that the flow conditions are such that only the smooth region of the NVD is being used for the bounded schemes. In other words, QUICK produces bounded results. This is due to the speed of the flow being relatively slow with no steep gradients in the flow variables.

It can also be seen that, as expected, the higher order schemes provide greater accuracy on the coarser meshes than the upwind scheme. Upwind is only able to approximate the benchmark solution when the grid is of size 128 × 128. Referring to figure 3.16, it can be seen that the higher order schemes - in this case the SMART scheme on the 32 × 32 grid - results in a solution comparable to the benchmark.

Results for the $Re = 400$ case are shown in figures 3.17 to 3.20. Increasing the

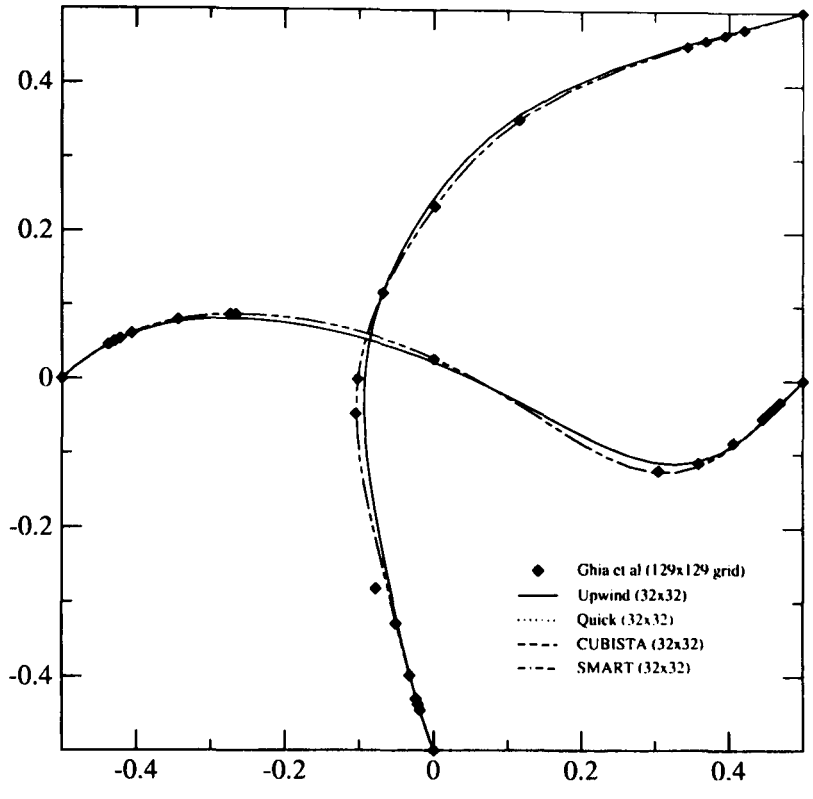

FIGURE 3.13: Results for different discretisation schemes on a 32×32 grid; $Re = 100$.

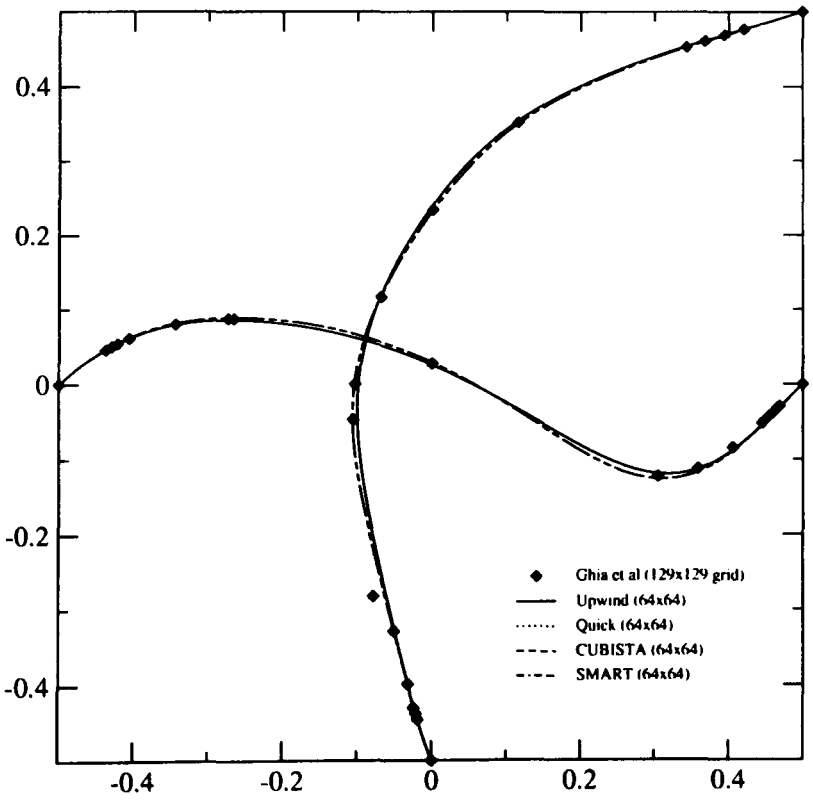

FIGURE 3.14: Results for different discretisation schemes on a 64×64 grid; $Re = 100$.

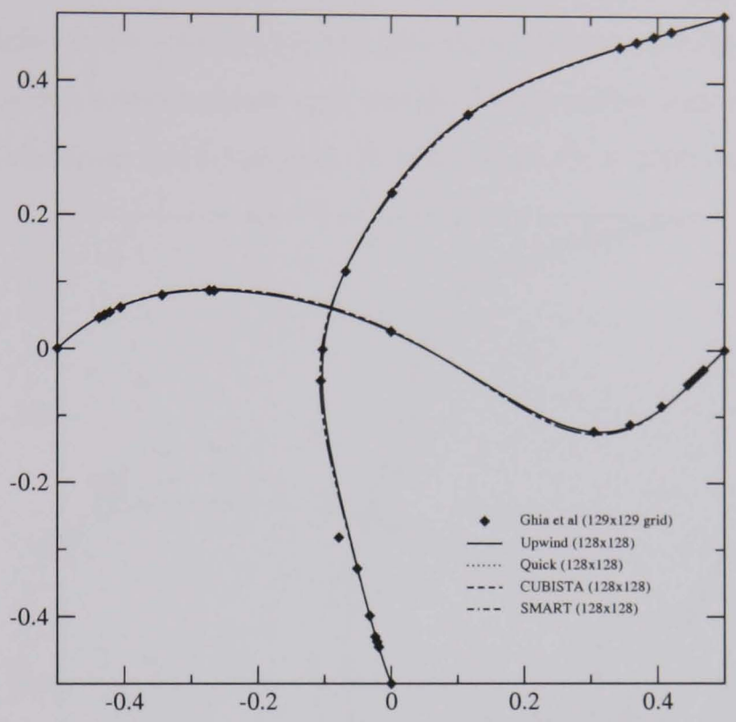

FIGURE 3.15: Results for different discretisation schemes on a 128×128 grid; $Re = 100$.

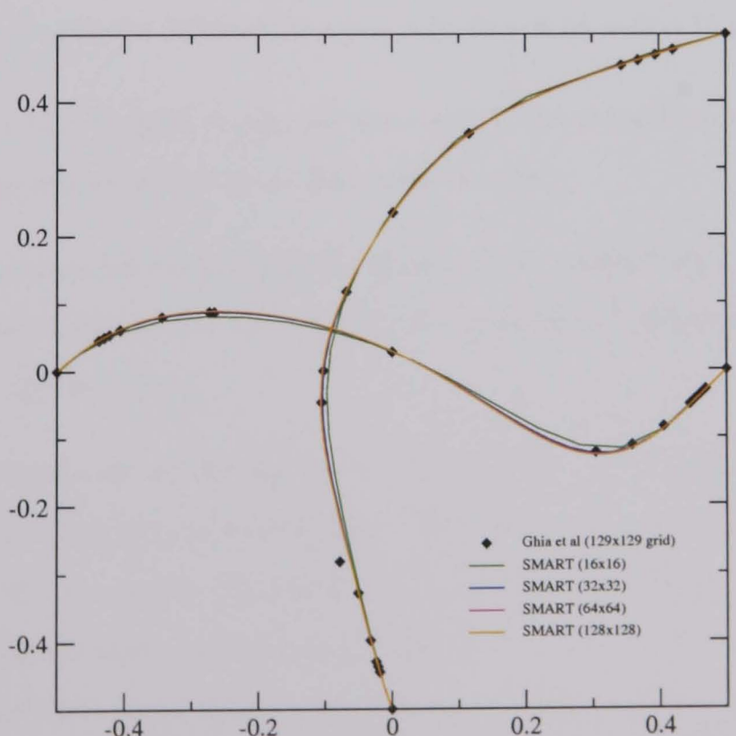

FIGURE 3.16: Grid independence tests for the SMART scheme at $Re = 100$.

Reynolds number degrades the performance of the upwind and higher order schemes on grids with a low mesh density; the effect being more pronounced for the upwind scheme. The higher order schemes predict grid independent results on a 64×64 grid, whereas the upwind scheme shows appreciable disagreement with the benchmark results even on the finest 128×128 grid. Results of the $Re = 1000$ case are shown in

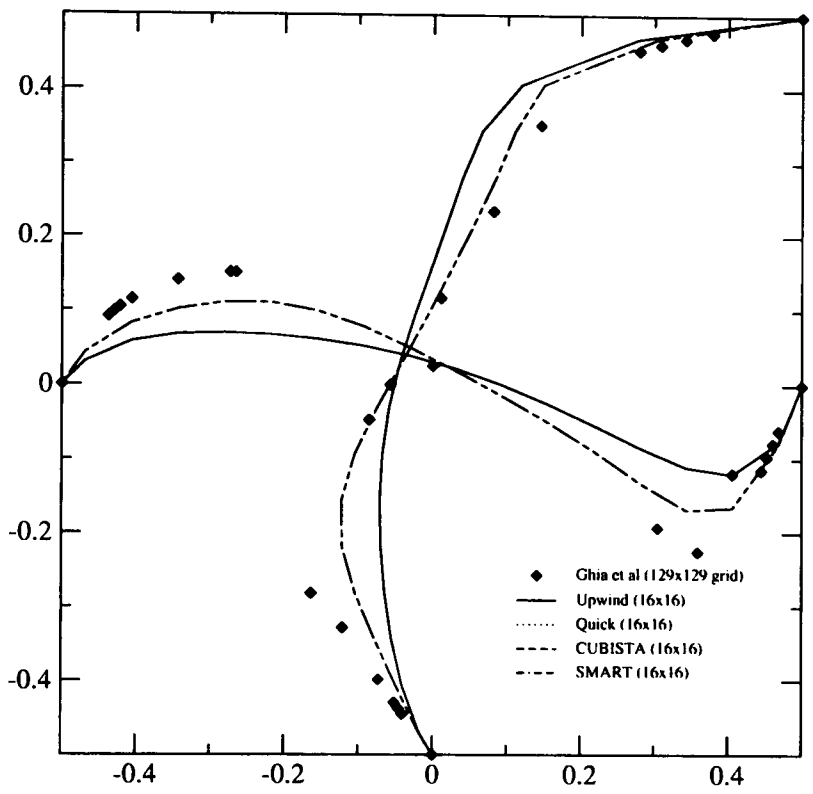

FIGURE 3.17: Results for different discretisation schemes on a 16×16 grid; $Re = 400$.

figure 3.21 for a 64×64 grid. Again the same trends mentioned above are apparent, with grid independence achieved at this mesh density.

Note that the reason for the poor performance of the upwind scheme is due to the numerical diffusion inherent in the scheme, and as predicted by equation (3.21), this reduces as the grid is refined.

The computational cost of the various schemes can be measured in terms of the CPU time required to achieve convergence. For this work the times were obtained using the Intel C++ compiler (for IA-32, version 8.1) on an AMD64 3200 processor. CPU times obtained with the PISO algorithm for the flow at $Re = 100$ are given in table 3.1. These CPU times increase from left to right due to the increased number of operations per iteration of the higher order schemes - although CUBISTA and SMART are identical. They also increase down the table due to the increased

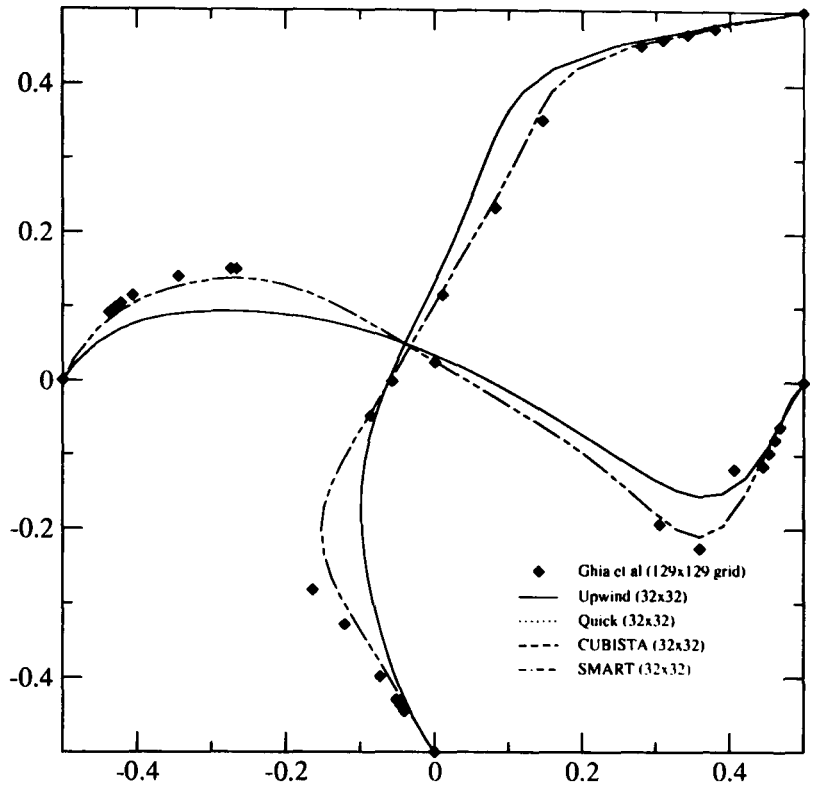

FIGURE 3.18: Results for different discretisation schemes on a 32×32 grid; $Re = 400$.

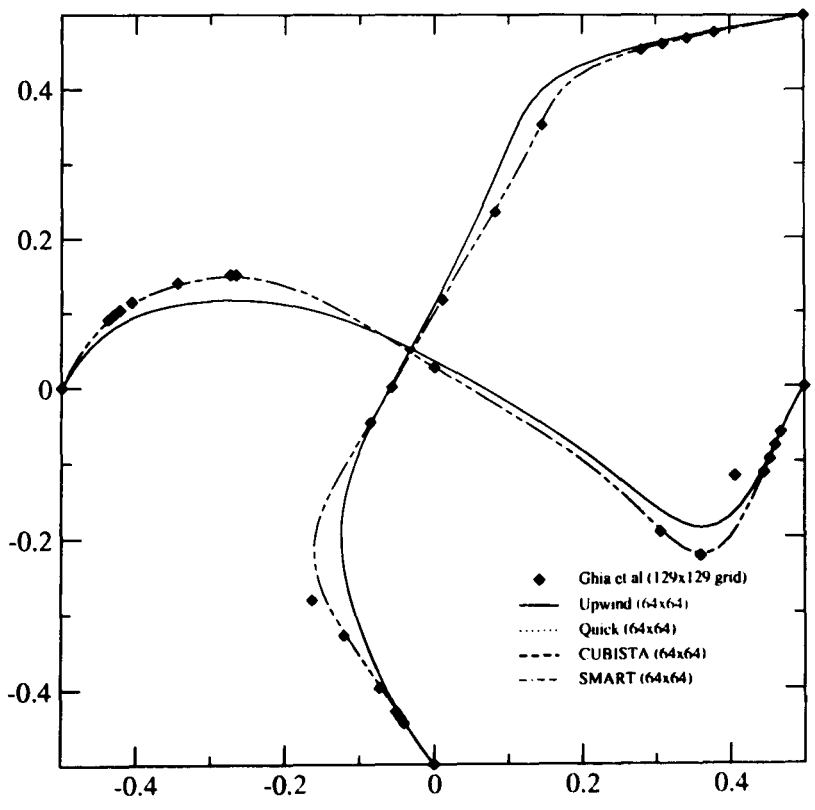

FIGURE 3.19: Results for different discretisation schemes on a 64×64 grid; $Re = 400$.

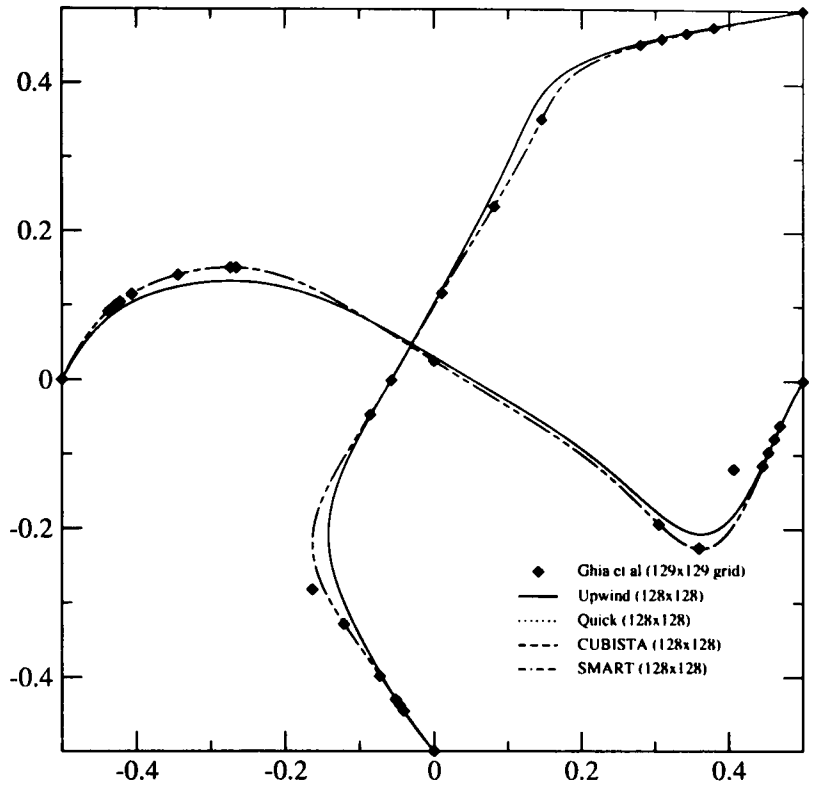

FIGURE 3.20: Results for different discretisation schemes on a 128×128 grid; $Re = 400$.

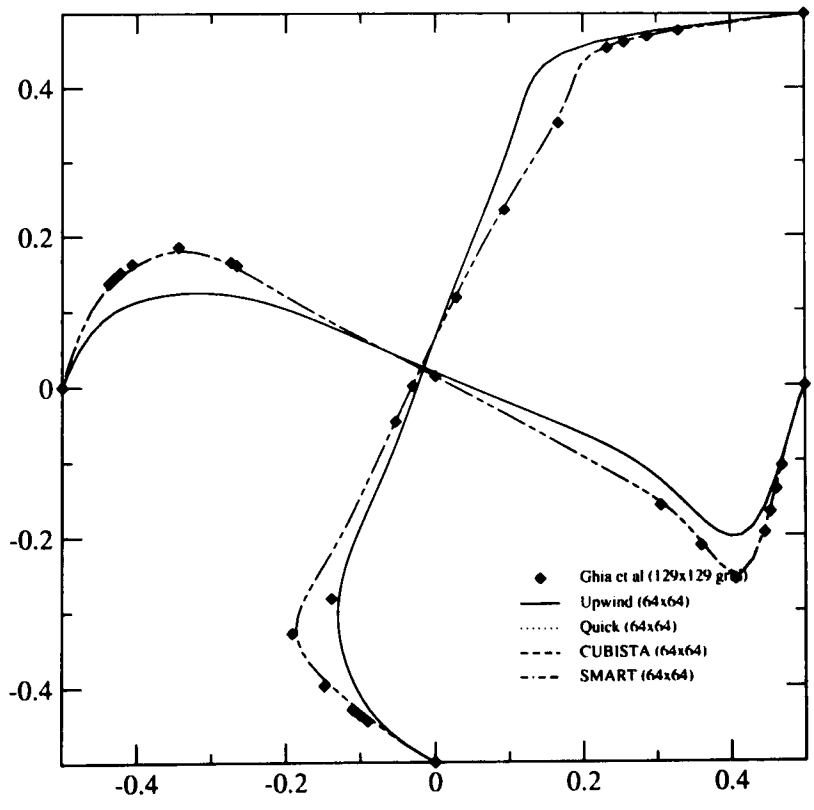

FIGURE 3.21: Results for different discretisation schemes on a 64×64 grid; $Re = 1000$.

Grid	Upwind	QUICK	SMART	CUBISTA
16×16	0.130	0.200	0.200	0.200
32×32	1.650	2.270	2.550	2.560
64×64	27.940	39.010	42.780	43.400
128×128	611.320	839.380	965.110	984.190

TABLE 3.1: CPU times (in seconds) for the lid driven cavity problem using PISO @ $Re = 100$.

Grid	PISO	SIMPLE
16×16	0.200 (181)	0.190 (213)
32×32	2.550 (642)	2.130 (675)
64×64	42.780 (2436)	34.900 (2455)
128×128	965.110 (9528)	756.460 (9525)

TABLE 3.2: CPU times and iteration numbers for SIMPLE and PISO @ $Re = 100$.

number of nodes in the computational domain, increasing the size of the matrix to invert and hence the number of operations required during the inversion.

As mentioned earlier, even though the high order schemes require more CPU time per iteration, the solution achieves grid independence much earlier than the upwind scheme. To illustrate this, the time for the CUBISTA scheme on the 32×32 grid is found to take less than 1/200th of the time of the less accurate upwind solution on a 128×128 grid.

Comparison of CPU times between the SIMPLE and PISO algorithms for the SMART scheme are shown in table 3.2. Even though the PISO scheme is seen to reduce the number of iterations in the computations, the CPU times are, in fact, greater than those of the SIMPLE scheme. This is due to additional time assembling the intermediate pressure-correction equations leading to an increase in time per iterate. The cause of the discrepancy between the results presented here and those in the literature (Kobayashi and Pereira, 1991) are due to the use of the steady state version of PISO. Although very effective for time-dependent problems, the steady state version of PISO is tantamount to SIMPLE with additional pressure-correction steps.

The CPU times for the higher Reynolds number case ($Re = 400$) are represented in table 3.3. Compared to the times for $Re = 100$, the two finest grids take less time to converge. The CPU time savings for the higher order scheme are smaller at this

Grid	Upwind	QUICK	SMART	CUBISTA
16 × 16	0.160	0.300	0.330	0.330
32 × 32	1.570	2.890	3.240	3.260
64 × 64	23.720	34.420	38.430	38.730
128 × 128	464.020	637.460	714.660	709.730

TABLE 3.3: CPU times (in seconds) for the lid driven cavity problem using PISO @ Re = 400.

Grid	PISO	SIMPLE
16 × 16	0.330 (301)	0.340 (322)
32 × 32	3.240 (821)	2.670 (838)
64 × 64	38.430 (2189)	31.640 (2255)
128 × 128	714.660 (7361)	617.000 (8052)

TABLE 3.4: CPU times and iteration numbers for SIMPLE and PISO @ $Re = 400$.

Reynolds number; the CUBISTA scheme on a 64×64 grid takes less than 21/250ths of the time that the upwind scheme takes on the 128×128 grid. The computational saving at this higher Reynolds number decreases and is approximately 1/20th of the saving at the lower Reynolds number.

The CPU times of the SIMPLE and PISO algorithms for the SMART scheme at $Re = 400$ are shown in table 3.4. Again the SIMPLE algorithm is the more CPU time efficient, despite the reduced number of iterations for the PISO algorithm.

3.7.2 2D Backward facing step

The case presented in this section is that studied by Armaly *et al.* (1983) and is also a benchmark problem for testing CFD schemes. Flow features present in the backward facing step - such as separation, reattachment and recirculation - are in common with the more complex situations to be studied later in this thesis. The flow schematic is shown in figure 3.22 where the Reynolds number of the flow is given by

$$Re = \frac{VH\rho}{\mu} \tag{3.90}$$

where V is two thirds of the maximum inlet velocity, U_{max}. In the computations

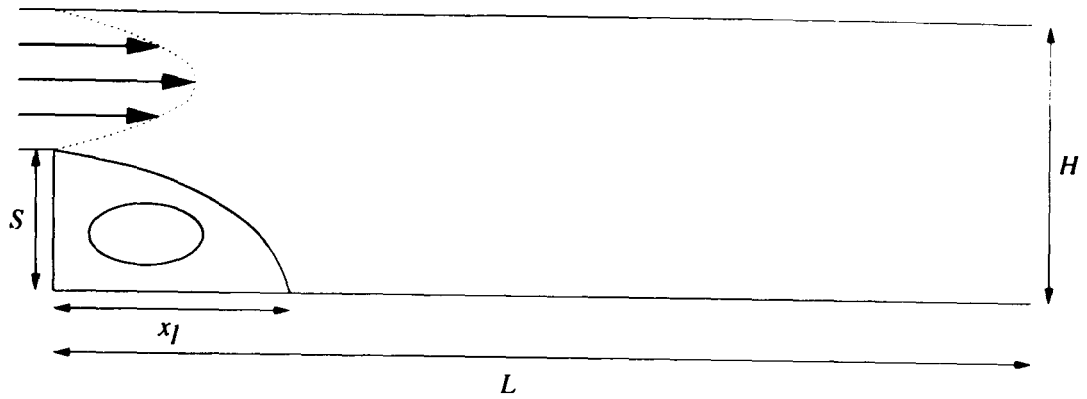

FIGURE 3.22: Flow schematic of the backward facing step flow of Armaly *et al.* (1983).

performed in this work the following values were used,

$$H = 1 \quad ; \quad \mu = 1$$
$$S = 0.5 \quad ; \quad \rho = 1 \quad . \tag{3.91}$$

At the inlet, a parabolic profile was adopted across the opening from the step to the upper wall. This profile is given by the formula

$$u(h) = u_0 h(S - h) \tag{3.92}$$

where

$$u_0 = \frac{4U_{max}}{S^2} \tag{3.93}$$

and the vertical coordinate, h, defines the distance from the corner of the step to the upper wall. At the channel exit, zero gradient boundary conditions were imposed for all flow variables, with non-slip conditions at all other surfaces.

Several different flow speeds were studied for this case from $Re = 100$ to $Re = 1000$. To minimise computational time, different domain lengths, L, were adopted so that a fully developed flow was achieved without using unnecessary grid points. For Reynolds numbers less than 200, $L = 30$ units with a computational mesh of 450×15 nodes. For Reynolds numbers up to 600, $L = 45$ units with a mesh size of 800×35. For $Re = 1000$, a mesh size of 2240×35 with $L = 126$ units was used. All of these grids were seen to achieve mesh independent results.

The results for the $Re = 100$ flow can be seen in figure 3.23. The upwind scheme

clearly shows an inability to capture the experimental data accurately due to the high numerical diffusion. The high order schemes, as in the previous test case, all predict the same profiles. Once again this is due to the fact the flow is in the smooth region of the NVD diagram, where QUICK is suitable for obtaining bounded results (the other schemes reduce to QUICK in this region). Even for the higher order schemes, the simulations do not match the experimental data exactly. This, as mentioned by Armaly *et al.* , is due to the simulation having a parabolic inlet profile imposed at the edge of the computational domain, instead of including an inlet pipe where the flow can develop fully before reaching the expansion. The results for

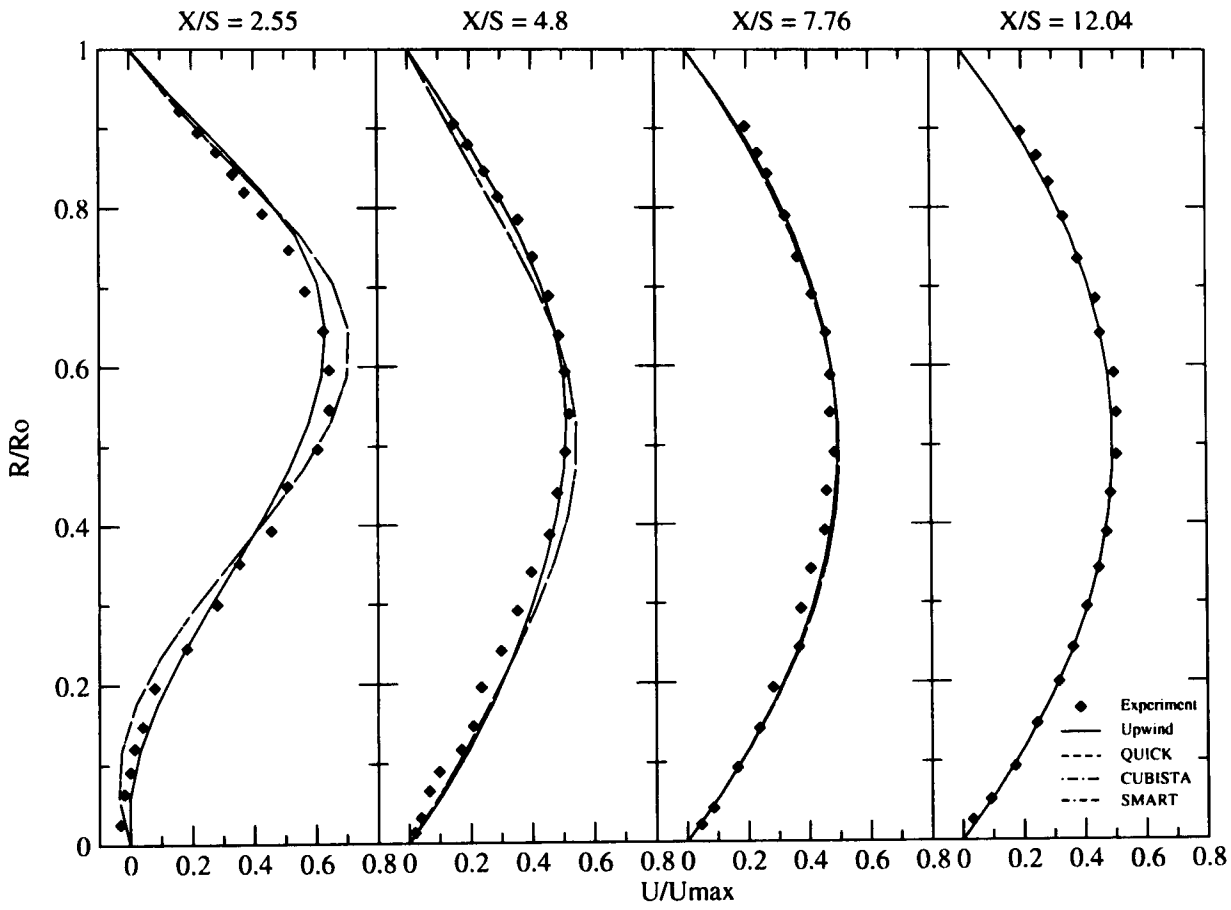

FIGURE 3.23: u-velocity profiles for the case of Armaly *et al.* (1983): $Re = 100$.

$Re = 389$ are shown in figure 3.24. As for the lid driven cavity problem, the high order convection schemes show a greater improvement at higher Reynolds numbers for the same size mesh over the upwind scheme.

The results for $Re = 1000$, are shown in figure 3.25. Here all of the convective discretisation schemes predict erroneous values. Luckily, this feature is not a problem with the numerical scheme, but a property of the experimental flow. Above this Reynolds number, Armaly *et al.* shows that the flow exhibits three dimensional ef-

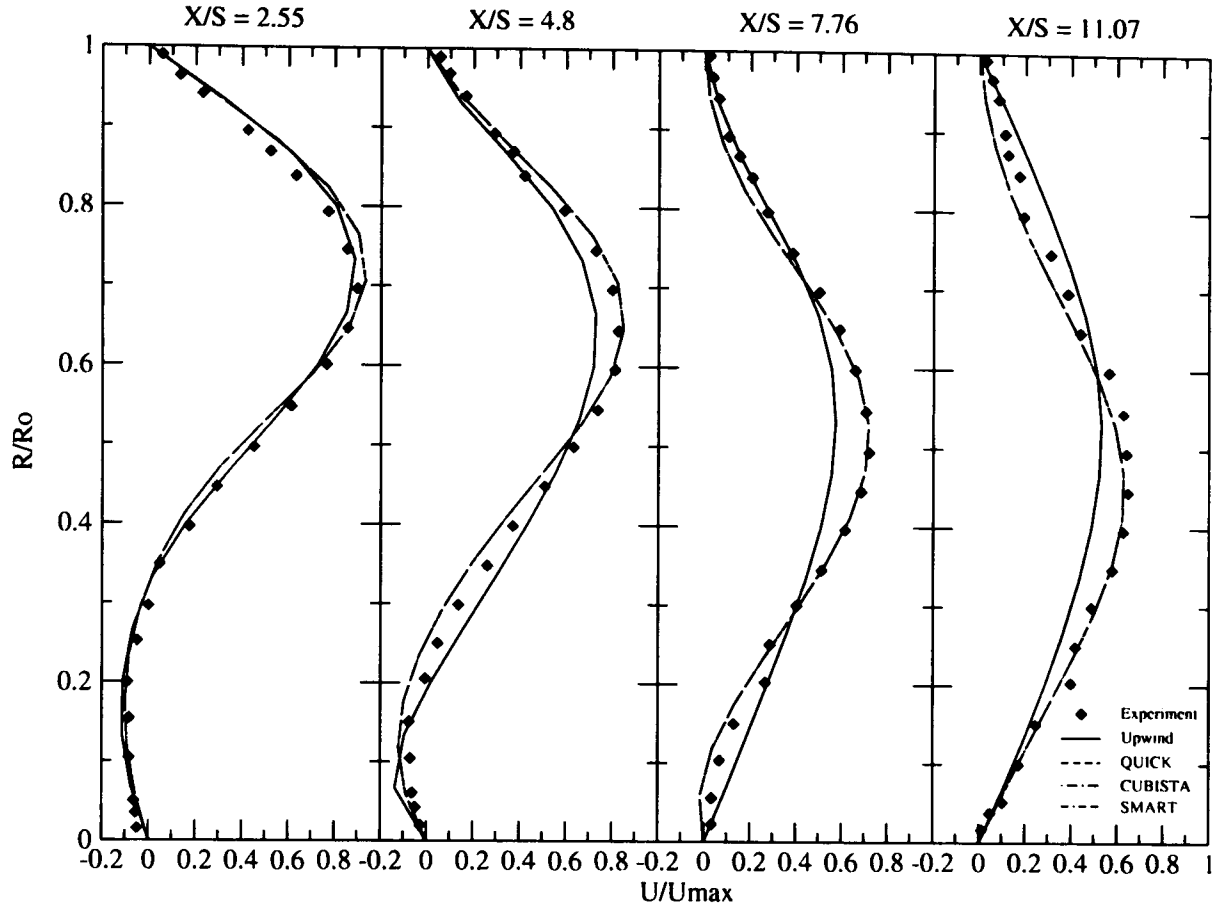

FIGURE 3.24: u-velocity profiles for the case of Armaly *et al.* (1983): $Re = 389$.

fects and is no longer a pure two dimensional flow. As the computations are strictly two dimensional, they are inherently unable to capture any three dimensionality, and hence discrepancies between measured and computed results exist.

As mentioned previously, this case is a good test of the numerical algorithm's ability to predict separation, reattachment and recirculation accurately. Figure 3.26 shows both the measured and computed reattachment length of the primary recirculation bubble (x_1 as shown in figure 3.22). For Reynolds numbers between 100 and 400, the numerical results agree well with the measured data, showing that for this laminar flow, the numerical schemes capture the flow features well. However, for Reynolds numbers above 400, it can be seen that the numerical predictions begin to differ from the experimental measurements. This is again due to the three dimensionality of the flow above $Re = 400$.

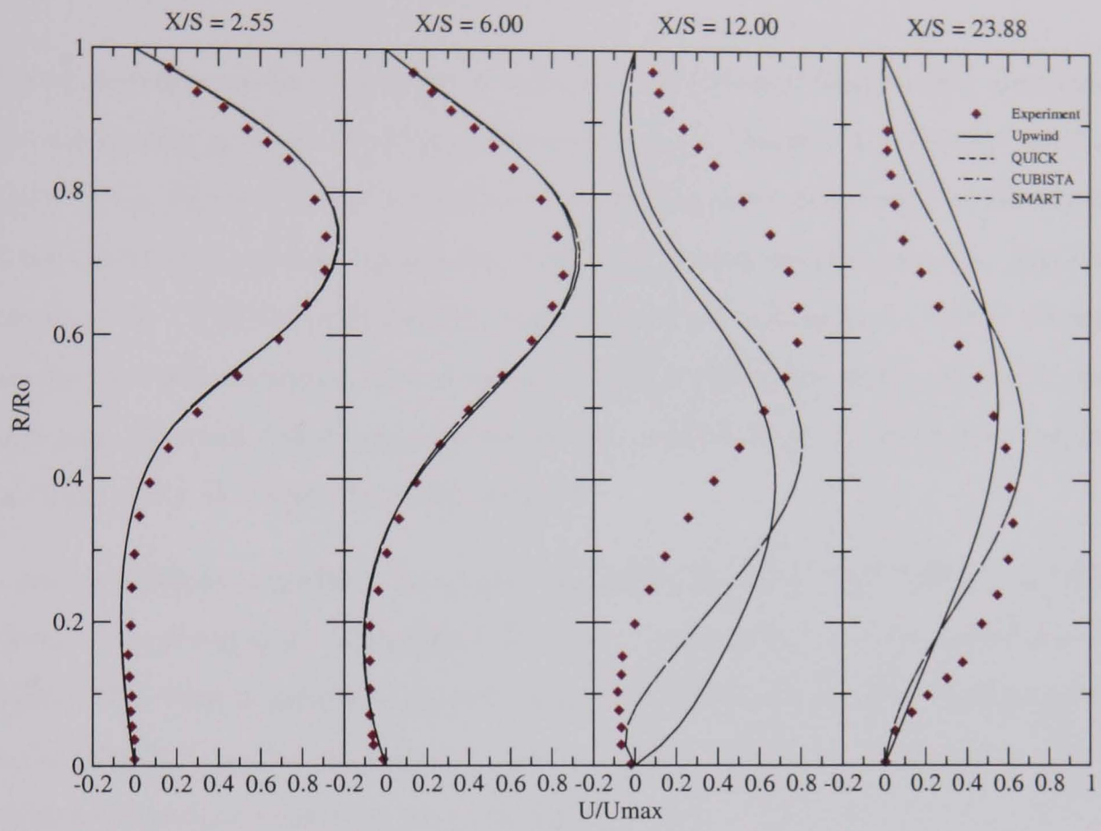

FIGURE 3.25: u-velocity profiles for the case of Armaly *et al.* (1983): $Re = 1000$.

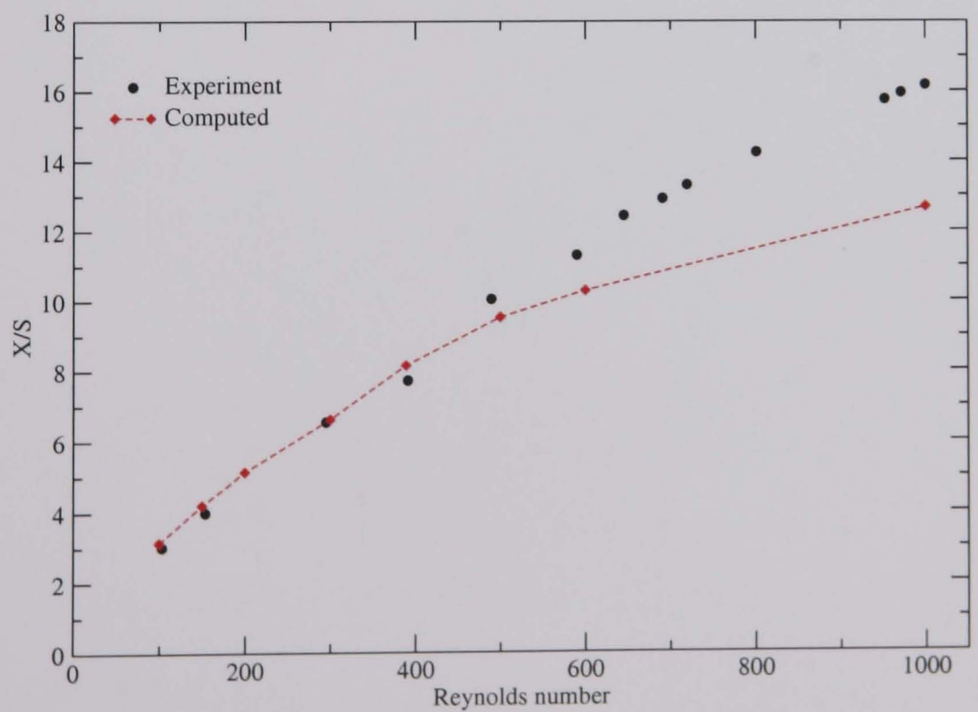

FIGURE 3.26: Reattachment lengths for the backward facing step flow at different Reynolds numbers.

3.8 Summary

This chapter has presented a suitable method for solution of laminar flow problems, that can also be applied to turbulent flows as shown in Chapter 4. The improved accuracy of the higher order discretisation schemes has been demonstrated for the lid driven cavity and backward facing step problems against benchmark data. The usefulness of the CUBISTA and SMART schemes over the unbounded QUICK scheme, although not demonstrated here, is in the convective discretisation of turbulent variables such as k and ϵ that are positive definite, as well as where steep flow variable gradients occur at higher Reynolds numbers.

A robust solution algorithm has been implemented using the SIMPLE or PISO pressure-based methods. Although PISO gives convergence in fewer iterations, the overall CPU time is greater than that of the SIMPLE scheme. This advocates the use of SIMPLE in the calculations in the following chapters, where large sets of coupled differential equations are to be solved.

Chapter 4

Isothermal Swirling Flows

Contents

4.1 Introduction

Isothermal swirling flow is often studied as a prerequisite for the study of turbulent reacting swirling flow. In the isothermal case, the effect of temperature on the fluctuating density is removed, thus enabling verification of the purely aerodynamic models used to describe the turbulence.

Flow features that are studied contain free vortex motion, forced vortex motion and the transition between the two. The first is usually present in confined flows with high swirl which retards the transition to forced vortex motion (or solid body rotation). This has been studied experimentally by Kitoh (1991) and Xia *et al.* (1997) for flow in a long cylindrical pipe and a model combustor, respectively. Free vortex motion is also present in unconfined flows, such as the swirling jet studied by Younis *et al.* (1996).

Forced vortex motion in confined flows appears when the swirl decays along the pipe so a transition occurs from the free vortex. Researchers such as Al-Masseeh (1991) and So *et al.* (1984) have experimentally studied these flows.

The difficulties presented to numerical analysts, is that most turbulent models are designed to predict, and hence calibrated using, flows such as homogeneous shear. These simpler flows do not incorporate the additional features that swirl brings, particularly the mean strains due to the radial gradient of the swirl, or tangential, velocity, $\partial W/\partial r$, and the additional radial gradient of axial velocity, $\partial U/\partial r$.

This chapter presents the results of simulation for two swirling flow test cases, the free vortex flow of Kitoh (1991) and the lower swirl case of Al-Masseeh (1991). The two equation $k-\epsilon$ and $k-\omega$ turbulence models (section 2.4.2) are used, as are the more complex SSG and LRR Reynolds stress closures (section 2.5.1). The addition of the anisotropic dissipation rate model to the SSG pressure-strain model (SSG-ADRM - section 2.5.2) is also assessed.

4.2 Swirling flow in a cylinder - Kitoh's swirling flow

The swirling flow case studied by Kitoh (1991) was chosen as a test case for the models and numerical methods outlined in previous chapters, due to its comparative simplicity. The geometry is that of a cylindrical pipe where swirling air is introduced at the open end via a mechanical swirl generator and is visualised as shown in figure 4.1 below. The flow is less complex than that of normal combustor geometries,

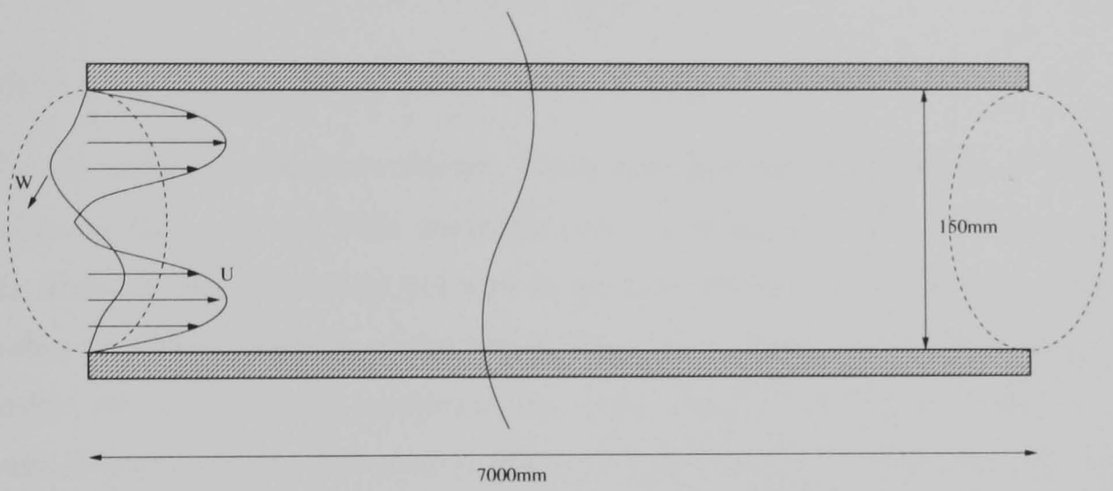

FIGURE 4.1: Flow schematic for the Kitoh case.

such as those with annular inlets, with smaller streamline curvature in the $u - v$ velocity plane, less recirculating regions, and a less complex strain field due to the small values of v velocity present. The strong swirl imposed at the inlet provides fluid motion predominantly of the free vortex type along the length of the pipe, leading to areas of high velocity gradients near the pipe walls and boundaries of the vortex. These factors provide a relatively simple test case for the turbulence models mentioned previously.

The section of pipe simulated begins from the first test section (TS1) from which measurements were obtained, to the ninth (TS9) (Kitoh, 1991). The laboratory locations of the test stations used here are: TS1=855mm, TS3=1845mm, TS5=2850mm, TS7=3855mm and TS9=4860mm. The inlet conditions for the simulation were obtained from the experimental measurements at the axial distance of 855mm. The swirl at the inlet of the pipe was generated by a series of guiding vanes mounted on a rotating disc. The swirl intensity produced by the equipment is provided by the

expression,

$$\Omega = \frac{2\pi \int_0^{r_0} UWr^2 \mathrm{d}r}{\pi r_0^3 U_m^2}, \tag{4.1}$$

where U and W are the mean axial and tangential velocities, r the radial distance and U_m the bulk velocity, giving a swirl intensity of 0.97 at the simulation inlet. For this flow $Re = 50000$ and is obtained using the bulk velocity, $U_m = 5.23\mathrm{ms}^{-1}$ and the pipe diameter, $d = 150\mathrm{mm}$

$$Re = \frac{\rho U_m d}{\mu} \tag{4.2}$$

where $\mu = 1.85 \times 10^{-5}\mathrm{Ns/m}^2$ for air and $\rho = 1.18\mathrm{kg/m}^3$ for air.

For the experimental measurements, Kitoh used hot wire anemometry to obtain values for the mean and RMS fluctuating velocity components. He comments that the nonlinear response of the hot wire to the fluid velocity can cause error in measurement. When moments of the fluctuating velocity components higher than the second are ignored in the measurements, errors may be incurred when the turbulence intensity exceeds 20%. Also as the wires have a finite size, Kitoh mentions that in regions of high variable gradients, the accuracy of experimental measurements may be compromised. After these considerations, Kitoh stated that the measured Reynolds stress results were reliable to within $\pm 0.001 U_m^2$ except in regions of high turbulence intensity (greater than 10%) and high velocity gradients. These regions occur mainly in the central vortex core at $0 < r \lesssim 0.0225\mathrm{mm}$ (the reader is referred to Kitoh, 1991).

4.2.1 Numerical Procedure

After grid independence tests, the calculation domain was created using an irregularly spaced grid consisting of 250x100 nodes. The mesh was refined in the inlet regions and close to the wall as shown in figure 4.2. The total length of the calculation domain is 6145mm (7000-855)mm, as the simulation starts from the first measurement position, not the laboratory pipe inlet, with a width of 75mm. The width corresponds to the radius of the pipe, as the simulation is assumed to be axisymmetric in nature with the symmetry line at the lower edge of the computational grid.

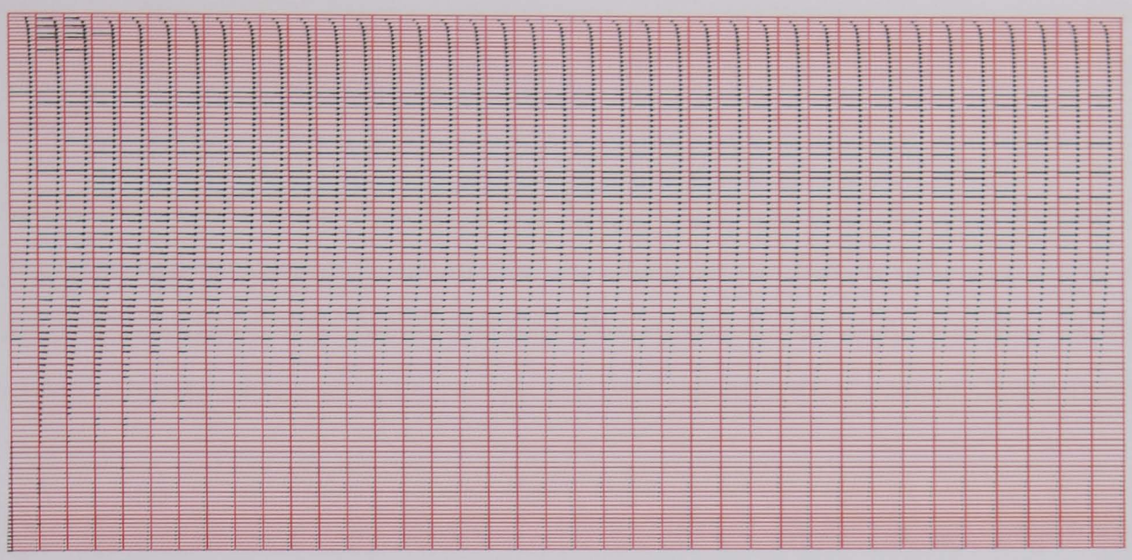

FIGURE 4.2: Velocity vectors computed using the SSG model for Kitoh's case.

Boundary Conditions

The inlet boundary conditions were obtained directly from the experimental data of Kitoh (1991) at the first test section (855mm in the laboratory) with a swirl intensity equal to 0.97. From the experiments, values of U, V, W, $\overline{u^2}$, $\overline{v^2}$, $\overline{w^2}$, $\overline{uv}$, $\overline{uw}$ and $\overline{vw}$ were imposed there by linearly interpolating the measured data points onto the computational grid points as shown in figure 4.3 for the axial inlet velocity. For the

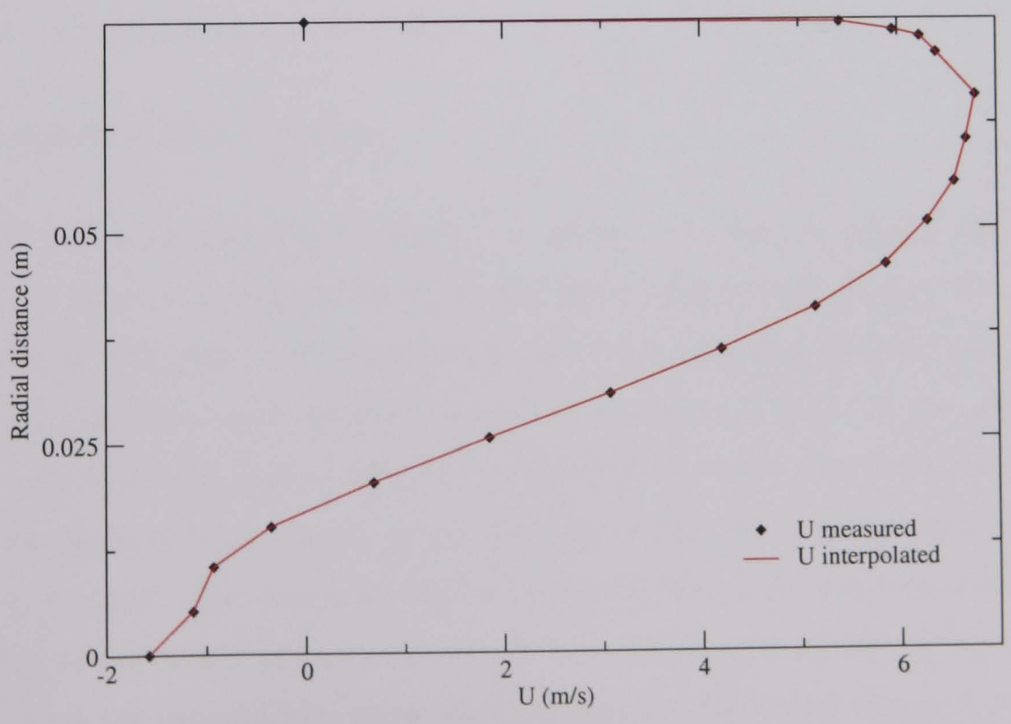

FIGURE 4.3: Interpolation of measured u-velocity at the pipe inlet.

upper boundary of the domain a no slip boundary condition was implemented, with the addition of the logarithmic wall functions to account for variables close to the wall.

At the exit of the domain on the right hand side, a zero axial gradient boundary condition was implemented for all flow variables, as the flow is fully developed at this axial distance. The same condition also applies to the symmetry line on the lower boundary of the domain, except that here zero gradient applies in the radial direction.

The inlet condition for the dissipation rate of turbulent kinetic energy, ϵ, was found using the method of Hogg and Leschziner (1989), where, using dimensional analysis,

$$\epsilon = C_{\mu\epsilon}\frac{k^{3/2}}{l} \tag{4.3}$$

with l being the integral length scale of the turbulence at the inlet and $C_{\mu\epsilon} = 0.09$ as in the $k-\epsilon$ model. Following numerical experiments, where l was adjusted to find a value of ϵ that gave good agreement with experimental turbulent data, it was found that its value giving the most adequate predictions was $\frac{1}{128}d$.

4.2.2 Computational Results

Two-equation model results

Firstly the two equation $k-\epsilon$ and $k-\omega$ models were used to predict the mean flow and value of k. Figure 4.4 shows the mean axial velocity profiles from TS3 through to TS9. Both models are seen to predict an erroneous positive velocity at the axis, which shows an inability to predict the effects of swirl. At the wall, the axial velocity is also under-predicted. As the flow develops downstream, the axial velocity profile becomes flatter where its value at the axis becomes greater than that at the wall. The reason for the erroneous prediction for axial velocity is the inability of the models to capture swirl and hence the tangential velocity (see figure 4.5). Note the experimental and computed values of the radial velocity (denoted by open diamonds and dotted line, respectively) are shown alongside those for axial

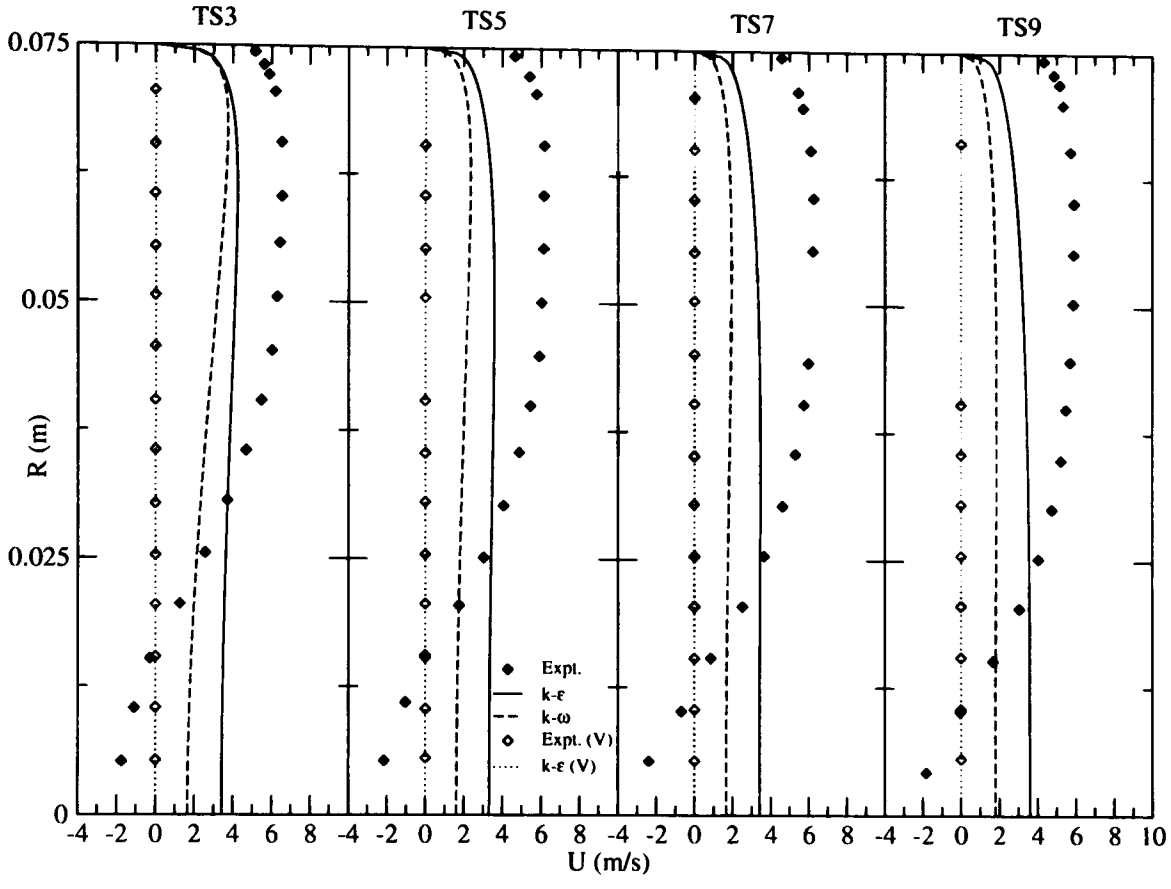

FIGURE 4.4: Two equation model results for axial velocity - also showing radial velocity; Kitoh's case.

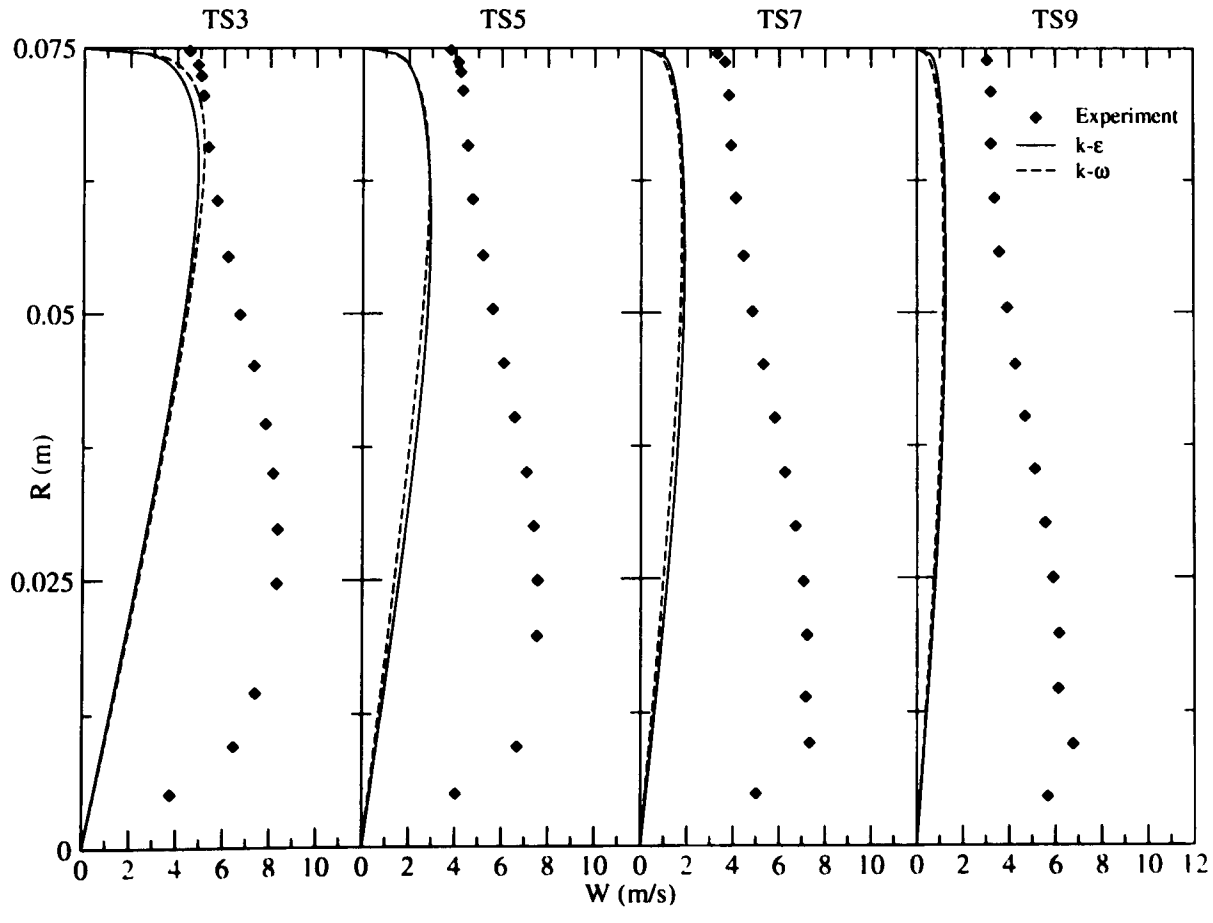

FIGURE 4.5: Two equation model results for tangential velocity; Kitoh's case.

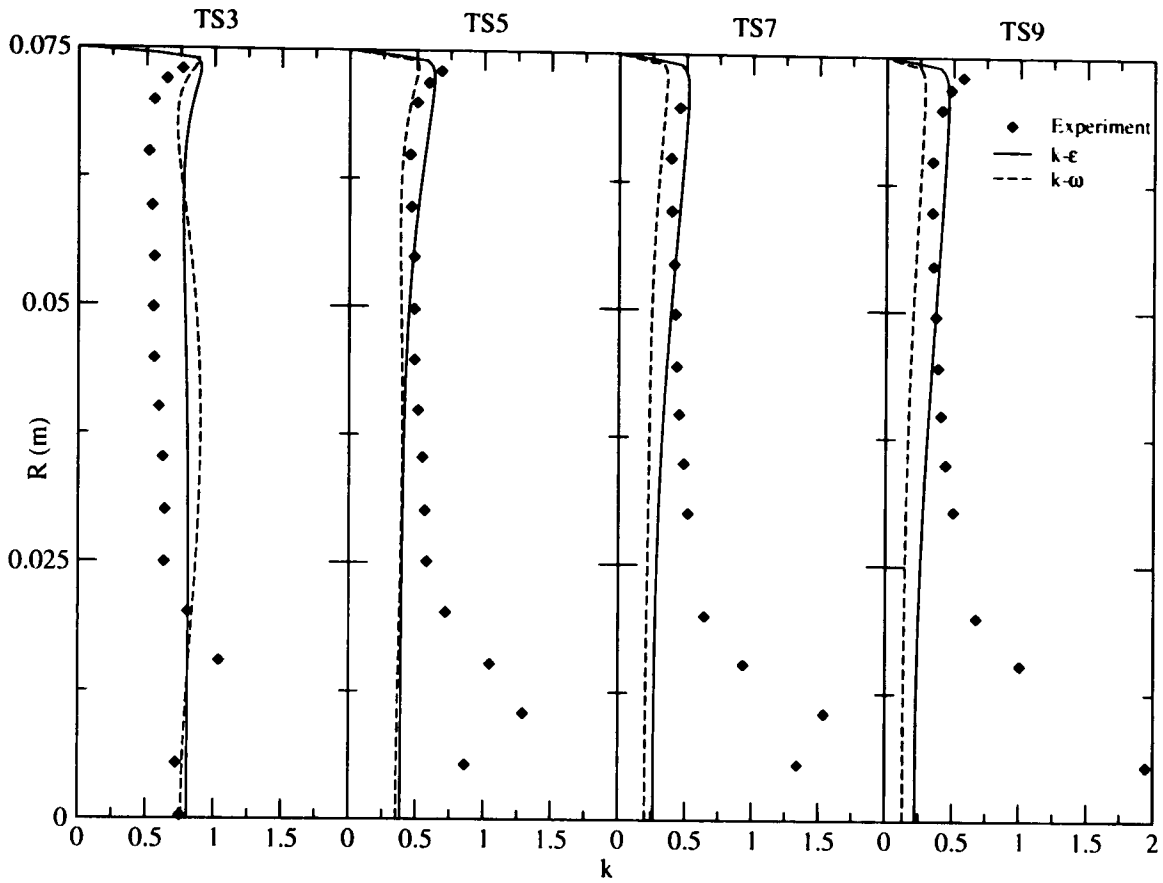

FIGURE 4.6: Two equation model results for turbulent kinetic energy; Kitoh's case.

velocity in figure 4.4. The size of the predicted radial velocity is approximately two orders of magnitude smaller than the other mean velocities and so has a small effect on the flow field in general.

Both models produce tangential velocities characteristic of forced vortex motion (figure 4.5). The high experimental values at the axis, representative of free vortex motion type, are not predicted at all. The strength of this solid body rotation also decays quickly downstream. This is responsible for the erroneous 'plug' shape axial velocity profile predicted for the axial velocity in figure 4.4. In the region close to the wall, both models initially predict values close to those given by experiment. However, the agreement rapidly decays downstream.

Looking at the predictions for k in figure 4.6, again both models under-predict this quantity at the central axis. Near the wall, model predictions improve, with the $k-\omega$ model showing greater accuracy upstream and the $k-\epsilon$ model proving more accurate downstream. Both models appear to overestimate the value of k in the wall region at TS3 but the $k-\omega$ model tends to increasingly under-predict it as the flow develops further downstream.

The experiments of Kitoh (1991) show that the eddy-viscosity is anisotropic in nature. Both two equation models tested use the Bousinesq eddy-viscosity hypothesis, stating that the Reynolds stresses are linearly dependent on the mean rate of strain tensor; equation (2.25). This effectively means that the eddy-viscosity, ν_T, acts like a constant of proportionality. The anisotropic nature of ν_T in this particular case, invalidates the eddy-viscosity hypothesis due to its differing effects on the various components of the Reynolds stress tensor.

Reynolds stress model results

Results using the Reynolds stress transport equation were obtained using the aforementioned LRR, SSG and SSG-ADRM models. Figure 4.7 shows the predictions for the mean axial velocity. Comparison against the results for the two equation models clearly shows the superior predictive capability of all the Reynolds stress models. All predict a large negative velocity at the axis, coinciding with the swirl induced reverse pressure gradient.

In the wall region, all the models under-predict the velocity gradient, although only to a small degree. This is due to the use of wall functions as opposed to integrating the governing equations up to the wall. Wall functions model the flow in the near wall region without the need for excessive computational nodes, whereas full integration includes additional nodal points in the near wall region, providing greater resolution. Overall, the predictions using the wall functions are adequate for engineering applications as Kitoh (1991) showed that the experimental data agreed with the log-law up to values of $y^+ = 200$. To provide improvement, full integration to the wall must be sought at the expense of additional computational cost.

In this region the LRR model under-predicts the gradient of axial velocity in the upstream region, leading to an under-prediction of the velocity. Further downstream, the LRR prediction of the gradient improves; where eventually an overestimation of the velocity occurs, especially at TS9. The SSG and SSG-ADRM models provide predictions for axial velocity and its gradient in close agreement with experiment. An initial under-prediction of U at TS3 is given by both SSG and SSG-ADRM mod-

els which turns into an over-prediction at TS9 for SSG. The SSG-ADRM provides the best prediction overall in this region.

For the annular part of the profile ($0.025 \lesssim R \lesssim 0.07$), the LRR model initially over-predicts the velocity at TS3. As the flow develops, this disparity increases steadily until at TS9 the U velocity is overestimated by as much as 4ms^{-1} in places. The same trend occurs for the SSG model but to a much smaller extent. At TS3 the velocity is initially under-predicted. As the flow develops, the SSG model over-predicts the measurements until at TS9 it provides predictions approximately 1ms^{-1} greater than the measurements. The SSG-ADRM model bucks this trend, showing a resistance to the growing over-predictions of the other models, providing the most accurate prediction of the experimental measurements. All of the models, however, over-predict the axial velocity as the outer region of the vortex core is approached.

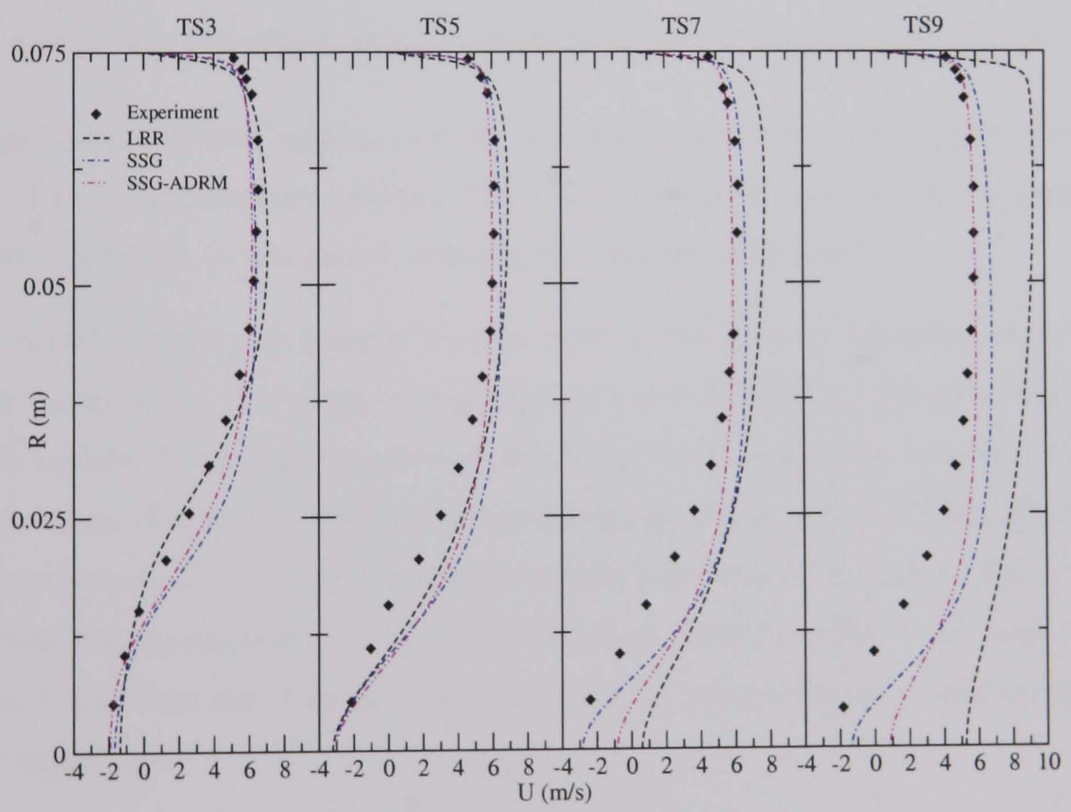

FIGURE 4.7: Reynolds stress model results for axial velocity; Kitoh's case.

The predicted axial velocity at the axis is a good indicator of a model's ability to capture the decay of the swirl correctly. Kitoh (1991) made similar measurements to show the axial decay of swirl along the pipe. Predictions are shown in figure 4.8 with reference to figure 4.7. Between 1 and 2 metres, the SSG-ADRM and SSG

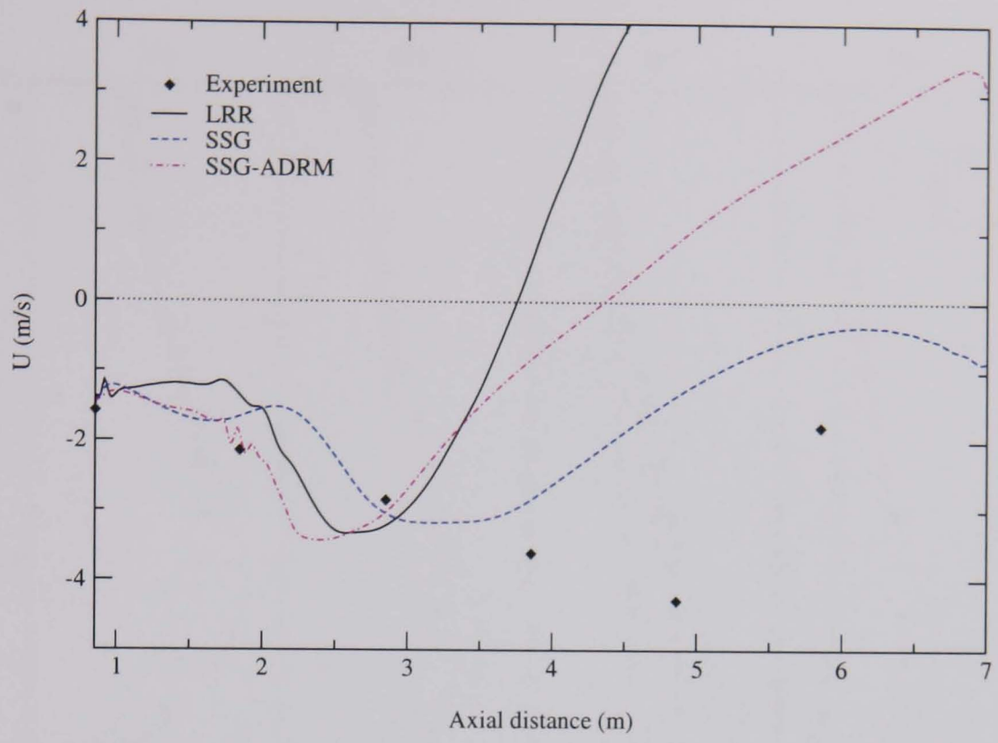

FIGURE 4.8: Reynolds stress model results for U velocity at the axis; Kitoh's case.

models show greatest agreement with experiment, correctly predicting the gradient of increasing negative velocity. The LRR model incorrectly predicts a slightly positive gradient in this region, reducing the negative axial velocity.

All models predict a premature turning point in the velocity gradient between 2 and 4 metres, the first being the SSG-ADRM model followed by the LRR and the SSG models. The positive gradient predicted by the LRR model is, however, much larger than that of the SSG-ADRM model giving rise to a flow reattachment at approximately 3.75m. The SSG-ADRM model also shows a premature flow reattachment at approximately 4.3m. The SSG model shows an ability to maintain the swirl better than the other models by maintaining the reverse axial velocity along the whole pipe.

Tangential velocities are predicted as shown in figure 4.9. As mentioned previously, the results for the LRR model show a premature decay of the swirl, tending toward a solid body rotation at TS9. The SSG model shows the reverse behaviour, where the tangential velocity is actually over-predicted in the upstream regions of the pipe (TS3 and TS5). Even though the swirl decays prematurely as shown by figure 4.8, the initial over-prediction of tangential velocity is convected downstream, preserving

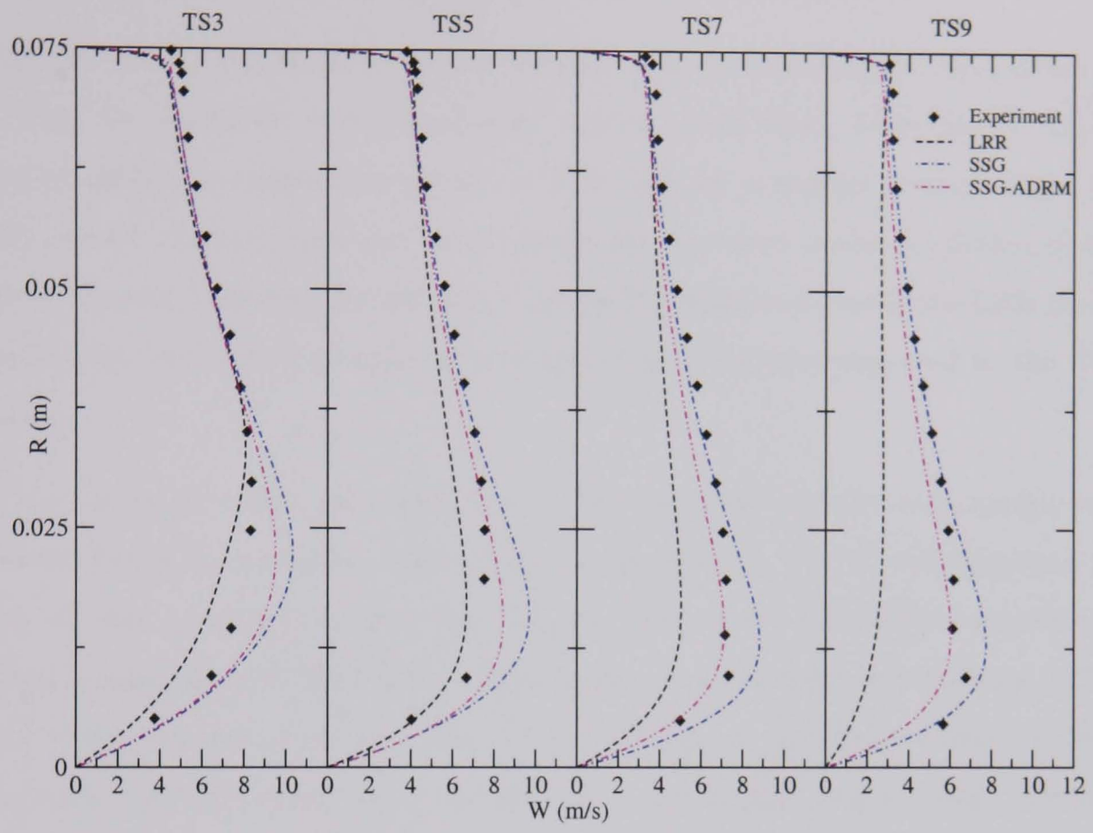

FIGURE 4.9: Reynolds stress model results for tangential velocity; Kitoh's case.

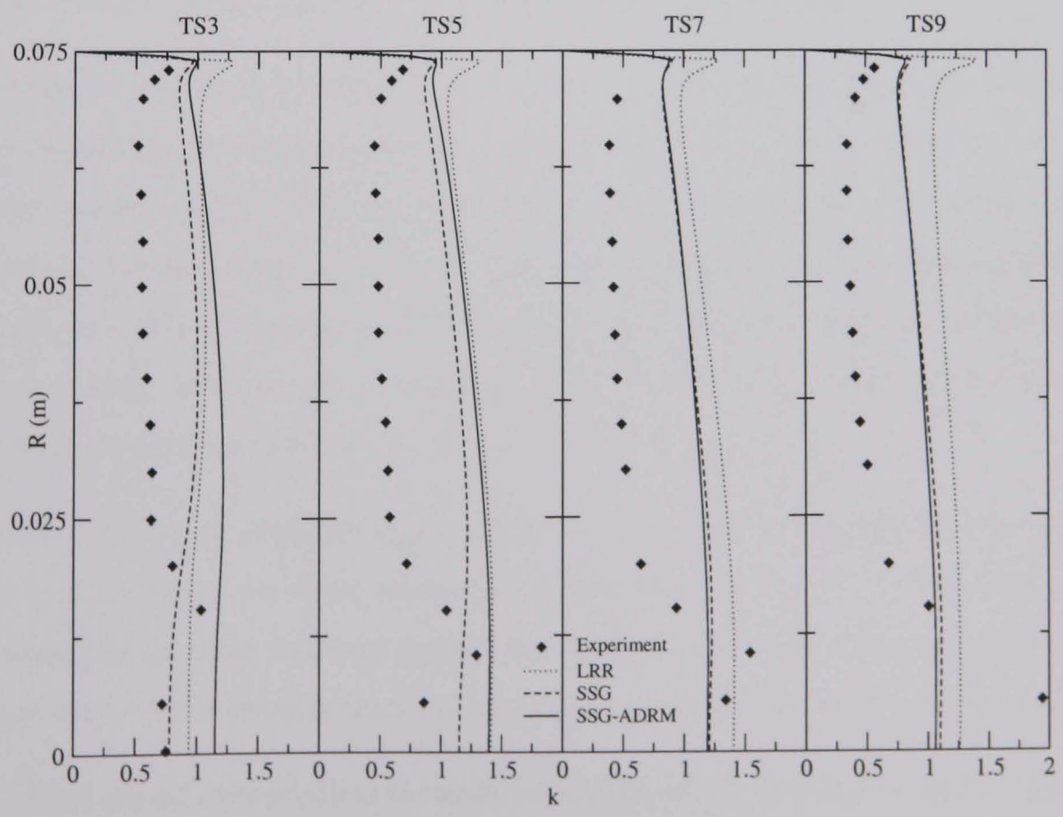

FIGURE 4.10: Reynolds stress model results for turbulent kinetic energy; Kitoh's case.

the swirl to a greater degree than the predictions of the LRR model.

The SSG-ADRM model shows good agreement with the experimental measurements in both the upstream and downstream regions of the flow. Initially, the model over-predicts the tangential velocity at TS3, but by a smaller amount than the SSG model. Downstream the model shows an increased under-prediction of the measurements, however, the free vortex profile is maintained (unlike the LRR model predictions) and better prediction is found at $R \approx 0.013$m compared to the SSG model.

In the near wall region, all models predict the tangential velocity well, except very close to the wall, where the velocity is under-predicted. Use of wall functions for this velocity component is more questionable than for others as the standard wall function approach was developed for plane shear flows (Launder and Spalding, 1972). Due to the premature return to solid body motion, as the distance from the wall increases, the LRR model under-predicts the experimental measurements. Despite the inability of the models to reproduce the tangential velocity at the wall, better agreement with experiment is provided by the SSG and SSG-ADRM models as distance from the wall increases into the annular part of the flow.

Despite the improved predicting power of the Reynolds stress models for the mean flow quantities, the turbulent quantity predictions do not show as good agreement. Figure 4.10 shows that all of the turbulence models over-predict the value of the turbulent kinetic energy at TS3. As the flow develops, the measurements show a growth in k at the central axis, with a reduction in the annular region. The Reynolds stress models, however, are unable to predict the drop in k in the annular part of the flow, or the increasing value of k in the axial vortex core.

Figures 4.11 to 4.13 illustrate this point for the individual normal stress components. The measurements for these components show a nearly isotropic stress field, with exception of the near wall and central axis regions. The models generally predict a larger value of the stresses than the experimental measurements from TS3 to TS9.

The LRR model over-predicts the axial normal stress component at all locations in the fluid, especially in the near wall region shown in figure 4.11. The SSG model,

however, shows improved agreement with the measurements at all axial locations. The SSG-ADRM model gives predictions larger than those of the SSG model in the upstream region, but this decays to values below the SSG model downstream.

For the radial normal stress in figure 4.12, all of the models predict the same trend with a large over-prediction in the annular region, reducing towards the central axis. Again the SSG-ADRM shows an initial over-prediction upstream that decays faster than the other models. The predictions of the LRR and SSG models are shown to be of comparable accuracy.

The tangential normal stress predictions are shown in figure 4.13. The trends for this stress repeat those of the $\overline{u^2}$ stress component. The predictions of the LRR model are, however, not over-predicted to the same degree as for $\overline{u^2}$ with the SSG-ADRM model showing a larger, erroneous prediction at TS3 and TS5 due to the over-prediction affected by this model upstream.

The inability of the Reynolds stress models to capture the increase of the normal stresses at the central axis needs further discussion. From figure 4.17 it is seen that the dissipation of turbulent kinetic energy takes the form of a flat radial profile except in the near wall region. This means that the loss in the values of the normal stress components in the axial vortex core is not effected by the dissipative process.

As noted previously, the normal stress components are close to isotropy in this region. If isotropic turbulence is present in a flow, the 'slow' (or return to isotropy) term in the stress-redistribution model becomes small, due to its dependence on the stress anisotropy tensor [see equations (2.50) and (2.69) for the LRR and SSG models]. Redistribution of the larger normal stresses to the shear stresses is also small in this region as illustrated in figures 4.14 to 4.16. Both the SSG and LRR models describe the redistribution process in the 'fast' models of equations (2.55) and (2.66). Here, the stress anisotropy tensor is used, but its effect is minimised as discussed above.

The other terms in the 'fast' models involve the mean rate of strain and vorticity tensors, $\overline{S}_{ij}$ and $\overline{W}_{ij}$ which take into account the effect of the mean velocity gradients. In this region of the flow, the dominant radial gradient of the velocity must

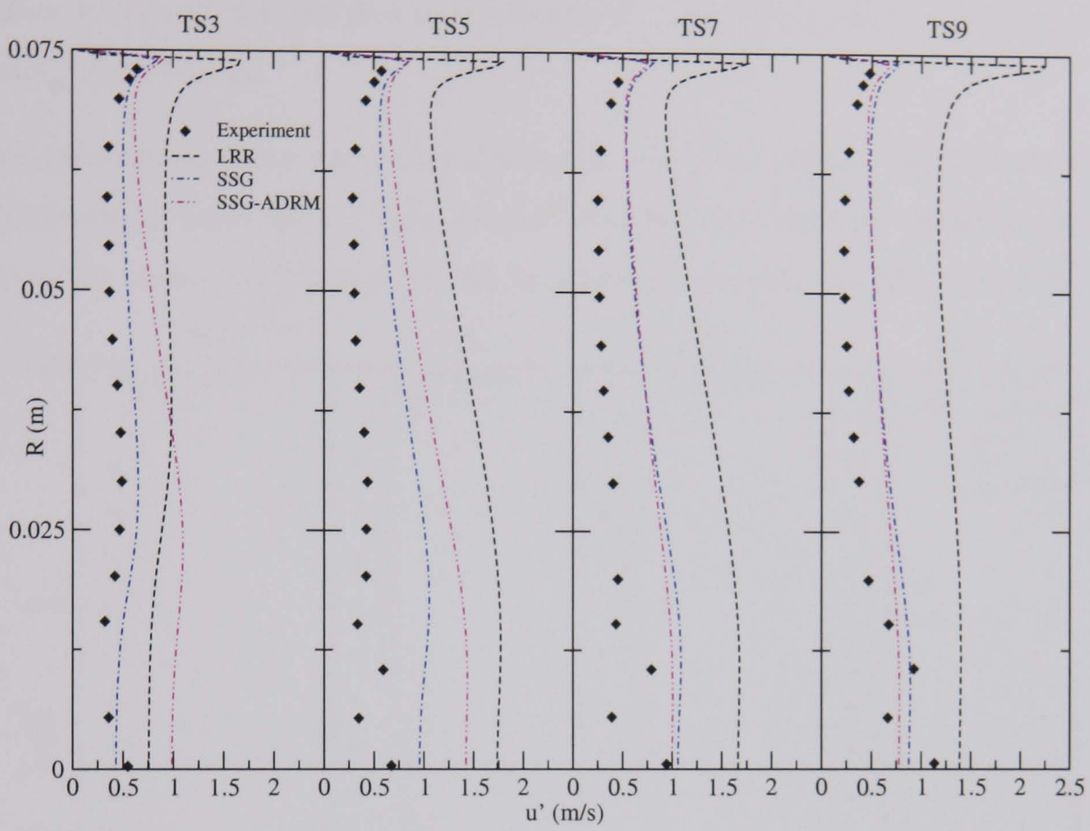

FIGURE 4.11: Reynolds stress model results for axial stress; Kitoh's case.

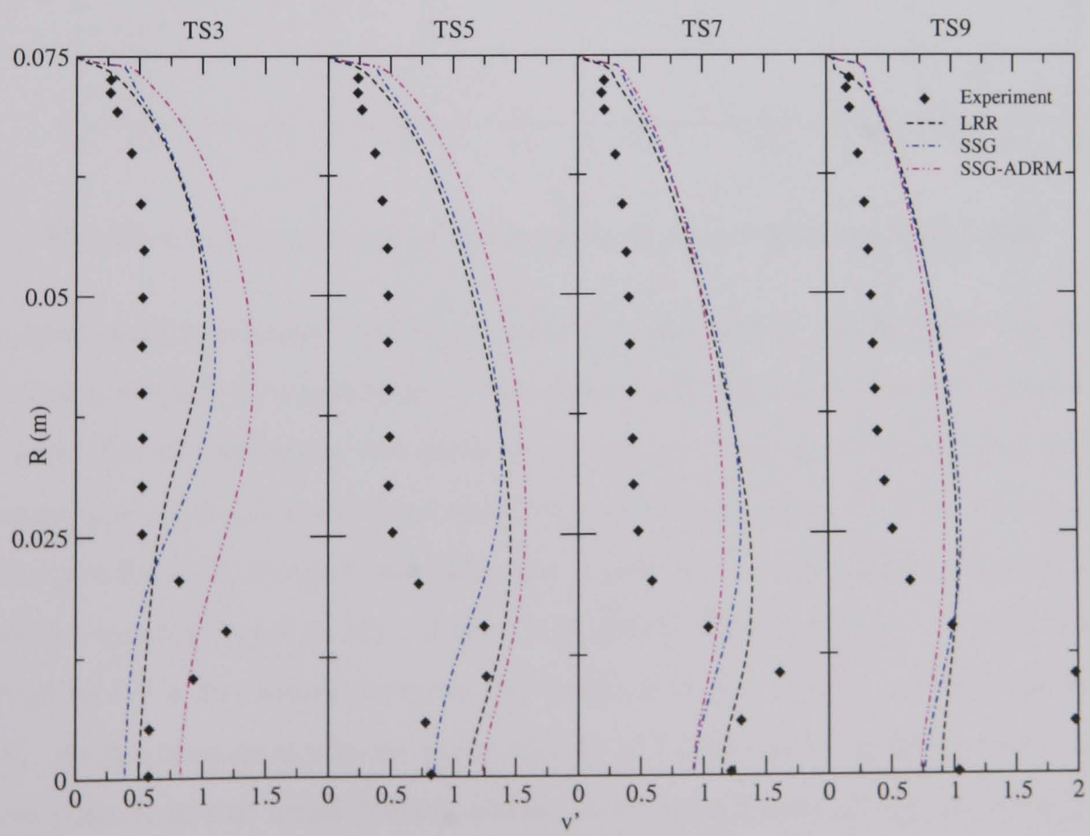

FIGURE 4.12: Reynolds stress model results for radial stress; Kitoh's case.

reduce to zero at the axis due to the symmetry boundary condition, reducing the stress redistribution.

The reduction in mean shear near the vortex core, also reduces the production of turbulence by mean shear. This, coupled with the near isotropy conditions, gives rise to the under-prediction of the normal stress components near the chamber axis.

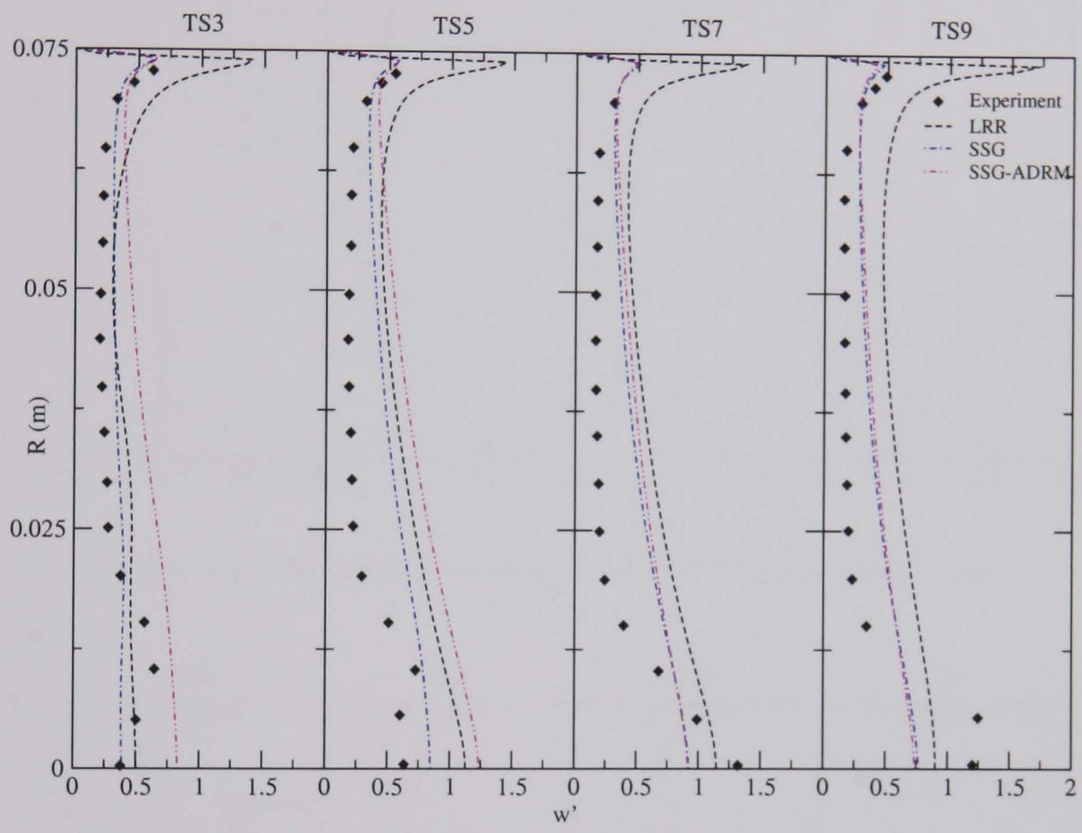

FIGURE 4.13: Reynolds stress model results for tangential stress; Kitoh's case.

As mentioned previously, due to the near isotropic nature of the flow, the shear stresses are small in comparison to the normal stresses, as is seen in figures 4.14 to 4.16. For the $\overline{uv}$ stress, the LRR model captures the experimental data in the annular part of the flow more accurately than the other models except when in the vicinity of the wall. Downstream, however, it predicts a larger negative value at TS9 and to a certain degree at TS7. This occurs because of dependency of the equation for $\overline{uv}$ to W in the source terms for its production and convection (see Appendix A.1). As the tangential velocity is retarded by the LRR model as the flow develops, these positive source terms become smaller, leading to increased negative values $\overline{uv}$.

For this shear stress, the other models show the opposite, $\overline{uv}$ is over-predicted for

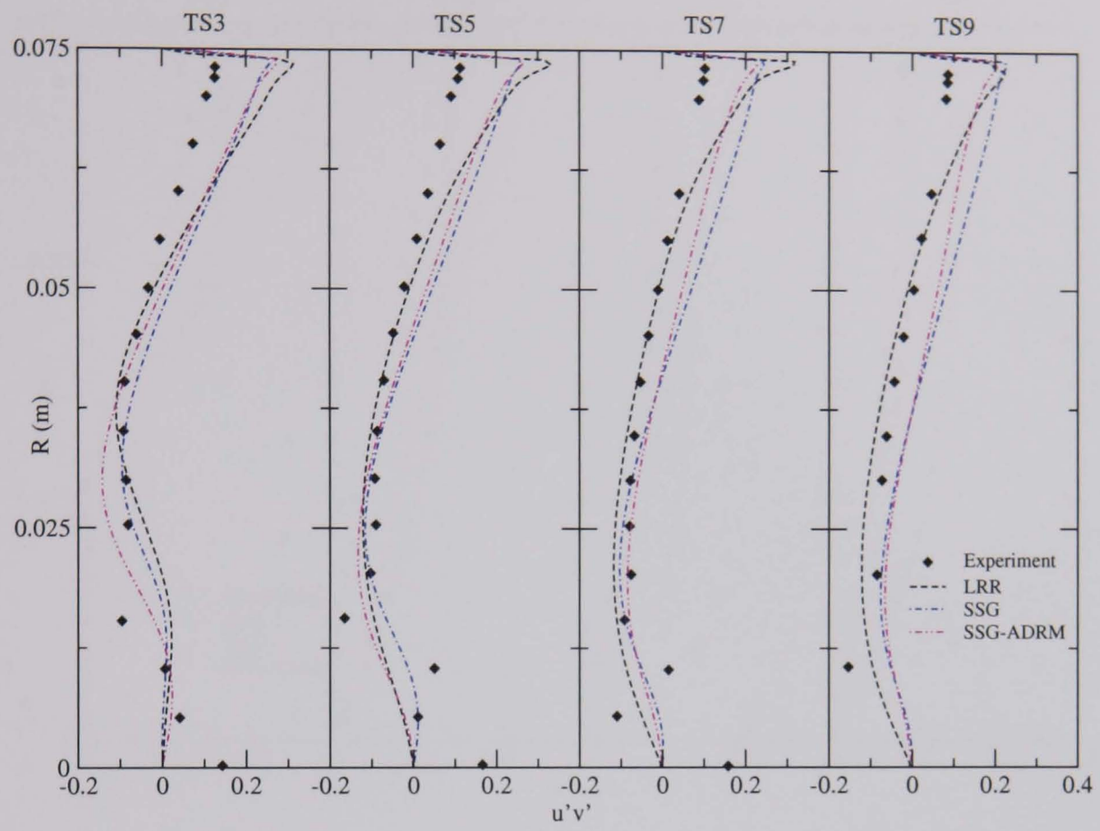

FIGURE 4.14: Reynolds stress model results for $\overline{uv}$ stress; Kitoh's case.

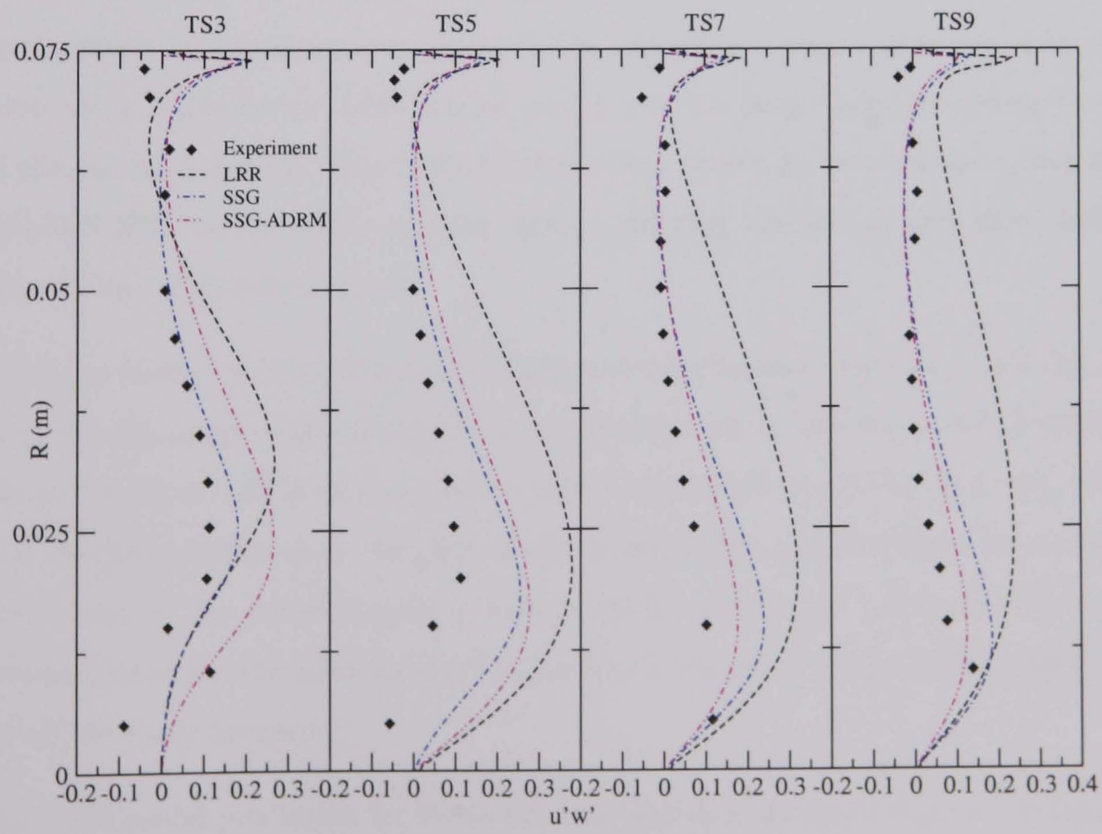

FIGURE 4.15: Reynolds stress model results for $\overline{uw}$ stress; Kitoh's case.

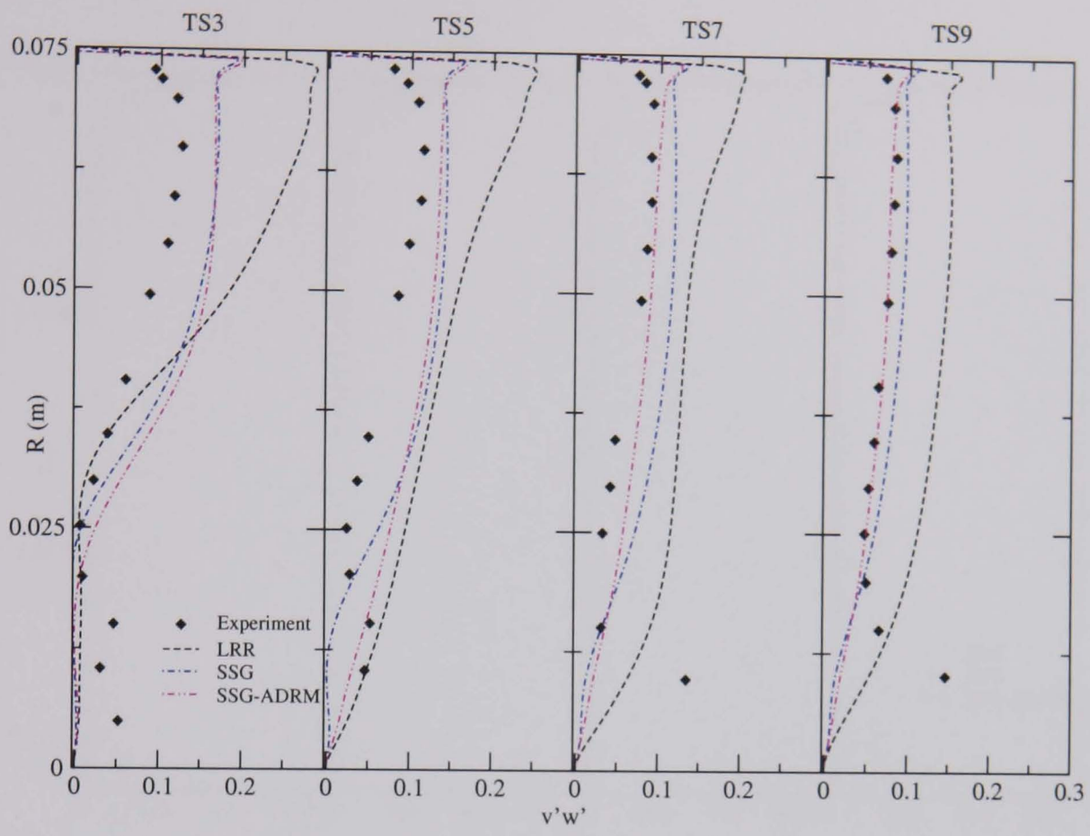

FIGURE 4.16: Reynolds stress model results for $\overline{vw}$ stress; Kitoh's case.

all test sections in the annular flow region. As the tangential velocity predictions are in much better agreement with the measurements, they are larger than the predictions made by the LRR model and so provide larger positive source terms in the equation for $\overline{uv}$. The SSG-ADRM model shows an improvement over the standard SSG model in the annular region, reducing the size of this shear stress more in line with measurements.

All of the models used provide overestimates of the $\overline{uv}$ stress in the near wall region. However, the tangential velocity, W is underestimated in this region by all models due to the use of wall functions, and the above arguments cannot be used. It is clear that the peak produced by the LRR model is larger than those of the other models. This is due to the redistribution of turbulence from the normal stresses which are over-predicted for the LRR model. This effect is observed in the LRR predictions for all the shear stresses.

The LRR model prediction for $\overline{vw}$ in the wall region is greatly over-predicted compared to the other models. This is due to the above reason as well as the size of the

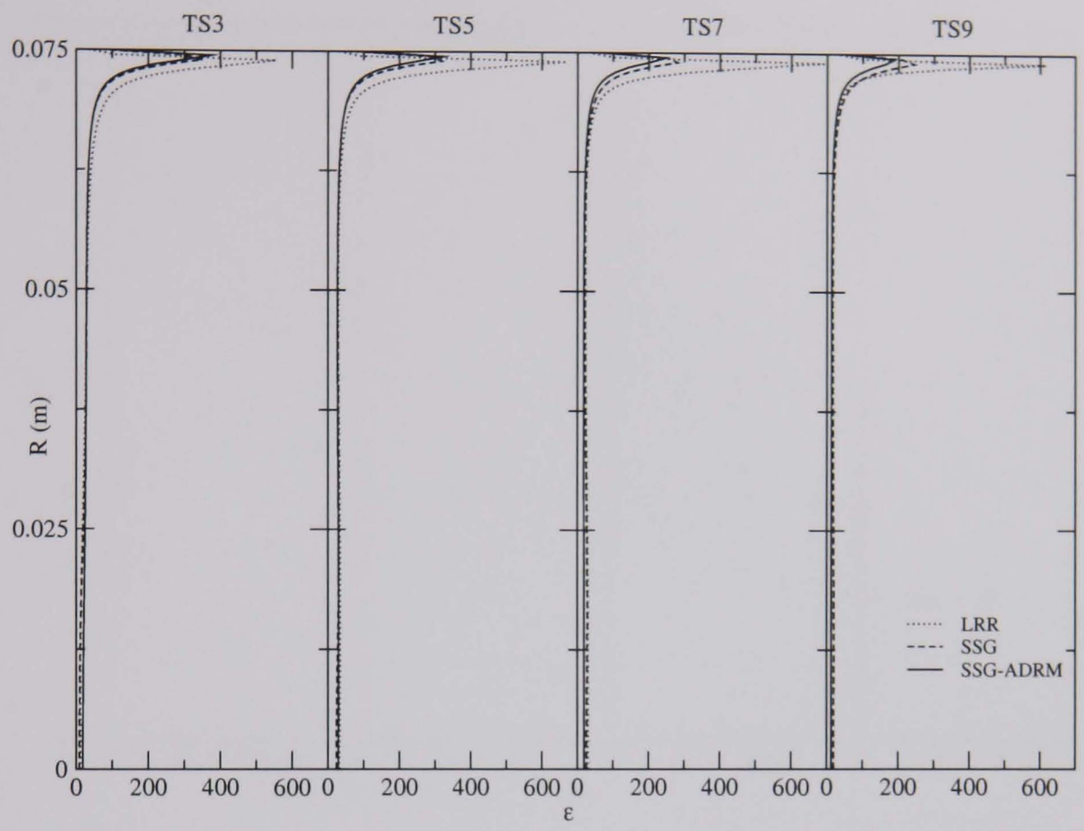

FIGURE 4.17: Reynolds stress model results for scalar dissipation rate; Kitoh's case.

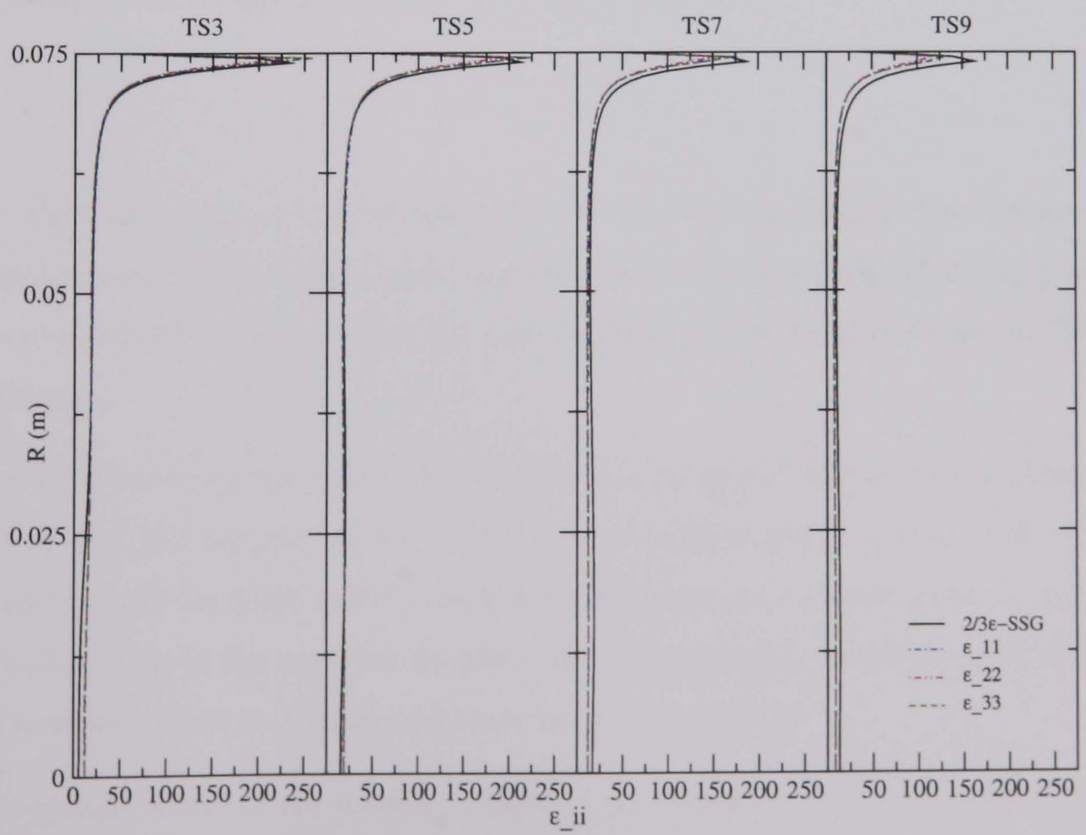

FIGURE 4.18: Reynolds stress model results for diagonal components of ϵ_{ij}; Kitoh's case.

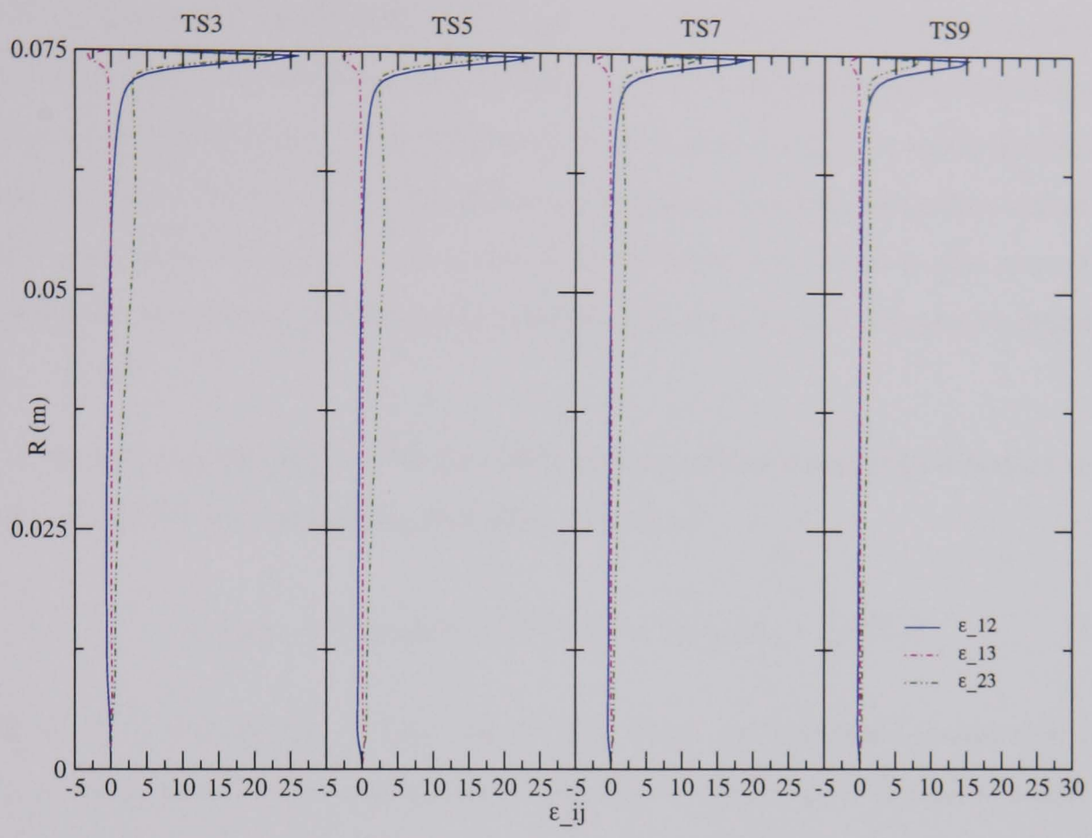

FIGURE 4.19: Reynolds stress model results for off-diagonal components of ϵ_{ij}; Kitoh's case.

convective source term of $\overline{vw}$ as given by (Appendix A.1)

$$\left(\overline{w^2} - \overline{v^2}\right) \frac{W}{r} \quad . \tag{4.4}$$

For the LRR model, it can be seen that the values of the normal radial stress are underestimated for the LRR model compared to the other models. This, along with the overestimation of the $\overline{w^2}$ stress, has the effect of increasing the value of $\overline{vw}$ in this region.

The $\overline{uw}$ shear stress predictions by the models in figure 4.15 for the near wall region fail to give the negative values illustrated by the measurements. The wall effect terms provide the LRR model with the closest result to the experiment by acting as a sink term in the equation for $\overline{uw}$. This gives a slightly negative value of this shear stress, albeit at a further location away from the wall.

The overall failure of the models to capture the sharp gradients that lead to negative values of the $\overline{uw}$ shear stress can be explained by the production and source terms in its modelled equation. The source term due to production of $\overline{uw}$, $-\overline{uw}V/r$,

is small due to the small value of V, and can be neglected. The remaining dominant terms are the convective source term, $-\overline{uv}W/r$, the production term and the stress-redistribution term. The production term is positive in this region due to the negative signs of the U and W gradients in the radial direction, while the convective term is negative. This implies that the stress-redistribution terms in the respective models are not able to provide a large enough sink term to give the correct negative value of $\overline{uw}$.

The difference between the SSG and LRR versions of the stress-redistribution term can be summarised (neglecting wall effect terms) as

$$\Pi_{ij,SSG} - \Pi_{ij,LRR} = -C_1^* P a_{ij} + C_2^* \epsilon (a_{ik}a_{kj} - \frac{1}{3} II \delta_{ij}) \tag{4.5}$$

where $C_1^* = 0.9$ and $C_2^* = 1.05$. In the first term, the increased production due to the high mean shear, and stress anisotropy in the near wall region works to decrease the value of $\overline{uw}$. However, the increased dissipation in the second term of (4.5) counteracts this for the SSG/SSG-ADRM models, increasing the value Π_{ij}. The wall effect terms for the LRR model have a greater effect in this region as shown in figure 4.15, except in the downstream region, where redistribution from its over-predicted normal stresses occurs.

Effects of the anisotropic dissipation rate model

The main effect of the ADRM, is through the coefficient $C_{\epsilon 1}^*$ in equation (2.82). This coefficient determines the amount of production of dissipation through the ratio ϵ/k and its values are shown in figure 4.23. In the absence of any mean strain or vorticity, $C_{\epsilon 1}^* \approx 1.36$, as is shown by the dotted line ($C_{\epsilon 1}^* - C_{\epsilon 1} \approx 0.36$).

The value of the anisotropic effect on the coefficient, $C_{\epsilon 1}^* - C_{\epsilon 1}$, increases with radius towards the annular part of the flow. In this region, the gradients of the mean velocities are at their lowest, and so the mean strain and vorticity has less effect on the value of $C_{\epsilon 1}^*$. With reference to figure 4.17, it is seen that the dissipation rate is initially (TS3) approximately equal to that predicted by the SSG model in this region. As the flow moves downstream, the value of the dissipation rate predicted

by SSG-ADRM falls below that of the SSG model.

In the upstream region, as the value of $C^*_{\epsilon 1}$ can never be (without additional tuning) as high as that specified by the SSG model ($C^*_{\epsilon 1} = 1.44$), the production of k in the annular region is initially higher than that predicted by the SSG model. This increased production of k then effects the production of ϵ that is directly proportional to it. For this reason, despite the lower value of $C^*_{\epsilon 1}$, predictions for ϵ in the annular region at TS3 and TS5 appear indistinguishable from the prediction of the SSG model. As the flow develops, isotropisation and turbulent diffusion act to reduce the value of k, and hence the normal stresses, in turn lowering the production of dissipation rate. At TS7 and TS9, this is seen in the annular region when compared to the SSG model.

This effect is reproduced in the vortex core region about the central axis. Due to the large radial gradients of W and U in this region, ξ and η, equation (2.79), also become large. This again leads to a small $C^*_{\epsilon 1}$ and hence the above argument as at the annular region is applicable. The larger size of the dissipation compared to the SSG model is due to the additional production of turbulence energy by mean shear in this region compared to that in the annular region. The combination of the shear reducing $C^*_{\epsilon 1}$ and also causing additional turbulence production causes the dissipation to be larger for the SSG-ADRM than the SSG model alone.

In the wall region, $C^*_{\epsilon 1}$ quickly reduces due to the presence of high shear, effectively reducing the amount of production of dissipation. This is reflected in figure 4.17, where the dissipation for the SSG-ADRM is less in the near wall region than for the SSG model. This reflects the non-equilibrium nature of turbulence in near wall flows, where production of turbulence is greater than its dissipation.

The components of ϵ_{ij} are shown in figures 4.18 and 4.19 with a breakdown of the isotropic and deviatoric parts for the diagonal components in figures 4.20 to 4.22. The main redistribution of the dissipation from the diagonal to off diagonal components occurs in the near wall region, where the mean strain is highest. The redistribution in the annular and core parts of the flow are reduced compared to this due to the much smaller mean flow gradients in these areas. The reason for

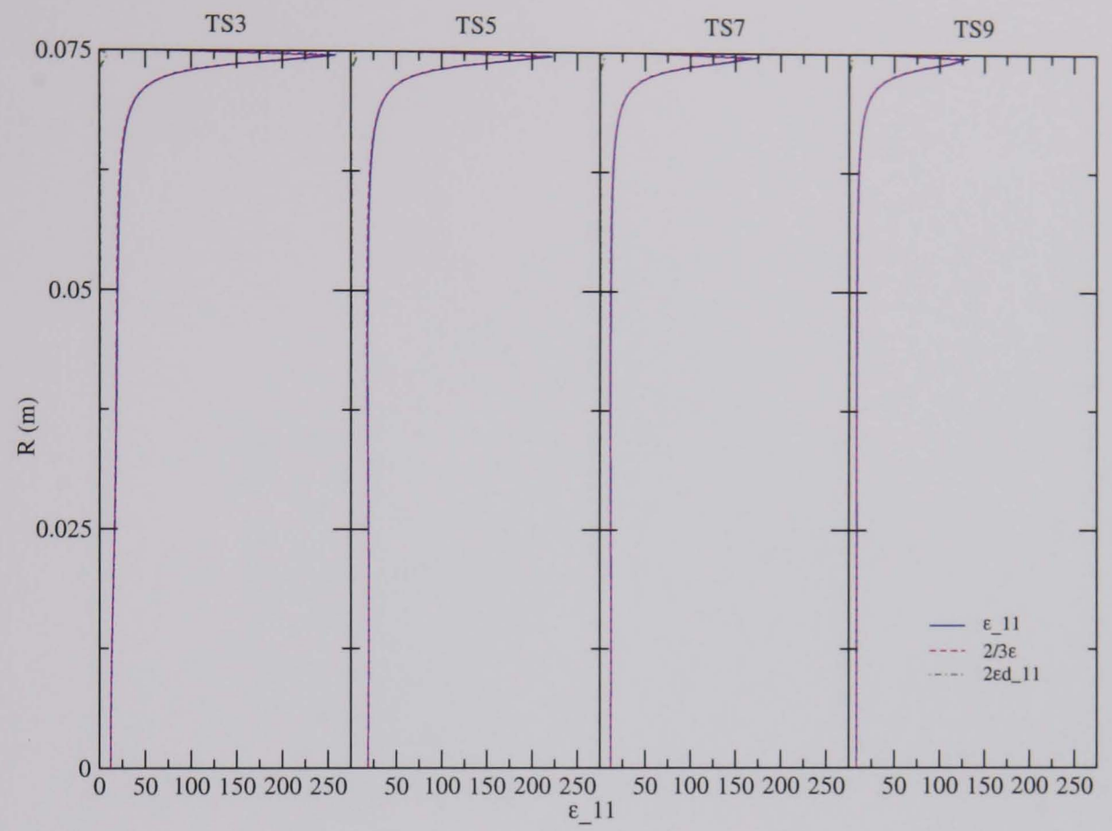

FIGURE 4.20: Reynolds stress model results for ϵ_{11} component; Kitoh's case.

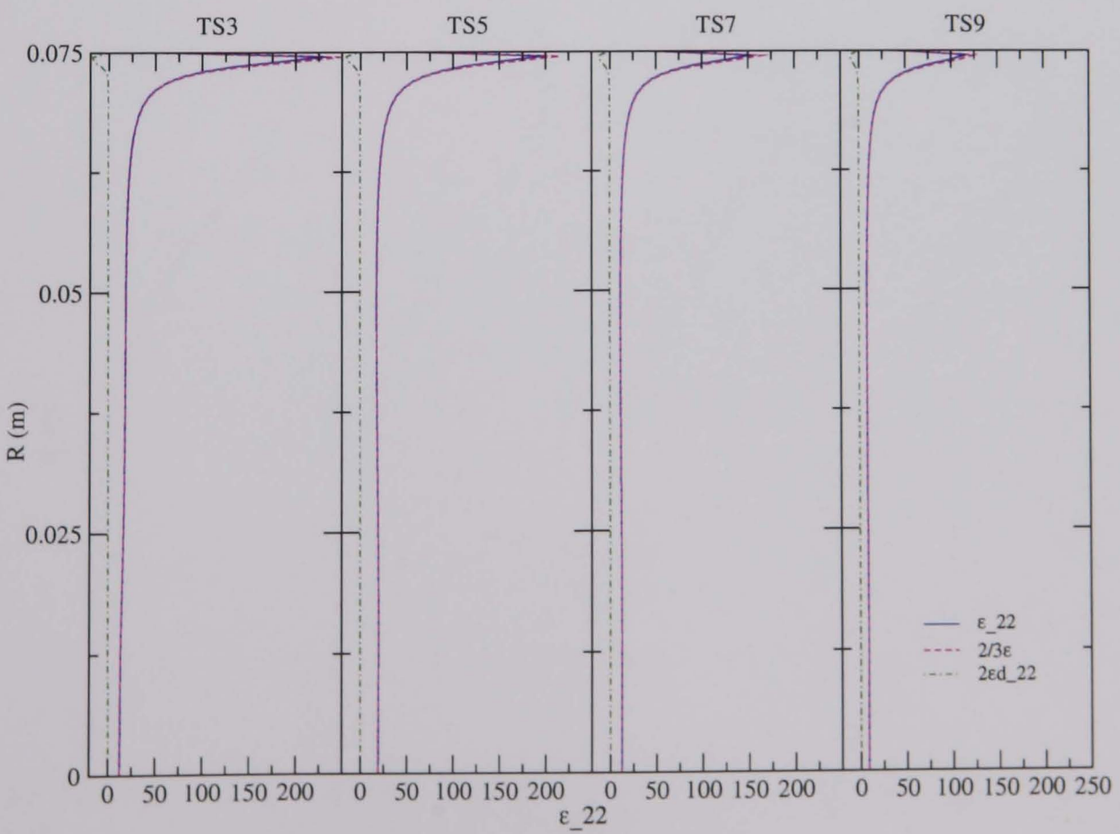

FIGURE 4.21: Reynolds stress model results for ϵ_{22} component; Kitoh's case.

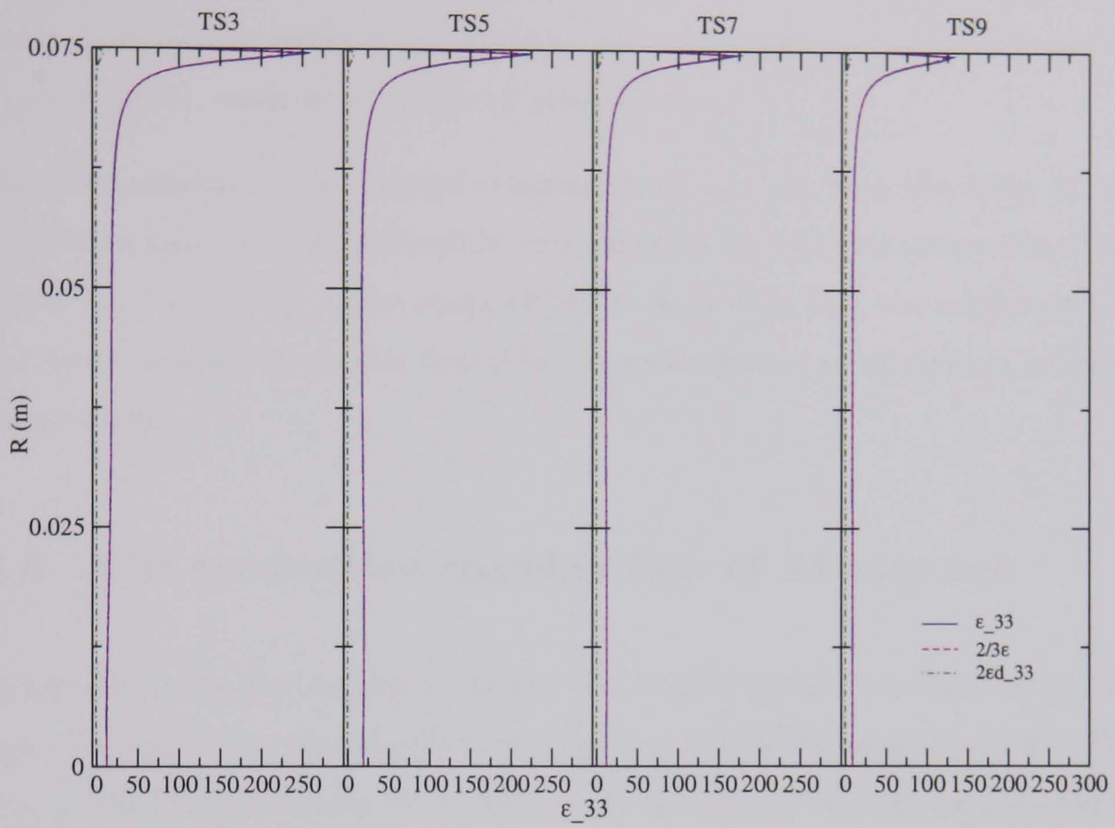

FIGURE 4.22: Reynolds stress model results for ϵ_{33} component; Kitoh's case.

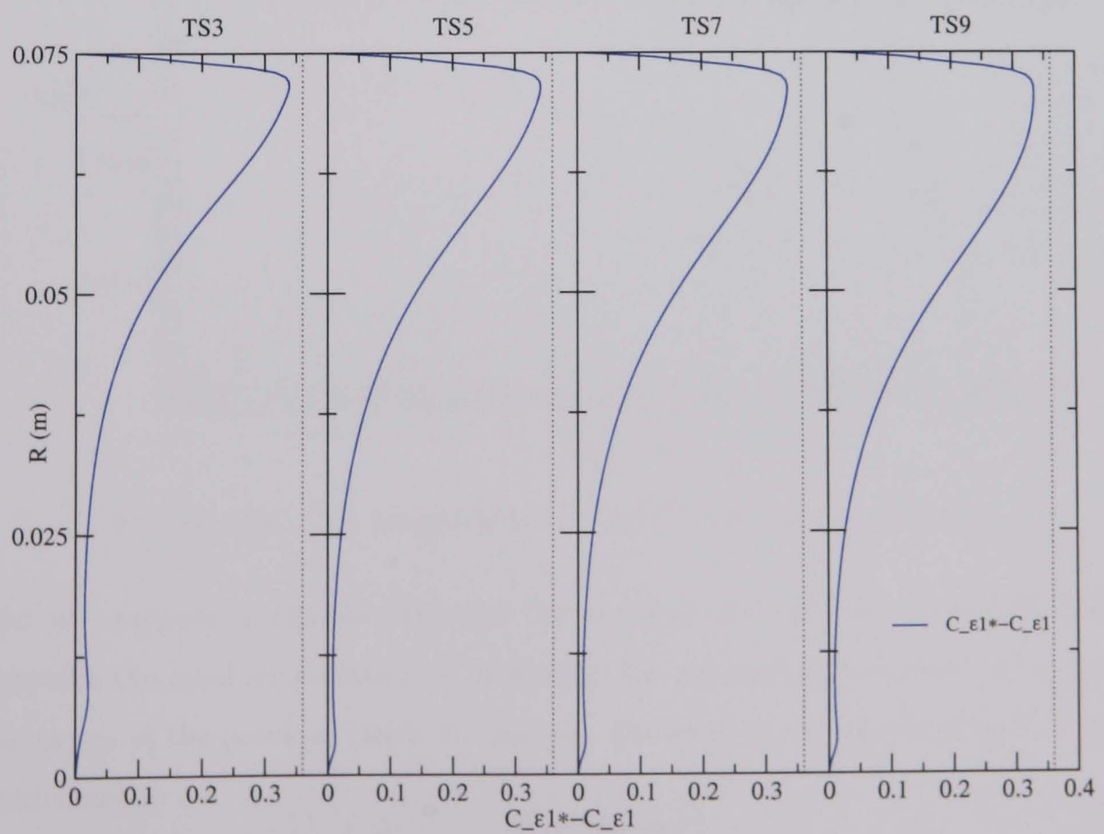

FIGURE 4.23: Reynolds stress model results for $C^*_{\epsilon 1} - C_{\epsilon 1}$; Kitoh's case.

the negative sign of ϵ_{13} in the wall region is due to the negative value of the axial gradient of the tangential mean velocity, counterbalanced by the other terms in equation (2.77), resulting in an overall positive value.

The compositions of the diagonal components of ϵ_{ij} show that the effect of the dissipation anisotropy, d_{ij}, is small in comparison to the isotropic component. This is due to values of d_{ij} in the range $\mathcal{O}(10^{-2})$. It is clear that the coefficient $C^*_{\epsilon 1}$ has far more influence in this flow than the redistribution of dissipation to other components.

4.3 The combustion chamber flow of Al-Masseeh

Compared to the flow studied by Kitoh, that studied by Al-Masseeh (1991) is far more complex due to the increased straining produced by the annular inlet jet. The flow field is shown schematically in figure 4.24, showing the annular inlet, leading to recirculation and high streamline curvature. For this flow, swirling air is introduced

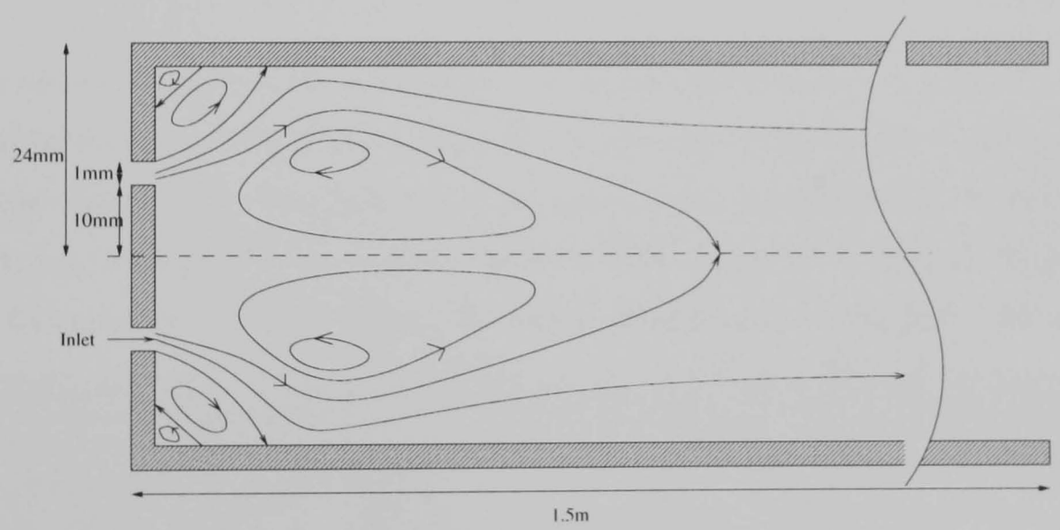

FIGURE 4.24: Flow schematic for Al-Masseeh's swirling flow problem.

into the combustion chamber through the annular inlet. The presence of the swirl enhances the axial recirculation by creating a low pressure at the centre of the axial vortex (as in the previous case). In this case the swirl at the inlet is defined by the swirl number

$$S = \frac{\int_0^{r_0} UWr^2 \mathrm{d}r}{r_0 \int_0^{r_0} U^2 r \mathrm{d}r} \tag{4.6}$$

which was set to be $S = 0.53$, where U and W are the mean axial and tangential inlet velocities (prescribed as below), and r is the radial distance from the central axis. The high streamline curvature and jet impingements near the wall due to the recirculation regions close to the inlet, provide a more complex flow field in terms of velocity and mean strain rate. These factors serve as a more stringent test for the computational models than Kitoh's case described above.

The experimental measurements were performed using laser doppler velocimetry (LDV). Unlike the hot wire method used by Kitoh, LDV is less invasive to the flow with only the presence of small 'seeds' - or particles - being carried by the flow itself. These particles reflect the laser light, from which calibrated electronics may calculate their velocities, and hence the fluid velocity, using the well known Doppler Effect relations. From these experiments values of the mean flow quantities were found along with data on the normal Reynolds stress components.

4.3.1 Numerical Procedure

The computational domain was created using an irregularly spaced, structured mesh. A nodal density of 100x56 nodes was found to give mesh independent results in the manner described in Chapter 3. The nodal density was increased close to the boundaries and the annular inlet, as shown in figure 4.25, to resolve the high gradients of the flow quantities in these regions. The length of the domain was equal to 1.5m with

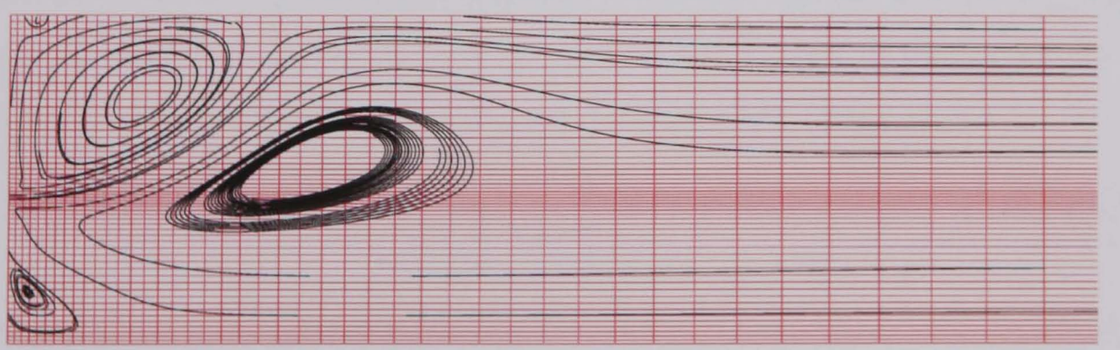

FIGURE 4.25: SSG model streaklines for the case of Al-Masseeh.

a pipe radius of 24mm. The inner and outer radii of the annular inlet are 10mm and 11.1mm respectively. Through the experimental observations of Al-Masseeh (1991), this flow was also found to be axisymmetric in nature, thus enabling the use of a

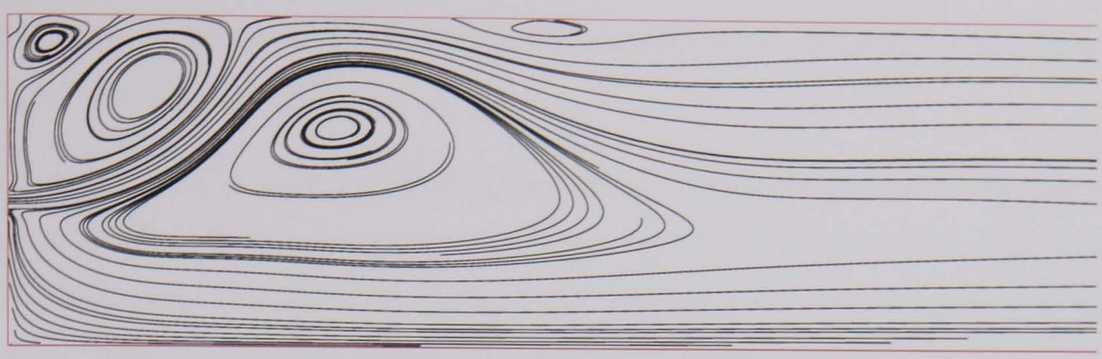

FIGURE 4.26: LRR model streaklines for the case of Al-Masseeh.

FIGURE 4.27: SSG-ADRM model streaklines for the case of Al-Masseeh.

two dimensional domain with an axis of symmetry at the lower boundary.

Boundary Conditions

Experimental data was not available for all of the turbulent stresses, and so could not be used to provide inlet boundary conditions as in Kitoh's case. The experimental data for turbulent kinetic energy measured at an axial distance of 2mm from the inlet was used to approximate inlet turbulent kinetic energy. It was found, after numerical experimentation and guidance from Al-Masseeh (1991), that

$$k = 0.09U^2, \tag{4.7}$$

where U is the mean axial inlet velocity, provided the best approximation of kinetic energy to those of the experiments. The axial inlet velocity, U, was set at 30ms^{-1}, uniform across the annular inlet. The turbulent dissipation rate at the inlet was approximated by

$$\epsilon = 0.09k^{\frac{3}{2}}L, \tag{4.8}$$

turbulence equations while the momentum equations are discretised with QUICK (U, V) and SMART (W).

Figures 4.28 to 4.31 show the effect of the different convective discretisation schemes on the solution of the mean momentum equations. The main area of the flow where the performance benefits of the higher order schemes are visible is in the near wall region. This is where the gradients of U and W are the greatest due to the high velocities meeting the no slip condition. This feature is seen for U velocity at axial locations $x = 5, 15, 30$mm, where a flow reversal is present between 15 and 30mm due to the presence of the corner recirculations.

The inlet jet region, $x = 5, 15$mm, is also where high order schemes outperform those of lower order. Here a fast moving jet is injected into slower moving fluid, creating high shear rates and velocity gradients. The widths of the inlet jet for the higher order schemes are thinner than those of the upwind and hybrid schemes, showing their greater interpolative accuracy and lack of numerical diffusion to give better agreement with experiment.

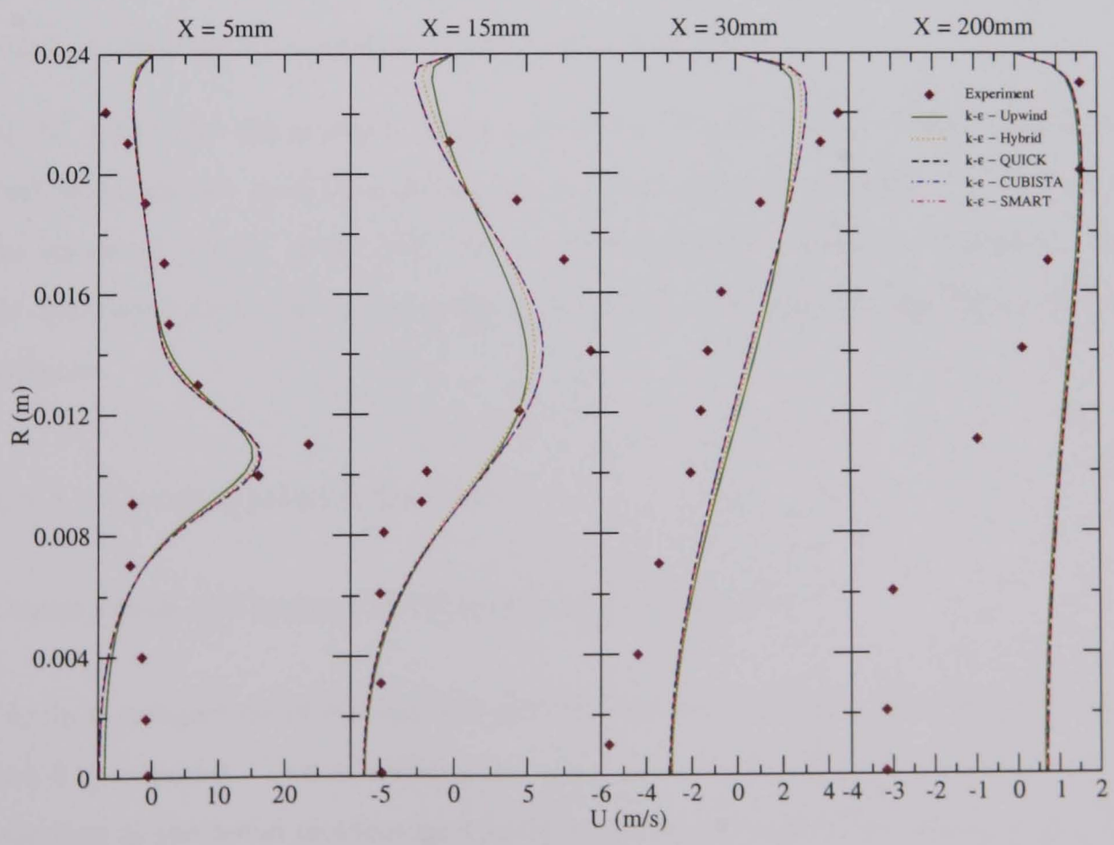

FIGURE 4.28: Axial velocity profiles testing effect of convective discretisation on momentum equations; $S = 0.53$.

where $L = 5.5 \times 10^{-4}$m - corresponding to half the inlet width - is an integral length scale and k is found from (4.7). The effective viscosity (turbulent plus molecular) was approximated by

$$\mu_{eff} = 0.202\rho k^{\frac{1}{2}} L. \tag{4.9}$$

The inlet tangential, or swirl velocity was specified by Al-Masseeh as a piecewise linear function, giving a triangular profile,

$$W = \begin{cases} \gamma \frac{U(r-r_i)}{r_o - r_i} & if \quad r \leq \frac{1}{2}(r_o + r_i) \\ \gamma \frac{U(r_o - r)}{r_o - r_i} & if \quad r > \frac{1}{2}(r_o + r_i), \end{cases} \tag{4.10}$$

where r_o and r_i are the outer and inner annulus radii, r the radial distance and γ a constant to be found. To find γ, one of the situations represented in (4.10) may be substituted into equation (4.6) where $S = 0.53$. After performing the integration of (4.6), the value of the gamma constant was found to be,

$$\gamma_{S=0.53} = 2.0, \tag{4.11}$$

which corresponds to a peak tangential velocity of 30ms^{-1}.

At the solid walls, the no slip boundary condition is applied and standard logarithmic wall functions are used to approximate variables close to the wall. At the exit of the chamber, a fully developed, zero gradient boundary condition is applied. For the symmetry axis, zero radial gradient boundary conditions are applied to all flow variables.

4.3.2 Computational Results

Comparison of Convective Discretisation Schemes

Firstly a comparison of the discretisation schemes is presented using the two equation $k - \epsilon$ model. Two situations are considered: effect of convective scheme on solutions of the mean momentum equations while the turbulence equations are discretised using the SMART scheme and effect of convection scheme on solutions of the

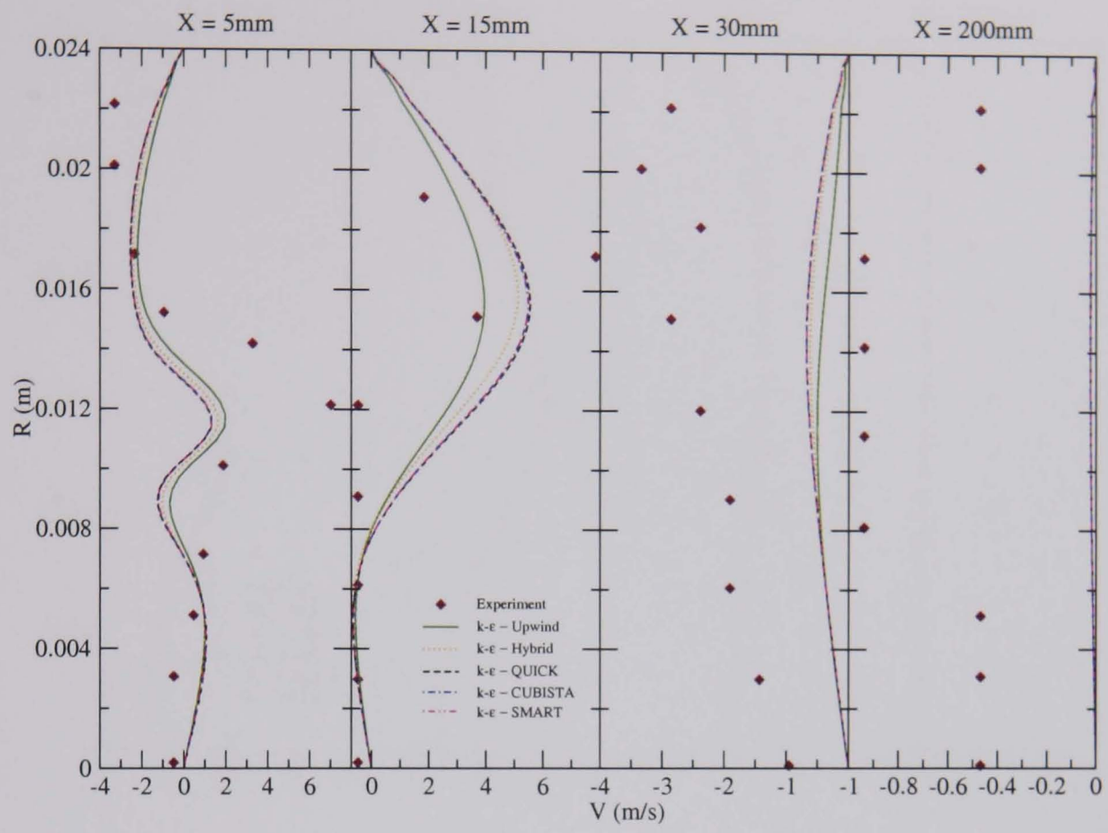

FIGURE 4.29: Radial velocity profiles testing effect of convective discretisation on momentum equations; $S = 0.53$.

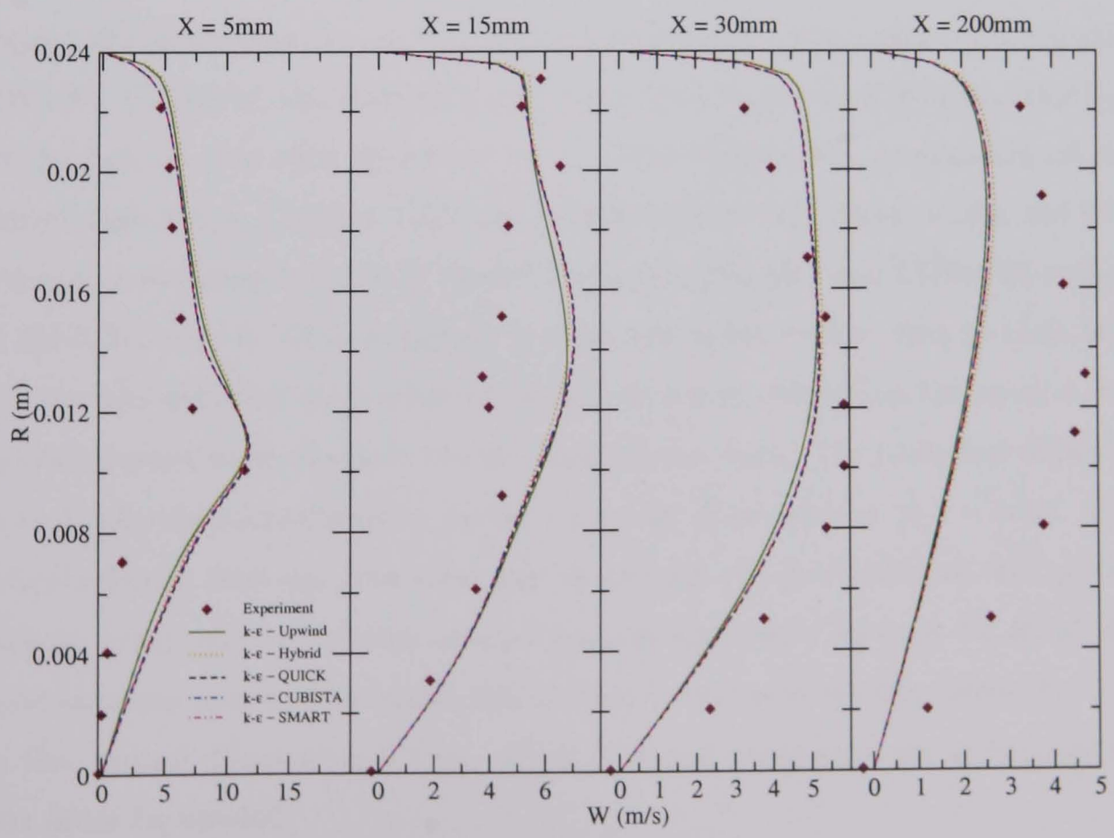

FIGURE 4.30: Tangential velocity profiles testing effect of convective discretisation on momentum equations; $S = 0.53$.

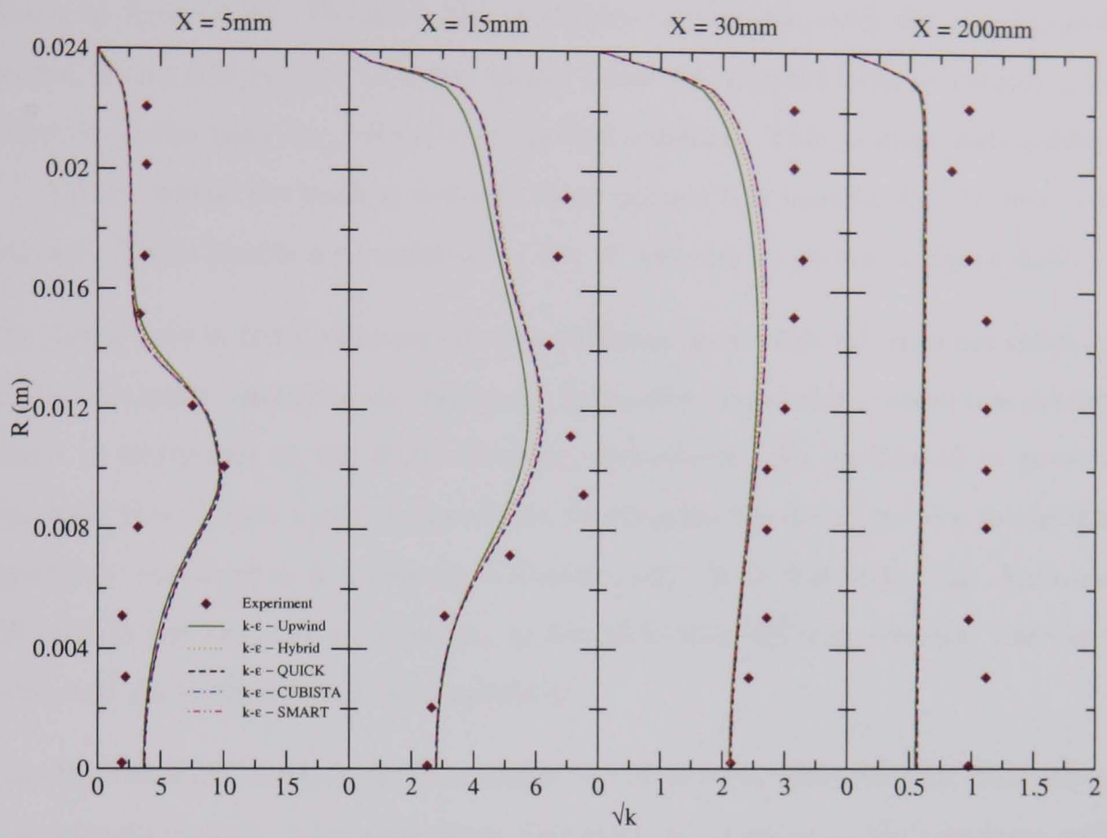

FIGURE 4.31: Turbulent kinetic energy profiles testing effect of convective discretisation on momentum equations; $S = 0.53$.

Figure 4.28 shows the effect on the mean axial velocity, U. The higher order schemes (QUICK, CUBISTA and SMART), give predictions that are indistinguishable due to the lack of very steep gradients in U. This behaviour is reminiscent of the results depicted in Chapter 3 for the two-dimensional test cases, where the flow remains in the smooth region of the NVD diagram (SMART and CUBISTA reduce to QUICK) and the QUICK scheme produces bounded results. Due to their lack of numerical diffusion, these schemes are also shown to outperform the upwind and hybrid schemes when compared to the experimental data. The numerical diffusion in such schemes is illustrated by the broader peak of the inlet jet at $x = 5$mm. The hybrid scheme, however, goes some way to improve the predictions of the upwind scheme, lying midway between upwind and the high order schemes for all of the axial locations shown. This shows that there are regions in the flow where $Pe < 2$, so that central differencing is used, which is second order accurate as opposed to first order for upwind.

The V velocity profiles show similar behaviour to those of the U velocity and are

shown in figure 4.29. Despite only qualitative agreement with the experimental results, it can still be seen that the higher order schemes are able to predict a less diffusive profile than the hybrid and upwind schemes. This is most noticeable at $x = 15$mm, where the peak is reduced in amplitude but broader for the low order schemes. These trends are repeated for the W velocity as shown in figure 4.30.

The differences in the predictions for the different convective schemes are relatively small. The main reason for this relatively insensitive response to convective discretisation is attributed to the Eddy-Viscosity hypothesis. As mentioned in previous chapters, this closure method introduces an effective viscosity into the momentum equations, resulting in a dominant diffusion term. It is this term that dominates diffusion in the momentum equation, as the molecular diffusion and any associated numerical diffusion is small in comparison.

The effect on k of changing the momentum equation convective discretisation scheme is seen in figure 4.31. The momentum equations are coupled to the transport equation (2.30) for k through the Eddy-Viscosity hypothesis, the various models used to close the equation and the explicit appearance of U_i, so there is a dependence on the discretisation scheme used. The term describing the production of k,

$$P = -\tau_{ik}\frac{\partial U_i}{\partial x_k} \tag{4.12}$$

is directly proportional to the gradient of the velocity. The hypothesis can be made that the production of k will be less when low order convective discretisation schemes are used in the momentum equations. Results in figure 4.31, with reference to figures 4.28 and 4.30, support this hypothesis. Where $x = 15$mm the gradients of the velocities are smaller for the low order schemes than for those of higher order. This is reflected in the size of the predicted value of k. At $x = 15$mm the values of k predicted when the momentum equations are discretised using low order convection schemes are smaller than those of the higher order schemes. This is compounded by the appearance of τ_{ij} in (4.12) that is modelled by the eddy-viscosity hypothesis, equation (2.25), which includes the velocity gradients in its formulation.

The effect of the convective discretisation scheme employed on ϵ and k can be seen

in figures 4.32 to 4.35. Again, the difference between the upwind scheme and the high order schemes is small for the approximation of the turbulence equations. For the axial and radial velocity profiles, the upwind scheme provides a result that is in better agreement with the experimental data. This is due to the prediction of k. Comparing figures 4.32 and 4.35 for U and k at $x = 15$mm, it is seen that k is under-predicted in the region $r > 0.012$m due to numerical diffusion. k appears in the source term of the U velocity equation in the model for τ_{ij},

$$\tau_{ij} = -2\nu_T S_{ij} + \frac{2}{3}k\delta_{ij} \tag{4.13}$$

where the turbulent viscosity, $\nu_T = C_\mu k^2/\epsilon$. As k is reduced in this region, the magnitude of the momentum equation source term involving τ_{ij} is also reduced. This reduces the effective viscosity of the U velocity equation allowing less 'effective diffusion' leading to sharper velocity gradients as shown in figure 4.32.

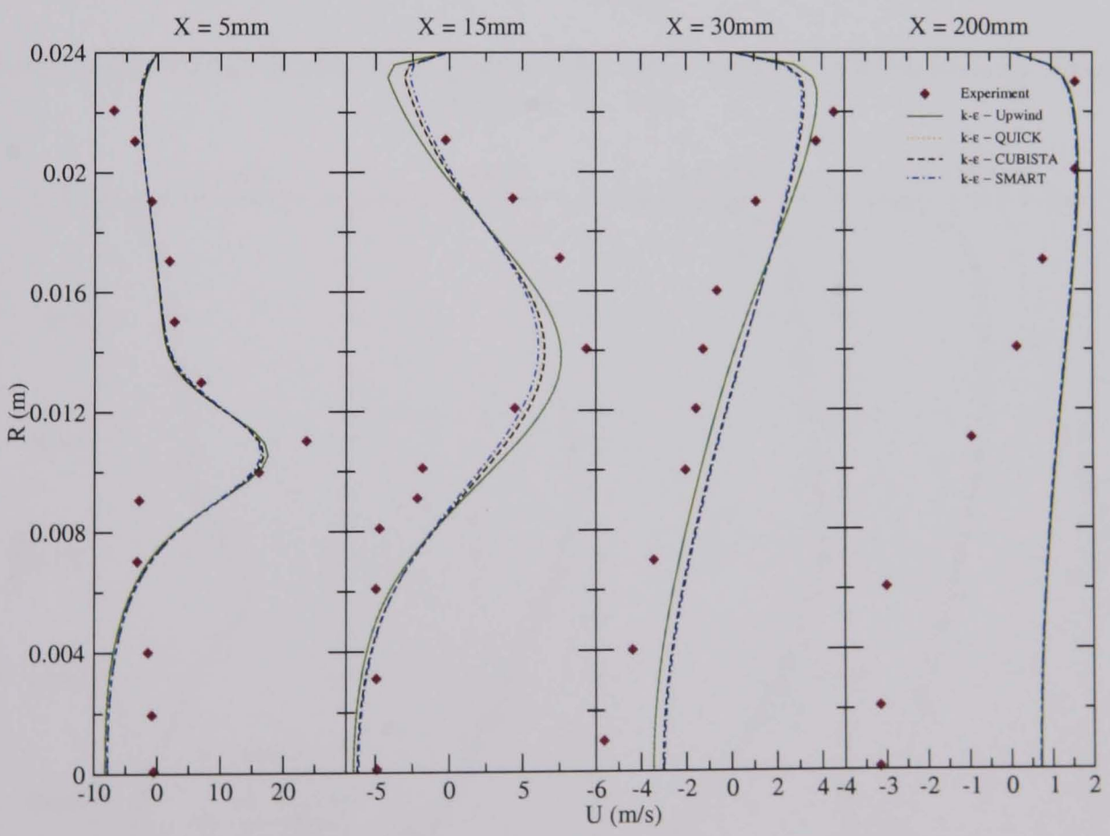

FIGURE 4.32: Axial velocity profiles testing effect of convective discretisation on turbulence equations; $S = 0.53$.

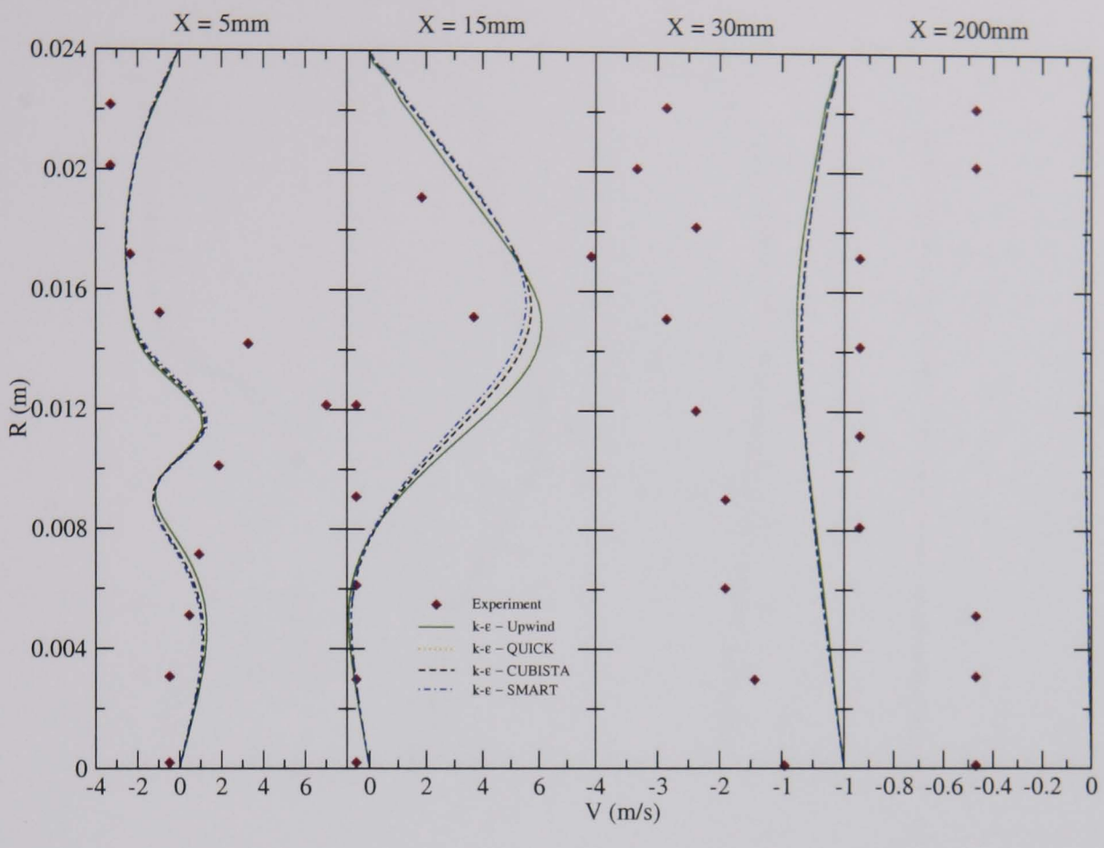

FIGURE 4.33: Radial velocity profiles testing effect of convective discretisation on turbulence equations; $S = 0.53$.

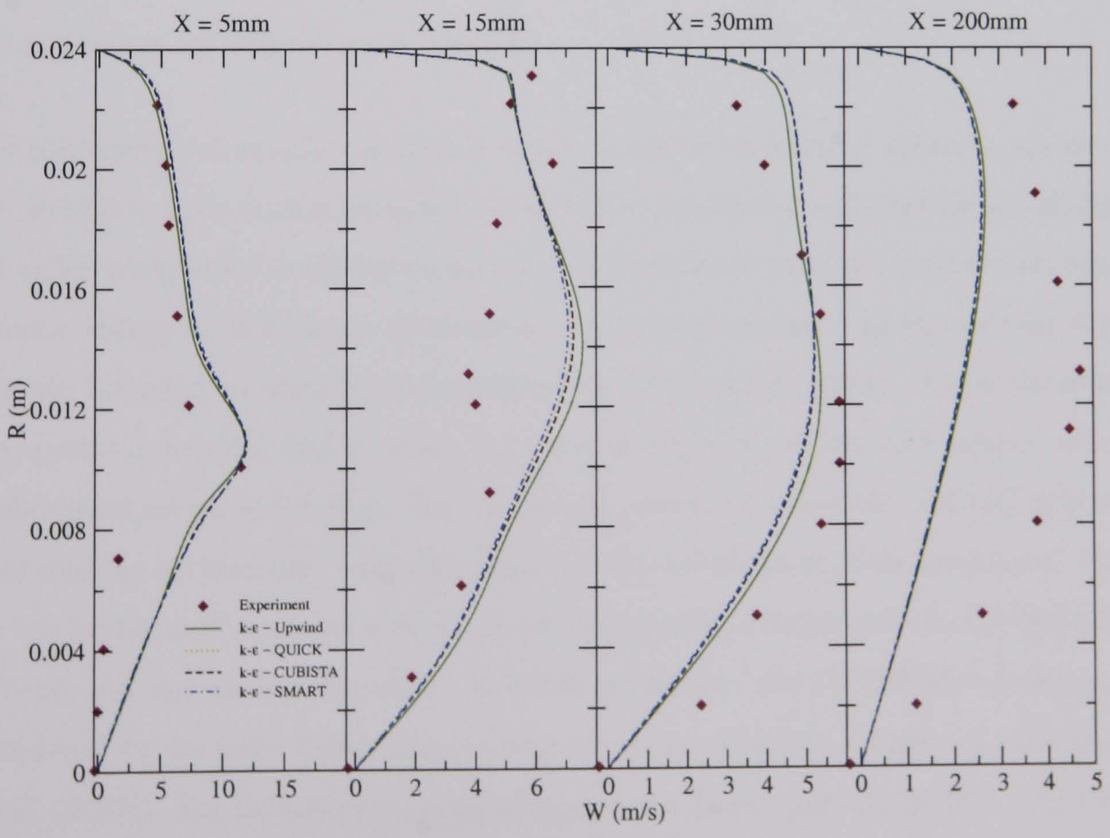

FIGURE 4.34: Tangential velocity profiles testing effect of convective discretisation on turbulence equations; $S = 0.53$.

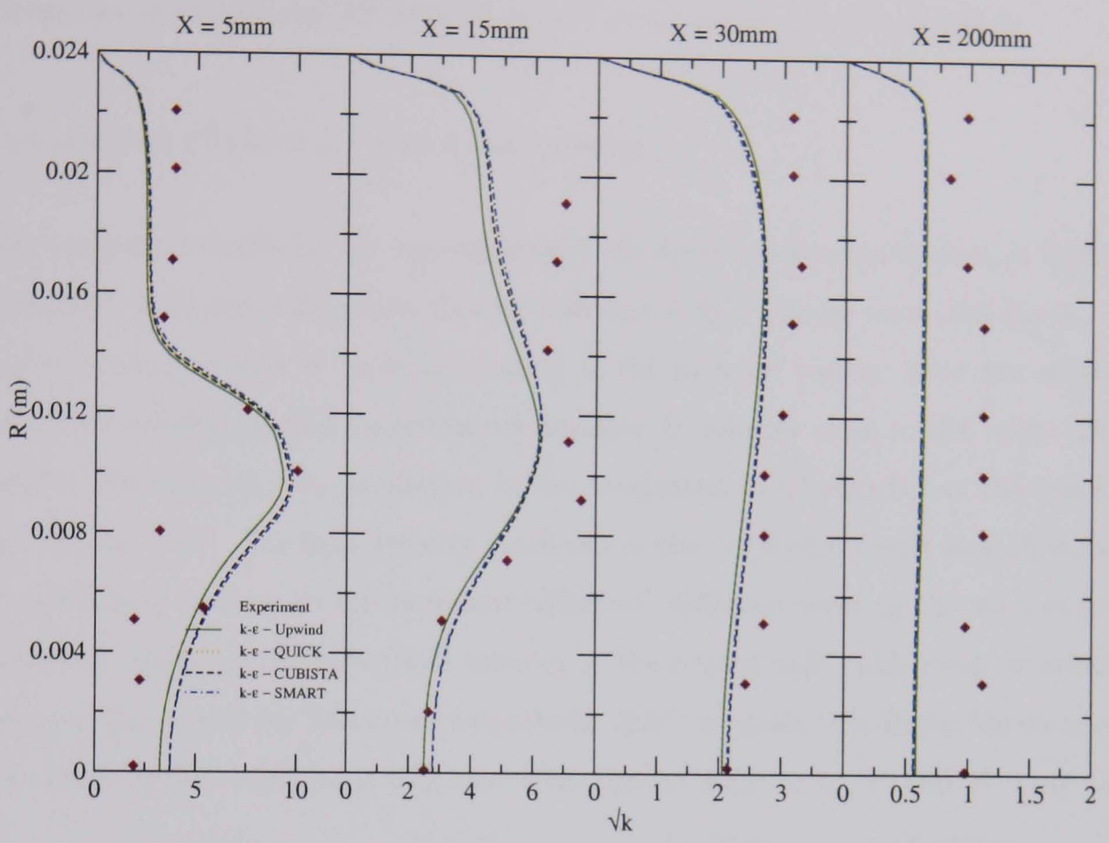

FIGURE 4.35: Turbulent kinetic energy profiles testing effect of convective discretisation on turbulence equations; $S = 0.53$.

Comparison of Turbulence Models

As mentioned previously the higher order, bounded convection schemes are most applicable to flows with steep gradients in flow variables to counteract the possibility of under/overshoots in the interpolation. For turbulence variables such as turbulent kinetic energy or turbulence dissipation rate, it is of utmost importance that they remain bounded to comply with realisability (see Lumley, 1978). These variables are positive definite, and so must not become negative, which may happen when unbounded schemes are used. For the results presented below the SMART scheme was used for *all* turbulent quantities in all of the turbulence models considered. Due to the highly stiff equation sets of the second moment closure models, the SMART scheme did not always converge. In these situations, the CUBISTA scheme was employed for its more favourable convergence properties (see Chapter 2 and Alves *et al.* (2003)). For the momentum equations, it was found that the QUICK, SMART and CUBISTA schemes all produced indistinguishable results. For this reason the QUICK scheme was used for the U and V momentum equations with a bounded

scheme for the tangential W velocity as this must also be positive definite.

Comparison of the $k-\epsilon$ and $k-\omega$ models

The computed results for the two-equation turbulence models can be seen in figures 4.36, 4.37, 4.38 and 4.39. From figures 4.36 and 4.38 it can be seen that the $k-\epsilon$ model predicts U and W more accurately in the inlet jet region. Near the central axis, both models predict an erroneous negative U velocity close to the inlet. This can be traced to an over-prediction of the tangential swirl velocity at the central axis (figure 4.38). The high velocity gradients in this jet region result in high values of strain rate leading to an increased 'effective' diffusion term in the momentum equations, diffusing the inlet swirl velocity to the central axis. This main drawback is due to the use of the Bousinesq hypothesis (2.25) to model the Reynolds stresses. The effect of this additional diffusion term can be seen for U, V and W near the

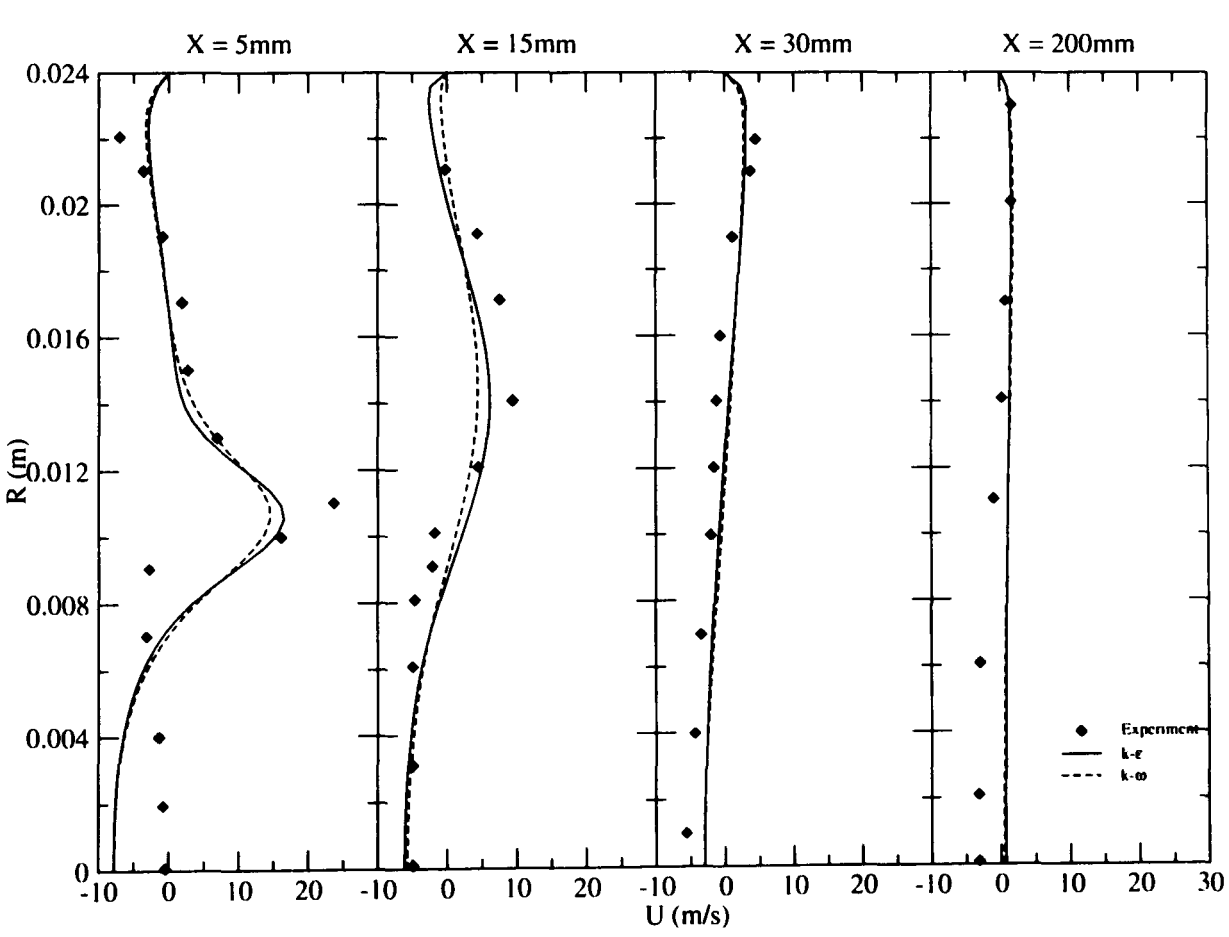

FIGURE 4.36: Axial velocity profiles for the case of Al-Masseeh (1991): $S = 0.53$.

inlet, where a spreading of the velocity profiles means that the steeper gradients and finer detail of the flow are not predicted accurately.

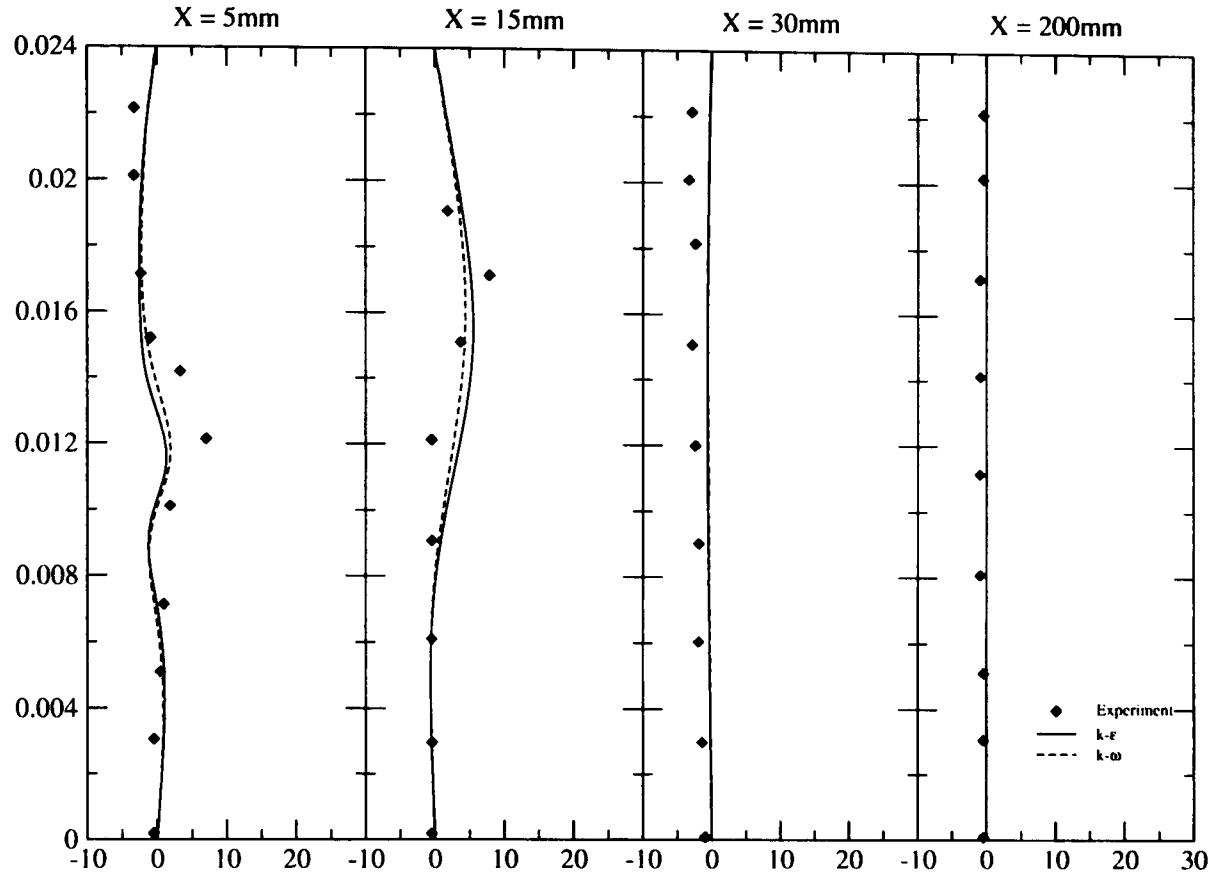

FIGURE 4.37: Radial velocity profiles for the case of Al-Masseeh (1991); $S = 0.53$.

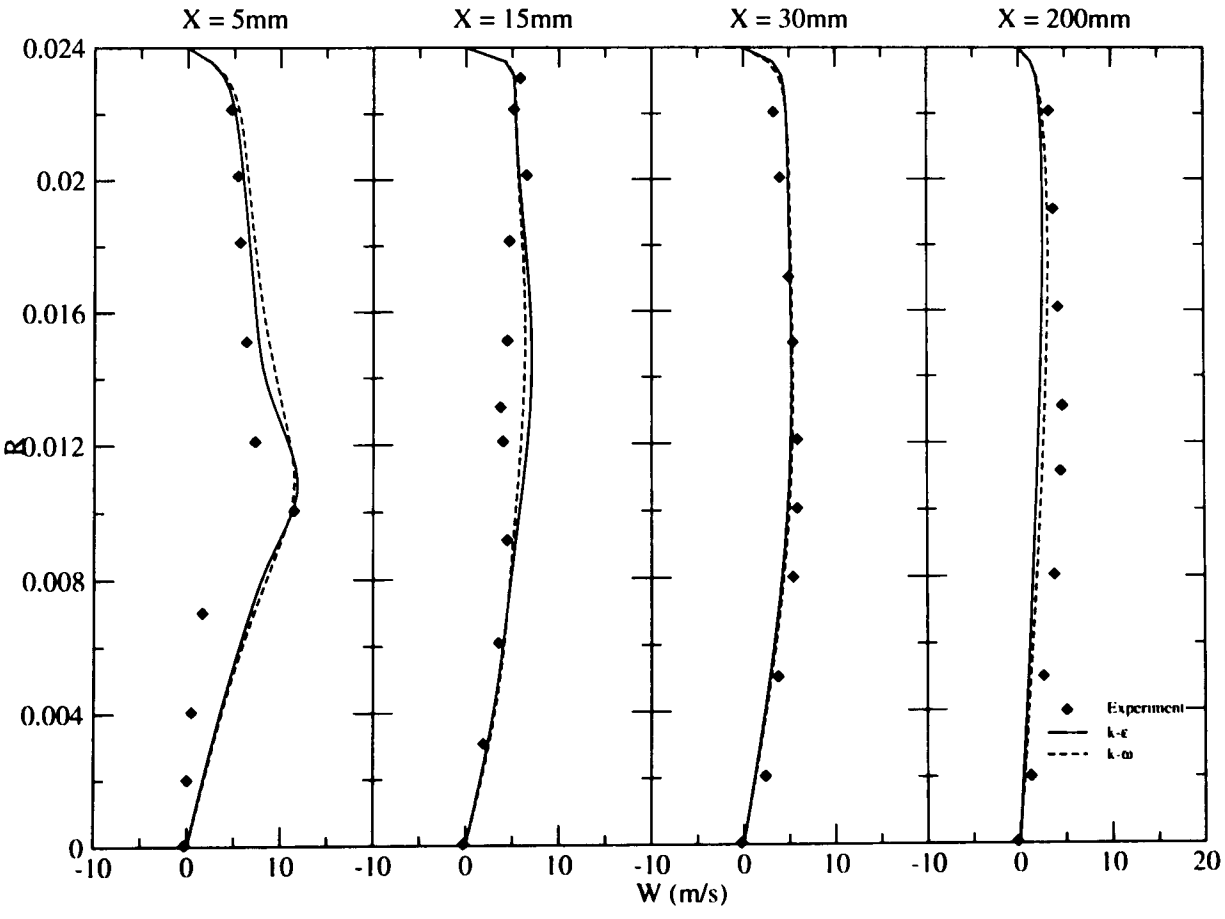

FIGURE 4.38: Tangential velocity profiles for the case of Al-Masseeh (1991); $S = 0.53$.

From figure 4.36 at $x = 200$mm, the flow is purely in the positive, downstream direction, showing that both two equation models predict a premature relaxation of the flow, with a smaller primary axial recirculation. This behaviour is also shown in the tangential velocity profiles. At $x = 30$ and $x = 200$mm both two equation models under-predict the size of the tangential velocity, where the profiles resemble more that of a solid body rotation (a linear profile from axis to wall).

Predictions for the turbulent kinetic energy are shown in figure 4.39. In the inlet region, the central peak is better predicted by the $k - \omega$ model where the profile returns more closely to the experimental results upon moving closer to the central axis. The $k - \epsilon$ model predicts a peak that is much too wide to agree with the experimental results, leading to an over-prediction at the central axis.

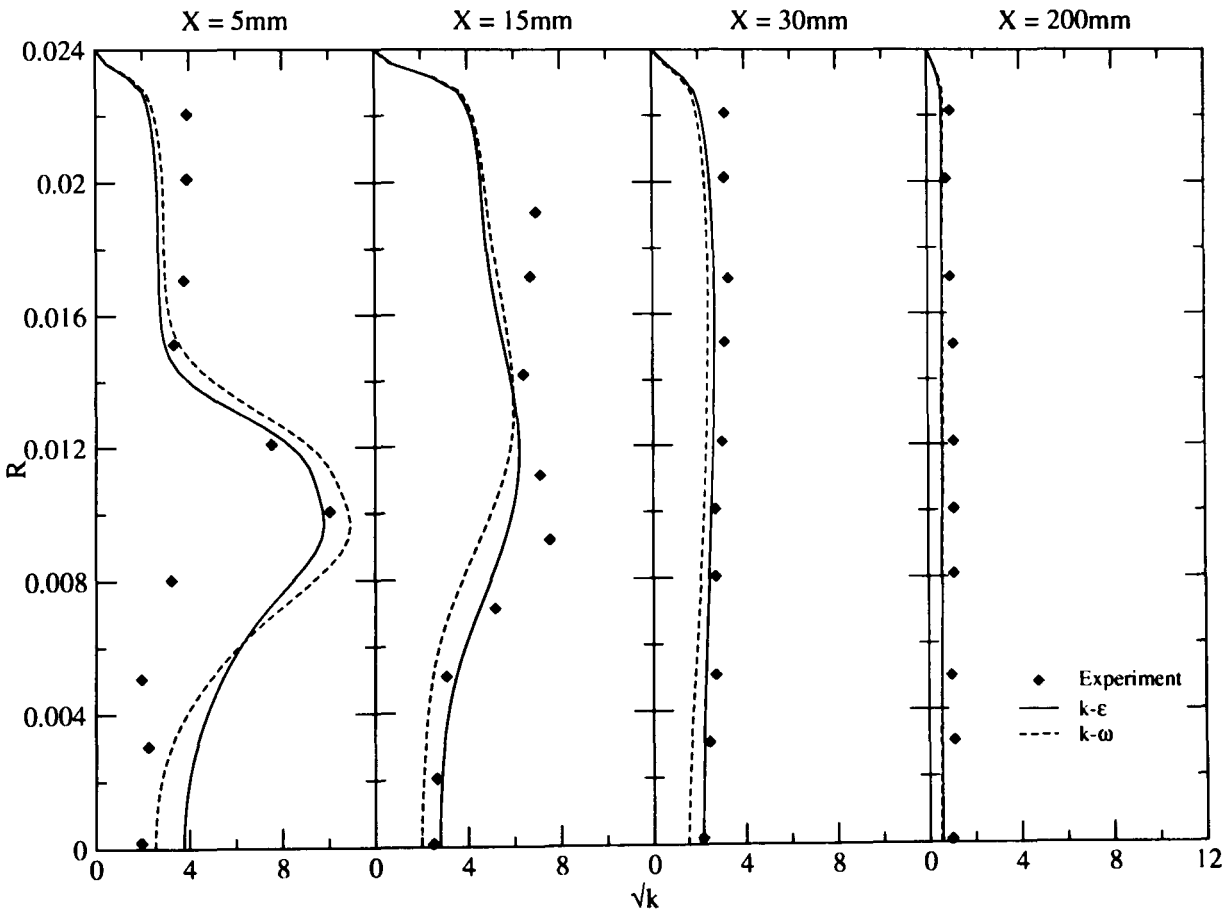

FIGURE 4.39: Turbulent kinetic energy profiles for the case of Al-Masseeh (1991); $S = 0.53$.

Further along the pipe axis, the $k - \epsilon$ model shows better agreement with experimental results than the $k - \omega$ model. At 15mm, $k - \epsilon$ behaves better at the central axis but both models under-predict the turbulent kinetic energy in the wall region. As the flow develops along the pipe the $k - \epsilon$ model matches the experimental data

more closely.

Overall, the two-equation models do not perform well when trying to capture the turbulent kinetic energy of the flow. This can be attributed in the main to the isotropic formulation of the model. No account is made for the differing values of the normal Reynolds stresses, especially in the steep gradient regions near the inlet. This means that their effect is not reintroduced into the momentum equations, which are unable to respond to differences in the Reynolds stresses.

Reynolds Stress Models

As mentioned in previous sections, the full second moment, or Reynolds stress, closure models include full transport equations for the individual stress components. This can overcome the deficiencies of isotropic two-equation models by modelling the individual stress components to the momentum equations, thus allowing for stress anisotropy. The modelling of the Reynolds shear stresses, as well as the normal stresses is also included to provide a closure that enables the incorporation of more turbulence physics of the flow.

The models tested here are the LRR, SSG and SSG-ADRM and their results shown in figures 4.41 to 4.47. An immediate improvement can be observed when compared to the predictions of the two equation models. For the mean velocity profiles in figures 4.41 to 4.43, it is clearly seen that the computations reproduce the steep gradients shown in the measured data. This is especially apparent at the inlet jet region for the mean axial and tangential velocities.

A more accurate prediction of the tangential velocity at the inlet, leads to a better prediction of the axial vortex due to the swirling inlet. As this quantity is reduced (in line with the experiments) when compared to two equation models, the speed of the axial vortex is reduced. This leads to a smaller negative axial pressure gradient and hence improves prediction of axial velocity at the chamber axis.

The Reynolds stress models also predict the axial recirculation length more accurately than the two equation models as shown in figure 4.40. At 200mm, the

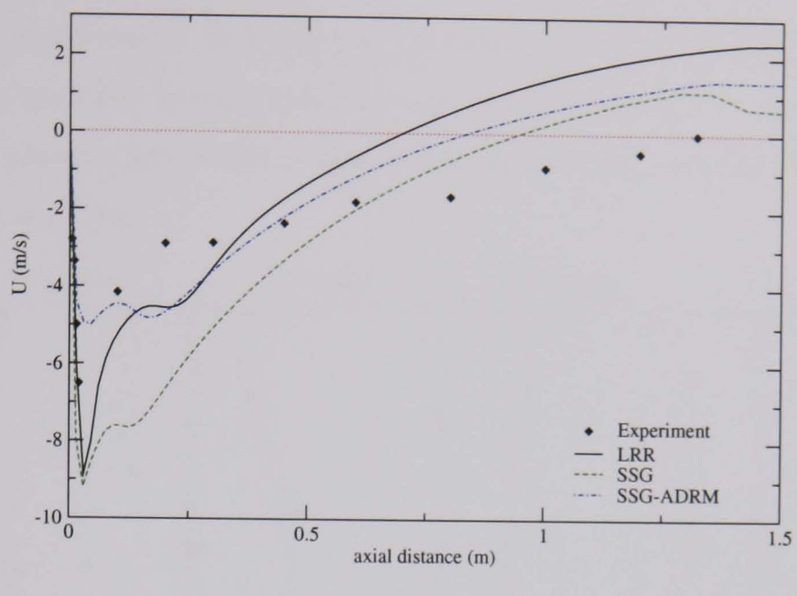

FIGURE 4.40: Axial velocity along the pipe axis; $S = 0.53$.

Reynolds stress models still predict a *negative* axial velocity in agreement with experiment. The two equation models, as mentioned previously, predict a positive sign here, indicating premature flow relaxation. This observation is again linked to the prediction of the tangential velocity. At the 200mm measurement location, the two equation models predict a linear profile from chamber axis to the wall. This indicates a solid body rotation of the fluid, in contrast to the measurements. The Reynolds stress models improve the prediction by delaying the transition to solid body rotation. Unfortunately, this effect is more pronounced, and although results agree more strongly with the measurements, this transition is retarded too much compared to the experiments.

This has a knock-on effect on the previously mentioned axial recirculation length. As the tangential velocity is slightly overestimated at the chamber axis, the negative axial velocity is slightly larger than the experiments show at the axis. However, as shown in figure 4.40, at around 250mm, the decay of the axial velocity is increased compared to the experimental data. This leads to premature flow reattachment, especially by the LRR model. The SSG-ADRM prediction shows an improvement with the SSG model providing the best prediction, albeit premature.

Prediction of the mean radial velocity also shows improvement over those of the two equation models. All of the Reynolds stress models used predict a positive radial velocity up to approximately one half of the chamber radius near the inlet,

in line with experiments. It is only in the outer region of the chamber that the sign becomes negative. Despite this more accurate prediction over the two equation models, the position and width of the central peak at the inlet still cannot match the experimental data.

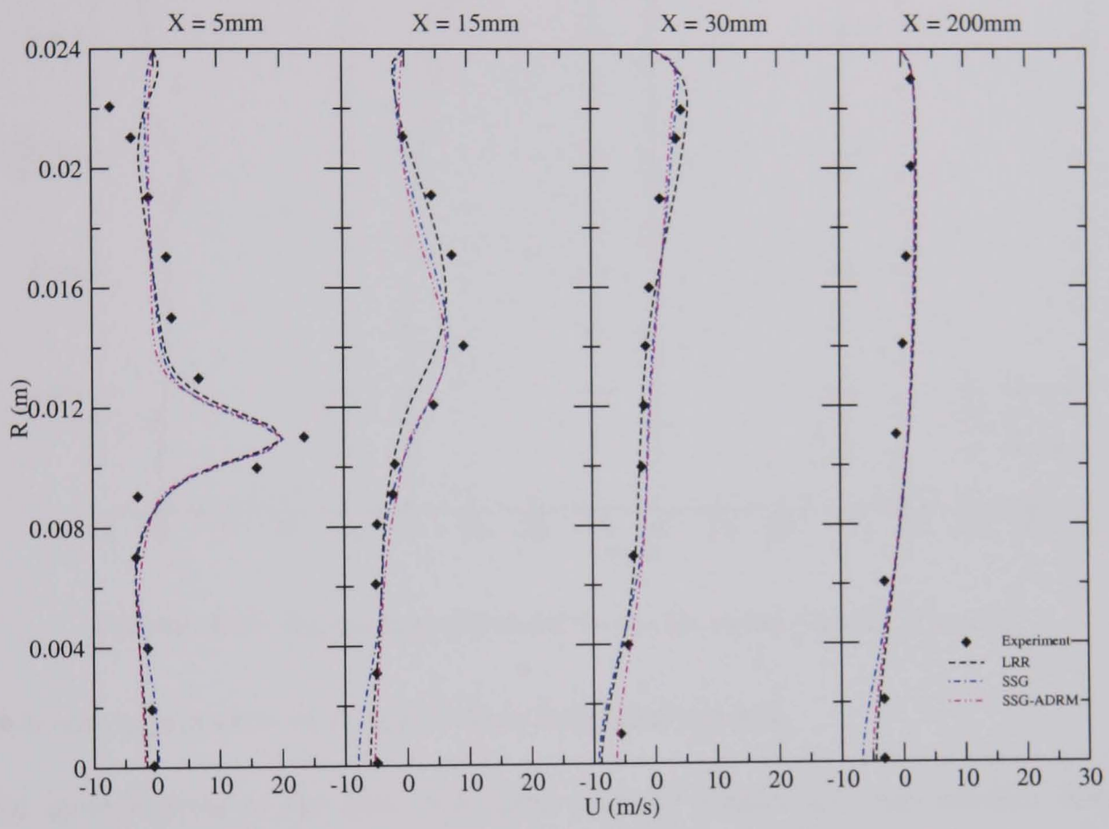

FIGURE 4.41: Reynolds stress model results for axial velocity; $S = 0.53$.

For the prediction of the turbulent kinetic energy shown in figure 4.44, the Reynolds stress models agree more closely with the experimental data, especially for the inlet region ($x = 5$mm). The peak in k at the inlet is more clearly defined returning to a flat profile at the chamber axis in agreement with measurements. Towards the wall region, however, the value of k is slightly under-predicted, showing similarity with the two equation models. As the flow develops down the chamber, the prediction continues to show discrepancies with experimental data in the wall region except at larger distances ($\geq$200mm).

As expected, the above results show that the Reynolds stress models generally give more accurate prediction compared to the two equation models. As mentioned previously three Reynolds stress closures were used: LRR, SSG and SSG-ADRM.

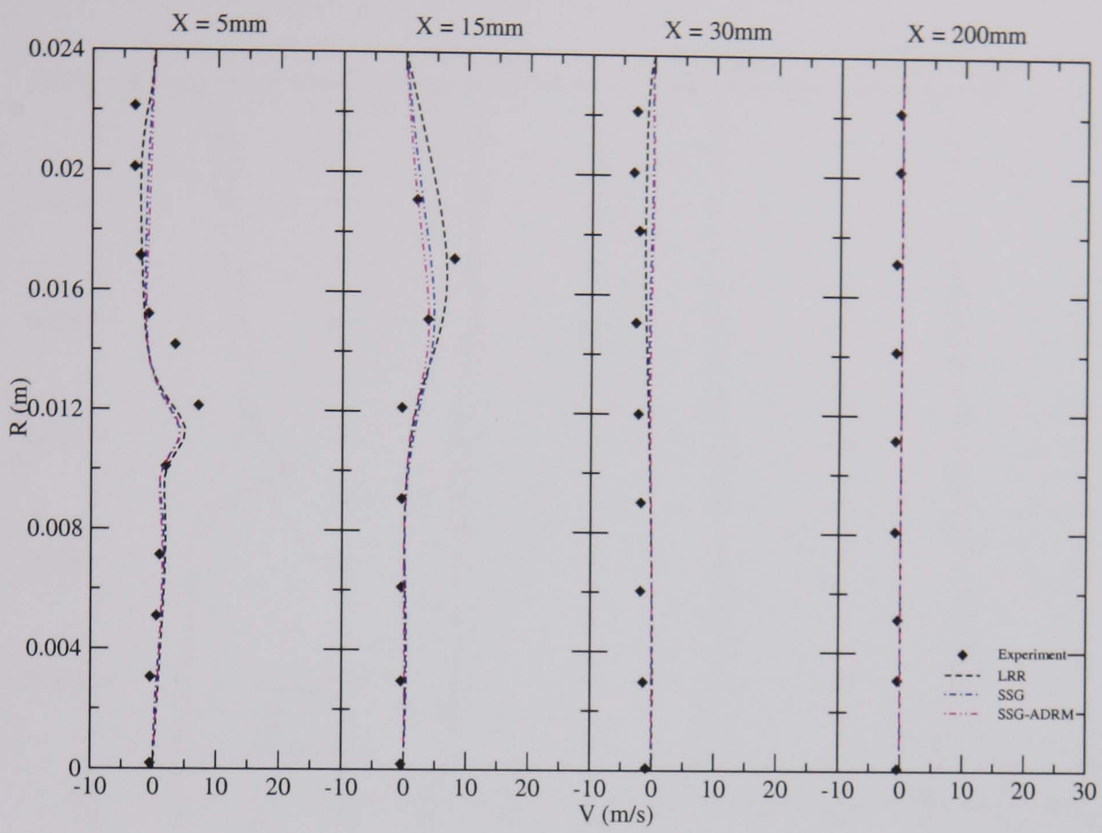

FIGURE 4.42: Reynolds stress model results for radial velocity; $S = 0.53$.

It is now appropriate to compare these individual models.

For most regions of the flow, the mean velocity profiles are very similar, but a few regions require attention. Firstly at the inlet, the axial velocity predictions near the wall are slightly different for the SSG and LRR models. The LRR model predicts a positive velocity at the wall quickly changing sign at a radial position of 22mm, indicating the presence of an additional axial recirculation compared to that predicted by the SSG model. Indeed, figure 4.26 illustrates this.

The SSG model produces a negative axial velocity in this region only returning to a positive sign at a radial position of around 17mm, indicating a larger axial recirculation (namely the primary corner recirculation). The real physical flow is unknown due to the lack of experimental data in this region. However, close to the wall, the measurements predict a larger negative value than those given by the computations. The difference between the LRR and SSG models in this area is the modelling of the wall echo effect in the pressure-strain correlation. The LRR model has a dedicated term to account for the proximity of a wall and the effect of eddy

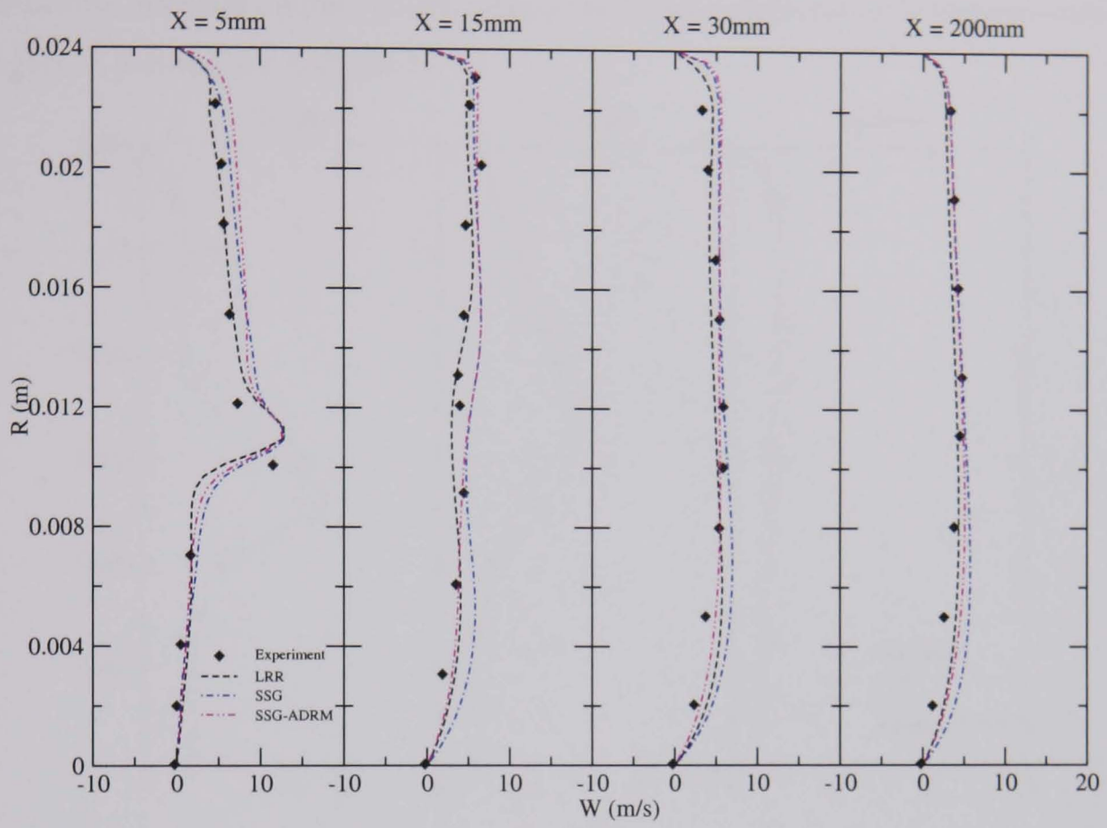

FIGURE 4.43: Reynolds stress model results for tangential velocity; $S = 0.53$.

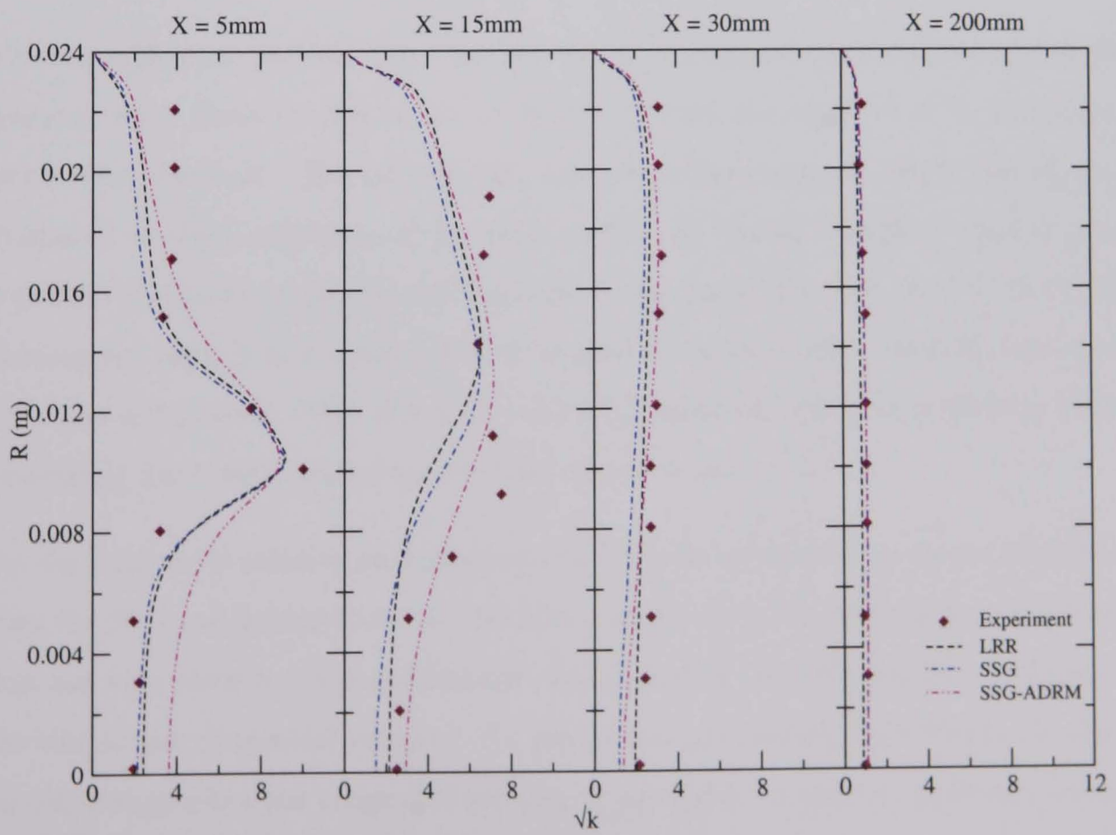

FIGURE 4.44: Reynolds stress model results for turbulent kinetic energy; $S = 0.53$.

squashing, whereas the SSG model relies on the nonlinear terms in its pressure-strain model to account for wall effects.

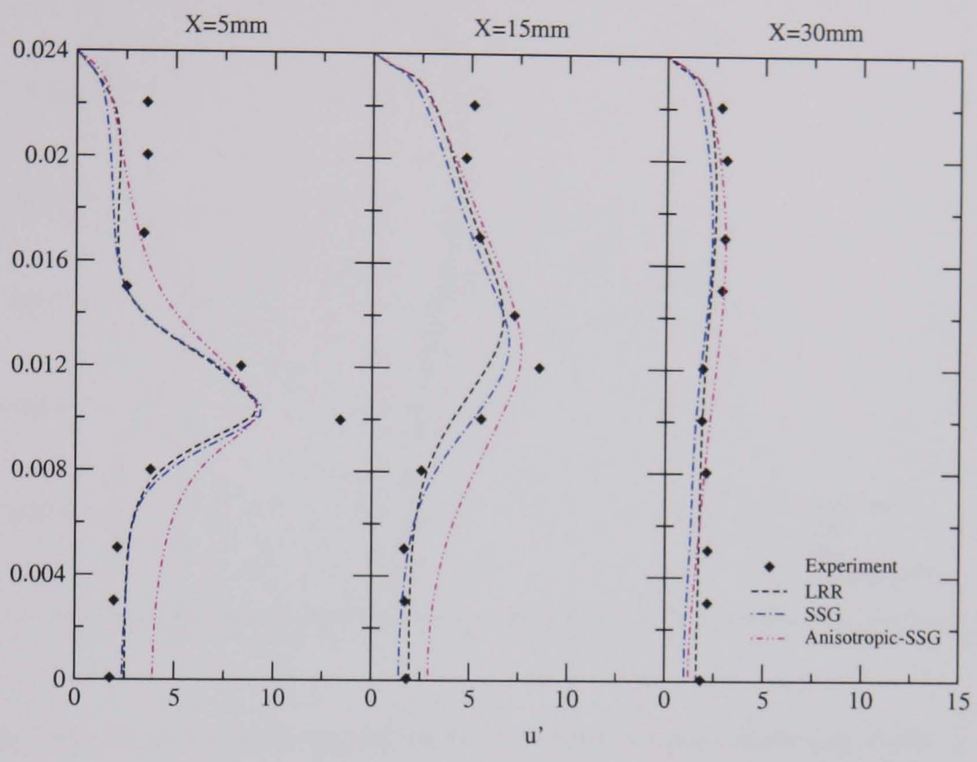

FIGURE 4.45: Reynolds stress model results for axial normal stress component; $S = 0.53$.

Another difference between the models is the prediction of the axial velocity at the chamber axis. Both models consistently over-predict the negative U in this region as the flow develops. The SSG model, however, shows a much larger discrepancy compared to the predictions of the LRR model. At 15mm, the axial velocity peak is pushed further towards the wall than the prediction of the SSG model. Both predictions are slightly inaccurate when compared to measurement, and only represent a portion of the peak. This shows that the LRR model is more sensitive here to the centrifugal force experienced by the fluid due to swirl.

For the tangential velocity prediction the LRR model gives more accurate prediction than the SSG implementation. At the inlet region, the LRR model gives predictions that are very close to the experimental data, whereas the SSG model over-predicts the size of the tangential velocity. As mentioned previously, both Reynolds stress models over-predict the tangential velocity at the chamber axis as the flow develops, having the effect of delaying the transition to solid body motion. The SSG model overestimates this value when compared to experiments, and to the predictions of

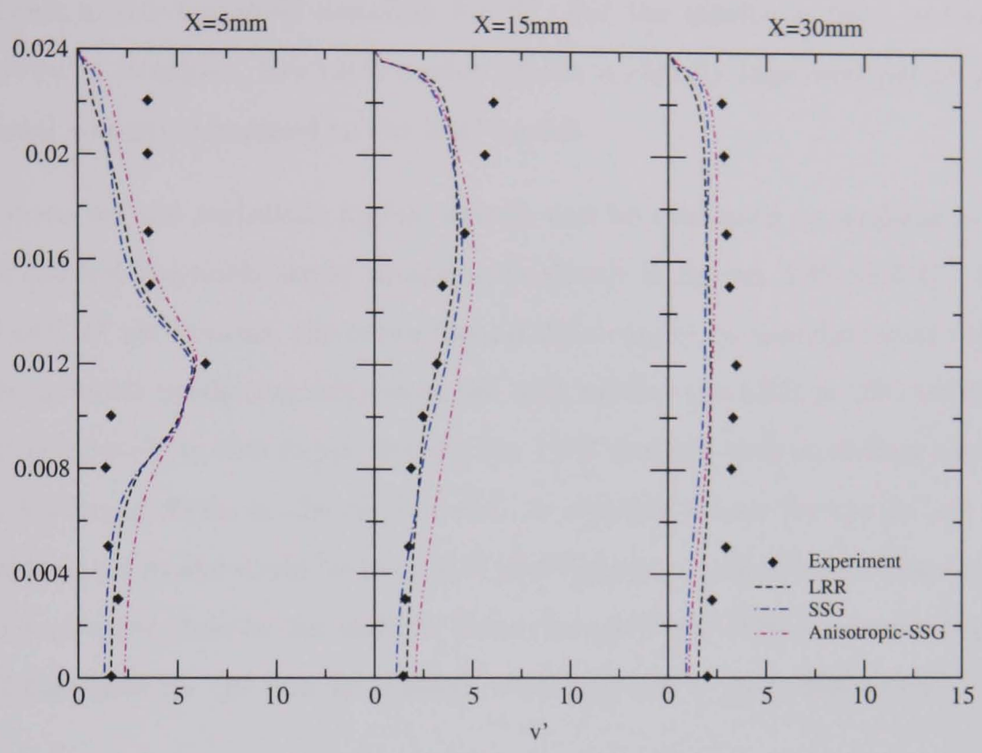

FIGURE 4.46: Reynolds stress model results for radial normal stress component; $S = 0.53$.

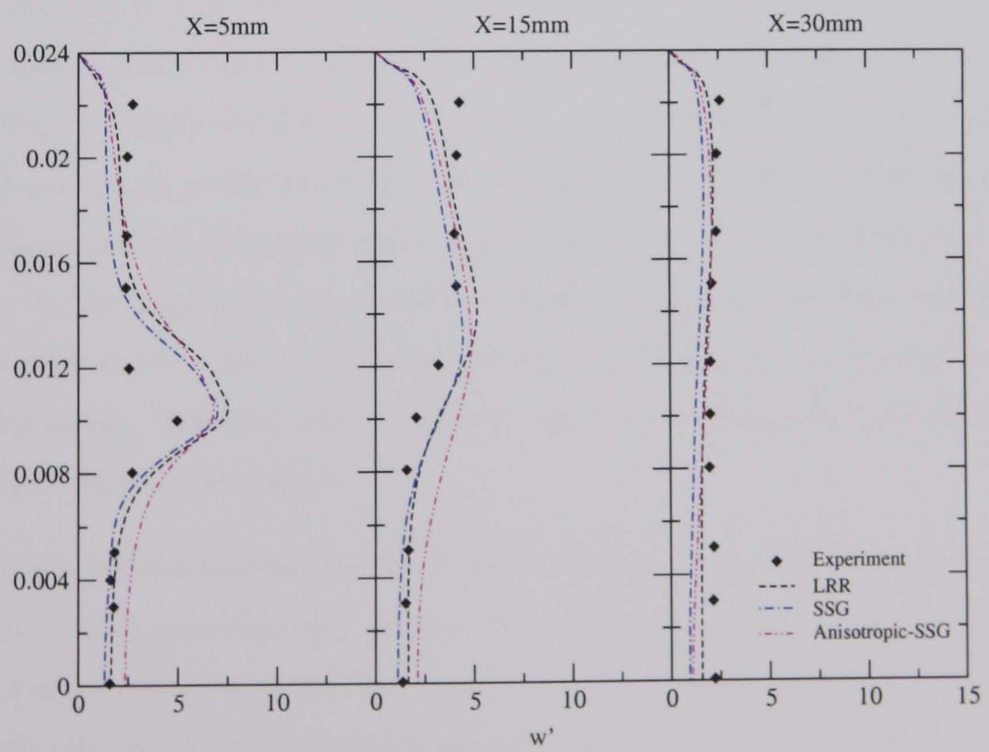

FIGURE 4.47: Reynolds stress model results for tangential normal stress component; $S = 0.53$.

the LRR model due to the smaller value of the $\overline{vw}$ and $\overline{w^2}$ stresses which act as sink terms in the transport equation for W. For the results at most of the axial measurement locations, the LRR model affords a slightly improved prediction for tangential velocity compared to the SSG model.

Predictions for the turbulent kinetic energy can be evaluated by looking at those for the normal Reynolds stress components shown in figures 4.45 to 4.47. For all $\overline{u}^2$, $\overline{v}^2$ and $\overline{w}^2$ predictions, the experimental data cannot be matched near the wall. Despite accurate prediction away from the wall, neither the LRR or SSG models can predict accurately in this region despite the LRR model's wall modelling approach, or the nonlinear terms in the SSG model. A possible reason for the failure of the Reynolds stress model could be the use of wall functions, where an assumed variable profile is adopted close to the surface. Even though Kitoh (1991) advocated the use of wall functions for the flow he studied, they may not be appropriate here.

For the SSG model, normal stress predictions are of the same accuracy as those for the LRR model near the chamber axis at the x=5mm and 15mm axial locations. As the flow develops, at x=30mm, the SSG prediction begins to underestimate the measured data to a greater extent than the LRR model. In the inlet region, the peak in the axial normal stress is under-predicted by both SSG and LRR, with the latter predicting a slightly smaller value. For the radial normal stress component, both models accurately predict the magnitude of the inlet peak. The width of this peak is overestimated by both models, showing an inability to resolve the sharp inlet peak. Again, for the tangential normal stress component, both models show inaccuracies at the inlet region. The peak in tangential normal stress is over-predicted, along with its width. The SSG model, however, gives results that are less exaggerated than those of the LRR model.

The reason for the inaccuracies of the predictions for normal stresses at the inlet are due to their specification. Only an inlet condition for k is given, and not the individual components themselves. As $k = 1/2[\overline{u^2} + \overline{v^2} + \overline{w^2}]$, it is assumed that the normal components are isotropic at the inlet. Further downstream at x = 30mm, the effect of the inlet is less pronounced, and the computed results are in better agreement with measurement. It can also be noticed that the flow becomes more

isotropic downstream. This is due to the reduction in production of turbulence as mean straining itself is reduced.

Effects of the anisotropic dissipation rate model

The effect of including anisotropic dissipation on the mean flow and normal stress components can be seen in figures 4.41 to 4.47. For the mean axial velocity profiles, this model improves the SSG predictions at the chamber axis, bringing better agreement with experiment and giving superior prediction compared to those from the LRR model for $x \leq 30$mm. This is due to the reduction of tangential velocity at the axis and a consequent reduction in the reverse pressure gradient brought about by the swirl. The axisymmetric source term for the mean tangential velocity equation, $-\overline{vw}/r$, helps to contribute to the reduction in tangential velocity at the axis. Figure 4.48 shows that this shear stress component is increased over isotropic methods. Also the increased prediction of the $\overline{w^2}$ stress (as shown in figure 4.47) acts to reduce the diffusion term in the transport equation for W.

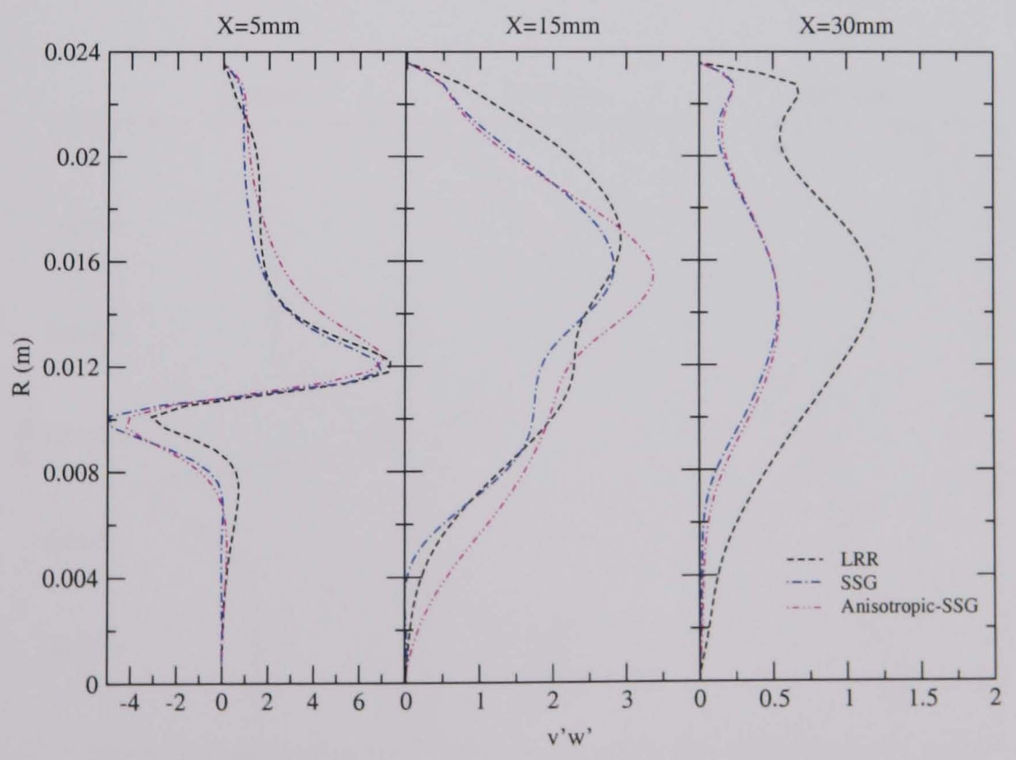

FIGURE 4.48: Reynolds stress model results for $\overline{vw}$ shear stress component; $S = 0.53$.

In the wall region, the predictions for U closely match those of the original SSG

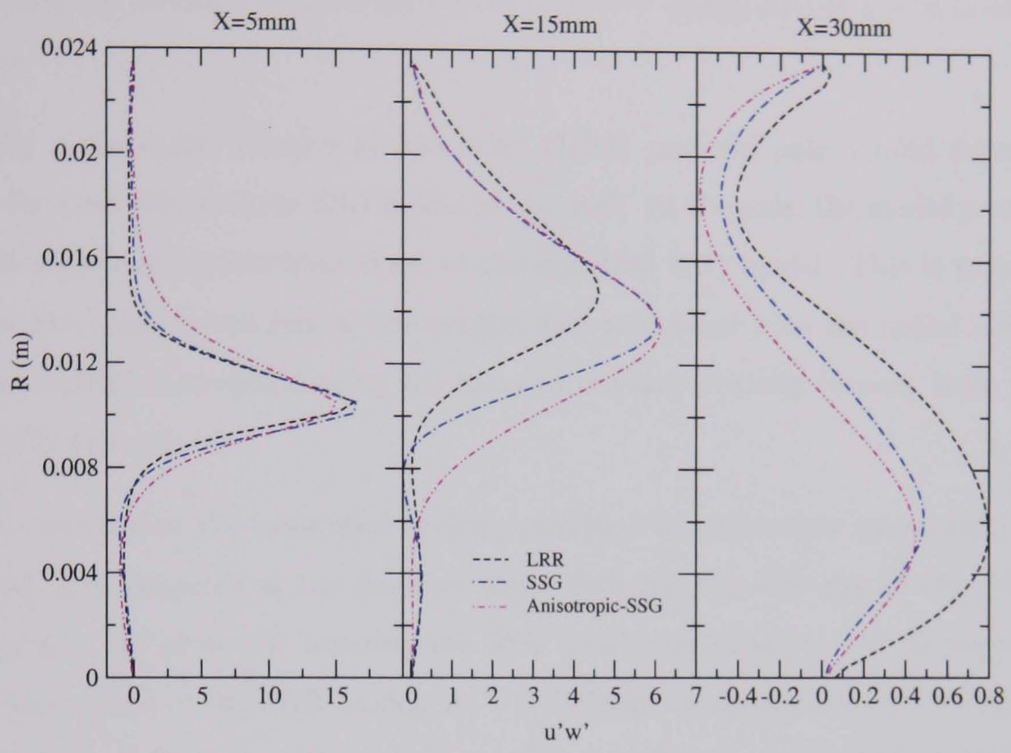

FIGURE 4.49: Reynolds stress model results for $\overline{uw}$ shear stress component; $S = 0.53$.

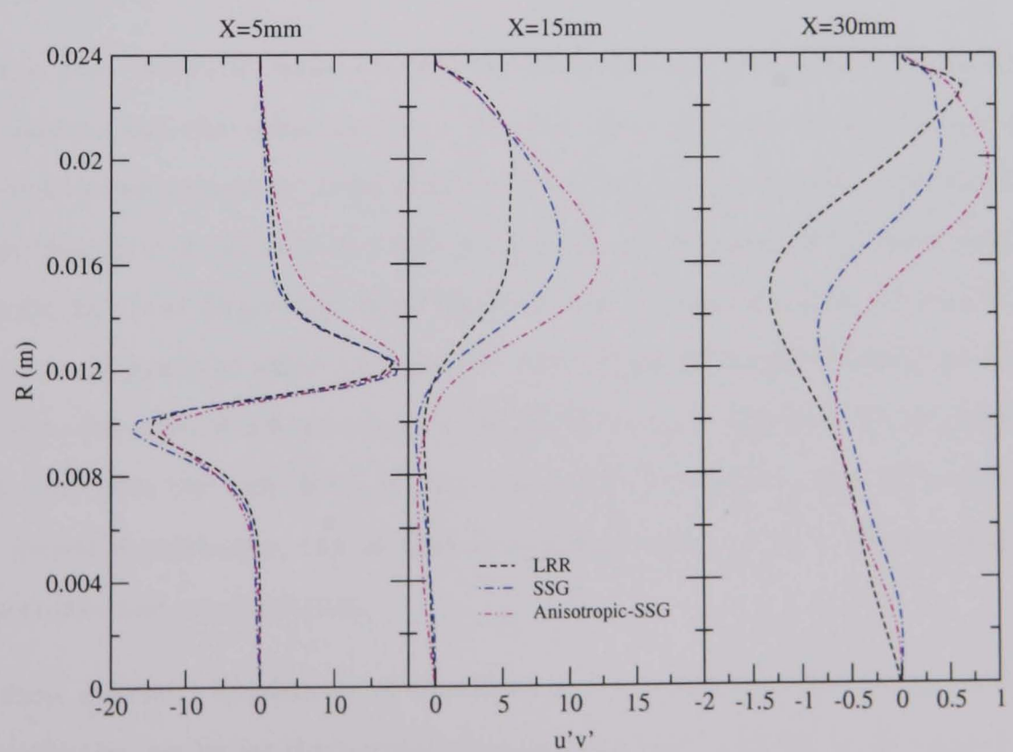

FIGURE 4.50: Reynolds stress model results for $\overline{uv}$ shear stress component; $S = 0.53$.

model with a small reduction in the size of the axial velocity predicted. This indicates that the strength of the corner recirculation is diminished at $x = 5, 15$mm, as shown.

For the mean radial velocity profiles, the ADRM provides only a mild departure from the predictions of the SSG model at the wall. At the axis, the model produces results indistinguishable from those of the standard SSG model. This is primarily due to the small strain rate at the central axis associated with the radial velocity. As the ADRM is modelled using the mean strain and vorticity tensors, little effect is seen in this region.

When considering the tangential velocity profiles, the anisotropic model offers significant improvements at the chamber axis. Reductions in the size of the velocity at the axis are achieved, bringing the SSG prediction closer to the measured results than those of the LRR model. At $x = 200$mm, the prediction still retards the transition to solid body rotation, but supplies a prediction comparable to the LRR model but improved over that made by the SSG model. This behaviour is observed in Kitoh's case due to the increased value of the predicted $\overline{vw}$ shear stress in this region, acting as a sink term in the W momentum equation.

For the area close the wall, the ADRM overestimates the velocity compared to experiments and the other models. At $x = 5$mm, this is due to the additional $\overline{vw}$ shear stress caused by redistribution from the normal stresses. As mentioned above, this shear stress acts as a sink term in the mean tangential velocity equation. However, as r is at its greatest value this sink term is reduced and so the contribution due to stress gradient takes precedence. The increased negative radial gradient of $\overline{vw}$ due to the ADRM acts as a positive source term in the equation for W, leading to its increase near the wall. Even though this gradient reduces to that of the standard SSG model downstream, the increased upstream value of W is then transported downstream due to convection.

The most dramatic illustration of the effect of the anisotropic dissipation model can be seen in the results for the normal stresses. The results for the axial normal stress in figure 4.45 show that the anisotropic profile near the inlet ($x = 5$mm) shows less

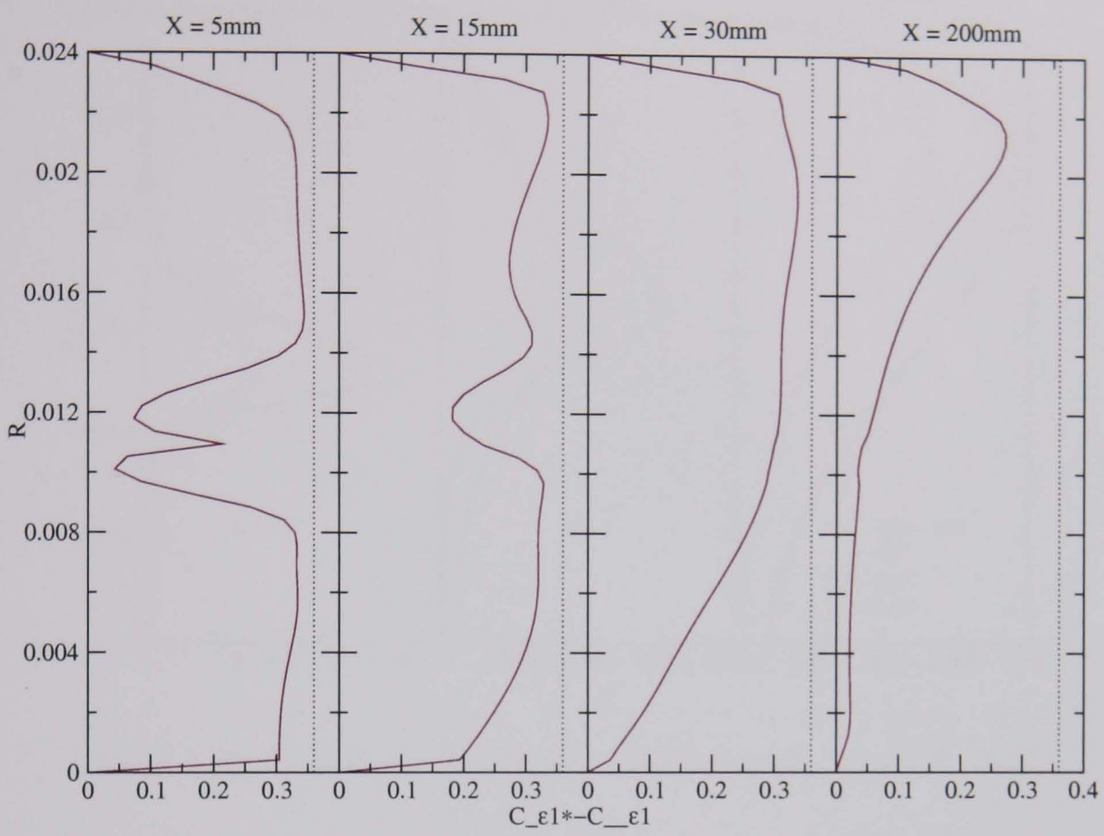

FIGURE 4.51: Value of $C^*_{\epsilon 1} - C_{\epsilon 1}$ for the production of dissipation of k; $S = 0.53$.

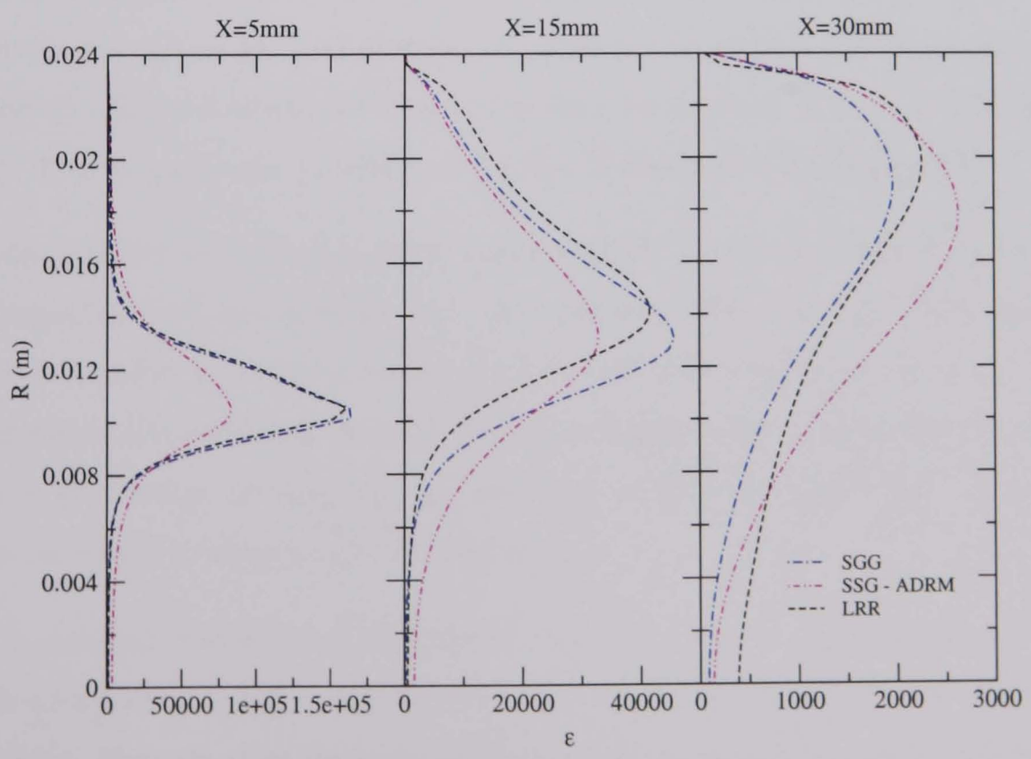

FIGURE 4.52: Dissipation rate of turbulent kinetic energy, ϵ for different Reynolds stress models; $S = 0.53$.

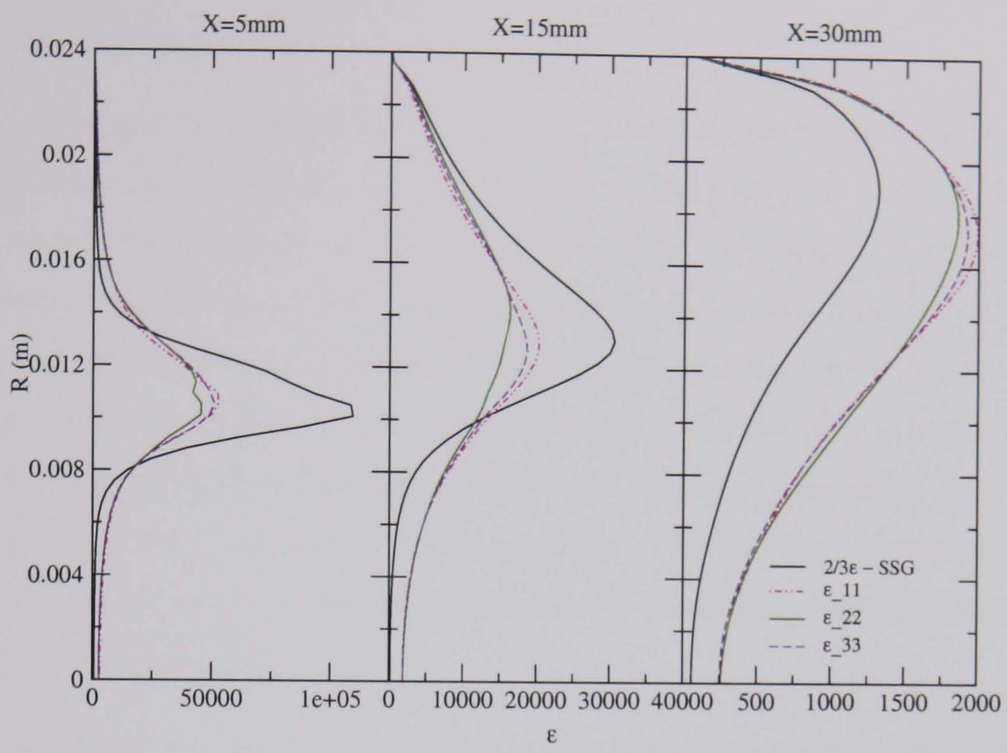

FIGURE 4.53: Diagonal components of the dissipation rate tensor; $S = 0.53$.

resolution than both other models by a broadening of the central peak. The value towards the chamber axis is also overestimated compared to the measured data and other model predictions. This behaviour is repeated further downstream albeit to a lesser degree. The other normal stress components, $\overline{v^2}$ and $\overline{w^2}$, also show this same behaviour (figures 4.46 and 4.47) as well as the shear stresses (figures 4.48, 4.49 and 4.50). This is due to the modified production of dissipation coefficient, $C^*_{\epsilon 1}$.

The contribution of the new model in equation (2.82) to the coefficient of production of dissipation is shown in figure 4.51. The standard SSG model sets this value as $C^*_{\epsilon 1} = 1.44$ and so when 1.0 (the value of $C_{\epsilon 1}$ in table 2.5) is added to the contribution in the figure, the coefficient does not achieve as high a value. This leads to an initial drop in production of dissipation at the inlet, causing the high values of normal stress, and thus k, to be predicted upstream.

If it is assumed that η and ξ in equation (2.82) are zero (i.e. the absence of mean strain and vorticity) $C^*_{\epsilon 1} - C_{\epsilon 1} \approx 0.36$. The dotted line in figure 4.51 represents this value. Near the inlet, only the region around the jet has appreciable straining, reflected in the reduction of $C^*_{\epsilon 1} - C_{\epsilon 1}$. The peak in the centre of the reduction is caused by the low straining in the core of the jet. Here, only flow deceleration occurs

in the axial direction.

In the wall region, the value of $C_{\epsilon 1}^* - C_{\epsilon 1}$ goes to zero as the strain of the flow increases due to shear. At the central axis, the most important strain rate is that associated with the tangential velocity, as this velocity component must return to zero as radius decreases. Figures 4.41 and 4.42 show that the contribution from U and, to a greater extent, V are much smaller. In the upstream region, near the inlet, $C_{\epsilon 1}^* - C_{\epsilon 1}$ takes a large value due to the absence of large velocity gradients. Downstream, where the transition to solid body rotation occurs, the dominant component in ξ and η becomes the radial tangential velocity gradient. This has the effect of reducing $C_{\epsilon 1}^* - C_{\epsilon 1}$ at the axis, thus reducing production of dissipation, leading to increased normal stress production.

Figure 4.54 shows a shaded plot of $C_{\epsilon 1}^* - C_{\epsilon 1}$ with overlaid momentum vector arrows. It can be seen that the lowest values of $C_{\epsilon 1}^* - C_{\epsilon 1}$ are present where the gradient of the momentum is largest. As alluded to above, these are at the sides of the inlet jet and the central axis as the flow develops into solid body rotation.

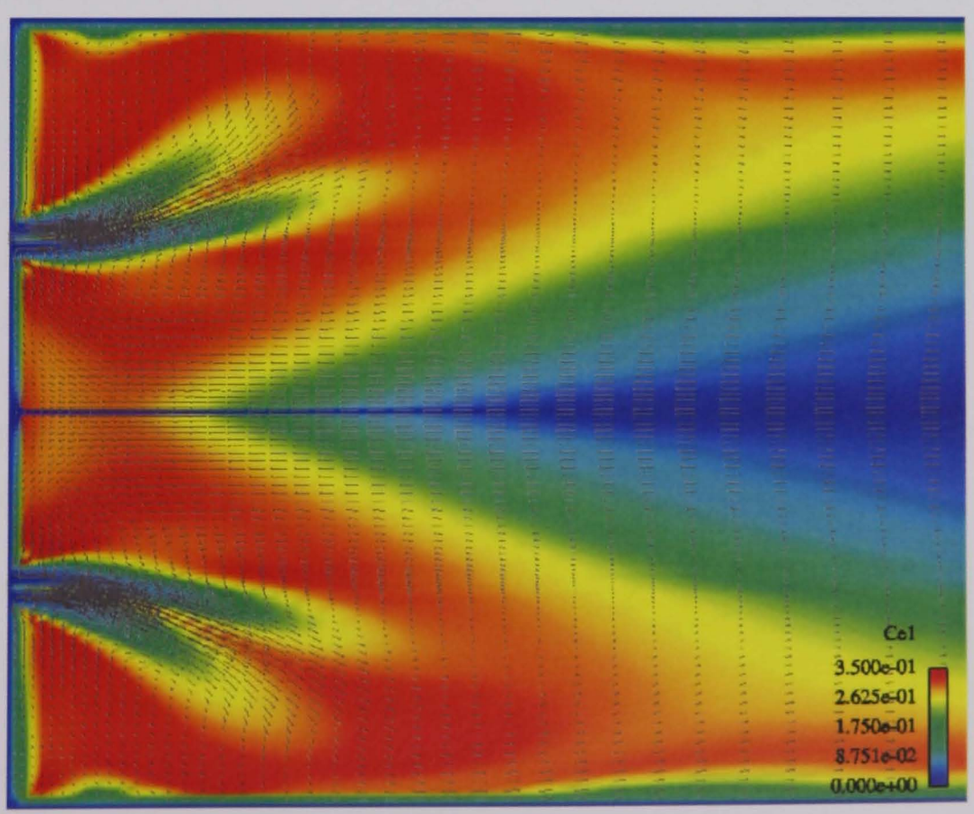

FIGURE 4.54: Plot of the velocity vectors with domain shaded as $C_{\epsilon 1}^* - C_{\epsilon 1}$; $S = 0.53$.

The effect of $C^*_{\epsilon 1}$ on the dissipation is seen in figures 4.52 to 4.58. The isotropic part of the dissipation tensor is shown in figure 4.52. At the inlet, the peaks of the dissipation predicted by the SSG-ADRM are much smaller than those using the standard SSG model. The reason for this lies in the production of dissipation in this region. The value of $C^*_{\epsilon 1}$ is lower than that of the isotropic model, thus reducing the production of dissipation.

Despite the reduced production of dissipation in this region, the value of k, and hence the normal stress components, remain unchanged. The specified inlet value of k does not decay, due to the high convection of the inlet jet.

The reduction in dissipation is also observed in figure 4.53 for the diagonal component of ϵ_{ij} directly responsible for the dissipation of the normal stresses. In the jet region, again, the diagonal components of dissipation are reduced compared to the equivalent isotropic SSG model predictions. However, adjacent to the main central peak, the SSG-ADRM predicts larger values of dissipation than the isotropic model. Here, the value of $C^*_{\epsilon 1}$ reduces greatly due to mean shear. This promotes production of turbulent kinetic energy from which increased dissipation arises, due to the dependence of production of ϵ on that of k.

Further downstream (x = 15mm), dissipation remains reduced compared to the isotropic models due to convection, but has increased relative to them because of the reduction in $C^*_{\epsilon 1} - C_{\epsilon 1}$. At x = 30mm, the dissipation predicted by the SSG-ADRM has increased beyond the values predicted by the isotropic models. In a similar way for the predictions for Kitoh's case, $C^*_{\epsilon 1} - C_{\epsilon 1}$ decreases from the wall towards the central axis due to the rotation of the fluid about the axis. This increases turbulent production, in turn increasing production of dissipation.

The redistribution of dissipation is shown in figure 4.55. This component is directly proportional to the value of the dissipation anisotropy, d_{ij}. Upstream, the dominant component of the mean strain and vorticity tensors is the radial gradient of mean axial velocity on which d_{ij} depends. Below the inlet jet this gradient is positive giving a negative value of d_{12}, and vice versa above the jet leading to the largest off diagonal component of ϵ_{ij}. The same effect is seen for the ϵ_{23} component, dependent

on radial gradient of tangential velocity. The ϵ_{13} component has little effect except at the inlet jet, where the axial deceleration of the tangential velocity has greatest effect on d_{13}.

The diagonal components of ϵ_{ij} shown in figures 4.56 to 4.58 show that the isotropic dissipation remains dominant. The small effects of the irrotational strains (flow acceleration or deceleration) cause the departure from isotropy. This is observed mainly at the peak positions of the respective velocities. For ϵ_{11} the axial deceleration causes an additional dissipation. The converse happens for ϵ_{22} where acceleration decreases the dissipation. For ϵ_{22}, there is no tangential gradient of tangential velocity due to the axisymmetric specification. The very small dissipation anisotropy in this case is due to nonlinear terms in d_{33} comprised of ξ, η and other combinations of mean strain and vorticity. These terms, however, have only a small effect for this dissipation component.

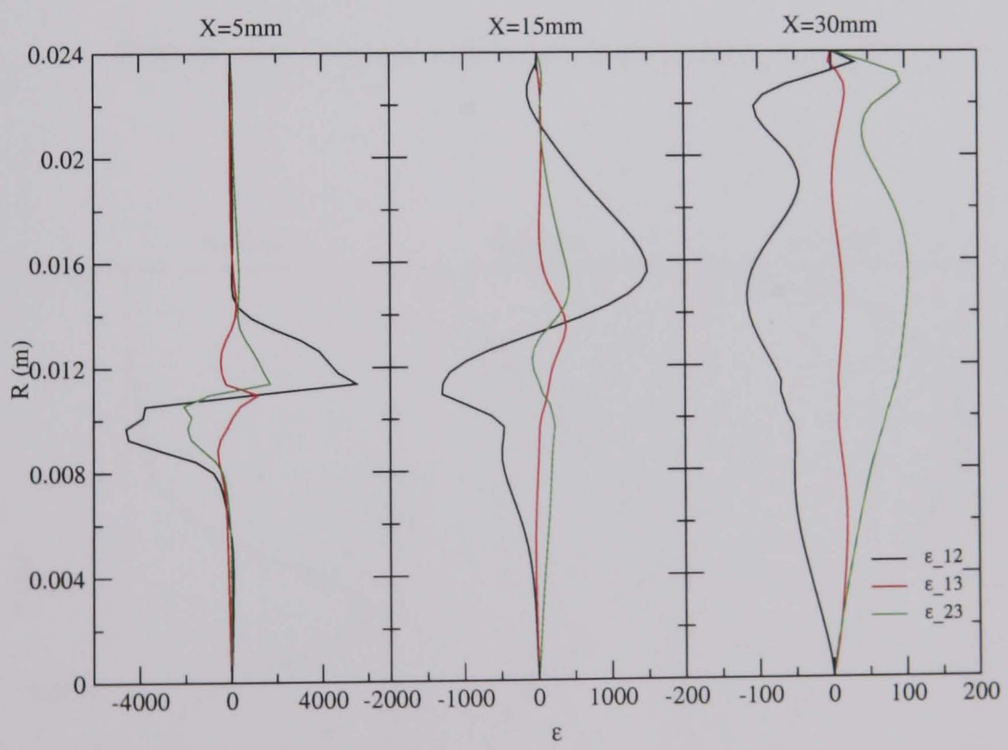

FIGURE 4.55: Off-diagonal components of the dissipation rate tensor; $S = 0.53$.

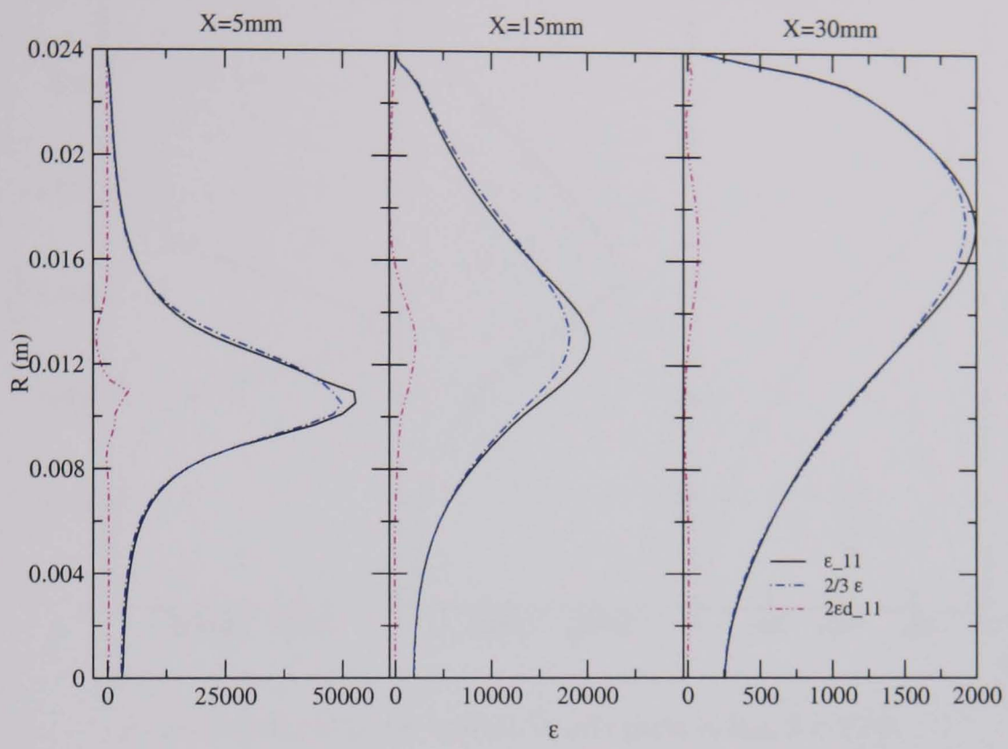

FIGURE 4.56: Isotropic and deviatoric parts of ϵ_{11}; $S = 0.53$.

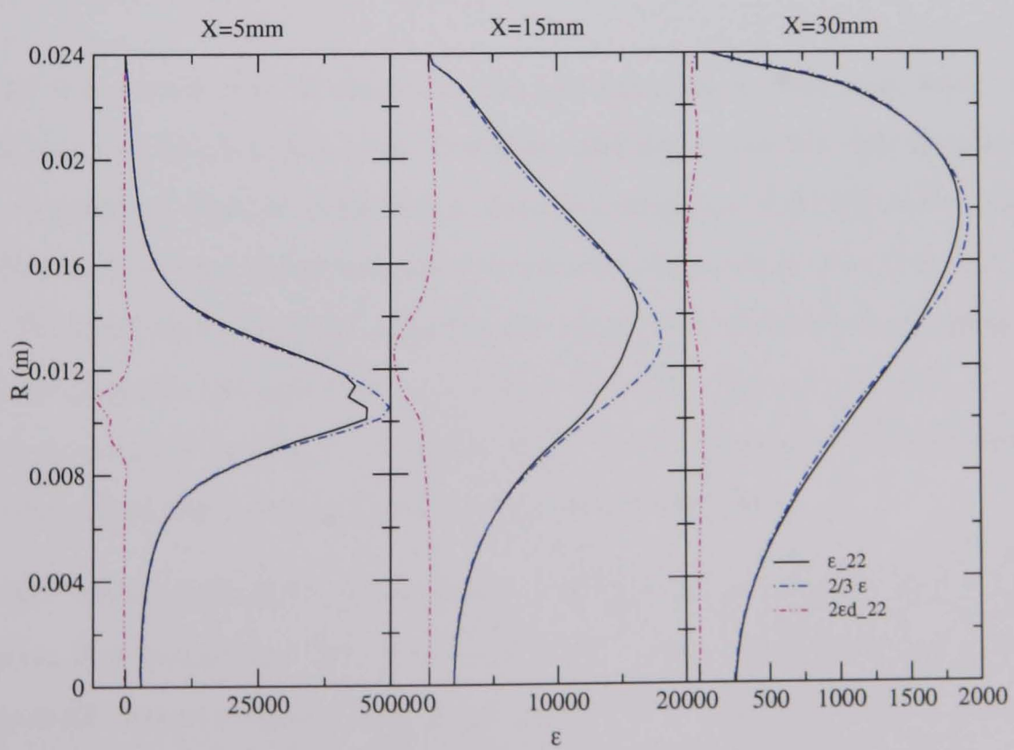

FIGURE 4.57: Isotropic and deviatoric parts of ϵ_{22}; $S = 0.53$.

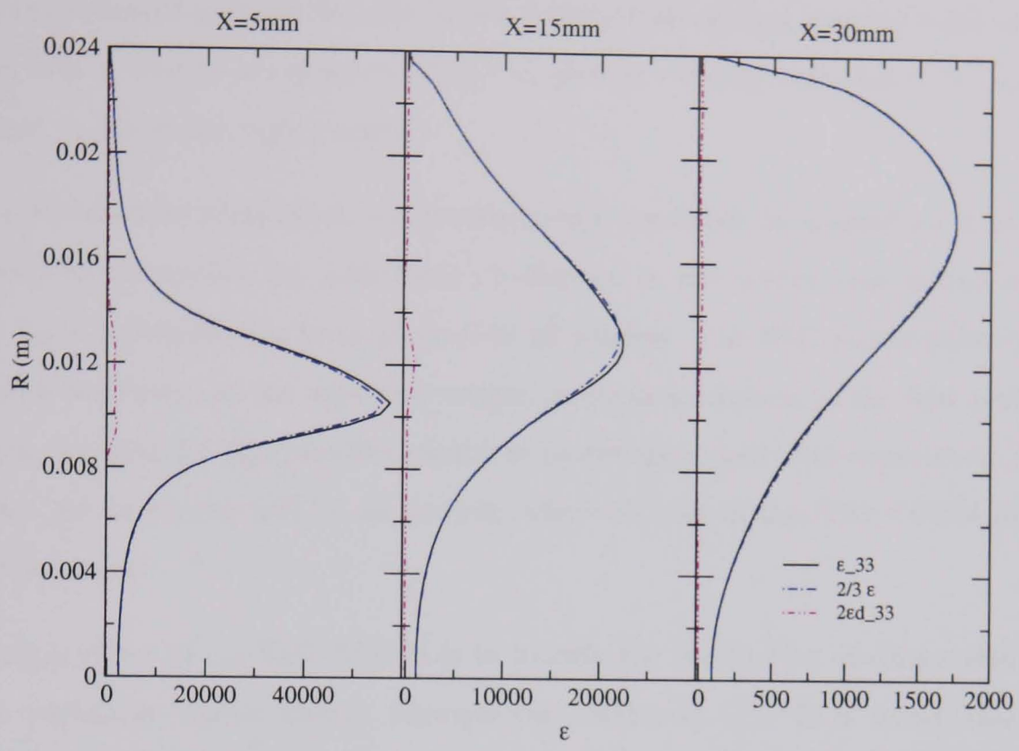

FIGURE 4.58: Isotropic and deviatoric parts of ϵ_{33}; $S = 0.53$.

4.4 Summary of main results

4.4.1 Swirling flow in a cylinder

For the free vortex flow in this case, the two equation models were found to be inadequate for predicting the mean flow quantities due to the isotropic nature of the eddy viscosities. Predictions consist of data characteristic of forced vortex motion. The Reynolds stress models provide a more accurate method of prediction of this flow. The LRR model predicts mean flow quantities that show reasonable agreement with experiment in the upstream region of the flow. Downstream, however, the swirl decays too rapidly, leading to erroneous prediction of mean axial velocity and flow reattachment at the central axis, in contrast to experiment.

The SSG model provides better agreement with experiment than the LRR model for the mean flow quantities. The reverse axial flow at the vortex core is preserved due to the small over-prediction of tangential velocity. This a due to the under-prediction of the $\overline{vw}$ shear stress that acts as a sink in the equation for W. The SSG-ADRM model shows similar results to that of the SSG model. The axial velocity shows a

flow reattachment point at the axis, albeit further downstream than the LRR model. Again this is due to a reduction of the tangential velocity, stimulated by a small increase in $\overline{vw}$ at the vortex core.

The normal stress component are generally over-predicted by a small amount, and an inability to resolve the additional production in the vortex core is due to the high stress redistribution term present in all models. The SSG model shows more accurate prediction in the upstream region, while downstream, as the flow partially relaxes, the SSG-ADRM provides results in better agreement with experiment.Shear stresses are predicted well by all models, where the use of the SSG-ADRM affords more accuracy.

The main effect of the SSG-ADRM is to modify the production of dissipation, and hence turbulent kinetic energy, through the coefficient $C^*_{\epsilon 1}$. It is shown that this coefficient is always lower than that used in isotropic dissipation models. This has the effect of increasing production of k when $C^*_{\epsilon 1}$ is reduced in areas of high shear, which leads to increasing dissipation. As the flow relaxes downstream, this effect is reduced.

4.4.2 Combustion chamber flow

Again the predictive capabilities of the two equation models are inferior to those of the Reynolds stress models. The mean flow quantities are predicted well for the LRR, SSG and SSG-ADRM models. The increased reverse axial velocity at the central axis, as in Kitoh's case, is caused by an over-prediction of the tangential velocity. Again the under prediction in the $\overline{vw}$ stress in this region, is responsible. Axial recirculation lengths are underestimated compared to experiment. The SSG model provides the closest prediction to the measurements, with the LRR model showing the largest decay of the swirl.

Normal stresses are predicted well for all models. The only discrepancies are due to the inlet specification of k, instead of the individual stress components, and the use of wall functions leading to under-predicted values near the wall. Downstream, as the flow relaxes, the SSG-ADRM model preserves the turbulence better than the

other models, in agreement with experiment. No comparison to experiment can be made for the shear stresses. However, computations show that the LRR model produces larger values of these stresses downstream.

Again the SSG-ADRM model contribution comes from the evaluation of the $C_{\epsilon 1}^{*}$ coefficient. Where the flow exhibits high strain rates due to shear at the inlet, dissipation is increased compared to the other models. This is especially noticeable on the boundaries of the inlet jet where increased dissipation is seen around the central peak. When the convective effects of the jet are reduced downstream, the dissipation increases as in Kitoh's case. This effect decreases further downstream as the flow becomes more isotropic.

As opposed to the previous case, a larger amount of redistribution of dissipation occurs due to the high strain rates at the inlet. As the flow develops, the strain rate decreases, having the same effect on the redistribution.

Chapter 5

Combustion Models

Contents

5.1 Introduction

Swirl is incorporated into many types of industrial flow. For confined combustion flows, such as inside the cylinder of an internal combustion engine or a swirl burner, swirl is used to enhance the mixing of fuel with oxidant, resulting in optimal reaction (Gupta *et al.*, 1984). Another important use of swirl is to anchor flame to prevent blow-off and extinction by providing flow recirculations in the flame region (Bradley, Gaskell, Gu, Lawes and Scott, 1998)

The remainder of this thesis will concentrate on testing the generality of the aerodynamic models described previously on a swirling, combustion flow. To facilitate the prediction of such flows, it is necessary to discuss the relevant methods of describing the combustion reactions and predicting the position of the flame.

In addition to the equations of motion presented in chapter 2, conservation equations for the individual species present are required, such as mixture fraction and mass fraction (described later). In continuation of the discussion on DNS for isothermal turbulent flows, it is worth mentioning the current capability of DNS for solving the aerodynamic and additional reaction equations. It has been mentioned previously that the mesh size for accurate resolution of the smallest turbulent scales using DNS must be of the order of the size of the Kolmogorov length scale. For reacting flows, where the reaction takes place over a very thin reaction zone, the impracticalities of using DNS are amplified. For this case the thickness of the reaction zone can be much smaller than the Kolmogorov length scale, as is the chemical reaction time to the smallest isothermal timescales. These phenomena serve to increase the range of length and timescales needed to resolve the additional conservation equations using DNS, making its use even more impractical than for isothermal, inert flows.

The above points show that to calculate reacting flows it is necessary to decouple the equations governing the reaction from those governing the aerodynamics due to the separation of time and length scales. The aerodynamics of the turbulent flow are dealt with in the manner shown in chapter 2, whilst new models must be introduced to accurately describe the combustion process. Once this is done, re-coupling of the models facilitates prediction of the flow and reaction dominated parameters. There

are several popular methods for predicting turbulent combustion in use, namely, probability density function (pdf) methods (Roekaerts, 2002), flamelet methods (Gu, 1993), conditional moment closure (CMC) pdf methods (Klimenko and Bilger, 1999) and the hybrid flamelet-CMC method (Bradley *et al.*, 2002).

Pdf methods are used for modelling the highly nonlinear thermo-chemical correlations present in the governing equations. The distribution of these correlations can be obtained by solving the joint velocity-scalar pdf using Monte-Carlo methods. Unfortunately, these methods are very computationally expensive pushing them beyond the boundaries of affordable engineering.

Flamelet models are employed when there is a clear separation between the reaction and turbulent timescales, with the 'fast' chemistry timescale much shorter than that of the turbulence. Also for the flamelet model to be useful, the length of the reaction zone must also be shorter than the Kolmogorov length-scale (Bray and Peters, 1994).

The flamelet methodology is based upon defining a region, the flamelet, where reactions occur. Different formulations of flamelet modelling exist for premixed and diffusion flame. For premixed flame, the mean volumetric heat release rate is expressed in terms of an *assumed* pdf and the laminar heat release rate. A library of laminar flames is provided to accomplish this for the varying flow conditions across the reaction zone. For diffusion flames, the assumed pdf incorporates the effect of mixture fraction to give the mean volumetric heat release rate. The effects of flame stretch are also considered for both cases, where flame curvature and straining leads to changes in heat release and, in some circumstances, flame extinction.

CMC methods provide a different approach by finding the conditional pdf of a scalar variable. This is done by providing conditional moment equations for quantities such as species mass fraction and temperature/energy (Klimenko and Bilger, 1999). These equations can then be solved using conventional methods, avoiding the highly expensive algorithms used in pdf methods.

The outcome of this chapter is the definition of the CMC-flamelet combustion model to be used in the study of the TECFLAM swirl burner presented in Chapter 6. To arrive at this outcome, an understanding of flamelet modelling is necessary,

and is presented. The final model presented is based on those used for the study of premixed laminar flame, with the effects of turbulence incorporated via flame stretch. Premixed flames, as opposed to diffusion flames, are used with a conserved scalar, the mixture fraction, to account for the amount of mixing of fuel and oxidant.

The CMC equations for the first and second moments of species mass fraction are then presented. After these equations are Favre averaged, they are then incorporated into the flamelet model structure to provide a more accurate description of the associated assumed pdfs.

5.2 Laminar flames

5.2.1 Laminar, premixed flames

Flamelet models are used to describe the position of flame within the fluid and the reaction characteristics within the small reaction zone. The simplest flamelet is that of the premixed, planar, one-dimensional laminar flame. In the review by Law and Sung (2000), three separate levels of complexity are used within the flamelet methodology.

The first assumes the reaction zone to be infinitely thin, the flamelet represented by a flame sheet propagating into unburnt mixture with flame velocity u_l, as shown in figure 5.1(a). At the flame sheet a discontinuity exists between the burnt, (b), and unburnt, (u), sides for temperature, T, and fuel mass fraction, Y. This type of flamelet is wholly governed by the fluid dynamics of the flow, where mass and energy are conserved, with a decoupling of the simple one-step reaction that occurs across the flame sheet.

In the second approximation the flame sheet is expanded to a finite length, δ_l, within which the conservation of heat and mass fraction is accounted for. Within this zone is an infinitely thin reaction sheet preceded by the preheat zone (see figure 5.1(b)). As the unburnt fuel enters the preheat zone it is heated by the heat release of the reaction sheet propagating towards it with velocity u_b. The temperature of the

unburnt fuel rises accordingly until enough heat has been absorbed to satisfy the activation energy of the mixture and reaction commences in the reaction sheet. At the reaction sheet, both the temperature and mass fraction profiles take their values in the burnt gas region causing the discontinuity at this location. The profiles of temperature and mass fraction across the preheat zone are dependent on the ratio of thermal to mass fraction diffusivity (known as the Lewis number, $Le = k_t/\rho D C_p$: D-diffusivity, k_t-thermal diffusivity, C_p-specific heat capacity at constant pressure).

The final approximation uses that of the second with an expanded reaction zone. In this zone, molecular diffusion plays the dominant role over the very short reaction distances. As shown by Law and Sung (2000), the heat release profile over this thin region rises very steeply towards a peak which falls as the fuel is exhausted (see figure 5.1(c)). Note that discontinuities do not exist at the boundary of the reaction zone and burnt gas regions.

The widths of the preheat zone and the reaction zone are dependent on the reaction rate for the reaction in the flame, and hence on the chemical kinetics therein. For hydrogen fuel, the propagation of the flame is governed by the production of the H radical. Williams (2000) gives the simple reactions involved: the branching reaction,

$$\mathrm{H} + \mathrm{O_2} \rightarrow \mathrm{OH} + \mathrm{O}, \tag{5.1}$$

which produces radicals and the recombination reaction,

$$\mathrm{H} + \mathrm{O_2} + \mathrm{M} \rightarrow \mathrm{HO_2} + \mathrm{M} \tag{5.2}$$

which reduces them (M represents the action of other species present that aid the reaction by providing collisional energy but is not consumed).

The branching reaction is stopped below a critical temperature, T_c, where the branching and recombination reaction rates are equal. This means that heat release in the preheat zone can only be possible by upstream radical diffusion from the reaction zone when the temperature is below T_c. In the reaction zone, where the adiabatic flame temperature, $T_{af} = T_b > T_c$, the branching reaction persists.

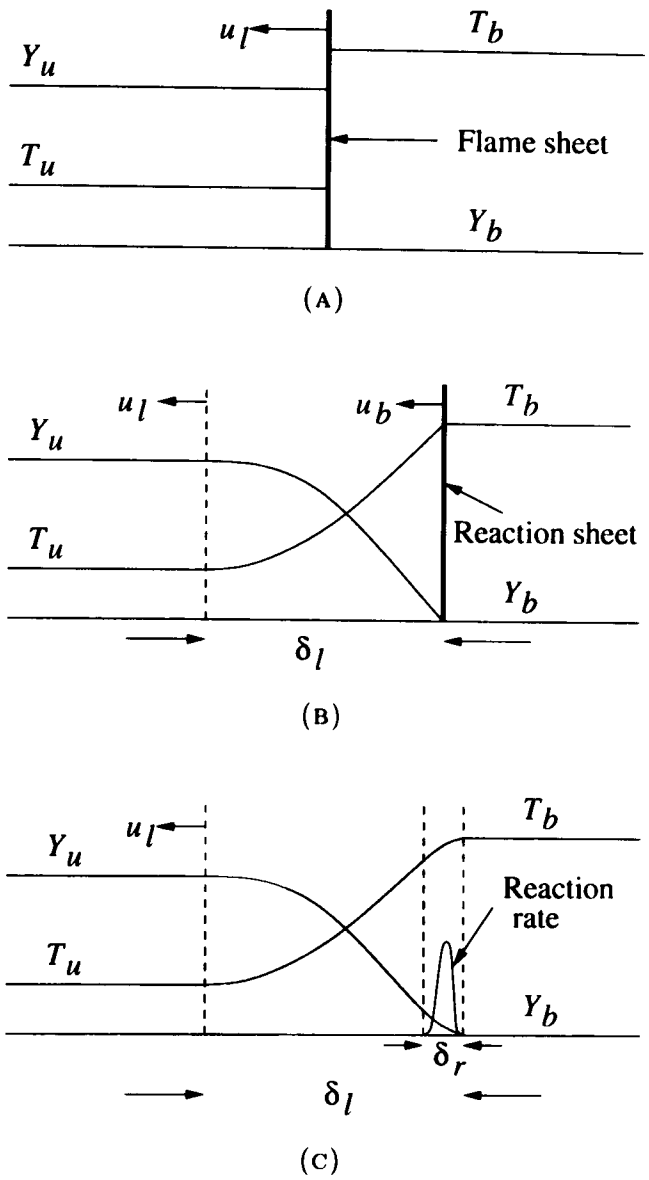

FIGURE 5.1: Representations of structure for premixed, one-dimensional, planar laminar flame: (a) simple model, (b) transport model, (c) diffusive reaction model.

As either T_b decreases or T_c increases (due to increased pressure), the reaction zone narrows, increasing the activation energy. At $T_b = T_c$ a flammability limit is defined by the chemical kinetics. For $T_b < T_c$ energy loss due to radiation would be sufficient to cause flame extinction.

The laminar burning velocity, u_l may be defined by numerical computation of the chemistry (Dixon-Lewis, 1990). The chemical length and time scales are represented as (Abraham *et al.*, 1985)

$$\delta_l = \frac{\nu_u}{u_l}, \quad \tau_c = \frac{\delta_l}{u_l} = \frac{\nu_u}{u_l^2} \tag{5.3}$$

where δ_l is the laminar flame thickness and τ_c is the chemical time-scale.

The planar laminar flame is a simplification to those present in real flows but is instructive in their understanding (Gu, 1993). Turbulent flamelets must take into account flame stretch both tangential and normal to the flame surface, affecting the burning rates within. Considering the flame model in figure 5.1(a), the effect of stretch tangential to the flame alters its surface area, in turn changing the burning rate. The normal velocity alters the flame front position so that flame speed and flame front velocity are balanced.

Tangential velocity in the reaction zone effects the reaction by transport of heat and mass (temperature and concentration) through it, resulting in changes in reaction rate and heat release. Also changes in normal velocity affects the time the mixture is in the reaction zone. These points make it necessary to describe the effects of flame stretch.

5.2.2 Stretched, laminar premixed flames

Flame stretch rate is described by using the expression of Williams (1985)

$$s = \frac{1}{A}\frac{\mathrm{d}A}{\mathrm{d}t} \tag{5.4}$$

where s is the rate of change of an infinitesimal surface area, A, at a point on the flame surface normalised by A. The stretch rate can then be decomposed into components arising from flame curvature, s_c, and flame straining, s_s,

$$s = s_c + s_s \quad . \tag{5.5}$$

The tensorial representation of this equation is given by Candel and Poinsot (1990) as

$$s = \underbrace{-\mathbf{nn} : \nabla\mathbf{v} + \nabla \cdot \mathbf{v}}_{s_c} + \underbrace{S_n \nabla \cdot \mathbf{n}}_{s_s} \quad . \tag{5.6}$$

Note that in the above, the second term would be zero if there was zero curvature of the flame surface.

For small strain and curvature, Clavin (1985) describes the dependence of the stretched laminar burning velocity, u_n, in terms of the stretch rate, s, via,

$$u_l - u_n = \mathcal{L}s \tag{5.7}$$

where $\mathcal{L}$ is the Markstein length, relating change in burning velocity to flame stretch. The associated non-dimensional parameter of the Markstein length is the Markstein number, $Ma = L/\delta_l$. Bradley *et al.* (1996) found that not only are the influences of strain and curvature different for premixed flame, but so are the responses of the flame front and the reaction zone to strain and curvature. This leads to the definition of two burning velocities, u_n and u_{nr}, the former based on the rate of disappearance of unburned gas, the latter on the rate of appearance of burned gas. From their computational study of propagating spherical laminar methane flames, it was found (Bradley *et al.*, 1996)

$$u_l - u_n = \mathcal{L}_c s_c + \mathcal{L}_s s_s \tag{5.8}$$

$$u_l - u_{nr} = \mathcal{L}_{cr} s_c + \mathcal{L}_{sr} s_s \tag{5.9}$$

where $\mathcal{L}_c$, $\mathcal{L}_{cr}$ and $\mathcal{L}_s$, $\mathcal{L}_{sr}$ are the Markstein lengths of a laminar flame for curvature stretch and straining, respectively.

The unstretched volumetric laminar heat release rate, q_{l0}, is affected by the completeness of the reaction in the flame. This is expressed using the reaction progress variable, θ, which is expressed as the fractional change in concentration of a permanent reaction product species, such as H_2O,

$$\theta = \frac{Y_{H_2O}}{(Y_{H_2O})_{max}} \quad . \tag{5.10}$$

Laminar heat release is also affected by flame stretch in a manner discussed by Bradley, Gaskell and Gu (1998*b*) as,

$$q_l(\theta, s) = f(s) q_{l0}(\theta), \tag{5.11}$$

where $f(s)$ is a function derived from the chemical kinetics that depends on both s and the Markstein numbers of the mixture. The function $f(s)$ is used to attenuate the laminar heat release rate when stretching occurs and is given by Bradley *et al.* (1996), after analysis of computed results for propane-air and methane-air spherical flames, as

$$f(s) = \begin{cases} 1 - 0.8(1 - u_{nr}/u_l) & \text{if} \quad 1 - u_{nr}/u_l \geq 0 \\ 1 - 0.8(1 - u_n/u_l) & \text{if} \quad 1 - u_{nr}/u_l < 0 \end{cases} \tag{5.12}$$

5.3 Premixed, turbulent flames

Laminar flamelets in turbulent flows are stretched due to the effects of strain or curvature, which modify their internal structure and the value of laminar burning velocity as described above. For turbulent premixed flame, the mean volumetric heat release rate, $\overline{q_l}$, is expressed in terms of an assumed pdf, $p(\theta, s)$, of the reaction progress variable, θ, the stretch rate, and the laminar heat release rate, $q_l(\theta, s)$, i.e.

$$\overline{q_l} = \int_{-\infty}^{+\infty} \int_0^1 q_l(\theta, s) p(\theta, s) \mathrm{d}\theta \mathrm{d}s \tag{5.13}$$

Excessive flame stretch can lead to flame extinction at the stretch limits s_{q+} and s_{q-} under positive and negative stretch rates, respectively. If the influences of θ and s are assumed to be statistically independent (Gu, 1993), the joint pdf of θ and s, $p(\theta, s)$, may be expressed by the product of the two separate pdfs, $p(s)p(\theta)$ and

$$\begin{aligned} \overline{q_l} &= \int_{s_{q-}}^{s_{q+}} \int_0^1 f(s) q_{l0}(\theta) p(\theta) p(s) \mathrm{d}\theta \mathrm{d}s \\ &= \int_{s_{q-}}^{s_{q+}} f(s) p(s) \mathrm{d}s \int_0^1 q_{l0}(\theta) p(\theta) \mathrm{d}\theta \\ &= P_b \int_0^1 q_{l0}(\theta) p(\theta) \mathrm{d}\theta \end{aligned} \tag{5.14}$$

Here

$$P_b = \int_{s_{q-}}^{s_{q+}} f(s) p(s) \mathrm{d}s \tag{5.15}$$

is the probability of burning factor, which has been studied extensively by Bradley (2002) and Bradley, Gaskell and Gu (1998*b*). The pdf of stretch rate is assumed by

Bradley, Gaskell and Gu (1998*b*) to be a Gaussian distribution,

$$p(s) = \frac{1}{\sqrt{2\pi}\sigma_s}\exp\left[-\left(\frac{s_s - \overline{s_s}}{\sqrt{2}\sigma_s}\right)^2\right] \tag{5.16}$$

where s_s is the aerodynamic strain rate, with its mean and r.m.s. values given by (Bradley, Gaskell and Gu, 1998*b*),

$$\overline{s_s} = 1.08\frac{u'}{\lambda}, \qquad \sigma_s = 1.32\frac{u'}{\lambda} \quad . \tag{5.17}$$

The term u'/λ is the Eulerian strain rate comprising the turbulent velocity and the Taylor microscale, λ and is approximated by (Gu, 1993),

$$\frac{u'}{\lambda} = \left(\frac{\epsilon}{15\nu}\right)^{1/2} \quad . \tag{5.18}$$

The stretched laminar flamelet model is used to account for the physics of turbulent, premixed flame. For non-premixed systems, the relevant concentrations of the fuel and oxidant species changes over the flow field due to aerodynamic and diffusive mixing effects, unlike the fixed concentrations of premixed gas. The theory of premixed, stretched laminar flames can, however, be applied to these so-called diffusion flames, as shown below.

5.3.1 Non-premixed, turbulent flames

For turbulent non-premixed flames, a conserved scalar approach is adopted. Laminar diffusion flamelet structures can conveniently be exhibited employing the mixture fraction, ξ (not to be confused with ξ in chapter 2 regarding the mean vorticity), a conserved scalar described in the next section, as the independent variable. The mixture fraction is defined as the fraction of the local mixture that originated in the fuel stream, giving $\xi = 0$ in the oxidant stream and $\xi = 1$ in the fuel stream. Most of the chemistry typically occurs in the vicinity of the stoichiometric value of ξ (i.e. when the molar concentrations of the reactants are in the ideal proportions for a reaction to occur). In laminar diffusion flames, fuel and oxidant are on both

sides of a reaction zone where diffusion of these reactants into the zone provides the appropriate concentrations for reaction to occur. At the reaction zone the maximum heat for the concentration of reactants is released.

The burning rate of such flames is controlled by the molecular diffusion of the reactants towards the reaction zone. The scalar dissipation rate of the mixture fraction is defined by (Libby and Williams, 1994):

$$\chi = D\left(\frac{\partial \xi}{\partial x_k}\frac{\partial \xi}{\partial x_k}\right) \tag{5.19}$$

which is a measure of the inverse diffusion time. As this time decreases, heat and mass transfer through the stoichiometric surface is enhanced.

The mean properties of turbulent non-premixed flames, such as the mean temperature, may be calculated as,

$$\overline{T} = \int_0^1 \int_0^\infty T(\xi,\chi)p(\xi,\chi)\mathrm{d}\xi\mathrm{d}\chi, \tag{5.20}$$

where $T(\xi,\chi)$ is the local flame structure in mixture fraction space and the joint pdf of ξ and χ captures the statistics of the fuel/air mixing.

The expression for the mean volumetric heat release must now be altered to take into account the mixture fraction. From equation (5.14)

$$\overline{q}_t(\xi) = P_b(\xi)\int_0^1 q_{l0}(\theta,\xi)p(\theta,\xi)\mathrm{d}\theta, \tag{5.21}$$

and the total mean volumetric heat release rate is given by

$$\overline{q}_t = \int_{\xi_{min}}^{\xi_{max}} P_b(\xi)\int_0^1 q_{l0}(\theta,\xi)p(\theta,\xi)\mathrm{d}\theta\mathrm{d}\xi, \tag{5.22}$$

where ξ_{min} and ξ_{max} are the flammability limits of mixture fraction.

When the fuel is discharged into the air, the shear-generated aerodynamic strain rate is initially sufficiently high to not only mix the fuel and air but also to quench both premixed and diffusion flamelets. Further downstream, the strain rate relaxes and premixed burning is initiated. Premixed, not diffusion flamelets are employed

by Bradley, Gaskell and Gu (1998*a*) to account for the turbulent non-premixed flames at high strain rate to predict liftoff heights for different methane flows from a pipe into still air. However, instead of assuming that the effects of ξ and θ are uncorrelated, a conditional pdf of the reaction progress variable on the mixture fraction is used,

$$p(\theta, \xi) = p(\theta|\xi = \eta)p(\xi) \quad . \tag{5.23}$$

Recently a conditional moment closure (CMC) for turbulent non-premixed flames has been developed by Klimenko and Bilger (1999). CMC methods predict the conditional averages and higher moments of quantities such as species mass fraction and temperature, conditional on the mixture fraction, allowing the calculation of the conditional pdfs.

A combined CMC-flamelet model has been developed by Bradley *et al.* (2002) and this model is used in the present study to compute the TECFLAM research flame as described in Chapter 6.

5.4 Mixture fraction - a conserved scalar

The steady state conservation equations for the relevant reacting species can be written as (Libby and Williams, 1994)

$$\frac{\partial}{\partial x_k}(\rho u_k Y_F) - \frac{\partial}{\partial x_k}\left(\rho D_F \frac{\partial Y_F}{\partial x_k}\right) = W_F \tag{5.24}$$

$$\frac{\partial}{\partial x_k}(\rho u_k Y_O) - \frac{\partial}{\partial x_k}\left(\rho D_O \frac{\partial Y_O}{\partial x_k}\right) = W_O \tag{5.25}$$

where Y_F and Y_O are the fuel and oxidant mass fractions, D_F and D_O are the diffusion coefficients for fuel and oxidant and W is the relevant mass volumetric reaction rate. The mass fraction, Y, indicates the ratio of the mass for a specific chemical species to the total mass in the fluid and may be defined by its molar concentration, C as

$$C_X = \rho \frac{Y_X}{M_X}, \tag{5.26}$$

for a species X with molecular mass M_X. If it is assumed that 1 kilogram of fuel reacts with n kilograms of oxidant, then it is possible to write

$$\frac{W_O}{W_F} = n \quad . \tag{5.27}$$

By defining a parameter, F, such that

$$F = Y_F - \frac{Y_O}{n}; \tag{5.28}$$

dividing (5.25) by n and then combining with (5.24), a transport equation for F is obtained,

$$\frac{\partial}{\partial x_k}(\rho u_k F) = \frac{\partial}{\partial x_k}\left(\rho D \frac{\partial F}{\partial x_k}\right), \tag{5.29}$$

where $D_F = D_O = D$. The mixture fraction, ξ, may be defined by F as

$$\xi = \frac{F - F_O}{F_F - F_O} \tag{5.30}$$

where F_O is the value of F in the separated oxidant stream and F_F is the value on the separated fuel stream for which ξ takes values of zero and unity, respectively. From equations (5.29) and (5.30), a transport equation for mixture fraction may be derived,

$$\frac{\partial}{\partial x_k}(\rho u_k \xi) = \frac{\partial}{\partial x_k}\left(\rho D \frac{\partial \xi}{\partial x_k}\right) \quad . \tag{5.31}$$

By using Favre decomposition and averaging, the transport equation for the mean mixture fraction at high Reynolds numbers reads,

$$\frac{\partial}{\partial x_k}(\bar{\rho}\tilde{u}_k\tilde{\xi}) = -\frac{\partial}{\partial x_k}(\bar{\rho}\widetilde{u_k''\xi''}) \quad . \tag{5.32}$$

Equation (5.32) is not closed due to the presence of the velocity-mixture fraction correlation, $\widetilde{u_k''\xi''}$. A transport equation can be obtained for this correlation in a similar manner for that of the Reynolds stresses in equation (2.89), leading to

$$\bar{\rho}\tilde{u}_k \frac{\partial \widetilde{u_i''\xi''}}{\partial x_k} \quad - \quad \frac{\partial}{\partial x_k}\left(C_{st}\bar{\rho}\frac{k}{\epsilon}\widetilde{u_l''u_k''}\frac{\partial \widetilde{u_i''\xi''}}{\partial x_l}\right)$$

$$= -\left(\widetilde{\overline{\rho}u_k''\xi''}\frac{\partial\tilde{u}_i}{\partial x_k} + \widetilde{\overline{\rho}u_k''u_i''}\frac{\partial\tilde{\xi}}{\partial x_k}\right) + \Pi_{i\xi} + \Pi_{i\xi,w} - \overline{\xi''}\frac{\partial\overline{p}}{\partial x_i} \quad (5.33)$$

where the first term on the right is the production term and

$$\begin{aligned}
\Pi_{i\xi} &= -C_{1T}\overline{\rho}\frac{\epsilon}{k}\widetilde{\overline{u_i''\xi''}} + C_{2T}\overline{\rho}\frac{\epsilon}{k}\widetilde{\overline{u_k''\xi''}}\frac{\partial\tilde{u}_i}{\partial x_k} \\
\Pi_{i\xi,w} &= -\left[\overline{\rho}\frac{\epsilon}{k}C_{1T}'\widetilde{\overline{u_n''\xi''}}\right]\frac{k^{\frac{3}{2}}}{\epsilon x_2} \\
\overline{\xi''} &= \int_0^1(\xi-\tilde{\xi})\frac{\overline{\rho}\tilde{p}(\xi)}{\rho}\mathrm{d}\xi, \qquad (5.34)
\end{aligned}$$

where the pdf, $p(\xi)$ is expressed in terms of its Favre averaged counterpart using

$$p(\xi) = \frac{\overline{\rho}\tilde{p}(\xi)}{\rho} \quad . \qquad (5.35)$$

A transport equation for the second moment of mixture fraction is derived as (Gu, 1993),

$$\overline{\rho}\tilde{u}_k\frac{\partial\widetilde{\overline{\xi''^2}}}{\partial x_k} - \frac{\partial}{\partial x_k}\left(C_t\overline{\rho}\frac{k}{\epsilon}\widetilde{\overline{u_l''u_k''}}\frac{\partial\widetilde{\overline{\xi''^2}}}{\partial x_l}\right) = -2\overline{\rho}\widetilde{\overline{u_k''\xi''}}\frac{\partial\tilde{\xi}}{\partial x_k} - C_T\overline{\rho}\frac{\epsilon}{k}\widetilde{\overline{\xi''^2}} \quad . \qquad (5.36)$$

The coefficient C_T in equation (5.36) is defined by Chomiak *et al.* (1991) after studying the ratio of dissipation for k and variance of temperature, giving

$$C_T = \left(1 + \frac{2\times 15^{1/4}}{Re_\lambda^{1/2}}\right)\frac{1}{Pr}, \qquad (5.37)$$

where Pr is the Prandtl number. The Taylor Reynolds number, Re_λ is based on the Taylor length-scale,

$$\lambda = \left(\frac{\nu u'^2}{\epsilon}\right)^{1/2}, \qquad (5.38)$$

and the r.m.s. velocity fluctuation, u' and has the same form as the conventional Reynolds number expression. The other coefficients for the above equations are shown in table 5.1.

To define the above equations in the present work, consideration of some of the reaction chemistry is necessary. The stoichiometry of the reaction of methane in

Coefficient	Value
C_{st}	0.15
C_{1T}	3.0
C_{2T}	0.33
C'_{1T}	0.5
C_t	0.15
C_T	$\left(1 + \frac{2\times 15^{1/4}}{Re_\lambda^{1/2}}\right)\frac{1}{Pr}$

TABLE 5.1: Values of coefficients used in the first and second moment equations for mixture fraction (Gu, 1993).

oxygen is expressed by the equation

$$CH_4 + 2O_2 \rightleftharpoons CO_2 + 2H_2O \quad . \tag{5.39}$$

From equation (5.28), when 16kg of methane react with 64kg of oxygen and $n = 4$, the value of F becomes,

$$F = Y_{CH_4} - \frac{Y_O}{4} \quad . \tag{5.40}$$

The stoichiometric mole proportions for the above reaction may be given by

$$CH_4 + y(0.21O_2 + 0.79N_2) \longrightarrow CO_2 + 2H_2O \tag{5.41}$$

where, from (5.39), $0.21y = 2$. When the fuel-air mixture dictates that one mole of methane is present in x moles of air, it is possible to define an equivalence ratio,

$$\phi = \frac{1/x}{1/y} = \frac{y}{x}, \tag{5.42}$$

which can then be used to find the value of x by

$$x = \frac{y}{\phi} = \frac{2}{0.21\phi} \quad . \tag{5.43}$$

Using this, the mass fractions of methane and oxygen in the mixture may be given as,

$$\begin{aligned} Y_{CH_4} &= \frac{16}{16 + x(0.21 \times 32 + 0.79 \times 28)} \\ &= \frac{\phi}{\phi + 17.167} \end{aligned} \tag{5.44}$$

$$Y_{O_2} = \frac{x(0.21 \times 32)}{16 + x(0.21 \times 32 + 0.79 \times 28)} = \frac{4}{\phi + 17.167} \quad . \tag{5.45}$$

From equations (5.44) and (5.45), (5.40) can be re-expressed for the reaction as

$$F = \frac{\phi - 1}{\phi + 17.167} \quad . \tag{5.46}$$

From (5.40) it can be seen that $F_F = 1$ in the pure fuel stream as the values of $Y_{CH_4} = 1$ and $Y_{O_2} = 0$. In the air stream $\phi = 0$ setting $Y_{CH_4} = 0$ and $Y_{O_2} = 0.233$ with $F_O = -0.0583$. The dependency of mixedness on the value of equivalence ratio may be expressed using equation (5.30),

$$\xi = \frac{(\phi - 1)/(\phi + 17.167) + 0.0583}{1 + 0.0583} = 0.0551 + \frac{\phi - 1}{1.0583\phi + 18.168} \quad . \tag{5.47}$$

For the methane-air mixture, the stoichiometric value of mixedness is equal to 0.0551. The flammability limits for cold premixture are, $\xi_{max} = 0.08$ when $\phi = 1.5$ and $\xi_{min} = 0.028$ when $\phi = 0.5$ for rich and lean mixtures, respectively (Strehlow, 1985; Andrews and Bradley, 1973).

5.5 Conditional Moment Closure equations

The Conditional Moment Closure (CMC) method defined by Klimenko and Bilger (1999) has its roots in the pdf methods described previously. Instead of solving the joint pdf, or using an assumed pdf to find the average value of a variable such as mass fraction, Y, a conditional pdf is defined, conditioned on another flow quantity such as mixture fraction, ξ. The methods described in this section are applied later to facilitate the CMC-flamelet model.

The joint probability of two events α and β occurring is commonly given by,

$$P(\alpha, \beta) = P(\alpha|\beta)P(\beta), \tag{5.48}$$

where $P(\alpha|\beta)$ is the probability of α occurring conditional on the event β occurring. The definition of the probability density function for a variable, y, taking values less than a number, z, is given as (Klimenko and Bilger, 1999),

$$p(z) = \frac{\mathrm{d}P(y < z)}{\mathrm{d}z} \quad . \tag{5.49}$$

By rearranging equation (5.49), multiplying by z and then integrating, the mean - or expected - value of y, $\langle y \rangle$, is obtained,

$$\langle y \rangle = \int_{-\infty}^{+\infty} z p(z) \mathrm{d}z = \int_{0}^{1} z \, \mathrm{d}P(y < z) \quad . \tag{5.50}$$

Note that equation (5.50) is similar to obtaining the first moment equations in Chapter 2 for the mean flow properties.

A conditional expectation can be derived by defining a conditional pdf from the joint pdf in the same way as in equation (5.48),

$$p(z_1, z_2) = p(z_1|y_2 = z_2)p(z_2), \tag{5.51}$$

where z_1 and z_2 are particular occurrences of y_1 and y_2, respectively. The conditional expectation of y_1 on a particular value of y_2 can thus be defined

$$\langle y_1|y_2 = z_2 \rangle = \int_{-\infty}^{+\infty} z_1 p(z_1|y_2 = z_2) \mathrm{d}z_1 \quad . \tag{5.52}$$

Using the method of conditional expectations, Klimenko and Bilger (1999) derived a conditional transport equation for the mass fraction based on values of mixture fraction. The full unconditioned transport equation for the mass fraction of a particular species is given by Libby and Williams (1994) as,

$$\rho \frac{\partial Y}{\partial t} + \rho u_i \frac{\partial}{\partial x_i} Y - \frac{\partial}{\partial x_i} \left(\rho D \frac{\partial}{\partial x_i} Y \right) = \rho W, \tag{5.53}$$

where D is the diffusion coefficient of the species of interest in Y and W is the rate of formation of the species of interest in Y per unit mass. By decomposing the value of Y into a conditional expectation, $Q = \langle Y|\eta \rangle$, where η is the value of ξ that is

being used for conditioning, and a fluctuation, Y'', about Q, such that

$$Y(\mathbf{x},t) = Q(\xi(\mathbf{x},t)\mathbf{x},t) + Y''(\mathbf{x},t), \tag{5.54}$$

a conditional equation for the mass fraction can be derived. Differentiating (5.54) with respect to time and space gives,

$$\frac{\partial Y}{\partial t} = \frac{\partial Q}{\partial t} + \frac{\partial Q}{\partial \eta}\frac{\partial \xi}{\partial t} + \frac{\partial Y''}{\partial t} \tag{5.55}$$

$$\frac{\partial Y}{\partial x_i} = \frac{\partial Q}{\partial x_i} + \frac{\partial Q}{\partial \eta}\frac{\partial \xi}{\partial x_i} + \frac{\partial Y''}{\partial x_i} \tag{5.56}$$

Substituting equations (5.55) and (5.56) into equation (5.53) obtains,

$$\begin{aligned}\rho\frac{\partial Q}{\partial t} &+ \rho u_i\frac{\partial Q}{\partial x_i} - \rho\chi\frac{\partial^2 Q}{\partial \eta^2} - \frac{\partial}{\partial x_i}\left(\rho D\frac{\partial Q}{\partial x_i}\right) - \rho D\frac{\partial \xi}{\partial x_i}\frac{\partial}{\partial x_i}\left(\frac{\partial Q}{\partial \eta}\right)\\ &+ \rho\frac{\partial Y''}{\partial t} + \rho u_i\frac{\partial Y''}{\partial x_i} - \frac{\partial}{\partial x_i}\left(\rho D\frac{\partial Y''}{\partial x_i}\right) = \rho W,\end{aligned} \tag{5.57}$$

from which the conditional expectation can be found, upon the condition that mixture fraction $\xi = \eta$,

$$\rho_\eta\frac{\partial Q}{\partial t} + \rho_\eta\langle u_i|\eta\rangle\frac{\partial Q}{\partial x_i} - \rho_\eta\langle\chi|\eta\rangle\frac{\partial^2 Q}{\partial \eta^2} = \rho_\eta\langle W|\eta\rangle + e_Q + e_Y \quad . \tag{5.58}$$

In equation (5.58) the values of e_Q and e_Y are given by,

$$e_Q = \left\langle \frac{\partial}{\partial x_i}\left(\rho D\frac{\partial Q}{\partial x_i}\right) + \rho D\frac{\partial \xi}{\partial x_i}\frac{\partial}{\partial x_i}\left(\frac{\partial Q}{\partial \eta}\right)\middle|\xi(x_i,t) = \eta\right\rangle \tag{5.59}$$

$$e_Y = -\left\langle \rho\frac{\partial Y''}{\partial t} + \rho u_i\frac{\partial Y''}{\partial x_i} - \frac{\partial}{\partial x_i}\left(\rho D\frac{\partial Y''}{\partial x_i}\right)\middle|\xi(x_i,t) = \eta\right\rangle, \tag{5.60}$$

and χ is the scalar dissipation rate of Y given by equation (5.19) and $\rho_\eta = \langle\rho|\eta\rangle$.

Klimenko and Bilger (1999) found that e_Q has a negligible effect at high Reynolds numbers and can be omitted. e_Y contains terms involving Y'' which are, at present, unknowns. Klimenko and Bilger (1999) noted that the unconditional and conditional expectation of the fluctuating terms $\langle Y''\rangle = \langle Y''|\eta\rangle = 0$. The expectation of the conditional gradients and time derivatives of the fluctuations cannot, however, be

set to zero. The integral of these terms with the pdf, $p(\eta)$, over all η, however, gives a zero result,

$$\int \left\langle \frac{\partial Y''}{\partial x_i} \middle| \eta \right\rangle p(\eta) \mathrm{d}\eta = \int \left\langle \frac{\partial Y''}{\partial t} \middle| \eta \right\rangle p(\eta) \mathrm{d}\eta = 0 \tag{5.61}$$

due to the zero expectation value of the unconditional gradients. Integrating e_Y over all η using the pdf, $p(\eta)$, in a similar manner to that in (5.61), gives (Klimenko and Bilger, 1999),

$$\int e_Y p(\eta) \mathrm{d}\eta = -\int \frac{\partial}{\partial x_i} \left(\rho_\eta \langle u_i'' Y'' | \eta \rangle p(\eta) \right) \mathrm{d}\eta \tag{5.62}$$

which gives

$$e_Y = -\frac{1}{p(\eta)} \frac{\partial}{\partial x_i} \left(\rho_\eta \langle u_i'' Y'' | \eta \rangle p(\eta) \right) \quad . \tag{5.63}$$

By substituting equation (5.63) into equation (5.58) the first moment CMC equation for mass fraction is obtained,

$$\frac{\partial Q}{\partial t} + \langle u_i | \eta \rangle \frac{\partial Q}{\partial x_i} + \frac{1}{p(\eta)\rho_\eta} \frac{\partial}{\partial x_i} \left(\rho_\eta \langle u_i'' Y'' | \eta \rangle p(\eta) \right) - \langle \chi | \eta \rangle \frac{\partial^2 Q}{\partial \eta^2} = \langle W | \eta \rangle \quad . \tag{5.64}$$

To represent the fluctuations in mass fraction, Y'', the equations for the conditional second moments of mass fraction are derived by Klimenko and Bilger (1999). Firstly the unconditional covariance for two mass fractions, $K_{12} = Y_1'' Y_2''$ is defined as,

$$\begin{aligned} \rho \frac{\partial K_{12}}{\partial t} \quad + \quad & \rho u_i \frac{\partial K_{12}}{\partial x_i} - \frac{\partial}{\partial x_i} \left(D\rho \frac{\partial K_{12}}{\partial x_i} \right) + 2D\rho \left(\frac{\partial Y_1''}{\partial x_i} \frac{\partial Y_2''}{\partial x_i} \right) \\ = \quad & \rho(W_1 Y_2'' + W_2 Y_1'') + E_{D12} + E_{D21} - E_{Q12} - E_{Q21} \end{aligned} \tag{5.65}$$

where

$$E_{Djk} = Y_j'' \rho D \frac{\partial \xi}{\partial x_i} \frac{\partial}{\partial x_i} \left(\frac{\partial Q_k}{\partial \eta} \right) + Y_j'' \frac{\partial}{\partial x_i} \left(\rho D \frac{\partial Q_k}{\partial x_i} \right) \tag{5.66}$$

$$E_{Qjk} = Y_j'' \left(\rho \frac{\partial Q_k}{\partial t} + \rho u_i \frac{\partial Q_k}{\partial x_i} - \rho \chi \frac{\partial^2 Q_k}{\partial \eta^2} \right) \tag{5.67}$$

Decomposing K_{12} into its conditional expectation and fluctuating parts, differentiating (as in equations (5.54) to (5.58)) and then taking the conditional expectation

gives,

$$\rho_\eta \frac{\partial G_{12}}{\partial t} + \rho_\eta \langle u_i|\eta\rangle \frac{\partial G_{12}}{\partial x_i} - \rho_\eta \langle \chi|\eta\rangle \frac{\partial^2 G_{12}}{\partial \eta^2} = \rho_\eta \langle (W_1'' Y_2'' + W_2'' Y_1'')|\eta\rangle - 2\rho_\eta \left\langle D\left(\frac{\partial Y_1''}{\partial x_i}\frac{\partial Y_2''}{\partial x_i}\right)\middle|\eta\right\rangle - e_K - e_{Q12} - e_{Q21} \tag{5.68}$$

where

$$e_K = \langle E_K|\eta\rangle \tag{5.69}$$

$$E_K = \rho \frac{\partial K_{12}''}{\partial t} + \rho\left(u_i \frac{\partial K_{12}''}{\partial x_i}\right) - \frac{\partial}{\partial x_i}\left(D\rho \frac{\partial K_{12}''}{\partial x_i}\right) \tag{5.70}$$

and

$$e_{Qjk} = \langle E_{Qjk}|\eta\rangle = \rho_\eta \left(\frac{\partial Q_k}{\partial x_i}\langle Y_j'' u_i''|\eta\rangle - \frac{\partial^2 Q_k}{\partial \eta^2}\langle Y_j'' \chi''|\eta\rangle\right) \quad . \tag{5.71}$$

In a similar manner to the e_Y term of equation (5.58), e_K is expressed as

$$e_K = \frac{1}{p(\eta)}\frac{\partial}{\partial x_i}\left(\rho_\eta \langle u_i'' K_{12}''|\eta\rangle p(\eta)\right) \quad . \tag{5.72}$$

The equation for the conditional variance can now be written as

$$\begin{aligned} \frac{\partial G_{12}}{\partial t} &+ \langle u_i|\eta\rangle \frac{\partial G_{12}}{\partial x_i} - \langle \chi|\eta\rangle \frac{\partial^2 G_{12}}{\partial \eta^2} + \frac{1}{p(\eta)\rho_\eta}\frac{\partial}{\partial x_i}\left(\rho_\eta \langle u_i'' K_{12}''|\eta\rangle p(\eta)\right) \\ &= \langle (W_1'' Y_2'' + W_2'' Y_1'')|\eta\rangle - 2\left\langle D\left(\frac{\partial Y_1''}{\partial x_i}\frac{\partial Y_2''}{\partial x_i}\right)\middle|\eta\right\rangle - \frac{\partial Q_1}{\partial x_i}\langle Y_2'' u_i''|\eta\rangle \\ &- \frac{\partial Q_2}{\partial x_i}\langle Y_1'' u_i''|\eta\rangle + \frac{\partial^2 Q_1}{\partial \eta^2}\langle Y_2'' \chi''|\eta\rangle + \frac{\partial^2 Q_2}{\partial \eta^2}\langle Y_1'' \chi''|\eta\rangle \quad . \end{aligned} \tag{5.73}$$

By assuming that species Y_1 and Y_2 are identical (Klimenko and Bilger, 1999), the conditional variance equation is obtained

$$\begin{aligned} \frac{\partial G}{\partial t} &+ \langle u_i|\eta\rangle \frac{\partial G}{\partial x_i} - \langle \chi|\eta\rangle \frac{\partial^2 G}{\partial \eta^2} + \frac{1}{p(\eta)\rho_\eta}\frac{\partial}{\partial x_i}\left(\rho_\eta \langle u_i'' K''|\eta\rangle p(\eta)\right) \\ &= 2\langle W'' Y''|\eta\rangle - 2\left\langle D\frac{\partial Y''^2}{\partial x_i}\middle|\eta\right\rangle \\ &- 2\frac{\partial Q}{\partial x_i}\langle Y'' u_i''|\eta\rangle + 2\frac{\partial^2 Q}{\partial \eta^2}\langle Y'' \chi''|\eta\rangle \quad . \end{aligned} \tag{5.74}$$

5.6 The CMC-flamelet model

Using the CMC equations outlined in the previous section, a hybrid CMC-flamelet model was created by Bradley *et al.* (2002). In flows with high strain rates, the conditional fluctuations of mass fraction and temperature become significant for a given mixture fraction, η, thus requiring the specification of the second moments of the reaction progress variable to determine the conditional Favre pdf, $\tilde{p}(\theta|\eta)$ of equation (5.23) and the chemical source terms.

The reaction progress variable is defined by equation (5.10) where $(Y_{H_2O})_{max}$ is the maximum mass concentration of H_2O for an unstretched laminar flamelet with mixture fraction η. The conditional first and second moments of reactedness are given by,

$$\langle\theta|\eta\rangle = \frac{Q_{H_2O}}{(Y(\eta)_{H_2O})_{max}} \tag{5.75}$$

$$\langle\theta''^2|\eta\rangle = \frac{G_{H_2O}}{(Y(\eta)_{H_2O})^2_{max}} \tag{5.76}$$

where Q_{H_2O} and G_{H_2O} are the Favre conditional mean and variance expectations of the mass fraction Y_{H_2O},

$$Q_{H_2O} = \frac{\langle\rho Y_{H_2O}|\eta\rangle}{\rho_\eta} \tag{5.77}$$

$$G_{H_2O} = \frac{\langle\rho Y''^2_{H_2O}|\eta\rangle}{\rho_\eta} \quad . \tag{5.78}$$

The Favre averaged forms of equations (5.64) and (5.74) may be used to define Q and G, where the pdf of mixture fraction at η may be expressed in Favre averaged form as

$$\rho_\eta p(\eta) = \overline{\rho}\tilde{p}(\eta) \quad . \tag{5.79}$$

Additional closure is required for the unknown terms in equations (5.64) and (5.74). The conditional fluctuating velocity-mass fraction covariance may be expressed using the closure of Klimenko and Bilger (1999),

$$\langle u_i'' Y''|\eta\rangle = -\frac{\nu_T}{Pr}\frac{\partial Q}{\partial x_i} \tag{5.80}$$

$$\langle u_i'' Y''^2 | \eta \rangle = -\frac{\nu_T}{Pr}\frac{\partial G}{\partial x_i} \tag{5.81}$$

where $Pr = 0.72$ is the Prandtl number.

Equations (5.64) and (5.74) can be cast into their steady state forms for time-independent calculations as (Bradley *et al.*, 2002),

$$\left(\rho_\eta \langle u_i|\eta\rangle + \frac{\overline{\rho}\nu_T}{Pr}\frac{\partial}{\partial x_i}\left(\frac{\rho_\eta}{\overline{\rho}}\right) - \frac{\rho_\eta \nu_T}{Pr}\frac{\partial}{\partial x_i}(\ln \tilde{p}(\eta))\right)\frac{\partial Q}{\partial x_i} - \frac{\partial}{\partial x_i}\left(\frac{\rho_\eta \nu_T}{Pr}\frac{\partial Q}{\partial x_i}\right) = \rho_\eta \chi_\eta \frac{\partial^2 Q}{\partial \eta^2} + \langle W|\eta\rangle \tag{5.82}$$

for the first moment equation and

$$\begin{aligned}\left(\rho_\eta \langle u_i|\eta\rangle + \frac{\overline{\rho}\nu_T}{Pr}\frac{\partial}{\partial x_i}\left(\frac{\rho_\eta}{\overline{\rho}}\right) - \frac{\rho_\eta \nu_T}{Pr}\frac{\partial}{\partial x_i}(\ln \tilde{p}(\eta))\right)\frac{\partial G}{\partial x_i} &- \frac{\partial}{\partial x_i}\left(\frac{\rho_\eta \nu_T}{Pr}\frac{\partial G}{\partial x_i}\right) = \rho_\eta \chi_\eta \frac{\partial^2 G}{\partial \eta^2} \\ &+ 2\frac{\rho_\eta \nu_T}{Pr}\frac{\partial Q}{\partial x_i}\frac{\partial Q}{\partial x_i} + 2\langle W'' Y''|\eta\rangle \\ &- 2\rho_\eta \left\langle D\left(\frac{\partial Y''}{\partial x_i}\right)^2 \middle| \eta \right\rangle + 2\rho_\eta \frac{\partial^2 Q}{\partial \eta^2}\langle Y'' \chi''|\eta\rangle\end{aligned} \tag{5.83}$$

for the second moment of conditional mass fraction.

The equation for the conditional temperature, $Q_T = \langle \rho T|\eta\rangle/\rho_\eta$, can be derived in the same manner as that of the conditional mass fraction

$$\left(\rho_\eta \langle u_i|\eta\rangle + \frac{\overline{\rho}\nu_T}{Pr}\frac{\partial}{\partial x_i}\left(\frac{\rho_\eta}{\overline{\rho}}\right) - \frac{\rho_\eta \nu_T}{Pr}\frac{\partial}{\partial x_i}(\ln \tilde{p}(\eta))\right)\frac{\partial Q_T}{\partial x_i} - \frac{\partial}{\partial x_i}\left(\frac{\rho_\eta \nu_T}{Pr}\frac{\partial Q_T}{\partial x_i}\right) = \rho_\eta \chi_\eta \frac{\partial^2 Q_T}{\partial \eta^2} + \left\langle \frac{q}{C_p}\middle|\eta\right\rangle - Q_R. \tag{5.84}$$

The conditional source terms in equations (5.82), (5.83) and (5.84), can be given using the conditional pdf of reactedness, $\tilde{p}(\theta|\eta)$. This pdf is assumed to be a beta function (Gu, 1993),

$$\tilde{p}(\theta|\eta) = \frac{\Gamma(\alpha+\beta)}{\Gamma(\alpha)\Gamma(\beta)}\theta^{\alpha-1}(1-\theta)^{\beta-1} \tag{5.85}$$

where

$$\alpha = \langle\theta|\eta\rangle\left(\frac{\langle\theta|\eta\rangle(1-\langle\theta|\eta\rangle)}{\langle\theta''^2|\eta\rangle}-1\right), \tag{5.86}$$

$$\beta = (1-\langle\theta|\eta\rangle)\left(\frac{\langle\theta|\eta\rangle(1-\langle\theta|\eta\rangle)}{\langle\theta''^2|\eta\rangle}-1\right) \tag{5.87}$$

and the gamma function is given by

$$\Gamma(x) = \int_0^\infty t^{x-1}e^{-t}\mathrm{d}t \quad . \tag{5.88}$$

The conditional volumetric heat release can now be expressed as

$$\left\langle \frac{q}{C_p}\middle|\eta\right\rangle = P_b(\eta)\int_0^1 \frac{q_{l0}(\theta,\eta)}{C_p(\theta,\eta)\rho(\theta,\eta)}\rho_\eta\tilde{p}(\theta|\eta)\mathrm{d}\theta \tag{5.89}$$

with the conditional mass rate of formation of a specific species given by,

$$\langle W|\eta\rangle = P_b(\eta)\int_0^1 \frac{W_{l0}(\theta,\eta)}{\rho(\theta,\eta)}\rho_\eta\tilde{p}(\theta|\eta)\mathrm{d}\theta, \tag{5.90}$$

where the unstretched laminar heat release profiles, q_{l0}, and laminar mass rate of formation, W_{l0}, for mixture fraction, η, are given in the flamelet library. The laminar flamelet data in the library are computed using the chemical kinetic code, CHEMKIN-II (Kee *et al.*, 1989) using the GRI-MECH 2.11 mechanism (Bowman *et al.*, 1996). The conditional covariance of mass formation rate and mass fraction in equation (5.83) can be expressed as,

$$\langle W''Y''|\eta\rangle = (Y(\eta)_{\mathrm{H_2O}})_{max}\,P_b(\eta)\int_0^1 \frac{W(\theta,\eta)}{\rho(\theta,\eta)}\left(\theta-\frac{Q_{\mathrm{H_2O}}}{(Y(\eta)_{\mathrm{H_2O}})_{max}}\right)\rho_\eta\tilde{p}(\theta|\eta)\mathrm{d}\theta \quad . \tag{5.91}$$

The value of Q_R is the conditional radiative heat loss from reaction products and is modelled using (Barlow *et al.*, 2001)

$$Q_R = 4\sigma\sum_i p_i a_{p,i}(T^4 - T_b^4) \tag{5.92}$$

where σ is the Stefan-Boltzmann constant, p_i is the partial pressure of species i, and $a_{p,i}$ is the Planck mean absorption coefficient of species i. The temperatures T and T_b

are the local flame temperature and the background temperature, respectively. The absorption coefficients for the different species are calculated using the RADCAL program (Grosshandler, 1993).

The unclosed terms on the right hand side of (5.83) are modelled using (Klimenko and Bilger, 1999),

$$2\rho_\eta \left\langle D\left(\frac{\partial Y''}{\partial x_i}\right)^2 \middle| \eta \right\rangle = C_1 \rho_\eta G \frac{\epsilon}{k} \tag{5.93}$$

$$2\rho_\eta \frac{\partial^2 Q}{\partial \eta^2} \langle Y''\chi'' | \eta \rangle = C_2 \rho_\eta \chi_\eta G^{1/2} \frac{\partial^2 Q}{\partial \eta^2}, \tag{5.94}$$

where C_1 and C_2 take the values of 2.0 and 1.1, respectively.

The conditional average scalar dissipation rate is modelled using the DNS mapping closure of O'Brien and Jiang (1991), where

$$\chi_\eta = C \exp\left[-2\left(\mathrm{erf}^{-1}(2\eta - 1)\right)^2\right], \tag{5.95}$$

and erf represents the well known error function. The coefficient, C, is then determined by

$$C = \widetilde{\chi}\left[\int_0^1 \left[-2\left(\mathrm{erf}^{-1}(2\eta - 1)\right)^2\right] \tilde{p}(\eta)\mathrm{d}\eta\right]^{-1} . \tag{5.96}$$

The Favre mean scalar dissipation rate, $\widetilde{\chi}$ is obtained by assuming equal diffusion timescales of species (Klimenko and Bilger, 1999),

$$\widetilde{\chi} = 2\frac{\tilde{\epsilon}}{\tilde{k}}\widetilde{\xi''^2} . \tag{5.97}$$

The conditional velocity is approximated in the popular form of Kuznetsov and Sabelnikov (1990),

$$\langle u_i | \eta \rangle = \tilde{u}_i + \frac{\widetilde{u_i''\xi''}}{\widetilde{\xi''^2}}(\eta - \tilde{\xi}) . \tag{5.98}$$

The unconditional Favre mean quantities may be obtained by integrating over the

mixture fraction space using the pdf of conditional mixture fraction, $\tilde{p}(\eta)$, such as

$$\widetilde{Y}_i = \int_0^1 Q_i \tilde{p}(\eta) \mathrm{d}\eta, \tag{5.99}$$

$$\widetilde{T} = \int_0^1 Q_T \tilde{p}(\eta) \mathrm{d}\eta, \tag{5.100}$$

for species mass fractions and temperature, respectively. The pdf of conditional mixture fraction is obtained by assuming the form of a beta function, analogous to the pdf of reactedness, $\tilde{p}(\theta)$. The Favre averaged first and second moments of mixture fraction are then used in equations (5.85) to (5.87) in place of the conditional reaction progress variable $\langle \theta | \eta \rangle$.

5.7 Summary

In this chapter a combustion model based on the hybrid CMC-flamelet model has been presented for the solution of non-premixed, turbulent flames. Instead of using assumed pdfs based on partial conditioning (Bradley, Gaskell and Gu, 1998*a*), for the modelling of the mean quantities, the latter were found using a pdf, conditioned on mixture fraction. The first and second moment CMC equations were then used to approximate the conditional mean and variance of the reaction progress variable, θ, facilitating the evaluation of the conditional pdf of the reaction progress variable, and hence, the conditional mean reaction quantities.

The model can be applied to non-premixed combustion flow cases without using a diffusion flamelet model. The next chapter introduces such a flow, the TECFLAM swirl burner, incorporating the effects of swirl to mix the separate fuel and air streams, combined with reaction.

Chapter 6

Turbulent, Combustion Flow

Contents

6.1 Introduction

The incorporation of reaction often has a significant effect on the underlying nature of the turbulent flow. For any reaction with significant heat release, there will be changes in fluid density due to the increased molecular spacing, and changes in pressure due to the increased kinetic energy of those molecules. These effects generate secondary flows in the fluid due to its expansion/contraction and the presence of additional pressure gradients, which can amplify or alternatively attenuate the straining already present in the flow and hence amplify/attenuate the turbulence.

Turbulence, however, also affects the heat release of chemical reactions, giving rise to high frequency straining of the fluid leading to rapid changes in concentration of reactants (Law and Sung, 2000). If the concentrations of the reactants are not in the stoichiometric molar proportions, the reaction rate slows from the maximum rate given for the current temperature and pressure. Thus, turbulence causes high frequency oscillations in reaction rate and, therefore, heat release due to the concentration fluctuations.

The present chapter illustrates the above, by the study of the combustion flow investigated by the TECFLAM research cooperation (Landenfeld *et al.*, 1997, 1998; Bergmann *et al.*, 1998; Meier *et al.*, 2000*b*). In an effort to provide a 'standard' research flame, the TECFLAM group have created a natural gas swirl burner that is able to run in either premixed or non-premixed configurations (see figure 6.1 below). Experimental work performed on the burner has produced detailed data for the velocity and turbulence quantities, by way of Laser Doppler Velocimetry, and the mean mass fractions of the major species present in the flame by Raman scattering (Landenfeld *et al.*, 1998; Bergmann *et al.*, 1998).

A previous numerical study has been performed by Meier *et al.* (2000*a*) using the Fluent 5 commercial code. For this calculation the LRR model has been used to close the Reynolds stress equations. The assumed pdf combustion model from Jones and Whitelaw (1982) is used with all relevant inlet data provided by the experimental measurements.

Here, the combined CMC-flamelet model presented in Chapter 5 is used along with the SSG-ADRM Reynolds stress closure to simulate the effect of turbulence, swirl, and combustion on the flow field. The effects of the anisotropic dissipation model appear in the models for the pdf of stretch from equation (5.16) and the Favre mean scalar dissipation rate in equation (5.97).

6.2 The TECFLAM swirl burner

The geometry of the burner is shown in figure 6.1, where the inlets for the air and fuel consist of two concentric annular openings at the nozzle in the base of the chamber. The fuel enters the chamber through the innermost annulus with inner radius, r_{fi} = 10mm, and the outer radius, r_{fo} = 13mm, with the air annulus corresponding to, r_{ai} = 15mm and r_{ao} = 30mm, for the inner and outer radii, respectively. The nozzle rises 30mm from the base of the chamber of length l = 1200mm and radius, R = 250mm. An annulus at the top of the chamber of inner radius R_i = 235mm, bounded by the exterior wall, is used to remove the exhaust gasses.

Swirl is introduced at the air inlet, the fuel having no swirl imparted, via a swirl generator mounted below the burner nozzle, giving a swirl number of S = 0.9. The Reynolds numbers of the fuel and air jets are Re_f = 7900 and Re_a = 42900, respectively (Keck *et al.*, 2002).

The experimental data was obtained using Laser Doppler Velocimetry and Laser Raman scattering for the aerodynamic quantities and species mass fractions. The error associated with the mean velocities is 5%, and those associated with the RMS fluctuating velocities is 6% as given by Landenfeld *et al.* (1997) and Landenfeld *et al.* (1998). The result of the Raman scattering performed by Bergmann *et al.* (1998) and Meier *et al.* (2000*b*) gives errors as: 3% (temperature), 2% (N_2), 7% (H_2O), 15% (O_2), 2% (CH_4) and 20% (CO). Measurements for these quantities were taken in the near field (in the region of the inlet nozzle) to capture the physics of the flame.

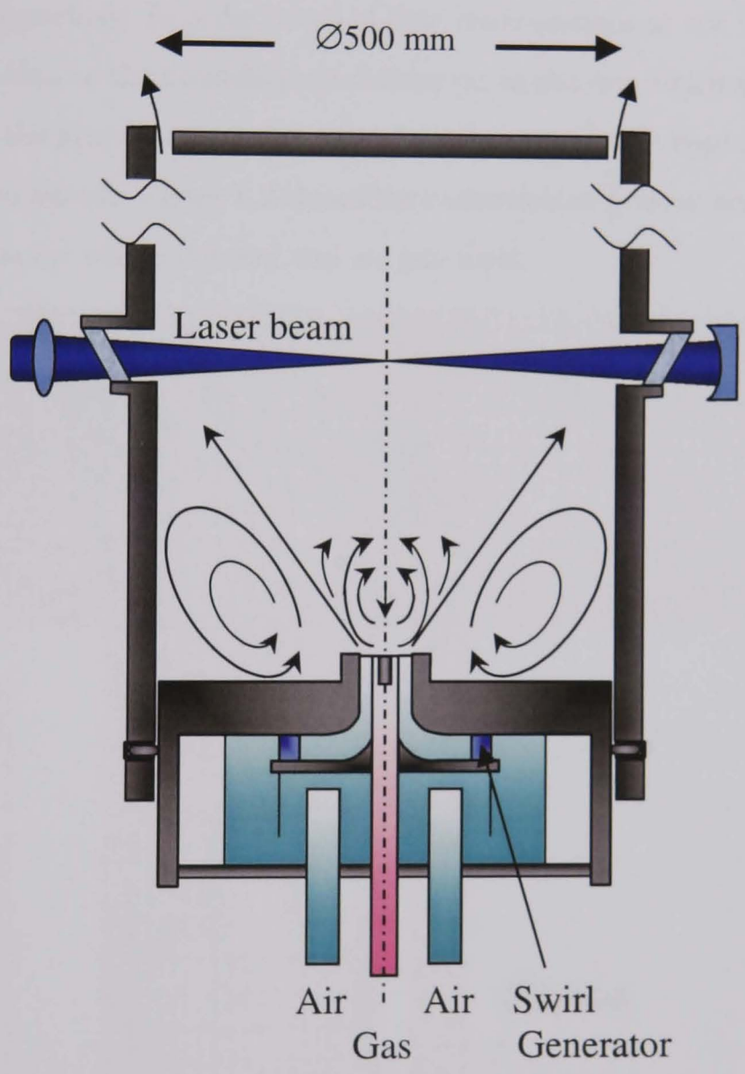

FIGURE 6.1: Flow schematic showing the burner and experimental setup; Meier *et al.* (2000*a*).

6.2.1 Numerical procedure

It was found that a structured, irregularly spaced grid consisting of 29984 nodes produced grid independent results, after grid refinement around the inlet region. The computations were performed using the PISO algorithm for stricter mass conservation per iteration, with the CUBISTA scheme to approximate the convective terms for all equations. In order to avoid flow recirculations at the inlet when using experimental data as the boundary conditions (as in the first swirling case presented in chapter 4), the grid is extended at the inlet in an attempt to capture these flow effects at the two annuli. Figure 6.2 shows the recirculation present across the annular opening for the air where the fuel and air jets meet.

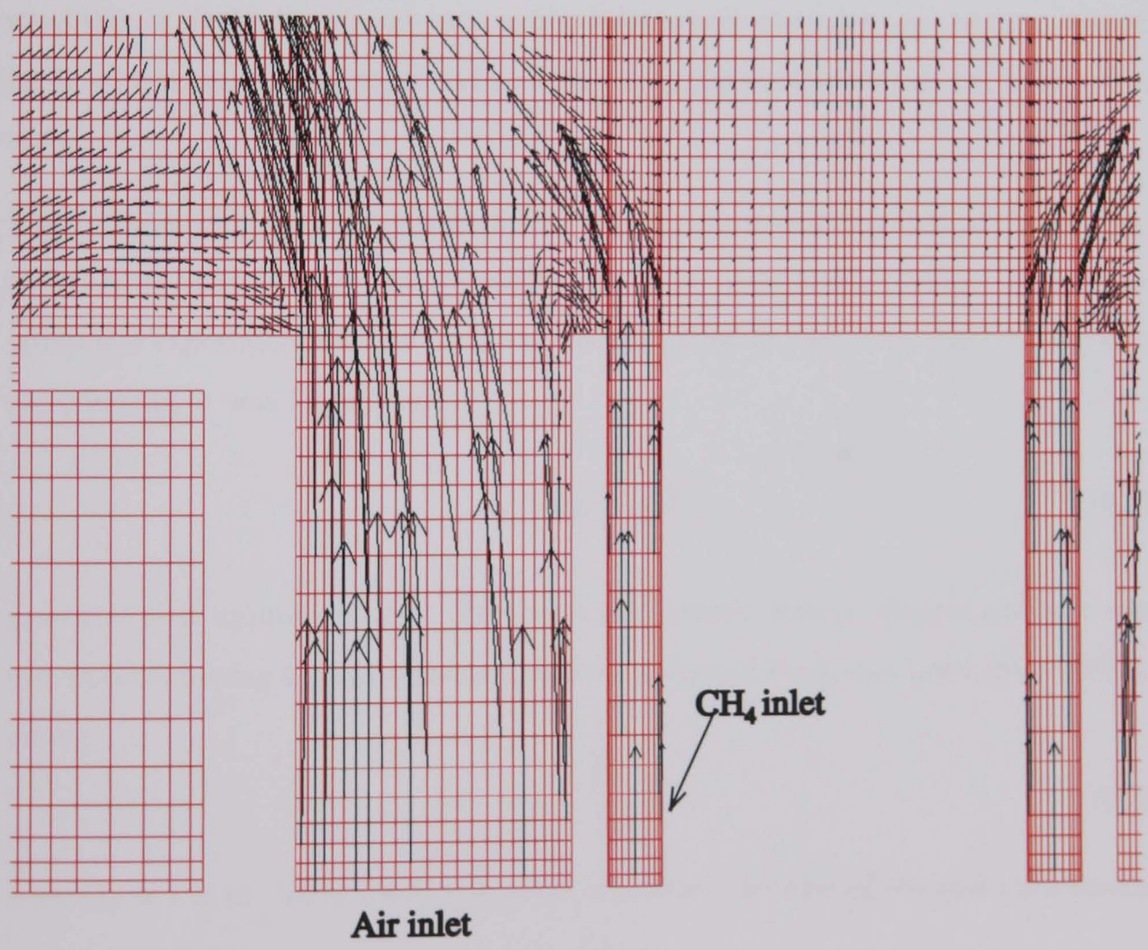

FIGURE 6.2: Computational domain of the inlet nozzle. Vector arrows show recirculation across the inlet.

Boundary conditions

For this flow, the boundary conditions are more complex than those in Chapter 4 due to the presence of the fuel and air inlets. At all walls the no slip condition is employed along with the standard wall functions discussed earlier for turbulent quantities. At the exhaust, the zero gradient condition is applied where the flow becomes fully developed. An axisymmetric boundary condition is applied at the central axis, deduced from the experimental measurements (Landenfeld *et al.*, 1997).

At the fuel inlet, the following boundary conditions are applied. The inlet velocity is specified using the experimental data given by Landenfeld *et al.* (1997) and Landenfeld *et al.* (1998), where the bulk axial inlet velocity $U_{bf} = 21\text{ms}^{-1}$. This condition is applied uniformly across the inlet where the inlet pipe is long enough for flow development to occur. The radial and tangential velocities are both set to zero.

The turbulent kinetic energy was chosen in a similar manner to that of the isothermal case in chapter 4, studied experimentally by Al-Masseeh (1991). After some numerical experimentation to fit the predicted values of turbulent kinetic energy to experiments, it was found that,

$$\tilde{k}_f = (0.1U_{bf})^2, \tag{6.1}$$

gave the best approximation. The turbulent kinetic energy dissipation rate was also specified using a similar method in the manner of Hogg and Leschziner (1989), giving

$$\tilde{\epsilon}_f = \frac{\tilde{k}_f^{3/2}}{l_f}, \tag{6.2}$$

where $l_f = 1 \times 10^{-3}\text{m}$ is the length scale, equal to one third of the fuel inlet width.

The Favre mean mixture fraction and variance are specified as,

$$\tilde{\xi}_f = 1 \qquad \widetilde{\xi''^2}_f = 0 \tag{6.3}$$

where unity signifies a pure fuel stream for the Favre mean mixture fraction. The

effective viscosity at the fuel inlet is given, using the expression in equation (2.37), by

$$\mu_{eff,f} = 0.202\rho_f \frac{\tilde{k}_f^2}{\tilde{\epsilon}} + \mu \tag{6.4}$$

where $\rho_f = 0.6885\text{kg/m}^3$ for methane and $\mu = 1 \times 10^{-5}\text{Ns/m}^2$. The inlet temperature is set at 300K.

The air inlet is more complex than that of the fuel, due to the presence of swirl. The method for specification of the tangential velocity is analogous to that expressed for the case of Al-Masseeh (1991) discussed previously. Equation (4.6) is integrated using a triangular, piecewise profile of the form in equation (4.10) for W. The resultant value of the coefficient used to find the tangential velocity from equation (4.10) is calculated to be,

$$\gamma_{S=0.9} = 2.356 \quad . \tag{6.5}$$

The bulk velocity of the air at the inlet is specified uniformly across the boundary from the experiments of Landenfeld *et al.* (1997) as,

$$U_{ba} = 23\text{ms}^{-1} \quad . \tag{6.6}$$

As for the fuel inlet the value of turbulent kinetic energy is given by

$$\tilde{k}_a = (0.1U_{ba})^2, \tag{6.7}$$

with its dissipation prescribed using

$$\tilde{\epsilon}_a = \frac{\tilde{k}_a^{3/2}}{l_a}, \tag{6.8}$$

where $l_a = 3.75 \times 10^{-3}\text{m}$, corresponds to one quarter of the air annulus width. The Favre mean and variance of the mixture fraction at the air inlet are

$$\tilde{\xi} = 0 \qquad \widetilde{\xi''^2} = 0. \tag{6.9}$$

The effective viscosity is specified as

$$\mu_{eff,a} = 0.202\rho_a \frac{\tilde{k}_a^2}{\tilde{\epsilon}_a} + \mu, \tag{6.10}$$

where $\rho_a = 1.2865\text{kg/m}^3$ for air with the same viscosity as for methane. As for the methane jet, the Favre mean temperature is set to 300K.

The initial conditions for the interior of the domain need to be specified for Favre mean species mass fractions and temperature, so that combustion is initiated in the simulation. From the first moment of conditional mass fraction and temperature equations, (5.82) and (5.84), the convective, diffusive and turbulent transport terms are neglected, leaving two Poisson equations in conditional mixture fraction space,

$$\frac{\partial^2 Q}{\partial \eta^2} = -\frac{1}{\rho_\eta \chi_\eta}\langle W|\eta\rangle, \tag{6.11}$$

$$\frac{\partial^2 Q_T}{\partial \eta^2} = \frac{1}{\rho_\eta \chi_\eta}\left[Q_R - \left\langle \frac{q}{C_p}|\eta \right\rangle\right] \quad . \tag{6.12}$$

These equations are then solved to produce the conditional Favre mean mass and temperature profiles against mixture fraction that are then used as the initial conditions in the domain. Figure 6.3 shows the profiles for the conditional Favre mean temperature and species mass fractions.

6.3 Computational results

6.3.1 Aerodynamic quantities

The computed flow field is shown in figure 6.4 where the heat release is shown at the bottom of the figure and the streaklines and $\tilde{Y}_{CO}$ contours to the left and right of the symmetry axis, respectively. The main axial recirculation zone is seen to recirculate reaction products to the base of the flame as expected.

In the following analysis of computational results, Favre averaged quantities are given for the aerodynamic variables. The experimental data, however, is Reynolds averaged and so discrepancies exist when the density gradient is high. This happens

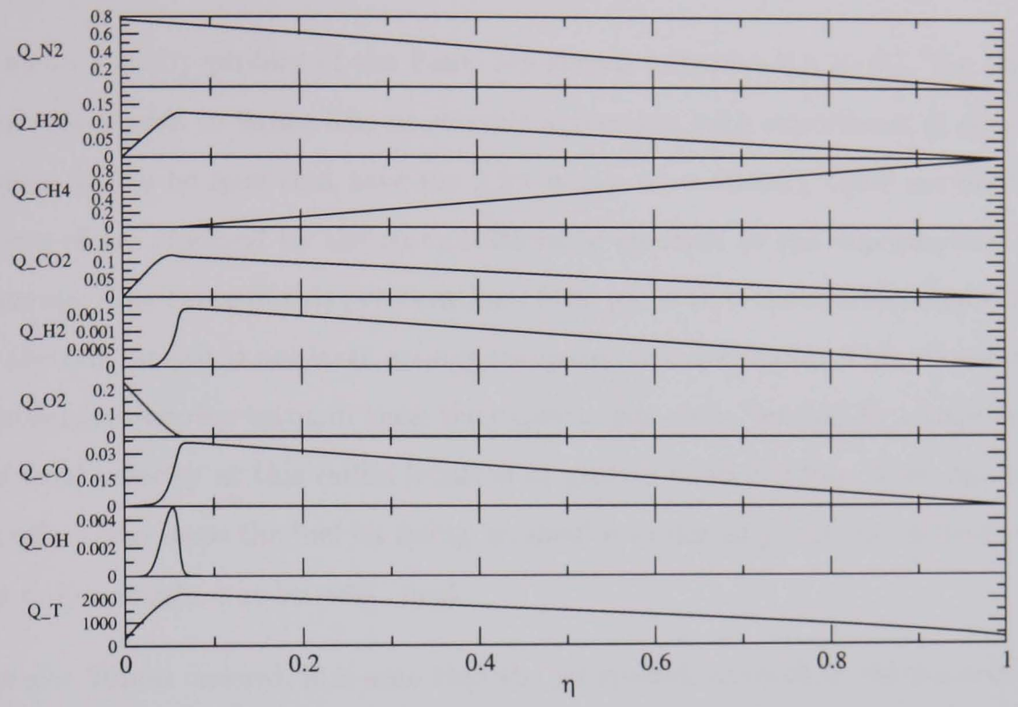

FIGURE 6.3: Initial profiles for conditional Favre mean species mass fractions and temperature.

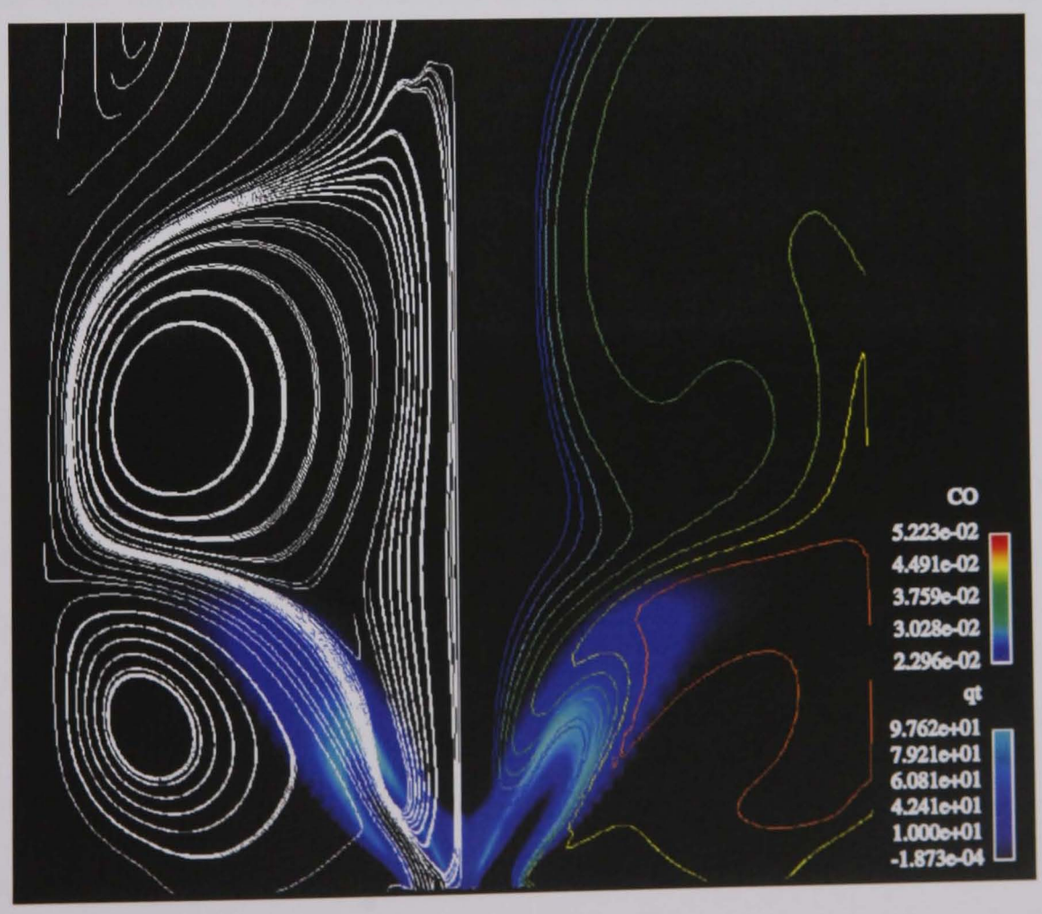

FIGURE 6.4: Computed flow field showing mean heat release rate, streaklines and CO mass fraction.

in the region of the flame close to the axis, where the temperature gradient is high.

The mean velocity profiles of the flame are shown in figures 6.5 to 6.7. For the axial velocity shown in figure 6.5, reasonable agreement with experiment is obtained. However, it can be seen that near the inlet nozzle ($x = 10$mm), there are distinctly two jets of gas resolved by the computations in contrast to the experimental measurements. The cause of this preservation of the jet, is that the reverse axial velocity near the central axis is not large enough compared to experiment. This allows the jet to persist further downstream than the experiments show, leading to a smaller negative axial velocity at this radial location at greater axial distance from the nozzle. This effect also stops the fuel jet being 'pushed' into the air jet as the measurements show only a single, but broader, peak.

From $x = 70$mm onward, it is seen that the jet spreads more than the experimental data shows. This is due to the loss of swirl near the central axis compared to that at other radial locations. The loss of swirl reduces the low pressure at the centre of the axial vortex. The force exerted on the fluid due to the low pressure can be seen as a counterbalance to the centrifugal force seen by the fluid as a consequence of the imparted swirl. As the tangential velocity decays too rapidly downstream near the axis, the force on the fluid due to the low pressure is reduced. However, this reduction is greater than that of the tangential velocity (after $x = 70$mm W is approximately constant in this region), resulting in the moving of the jet radially outward further downstream.

This result is corroborated by those shown in figure 6.6 for the mean radial velocities. The peak in the velocity profile is shifted radially outward, indicating the increased movement of the jet in this direction compared to experiment. Near the nozzle, it is seen that the computed results show two separate peaks, indicating that the fuel and air have not fully coalesced as the broad experimental peak shows. At $x = 20$mm, however, the computed results match those of the experiment, showing that the two independent peaks have merged albeit with an under-predicted size.

The tangential velocity profiles are shown in figure 6.7 showing the under-predicted values at axial locations $x = 70$mm and further for $0 < R < 0.025$. This contributes

directly to the under-predicted negative axial velocity as mentioned above. It can also be seen that the peak in tangential velocity at the jet is under-predicted from $x = 10$mm to $x = 30$mm denoting a premature decay of swirl compared to the experimental measurements. Further downstream, an annulus of tangential velocity is formed at a greater radial distance than the experimental results show. Indeed, the experiments predict the formation of two concentric annuli in the downstream region.

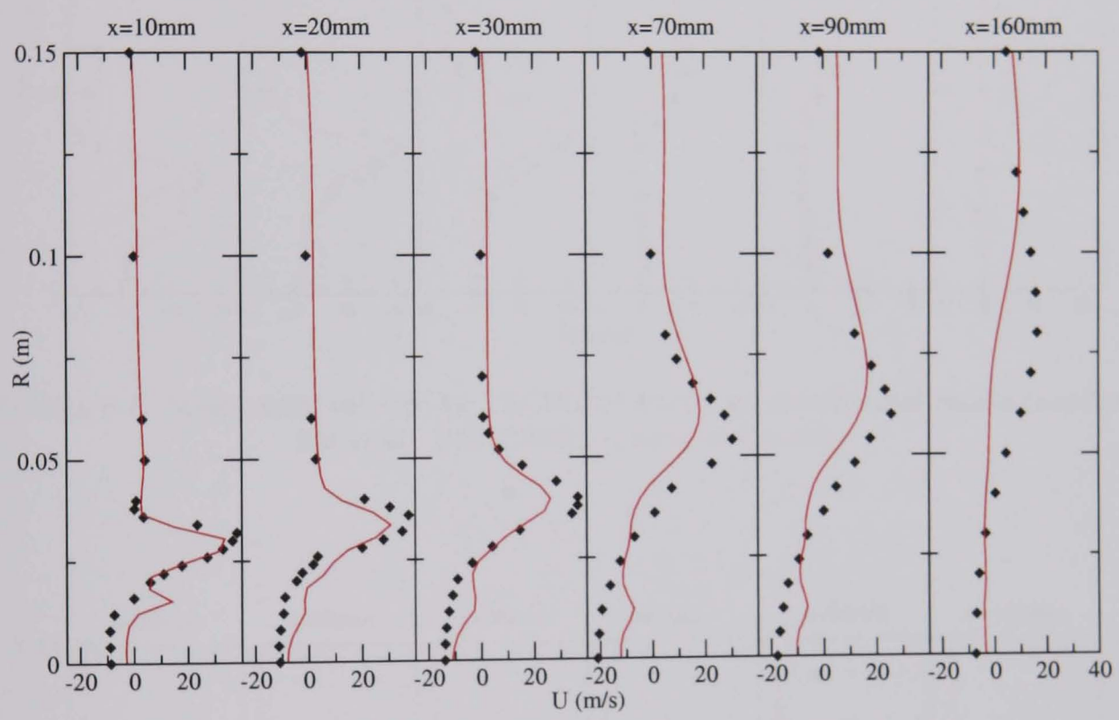

FIGURE 6.5: Mean axial velocity for TECFLAM flame: ♦, experimental results (Landenfeld *et al.*, 1997, 1998); −, computed result.

The components of the Reynolds stress tensor are shown in figures 6.8 to 6.12. At the nozzle the square root of the axial normal stress component does not resolve the different peaks shown by the experimental measurements of RMS fluctuating axial velocity (see figure 6.8). This is also a feature exhibited by the computed radial and tangential normal stress components as shown in figures 6.9 and 6.10. The primary reason for this discrepancy between computed and measured data is that the normal Reynolds stresses were prescribed at the inlet using k instead of a full anisotropic specification. To the author's knowledge, the only way to remedy this situation is to use experimental data for the input quantities, as for Kitoh's case previously. This, however, brings mass conservation difficulties due to the recirculation across

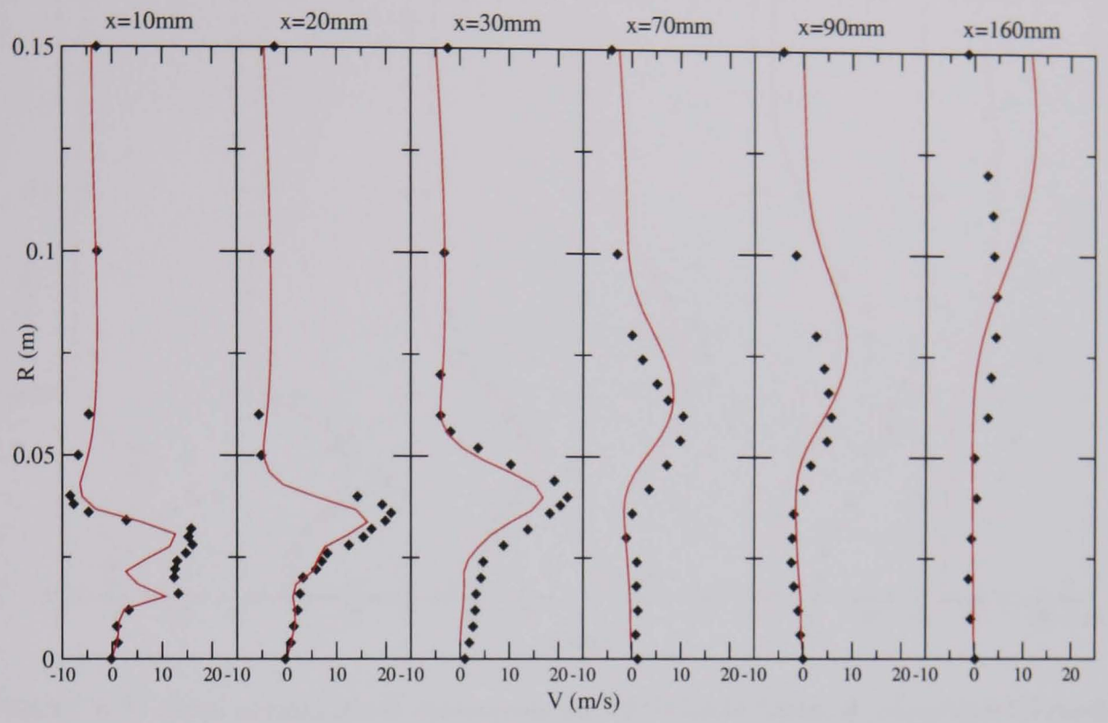

FIGURE 6.6: Mean radial velocity for TECFLAM flame: ♦, experimental results (Landenfeld *et al.*, 1997, 1998); −, computed result.

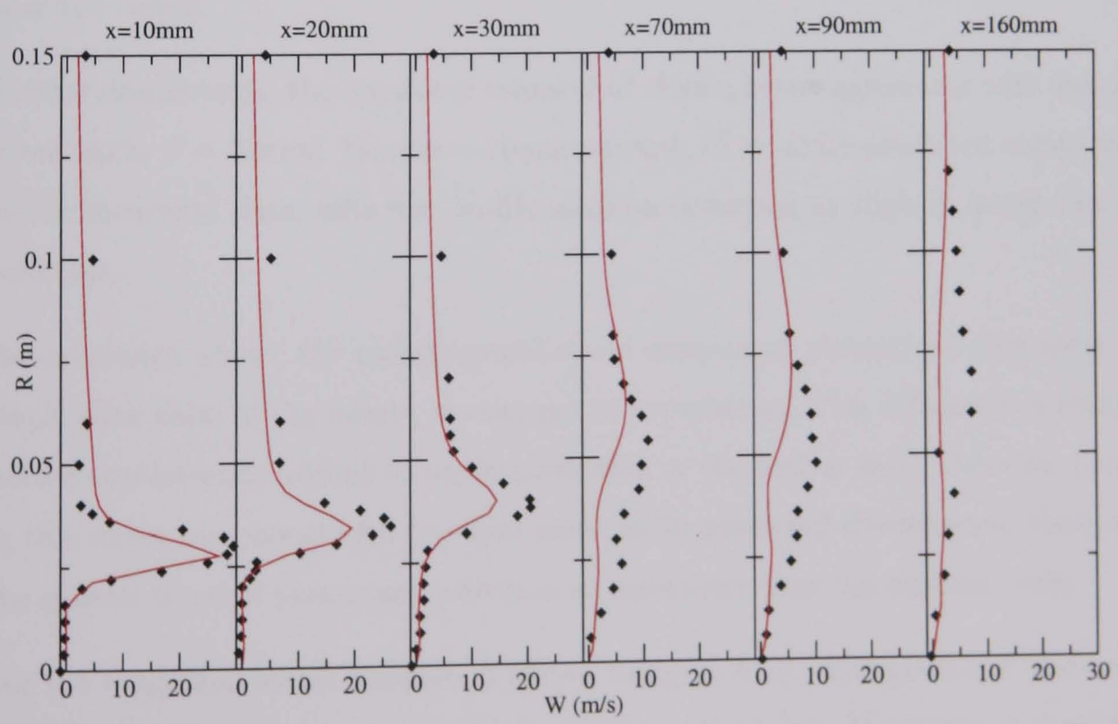

FIGURE 6.7: Mean tangential velocity for TECFLAM flame: ♦, experimental results (Landenfeld *et al.*, 1997, 1998); −, computed result.

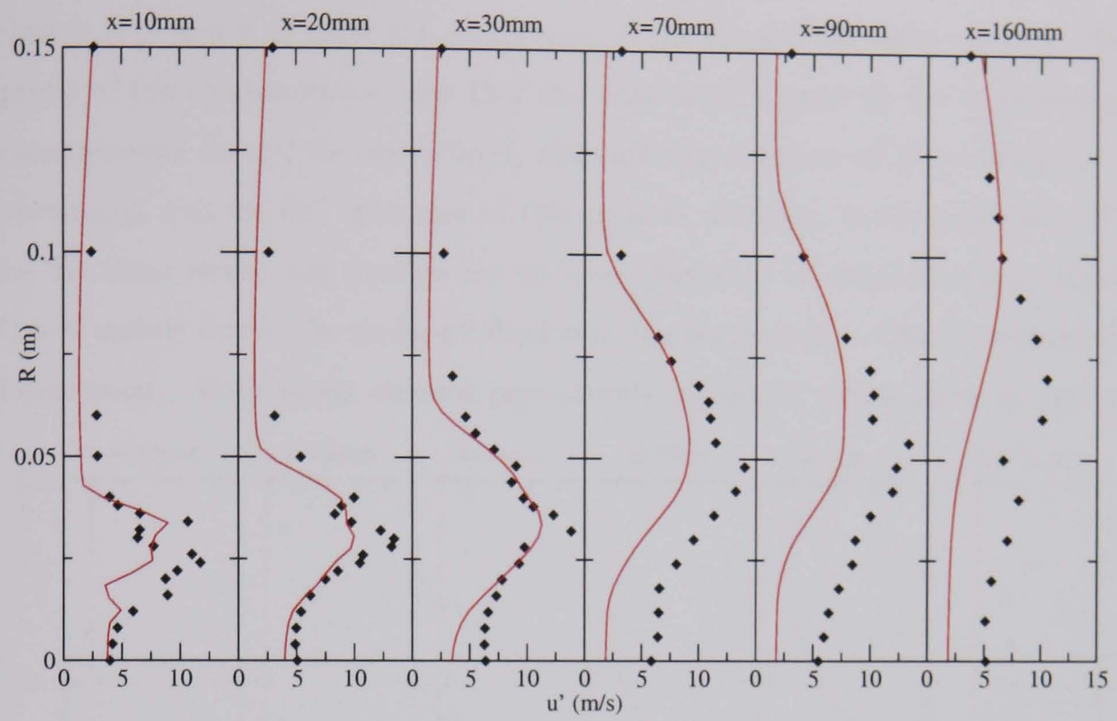

FIGURE 6.8: Axial normal stress component for TECFLAM flame: ♦, experimental results (Landenfeld *et al.*, 1997, 1998); −, computed result.

the inlet plane. Also the strength of k at the fuel jet is too small compared to that at the air jet, resulting in the loss of the double peak for the normal stress components near the nozzle.

Further downstream, the computed values of $\overline{u^2}$ show a better agreement with experiment up to $x = 30$mm. From $x = 70$mm onward, $\overline{u^2}$ is under-predicted compared to the measured data, with the profile maxima occurring at slightly larger radial positions.

As mentioned above, the radial normal stress component predictions only show a single peak close to the nozzle, in contrast to experiment. This deficiency is transported downstream, leading to under-prediction at the central axis. The main peak in this stress component also becomes more under-predicted downstream, showing the general trend of premature reduction of turbulence near the chamber axis.

For the tangential stress component shown in figure 6.10, the agreement with experiment at $x = 20$mm and $x = 30$mm is better than the other normal stresses, as both peaks are resolved. The central axis region is still under-predicted and the flow returns to a more isotropic state downstream at $x = 160$mm.

Figures 6.11 and 6.12 show the predictions of the $\overline{uv}$ and $\overline{uw}$ shear stresses. The results of the computations show that the finer detail gained by the experimental measurements cannot be reproduced, although the location of the main peak is reproduced well for $\overline{uv}$. The size of this peak is, however, under-predicted. For the $\overline{uw}$ shear stress, the profiles are under-predicted at all axial locations shown. This is mainly due to the under-prediction at the nozzle region, that is transported downstream. Both shear stresses prematurely return to values close to zero at

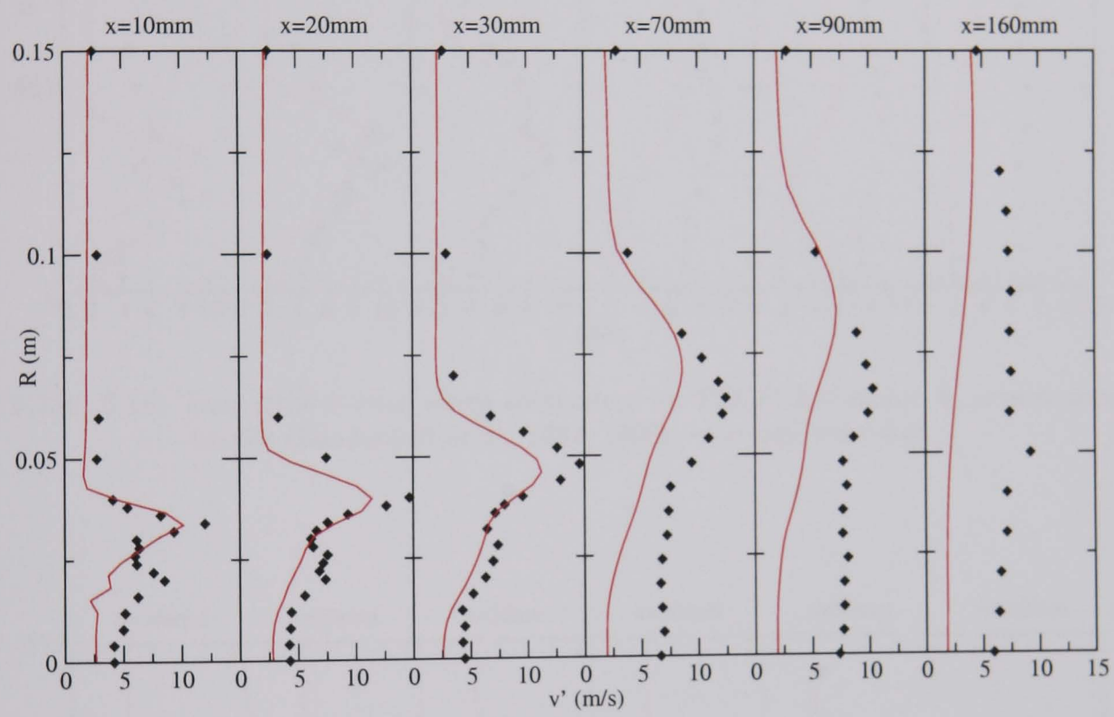

FIGURE 6.9: Radial normal stress component for TECFLAM flame: ♦, experimental results (Landenfeld *et al.*, 1997, 1998); −, computed result.

$x = 160$mm.

6.3.2 Reaction related quantities

The predictions concerned with the combustion in the flow are shown in figures 6.13 to 6.22. The temperature predictions show good agreement with the experimental measurements for all axial locations shown in figure 6.13. As axial distance increases from the nozzle, the temperature prediction becomes smaller than the measured data at $R \approx 0.025$m. This indicates the presence of incomplete combustion in this region, as shown by the higher than expected level of CO, and overestimated level of O_2

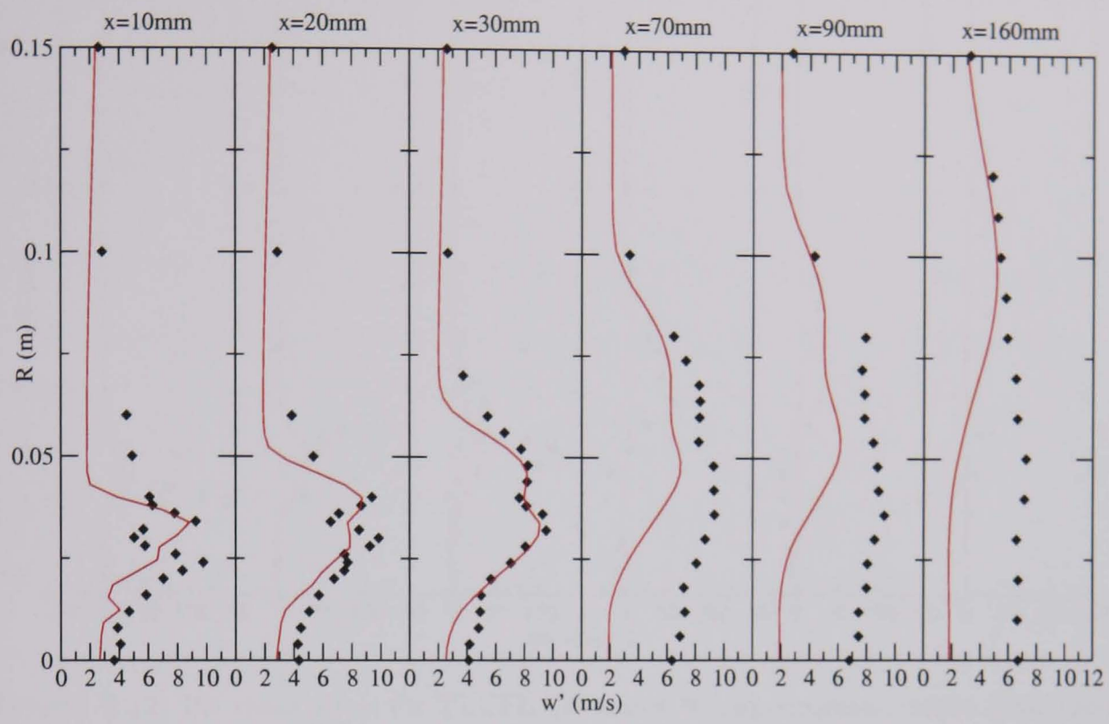

FIGURE 6.10: Tangential normal stress component for TECFLAM flame: ♦, experimental results (Landenfeld *et al.*, 1997, 1998); −, computed result.

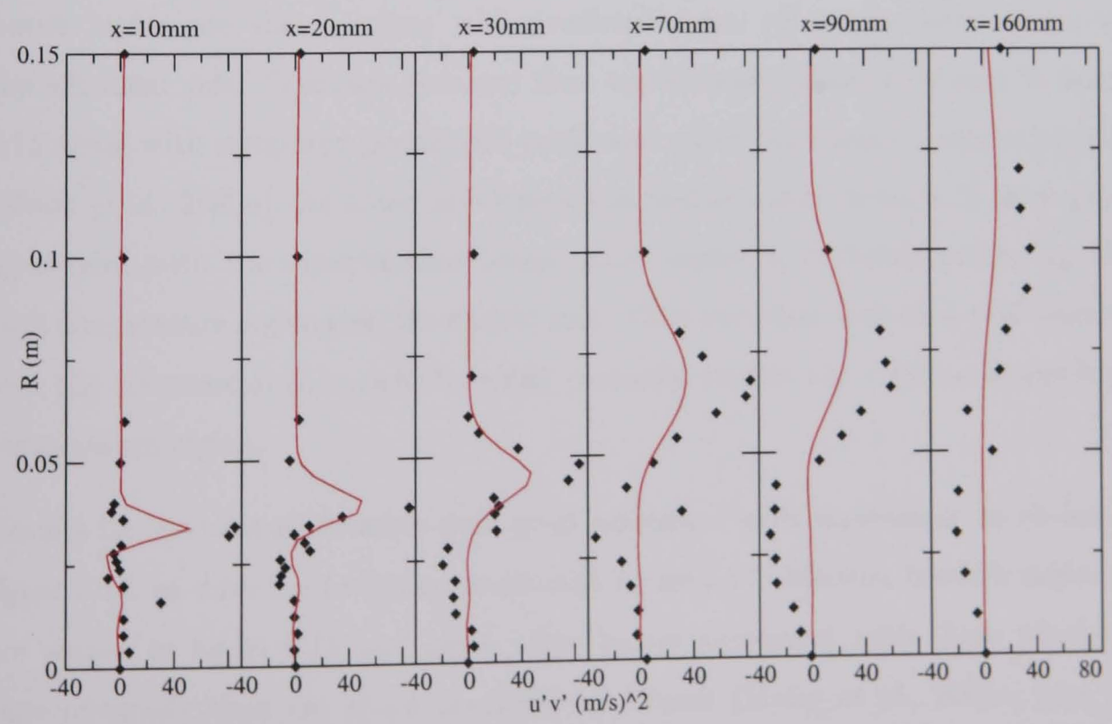

FIGURE 6.11: $\overline{uv}$ shear stress for TECFLAM flame: ♦, experimental results (Landenfeld *et al.*, 1997, 1998); −, computed result.

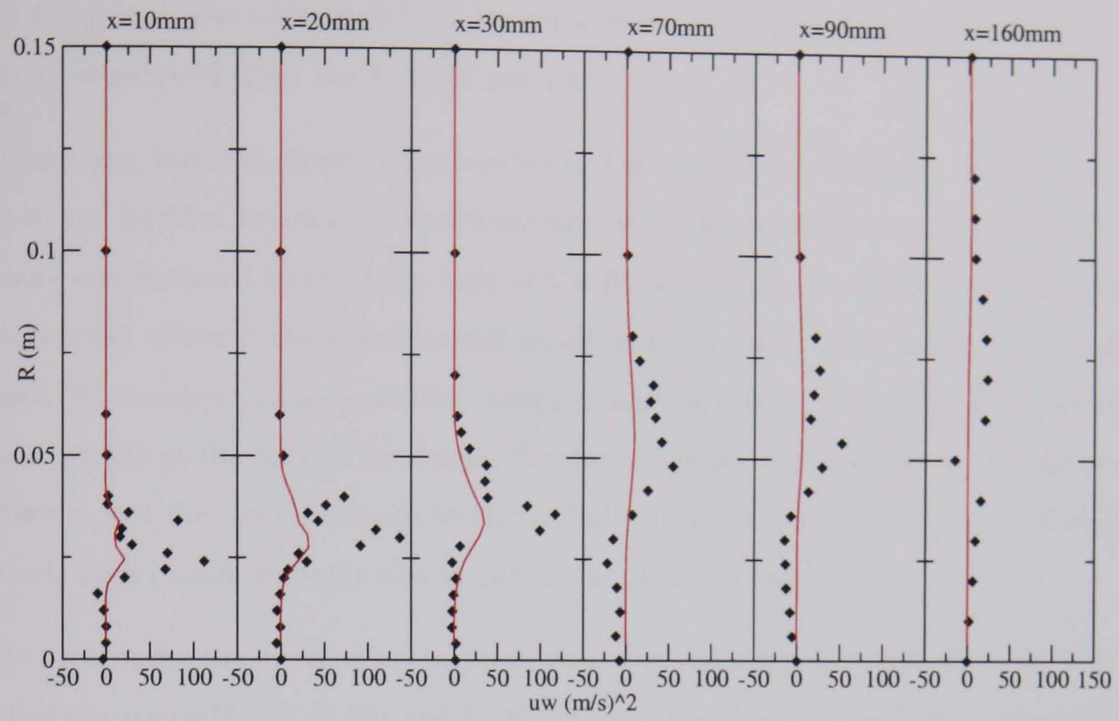

FIGURE 6.12: $\overline{uw}$ shear stress for TECFLAM flame: ♦, experimental results (Landenfeld *et al.*, 1997, 1998); −, computed result.

(see figures 6.21 and 6.22).

On the right hand side of figure 6.14, the predicted temperature contours in the nozzle region are shown, along with predicted mean volumetric heat release on the left hand side. Contours obtained from experimental data are shown in figure 6.15 along with computed predictions performed using the Fluent commercial code (Meier *et al.*, 2000*a*). As noted previously, the predictions in figure 6.13 show good agreement with the experimental temperature contours, correctly predicting the high temperature region near the central axis. They also show increased performance over the commercial code, which cannot correctly predict the location of the high temperature region.

Results for the mixture fraction show good agreement with experiment, as shown in figure 6.16, as does the fuel mass fraction in figure 6.17. Mixture fraction contours are shown in figure 6.18 and again show better agreement with those obtained experimentally than the those predicted by Fluent (Meier *et al.*, 2000*a*) seen in figure 6.19. This is probably due to the use of the LRR model for the Reynolds stresses in the Fluent code. For strongly swirling flows, such as Kitoh's swirling flow

in Chapter 4, the LRR model has shown a tendency to predict premature decay of swirl, which will effect the fuel/air mixing.

There are, however, some discrepancies in the current predictions. The region of mixture fraction around the stoichiometric value for methane-air ($\xi = 0.0551$) is more concentrated towards the base of the flame and the central axis for the computations, whereas the experimental result shows a much larger axial penetration into the chamber. This shows that computationally, the air and methane are mixing too quickly at the base of the flame. Similar behaviour is shown by the Fluent prediction, but the fuel jet extends too far radially outward compared to the predictions made here (again probably due to premature decay of swirl).

The reason for the discrepancy in prediction of mixture fraction must lie in the modelled equations (5.32), (5.33) and (5.36). These equations use modelling taken from a direct analogy of the LRR second moment closure of the aerodynamic quantities. This assumption of similarity between combustion related transport and aerodynamic transport is shown to break down.

The CO_2 mass fraction shown in figure 6.20, is under-predicted compared to the experimental result. Close to the central axis, the value is largely under-predicted for the axial locations shown. This shows that this reaction product, largely fed back to the root of the flame via the swirl induced reverse axial velocity, is not produced by the flame in as high a quantity as expected. Again, this evidence supports the presence of incomplete combustion in the flame as shown by the high levels of CO outside the main oxygen jet (figure 6.21).

The main concentration of CO is at a higher radial value than that of the inlet jet position. Figure 6.4, shows that the main concentration of CO lies in the corner recirculation. This indicates that the part of the flame closest to the wall is producing CO. As expected, the concentration of CO reduces as the hot reaction products approach the exhaust.

The O_2 mass fraction profiles are shown in figure 6.22. In general, good agreement with experiment is obtained, however, the mass fraction of this species is overestimated. The main regions of the flow where this occurs is at the central axis and

at the inlet jet. As would be expected, the inlet jet is high in oxygen due to the air inlet. However, the overestimation in this region suggests that less oxygen is being used for combustion in the flame. This is clearly shown by the decrease in the

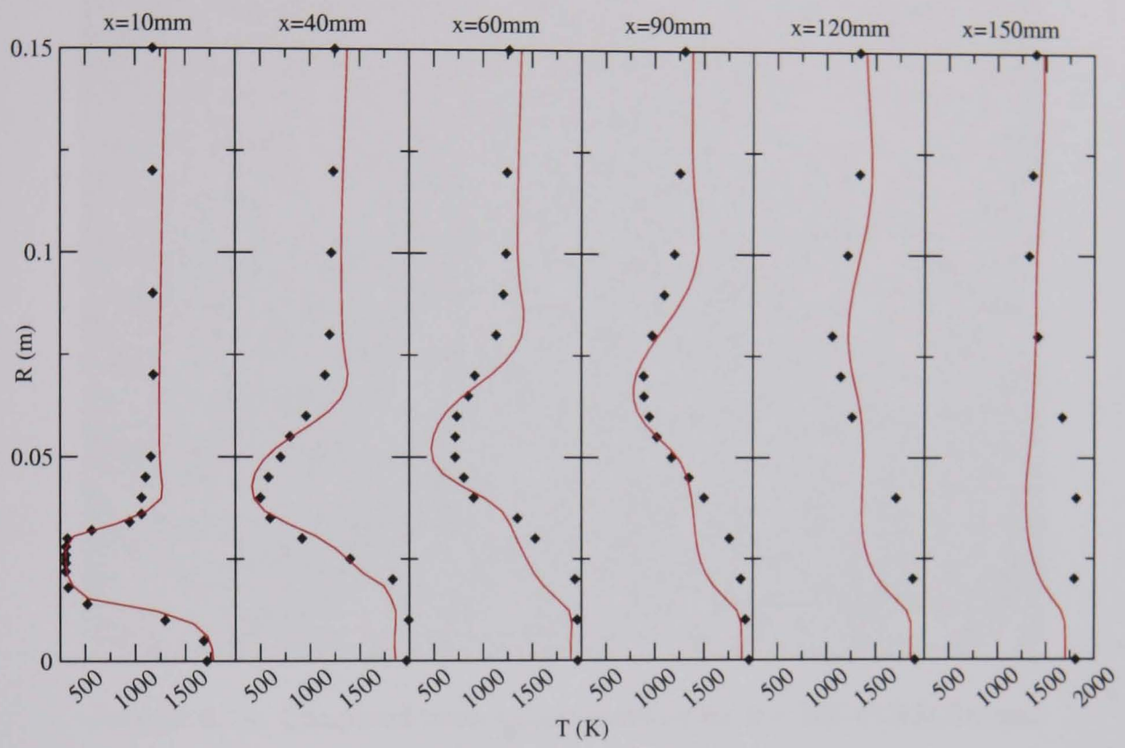

FIGURE 6.13: Temperature profiles for TECFLAM flame: ♦, experimental results (Bergmann *et al.*, 1998; Meier *et al.*, 2000*b*); −, computed result.

mass fractions of the H_2O (figure 6.23) and CO_2 reaction products in the flame/jet region.

At the axis region, the excess oxygen present can once again be explained using the mass fraction predictions of the reaction products. CO, CO_2 and H_2O mass fractions are all under-predicted at the axis. As the oxygen in the flame/jet region is not being consumed by the combustion process, the axial recirculation that feeds reaction products back to the root of the flame carries the excess oxygen along the axis.

The computational predictions of H_2O mass fractions are close to the experimental measurements except in the flame/jet region and the central axis. Again this is due to the lack of consumption of oxygen in the flame raising its own mass fraction and lowering those of other species.

The strain rate of the flame is an important factor due to its ability to stretch and

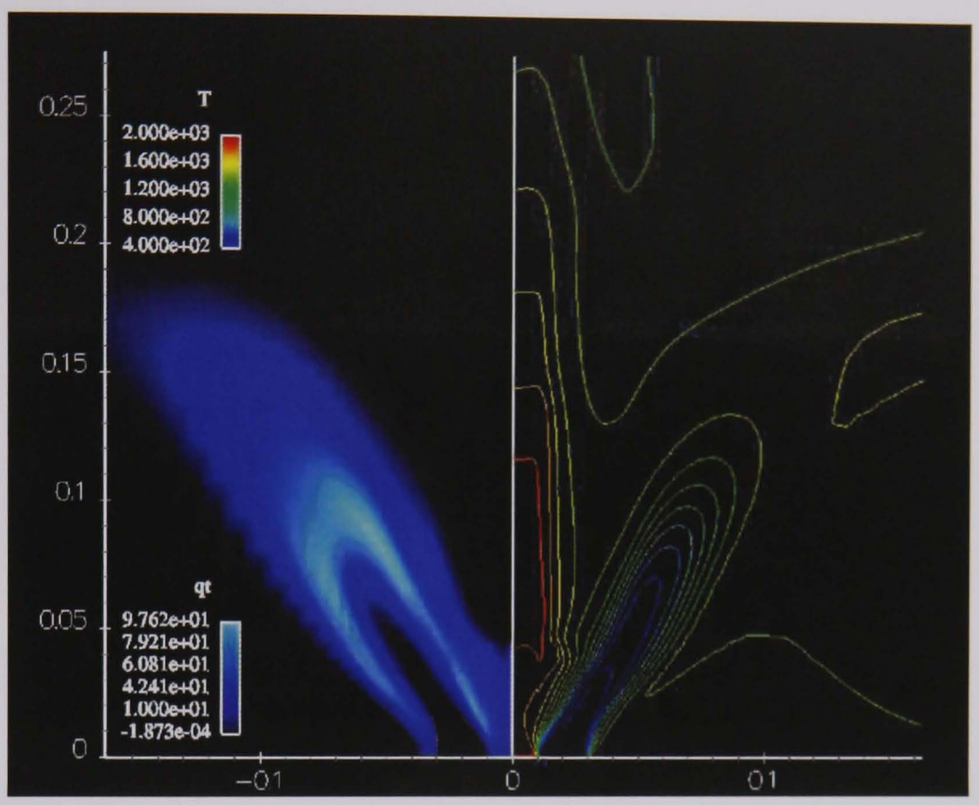

FIGURE 6.14: Computed temperature contours for the TECFLAM burner.

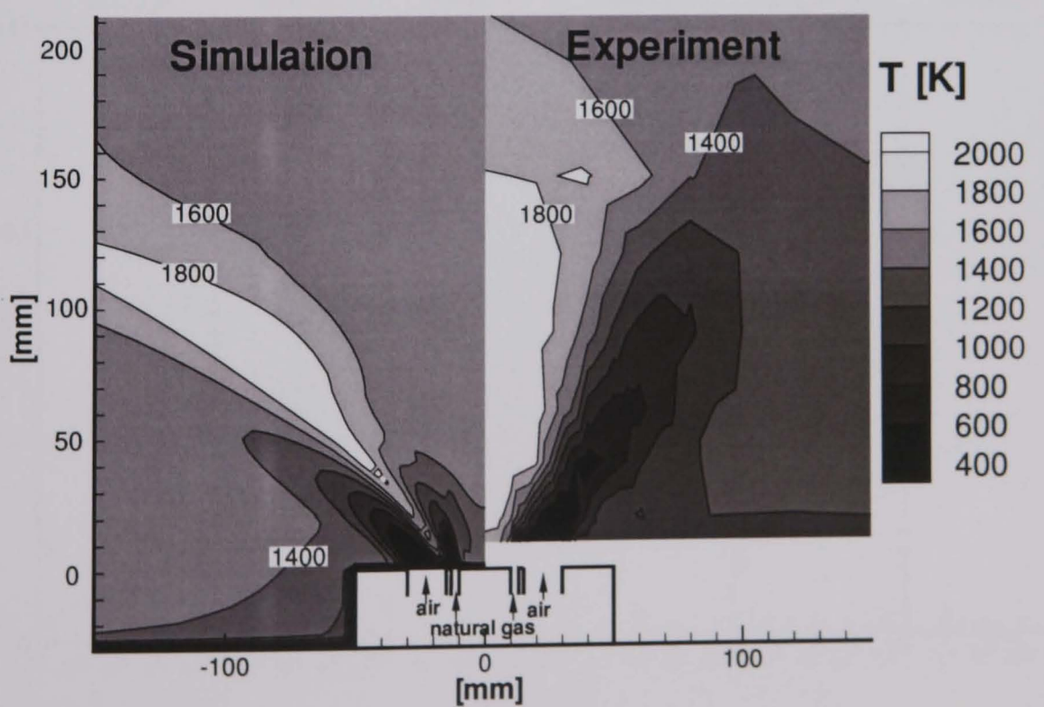

FIGURE 6.15: Measured and computed temperature contours for the TECFLAM burner (Meier *et al.*, 2000*a*).

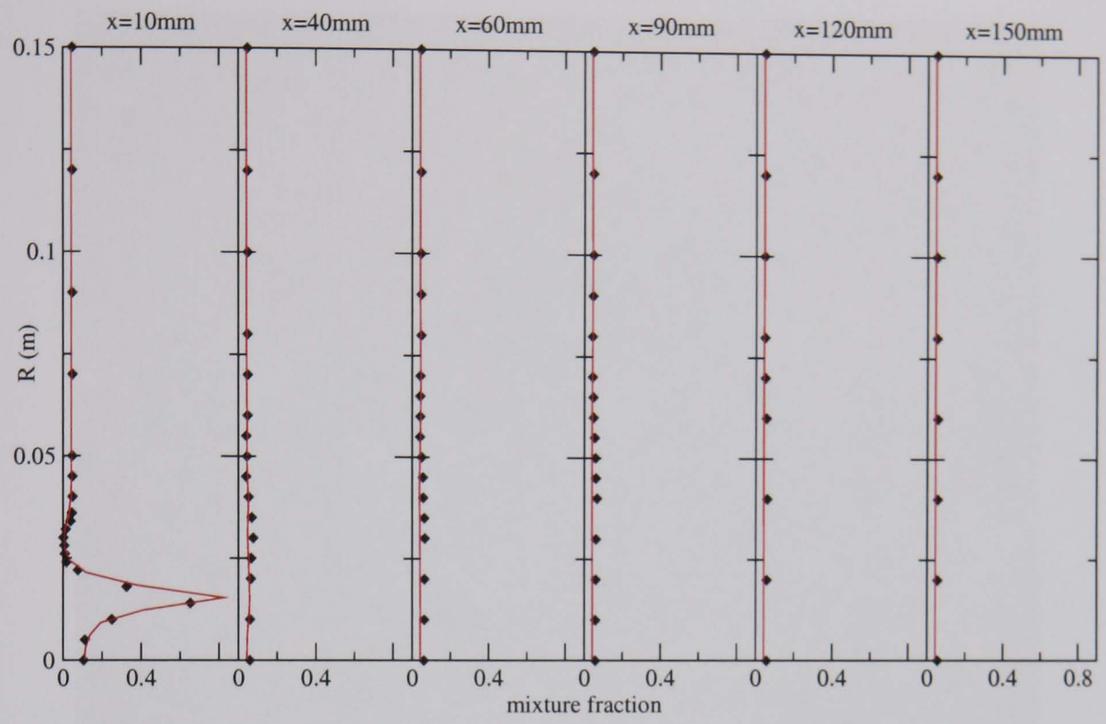

FIGURE 6.16: Mixture fraction profiles for TECFLAM flame: ♦, experimental results (Bergmann *et al.*, 1998; Meier *et al.*, 2000*b*); −, computed result.

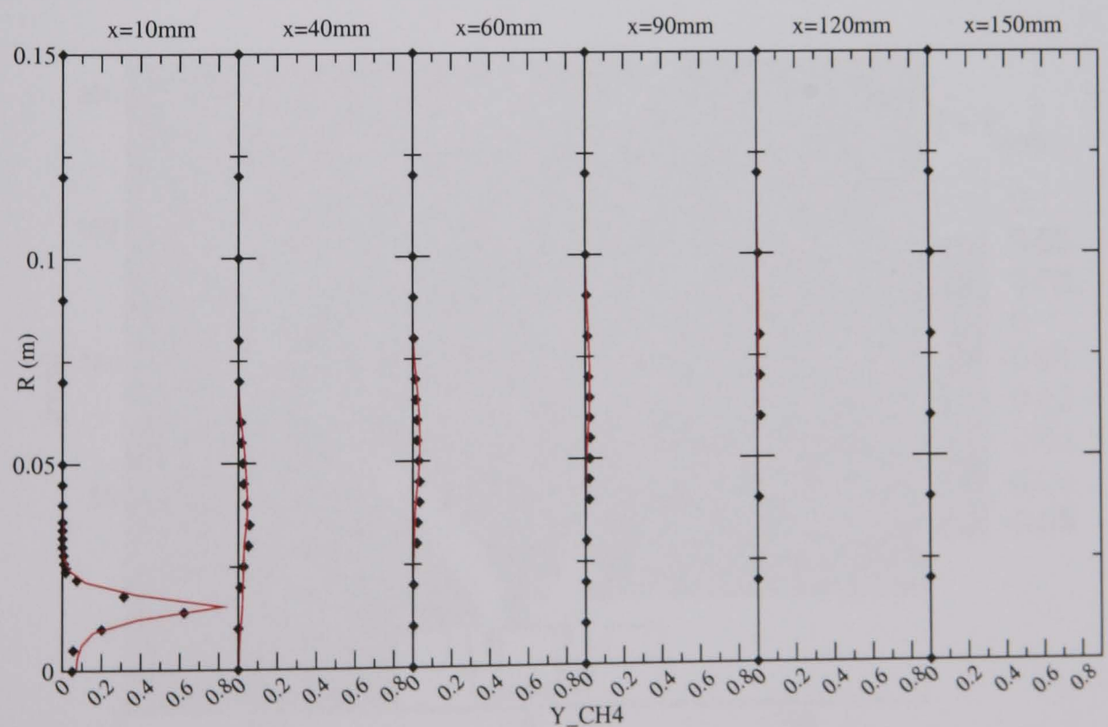

FIGURE 6.17: CH_4 mass fraction profiles for TECFLAM flame: ♦, experimental results (Bergmann *et al.*, 1998; Meier *et al.*, 2000*b*); −, computed result.

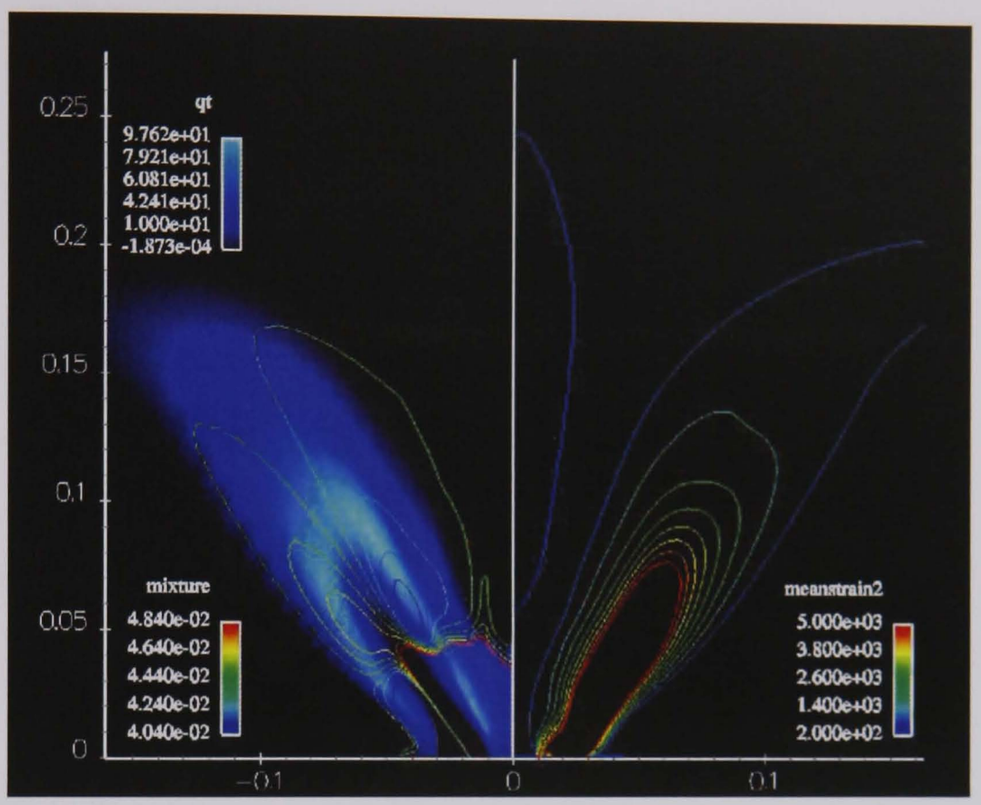

FIGURE 6.18: Mixture fraction and mean strain contours for the TECFLAM burner.

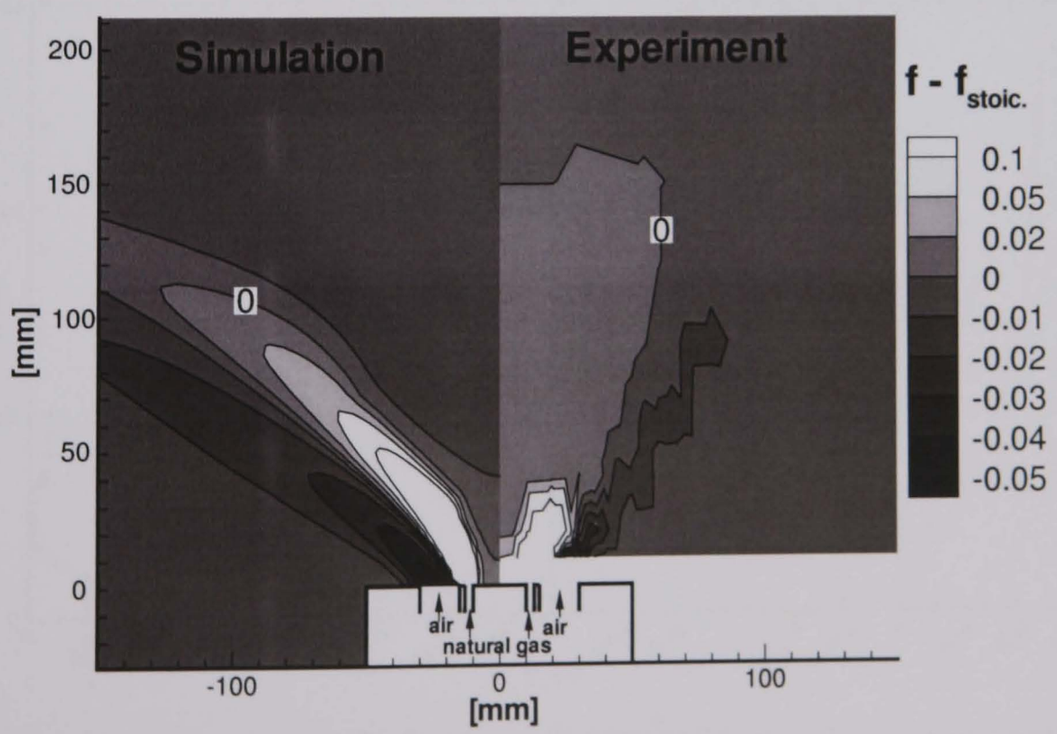

FIGURE 6.19: Measured and computed mixture fraction contours (Meier *et al.*, 2000*a*).

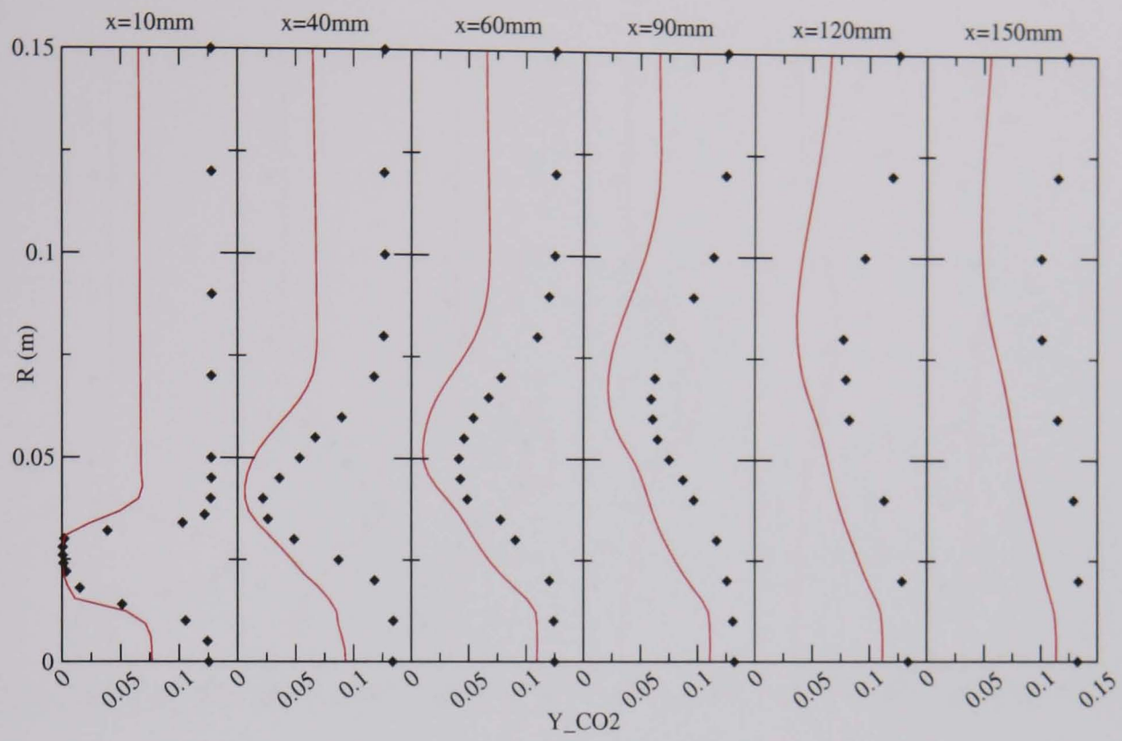

FIGURE 6.20: CO_2 mass fraction profiles for TECFLAM flame: ♦, experimental results (Bergmann *et al.*, 1998; Meier *et al.*, 2000*b*); −, computed result.

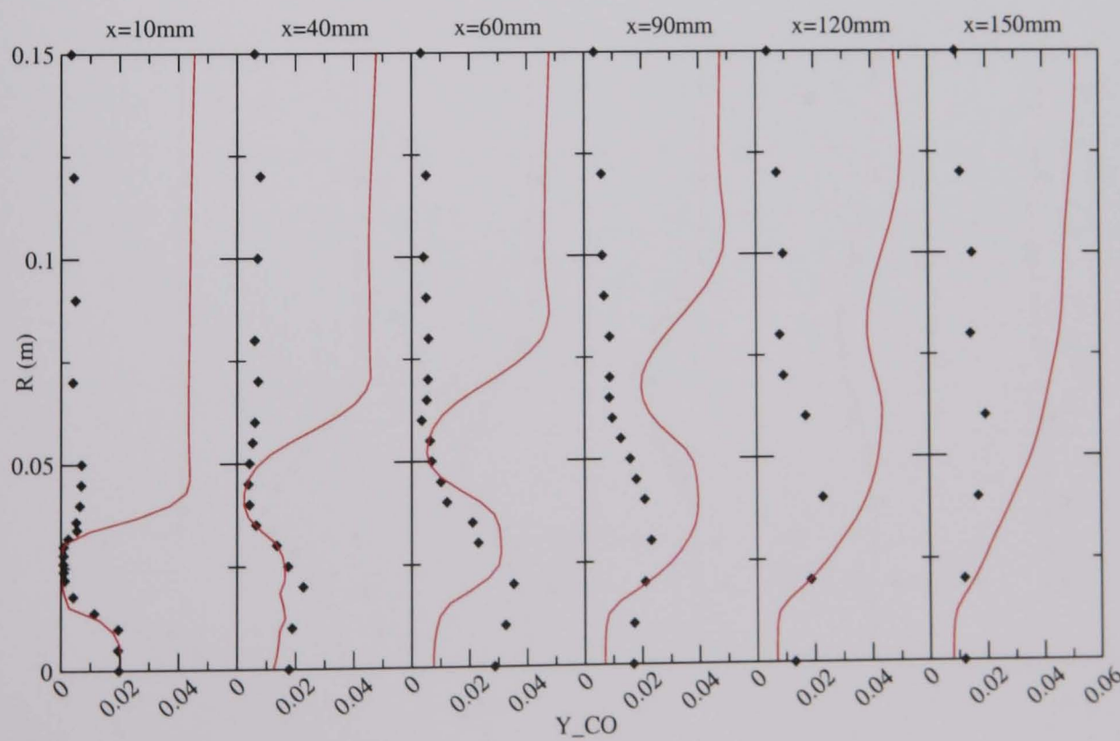

FIGURE 6.21: CO mass fraction profiles for TECFLAM flame: ♦, experimental results (Bergmann *et al.*, 1998; Meier *et al.*, 2000*b*); −, computed result.

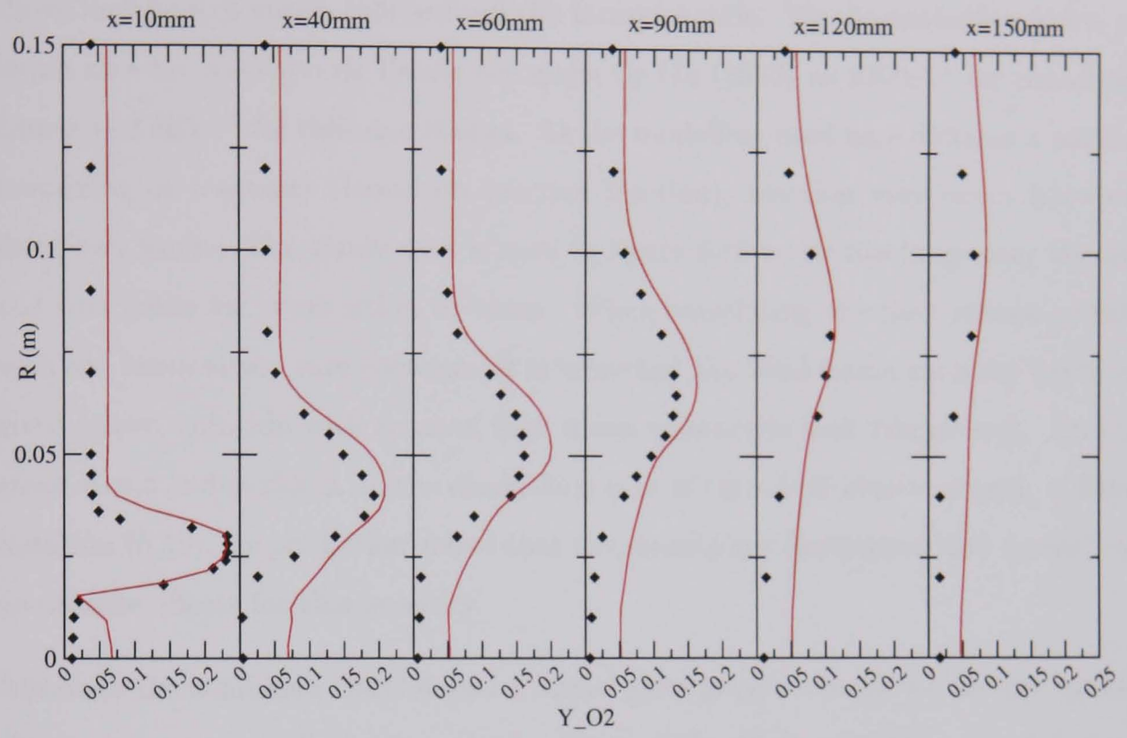

FIGURE 6.22: O_2 mass fraction profiles for TECFLAM flame: ♦, experimental results (Bergmann *et al.*, 1998; Meier *et al.*, 2000*b*); −, computed result.

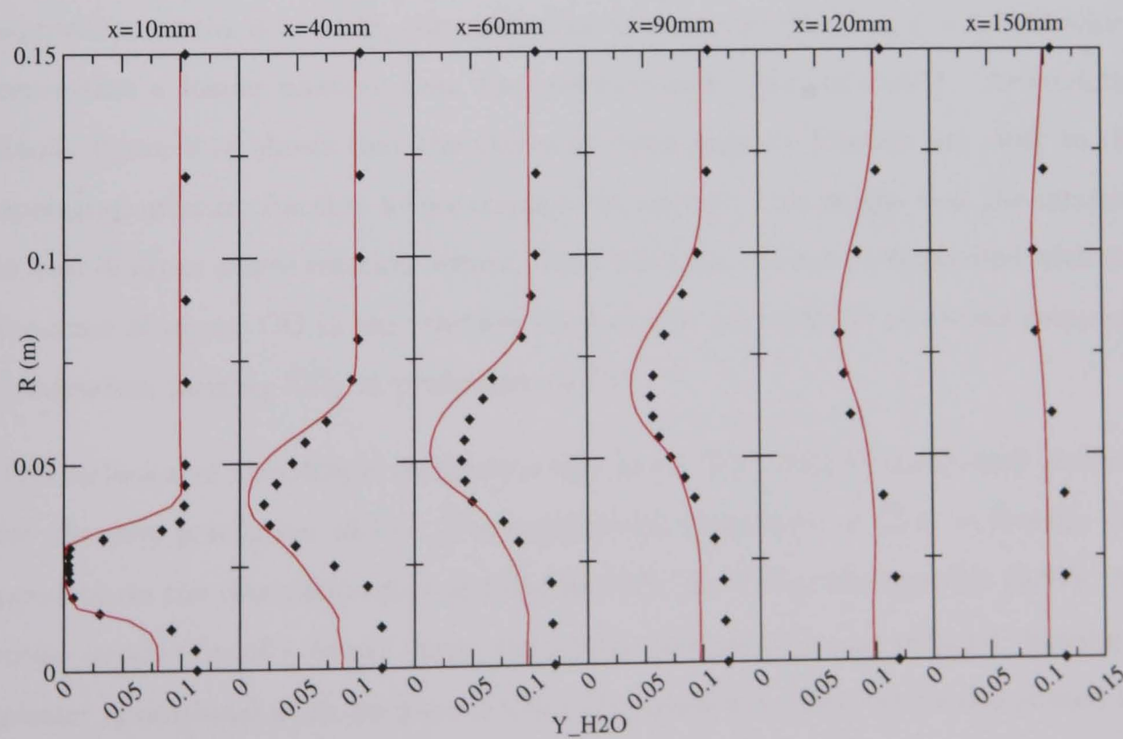

FIGURE 6.23: H_2O mass fraction profiles for TECFLAM flame: ♦, experimental results (Bergmann *et al.*, 1998; Meier *et al.*, 2000*b*); −, computed result.

extinguish the flame, as well as effect the flame reactant concentrations. Figure 6.18 shows contours of strain rate around the burner nozzle. The flammability limits of strain rate for methane-air flames are given by Gu (1993) as $2200s^{-1}$ for premixed flames and $360s^{-1}$ for diffusion flames. As the modelling used here dictates a partial premixing of reactants (based on mixture fraction), reaction may occur between these two limits. The strain rate is seen in figure 6.18 to be too large near the air and fuel inlets for combustion to occur. When correlating the heat release profile with the mean strain rate contours, it is seen that the ideal strain rates for reaction given above, coincide with areas of high mean volumetric heat release rate. As the mean strain is dependent on the dissipation rate of turbulent kinetic energy, ϵ, from equation (5.16), its prediction shows that the anisotropic dissipation rate model has no adverse effects for this quantity.

Although the combined CMC-flamelet model gives good accuracy for the prediction of temperature as well as the mass fractions of O_2, H_2O and CH_4, it is found to be unsatisfactory for the prediction of CO and CO_2 mass fractions. The main discrepancy is the presence of excess CO in the corner recirculation and the lack of CO_2 in the flow field. The experimental burner is operated with an overall equivalence ratio, $\phi = 0.833$, corresponding to a mixture fraction, $\xi = 0.0463$ which represents a leaner mixture than the stoichiometric value of 0.0551. Around the flame, figure 6.18 shows that the values of mean mixture fraction are close to the operating mixture fraction where combustion occurs. This means that the mixture is lean in areas where reaction occurs. This, however, cannot be reconciled with the presence of excess CO in the reaction products, as a lean flame promotes complete combustion forming CO_2 in preference to CO.

The inclusion of anisotropic dissipation rate in the SSG-ADRM model may account for the over-prediction of CO. The conditional dissipation of Q_{CO} is directly dependent on the dissipation rate of turbulent kinetic energy via equation (5.97). An under-prediction of ϵ would cause the scalar dissipation to be reduced, leaving a greater conditional mass fraction of CO to be predicted. This can be discounted by comparison with the isothermal results for the case of Al-Masseeh (1991) in figure 4.52. At the inlet of the annular jet in figure 4.52, the value of ϵ is under-predicted

compared to the other model predictions. However, at the 30mm axial location, the value of ϵ is comparable in size to the predictions of the other models.

The explanation for the excess CO can be shown to be a limitation of the flamelet model methodology. When the reaction time, and hence flame thickness, can be considered to be smaller than the Kolmogorov time and length scales, the assumption of the flamelet may be used to model the thin reaction zone without having to resolve this zone computationally (i.e. using DNS). The combustion reaction producing CO qualifies to be approximated using the flamelet model as shown by its rapid formation in figure 6.24 for a C_3H_8-air flame (Dibble *et al.*, 1999)

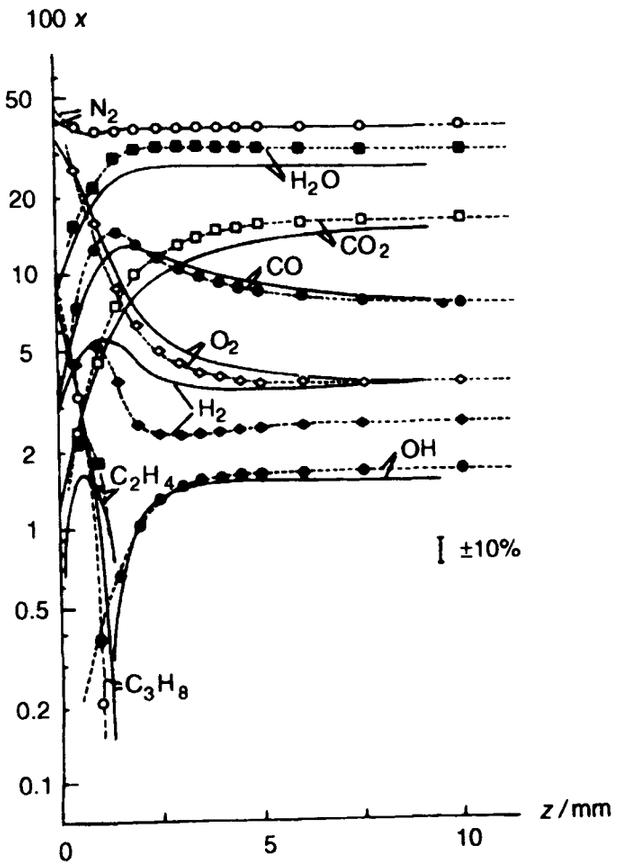

FIGURE 6.24: Flame structure in a C_3H_8-air flame (Dibble *et al.*, 1999).

At $z > 2.5$mm, the mass fraction of CO is seen to drop, along with that of O_2, with a corresponding rise in the mass fraction of CO_2. This is the oxidation layer described by Williams (2000) where reactions such as

$$3H_2 + O_2 \rightleftharpoons 2H_2O + 2H,$$

$$CO + H_2O \rightleftharpoons CO_2 + H_2. \tag{6.13}$$

occur, serving to remove CO from the reaction products. The oxidation layer extends to a larger distance than the main reaction layer, indicating that the actual flame thickness is larger than that assumed by the laminar flamelet model. The above reactions, therefore, are not included in the laminar flame library at this distance from the main reaction. This has the effect of stopping the production of CO_2 from CO, leading to the observed excess mass fraction of CO.

A way of modelling this behaviour could be to use the full CMC closure for the combustion terms (Klimenko and Bilger, 1999) or solution of the joint scalar pdfs via a Monte-Carlo method (Roekaerts, 2002) removing the need for flamelet modelling, but significantly increasing the computational cost. An extension of the flamelet model to take into account formation of oxides in the oxidation layer would involve modification of the mass formation rate source term in equation (5.90). To affect this, the removal of the dependency of (5.90) on flammability limits of flame stretch and mixture fraction to allow reaction outside the main reaction zone, is needed.

6.4 Summary of main results

The aerodynamic quantities were generally well predicted. The boundary conditions at the inlet are shown to be a source of discrepancy between computational and experimental results. This occurs due to the inability to provide adequate boundary conditions at the annular apertures for the fuel and air stream, necessitating the use of extended inlet pipes in an attempt to capture the recirculations present across the aperture plane.

Mean velocities are predicted well except for an under-prediction of axial and tangential velocity at the chamber axis. The position of the inlet jets are predicted at higher radial positions than the experimental results show downstream of the $x = 70$mm axial position. This is due to the decay of the tangential velocity at the centreline and also the expansion of the fluid in this region due to the onset of reaction and the associated increase in temperature. Some discrepancy is due to the

comparison between Favre averaged computational results and Reynolds averaged experimental data, as large variations in density occur in the region of the flame.

The predictions are underestimated for the turbulent stresses mainly due to the specification of k at the inlet boundary. The shear stresses are especially underpredicted indicating a premature isotropisation of the turbulence, together with its premature decay.

The reaction dependent quantities such as temperature, mixture fraction and species mass fraction are also in good agreement with experiment. The major differences are in the prediction of the mixture fraction and mass fraction of CO. The computed mixture fraction field is seen not to stretch out as far in the axial direction when compared to experiment, indicating a premature mixing of fuel and air. This is attributable to the inadequate modelling used for the mixture fraction related equations. The SSG-ADRM model is seen to provide adequate results due to the correct prediction of the mean strain in the flow.

The discrepancy between predicted and measured Favre mean mass fraction of CO lies in the limitation of the flamelet assumption. The flame thickness when including the oxidation of CO becomes larger than the laminar flame from which the chemical kinetic data is retrieved from the flame library.

Chapter 7

Conclusions and Suggestions for Further Research

Contents

7.1 Conclusions

The main research objective of this thesis was to provide methods for the accurate simulation of turbulent swirling flow and, where the situation arises, the prediction of reacting flow. Large Reynolds stress anisotropies were modelled, in the cases studied, using the differential second moment closure method for the RANS equations. To simulate the effect of anisotropy of the dissipation for the Reynolds stresses, an algebraic anisotropic dissipation rate model for the turbulent kinetic energy has been incorporated into the closure.

For flows involving combustion, a premixed laminar flamelet model has been used conditioned on the mixture fraction of the fluid to account for non-premixed combustion. The effect of flame stretch is embedded in the model, allowing prediction of the effects of turbulence on the flame due to the local fluctuation of velocity. By modelling the effects of flame stretch by straining, the turbulent kinetic energy dissipation rate is introduced into the flamelet model, thereby adding the effects of dissipation anisotropy.

A solution method using the SIMPLE or PISO solution algorithms has been shown to work robustly and accurately for laminar and turbulent flows. The higher order SMART and CUBISTA convection schemes have been used to increase accuracy at little additional computational cost, whilst maintaining boundedness of the solution - an important consideration for the realisability of turbulent flows.

7.1.1 Isothermal flows

As expected, the two-equation turbulence models used are incapable of accurately predicting the nature of swirling confined flows. The inability to predict differences in the normal Reynolds stresses, severely limits their ability to describe secondary flows (in this case the propagation of swirl by the tangential and radial Reynolds stress components). For the swirling case studied by Al-Masseeh (1991), the computed results for mean velocity show a qualitative agreement in the near field of the jet, but the agreement is reduced downstream, where solid body rotation is pre-

dicted. For the swirling flow studied by Kitoh (1991), qualitative agreement with experiment is not obtained; solid body rotation is predicted throughout.

The Reynolds stress closures show improved agreement with experiment compared to the predictions of the two-equation models. This is due to the ability to account for Reynolds stress anisotropy, and its initiation of secondary flow that preserves swirl.

For these flows the SSG-ADRM model demonstrates the following characteristics:

1. increased turbulence in the upstream region of the flow, leading to over-prediction of normal stress components, and shear stresses,
2. improved prediction of swirl velocity in the upstream region, as shown by axial decay results (figures 4.8 and 4.40), an important result for the consideration of flame position in combustion flows,
3. decreased turbulence in the downstream region compared to other models,
4. premature decay of swirl in the downstream region, affected by the reduction in turbulence downstream,
5. an inability to account for the sign of the mean strain and vorticity in the determination of the coefficient $C_{\epsilon 1}^{*}$, and hence the different effects upon the dissipation rate by the sign of these properties.

These effects are discussed in more detail below along with the predictions of the other second-moment closures.

For high swirl, in Kitoh's case, the LRR model failed to predict adequate mean flow results in comparison with experiment. The large reverse axial velocity along with the associated free vortex distribution of tangential velocity were not predicted well along the length of the pipe showing premature decay of the swirl. In contrast the SSG and SSG-ADRM model predictions show that the swirl is preserved in the axial coordinate, showing increased agreement with experiment for the axial and tangential velocity profiles. The additional nonlinear terms in the pressure-strain correlation for the SSG model improve its performance over the LRR model.

For the Reynolds stresses, it was found that the LRR, SSG and SSG-ADRM models over-predict the normal components, to a much greater extent when the LRR model is in use. The shear stresses are well produced by the SSG and SSG-ADRM models, while the LRR model is least accurate. The anisotropic dissipation rate terms in the SSG-ADRM model show only minor departures from the standard SSG model. Closer to the inlet, predicted turbulent quantities are greater than those of the SSG model as the it reduces the production of dissipation, thereby increasing turbulence. As the flow develops, and mean strain and vorticity relaxes, the turbulence is shown to decay more readily than predicted using the SSG model. This results in the increased axial decay of swirl when compared to the SSG model.

For the lower swirl case of Al-Masseeh (1991), the same limitations of the two-equation models are apparent as for the higher swirl flow. The Reynolds stress closures are again more accurate. The LRR model predicts a premature decay of swirl, as indicated by positive axial velocity occurring at a lower axial position at the centreline compared to the other models. However, the LRR model is shown to give more realistic prediction of the flow field near the inlet in the wall region due to the wall effect terms included in the pressure-strain correlation.

The SSG model over-predicts the tangential velocity at the chamber axis, delaying the onset of solid body motion in the upstream region, as seen in the strongly swirling flow. The SSG-ADRM model corrects this behaviour in the upstream region of the jet. However, this leads to premature decay of the tangential velocity downstream, and shortening of the axial recirculation.

The isotropic specification of turbulence at the inlet is shown to cause inaccuracy in the prediction of the normal Reynolds stresses only at the inlet jet region. As the flow relaxes quickly, and becomes more isotropic, the inlet effects subside rapidly with axial distance. However, the prediction of the normal Reynolds stresses in the near wall region is inadequate. This calls into question the use of wall functions for this particular flow due to the presence of flow reattachments in this region.

Again the effect of dissipation anisotropy in the SSG-ADRM model is seen to reduce the production of dissipation in the upstream region, leading to over-prediction of

turbulent quantities. This, however, reduces downstream for this flow as it becomes more isotropic. In the jet region, where the shear is greatest at the bounds of the jet, the anisotropic dissipation reduces, causing the increase in turbulence production. This increase is erroneous, as the tangential shear induced at the inlet has opposing signs above and below the jet, affecting the production and dissipation of turbulence differently (analogous to alignment of local vorticity with or against the bulk vorticity to stabilise or increase turbulence).

However, redistribution of the diagonal components of the dissipation rate tensor to the other components is observed at the jet region, with opposing effects that enhance and attenuate the turbulence above and below the jet. The smaller size of the off-diagonal dissipation rate components still suggests that the diagonal components, and hence the scalar turbulent dissipation rate, are dominant in this flow. The anisotropic effects are thus small compared to the isotropic dissipation.

7.1.2 Reacting flow

The SSG-ADRM model has shown an ability to capture the aerodynamic quantities of the TECFLAM turbulent, combustion flow well. The prediction of the jet position, and hence the flame, shows inaccuracies where the expansion of the gas at the central core pushes the jet too far radially outwards. Also the peak velocities in the jet are under-predicted by approximately 30% for axial velocity to 15% for tangential velocity.

The aerodynamic mixing of the fuel and air jets was also under-predicted in the region of the nozzle, where the fuel jet is seen to persist further than experiment shows. The inlet boundary conditions are the main culprit for this prediction, as the normal Reynolds stresses as well as the shear stresses are not resolved well in this region.

The prediction of mixture fraction and the mass fractions of CO and CO_2 show inaccuracies. The mixture fraction, although predicted within the flammability limits in the flame region, shows areas of non- uniformity across the width of the flame, with regions of greater richness on the outer edge of the flame. Despite this,

the air and fuel were shown to mix too rapidly at the base of the flame. The use of the LRR model to account for mean mixture fraction and its fluctuation may be unreliable for this application as it is based wholly on aerodynamic considerations, not taking into consideration the diffusive processes of the different species.

A limitation of the flamelet model has been identified for the prediction of excessive amounts of CO. The thin reaction zone assumption is valid for the main reactions, but the oxidation layer for CO, and noxious gasses where applicable, is not considered in the model. This leaves the reaction converting $CO \rightarrow CO_2$ untreated.

7.2 Suggestions for future research

Despite the increased computing cost required to integrate the equations fully up to the wall, it has been shown (Jakirlic *et al.*, 2001; Hanjalic and Jakirlic, 1998) that flows such as those studied here could benefit from this approach. Whilst the wall function assumption works well for the strongly swirling isothermal flow up to $y^+ \approx 200$ (Kitoh, 1991), its predictions for separating flows, as in the lower swirling flow of Al-Masseeh (1991), are not as accurate. To account for this, a low-Re number model needs to be developed to account for near wall effects.

As mentioned in chapter 2, the modelling of the pressure-strain correlation term in the transport equation for the Reynolds stresses is of great importance. All of the models used in the work presented here do not comply wholly with the realisability constraints prescribed by Lumley (1978). More recent models, such as those of Craft and Launder (2001) and Jovanovic *et al.* (2003), take into account the realisability constraints with additional modelling to capture the two-component nature of the normal Reynolds stresses when approaching a wall or a free surface. Testing of these types of models should be undertaken to validate them for swirling flows.

The anisotropic dissipation rate model used here is implemented by adjusting the production of dissipation with respect to the size of the mean strain and vorticity tensors. However, the coefficient $C_{\epsilon 1}^*$ has only a dependence on the modulus of these tensors, η and ξ. This shows an insensitivity to the sign of the strain and vorticity

that has an important effect in either attenuating or amplifying the production of turbulence. Even though the use of the stress anisotropy tensor to model dissipation anisotropies was discounted in this thesis, a combination of this along with effects of mean strain and vorticity should be investigated.

The prediction of the Reynolds stresses, particularly at the centre of the axis in strong swirl, has been shown to be inaccurate. By the use of DNS methods, more accurate modelling could be produced by identification of the current inadequacies in the Reynolds stress model terms (i.e. the pressure-strain correlation) by comparison of the same computed by DNS. However, for the flow speeds studied here, LES is the only viable option for Reynolds stress model improvement.

A significant improvement in the solution algorithms is required to reduce calculation time for the use of differential second-moment closure modelling. Possible solutions are multiresolution techniques such as those presented by Lien and Leschziner (1994), and parallelisation techniques. Without a reduction in computing times, the use of Reynolds stress models is not cost effective for industrial purposes.

Extension of the flamelet model to account for the oxidation layer also needs to be addressed when computing combusting flows. This should be performed by modifying the prediction of the rate of formation of species source terms in the equations for the relevant species mass fraction. Extension of the integrals for these source terms, outside the flammability limits for mixture fraction and flame stretch (effectively lengthening the flamelet width) should be incorporated.

Appendix A

Appendices

Contents

A.1 Reynolds Stress Models - RSM

The modelled equations for Reynolds stresses and dissipation rate read :

$$\frac{1}{r}\frac{\partial}{\partial x_k}\left(rU_k\overline{u_iu_j}\right) = \frac{1}{r}\frac{\partial}{\partial x_k}\left[r\left(\nu\delta_{kl} + C_s\frac{k}{\epsilon}\overline{u_ku_l}\right)\frac{\partial\overline{u_iu_j}}{\partial x_l}\right] + P_{ij} + \Phi_{ij} - \epsilon_{ij} + S_{\overline{u_iu_j}} \quad \text{(A.1)}$$

$$\frac{1}{r}\frac{\partial}{\partial x_k}\left(rU_k\epsilon\right) = \frac{1}{r}\frac{\partial}{\partial x_k}\left[r\left(\nu\delta_{kl} + C_\epsilon\frac{k}{\epsilon}\overline{u_ku_l}\right)\frac{\partial\epsilon}{\partial x_l}\right] + \left(C_{\epsilon 1} + E\right)\frac{\epsilon}{k}P_k - C_{\epsilon 2}\frac{\epsilon^2}{k} \quad \text{(A.2)}$$

$$P_{ij} = -\left(\overline{u_iu_k}\frac{\partial U_j}{\partial x_k} + \overline{u_ju_k}\frac{\partial U_i}{\partial x_k}\right) \quad \text{(A.3)}$$

$$D_{ij} = -\left(\overline{u_iu_k}\frac{\partial U_k}{\partial x_j} + \overline{u_ju_k}\frac{\partial U_k}{\partial x_i}\right) \quad \text{(A.4)}$$

$$\Phi_{ij} = \Phi_{ij,1} + \Phi_{ij,2} + \Phi_{ij}^w \quad \text{(A.5)}$$

$$\Phi_{ij,1} = -C_1\epsilon a_{ij} + C_1'\epsilon\left(a_{ik}a_{kj} - \frac{1}{3}A_2\delta_{ij}\right) \quad \text{(A.6)}$$

$$\begin{aligned}\Phi_{ij,2} = \; & - \; C_2'P_ka_{ij} + C_3k\overline{S}_{ij} + C_4k\left(a_{ik}\overline{S}_{jk} + a_{jk}\overline{S}_{ik} - \frac{2}{3}\delta_{ij}a_{kl}\overline{S}_{kl} + S_4\right) \\ & + \; C_5k\left(a_{ik}\overline{W}_{jk} + a_{jk}\overline{W}_{ik} + S_5\right)\end{aligned} \quad \text{(A.7)}$$

$$\Phi_{ij}^w = f_w\left[C_1^w\epsilon a_{ij} + C_2^w\left(P_{ij} - D_{ij}\right)\right] \quad \text{(A.8)}$$

$$f_w = \frac{k^{3/2}}{\epsilon x_n} \tag{A.9}$$

$$E = \frac{2\left(1+\alpha\right)}{15C_\mu^*}\left[\frac{C_{\epsilon 5} + 2C_\mu^*\eta^2 - 1}{\left(C_{\epsilon 5} + 2C_\mu^*\eta^2 - 1\right)^2 - \frac{2}{3}\beta_2^2\eta^2 + 2\beta_1^2\xi^2}\right] \tag{A.10}$$

$$\epsilon_{ij} = \frac{2}{3}\epsilon\delta_{ij} + 2\epsilon d_{ij} \tag{A.11}$$

	C_1	C_1'	C_2'	C_3	C_4	C_5
LRR	1.8	0.0	0.0	0.8	0.6	0.6
SSG	1.7	1.05	0.9	$0.8 - 0.65A_2^{1/2}$	0.625	0.2

	C_1^w	C_2^w	C_s
LRR	0.125	0.015	0.22
SSG	0.0	0.0	0.22

where P_k, a_{ij}, A_2, S_{ij} and $\overline{W}_{ij}$:

$A_2 = a_{ij}a_{ji}$; $a_{ij} = \frac{\overline{u_i u_j}}{k} - \frac{2}{3}\delta_{ij}$; $d_{ij} = \frac{\epsilon_{ij}}{\epsilon} - \frac{2}{3}\delta_{ij}$; $P_k = -\overline{u_i u_k}\frac{\partial U_i}{\partial x_j}$;
$\overline{S}_{ij} = \frac{1}{2}\left(\frac{\partial U_i}{\partial x_j} + \frac{\partial U_j}{\partial x_i}\right)$; $\overline{W}_{ij} = \frac{1}{2}\left(\frac{\partial U_i}{\partial x_j} - \frac{\partial U_j}{\partial x_i}\right)$

	$C_{\epsilon 1}$	$C_{\epsilon 2}$	C_ϵ	E	α_3	$C_{\epsilon 5}$	C_μ^*
LRR	1.44	1.92	0.18	0	-	-	-
SSG	1.44	1.83	0.18	0	-	-	-
SSG-ADRM	1.0	1.83	0.15	E	0.6	5.80	0.094

$S_{\overline{u_i u_j}}$	Convection	Production	Viscous Diffusion	Turbulent Diffusion
$S_{\overline{u^2}}$	-	-	-	-
$S_{\overline{v^2}}$	$+2\overline{vw}\frac{W}{r}$	$+2\overline{vw}\frac{W}{r}$	$-2\nu\frac{\overline{v^2}-\overline{w^2}}{r^2}$	$-2C_s\frac{k}{\epsilon}\overline{w^2}\frac{\overline{v^2}-\overline{w^2}}{r^2}$ $-2\frac{1}{r}\frac{\partial}{\partial x}\left(C_s\frac{k}{\epsilon}\overline{uw}\cdot\overline{vw}\right)$ $-2\frac{1}{r}\frac{\partial}{\partial r}\left(C_s\frac{k}{\epsilon}\overline{vw}\cdot\overline{vw}\right)$ $-2C_s\frac{1}{r}\frac{k}{\epsilon}\left(\overline{uw}\frac{\partial\overline{vw}}{\partial x}+\overline{vw}\frac{\partial\overline{vw}}{\partial r}\right)$
$S_{\overline{w^2}}$	$-2\overline{vw}\frac{W}{r}$	$-2\overline{w^2}\frac{V}{r}$	$+2\nu\frac{\overline{v^2}-\overline{w^2}}{r^2}$	$+2C_s\frac{k}{\epsilon}\overline{w^2}\frac{\overline{v^2}-\overline{w^2}}{r^2}$ $+2\frac{1}{r}\frac{\partial}{\partial x}\left(C_s\frac{k}{\epsilon}\overline{uw}\cdot\overline{vw}\right)$ $+2\frac{1}{r}\frac{\partial}{\partial r}\left(C_s\frac{k}{\epsilon}\overline{vw}\cdot\overline{vw}\right)$ $+2C_s\frac{1}{r}\frac{k}{\epsilon}\left(\overline{uw}\frac{\partial\overline{vw}}{\partial x}+\overline{vw}\frac{\partial\overline{vw}}{\partial r}\right)$
$S_{\overline{uv}}$	$+\overline{uw}\frac{W}{r}$	$+\overline{uw}\frac{W}{r}-\overline{uv}\frac{V}{r}$	$-\nu\frac{\overline{uv}}{r^2}$	$-C_s\frac{k}{\epsilon}\overline{w^2}\frac{\overline{uv}}{r^2}$ $-\frac{1}{r}\frac{\partial}{\partial x}\left(C_s\frac{k}{\epsilon}\overline{uw}\cdot\overline{uw}\right)$ $-\frac{1}{r}\frac{\partial}{\partial r}\left(C_s\frac{k}{\epsilon}\overline{vw}\cdot\overline{uw}\right)$ $-C_s\frac{1}{r}\frac{k}{\epsilon}\left(\overline{uw}\frac{\partial\overline{uw}}{\partial x}+\overline{vw}\frac{\partial\overline{uw}}{\partial r}\right)$
$S_{\overline{uw}}$	$-\overline{uv}\frac{W}{r}$	$-\overline{uw}\frac{V}{r}$	$-\nu\frac{\overline{uw}}{r^2}$	$-C_s\frac{k}{\epsilon}\overline{w^2}\frac{\overline{uw}}{r^2}$ $+\frac{1}{r}\frac{\partial}{\partial x}\left(C_s\frac{k}{\epsilon}\overline{uw}\cdot\overline{uv}\right)$ $+\frac{1}{r}\frac{\partial}{\partial r}\left(C_s\frac{k}{\epsilon}\overline{vw}\cdot\overline{uv}\right)$ $+C_s\frac{1}{r}\frac{k}{\epsilon}\left(\overline{uw}\frac{\partial\overline{uv}}{\partial x}+\overline{vw}\frac{\partial\overline{uv}}{\partial r}\right)$
$S_{\overline{vw}}$	$-\left(\overline{v^2}-\overline{w^2}\right)\frac{W}{r}$	$-\overline{vw}\frac{V}{r}+\overline{w^2}\frac{W}{r}$	$-4\nu\frac{\overline{vw}}{r^2}$	$-4C_s\frac{k}{\epsilon}\overline{w^2}\frac{\overline{vw}}{r^2}$ $+\frac{1}{r}\frac{\partial}{\partial x}\left[C_s\frac{k}{\epsilon}\overline{uw}\left(\overline{v^2}-\overline{w^2}\right)\right]$ $+\frac{1}{r}\frac{\partial}{\partial r}\left[C_s\frac{k}{\epsilon}\overline{vw}\left(\overline{v^2}-\overline{w^2}\right)\right]$ $+C_s\frac{1}{r}\frac{k}{\epsilon}\left[\overline{uw}\frac{\partial}{\partial x}\left(\overline{v^2}-\overline{w^2}\right)\right.$ $\left.+\overline{vw}\frac{\partial}{\partial r}\left(\overline{v^2}-\overline{w^2}\right)\right]$

TABLE A.1: List of source terms, $S_{\overline{u_i u_j}}$, arising from co-ordinate transformations.

	$i=j=1$	$i=j=2$	$i=j=3$
S_4	$\frac{\overline{vw}}{k}\frac{W}{r} - \frac{\overline{w^2}}{k}\frac{V}{r}$	$-2\frac{\overline{vw}}{k}\frac{W}{r} + \frac{1}{2}\frac{\overline{w^2}}{k}\frac{V}{r}$	$-\frac{\overline{vw}}{k}\frac{W}{r} - \frac{1}{2}\frac{\overline{w^2}}{k}\frac{V}{r}$
S_5	–	$-\frac{1}{2}\frac{\overline{w^2}}{k}\frac{V}{r}$	$\frac{1}{2}\frac{\overline{w^2}}{k}\frac{V}{r}$

	$i=1, j=2$	$i=1, j=3$	$i=2, j=3$
S_4	$\frac{\overline{uv}}{k}\frac{V}{r} - \frac{1}{2}\frac{\overline{uw}}{k}\frac{W}{r}$	$\frac{1}{2}\frac{\overline{uw}}{k}\frac{V}{r}$	$-\frac{1}{2}\frac{\overline{w^2}}{k}\frac{W}{r} + \frac{\overline{vw}}{k}\frac{V}{r}$
S_5	$-\frac{1}{2}\frac{\overline{uw}}{k}\frac{W}{r}$	$\frac{1}{2}\frac{\overline{uw}}{k}\frac{V}{r}$	$-\frac{1}{2}\frac{\overline{w^2}}{k}\frac{W}{r}$

TABLE A.2: List of source terms, S_4 and S_5, arising from co-ordinate transformations.

Bibliography

ABRAHAM, J., WILLIAMS, F.A. AND BRACCO, F. (1985) A discussion of turbulent flame structure in premixed charges. *SAE paper 850345* .

ACHESON, D.J. (1998) *Elementary fluid mechanics* Oxford University Press.

AL-MASSEEH, W.A.A. (1991) Fundamental aspects of combustion in swirling flow. PhD thesis, Mechanical Engineering, University of Leeds, UK.

ALVES, M.A., OLIVEIRA, P.J. AND PINHO, F.T. (2003) A convergent and universally bounded scheme for the treatment of advection. *Int. J. Numer. Meth. Fluids* **41**, 47–75.

ANDREWS, G.E. AND BRADLEY, D. (1973) Determination of burning velocity by double ignition in a closed vessel. *Combust. Flame* **20**, 77–89.

ARMALY, B.F., DURST, F., PEREIRA, J.C.F. AND SCHONUNG, B. (1983) Experimental and theoretical investigation of backward facing step flow. *J. Fluid Mech.* **127**, 473–496.

BALDWIN, B.S. AND LOMAX, H. (1978) Thin-layer approximation and algebraic model for separated turbulent flows. *AIAA paper 78-257* .

BARLOW, R.S., KARPETIS, A.N., FRANK, J.H. AND CHEN, J-Y. (2001) Scalar profiles and no formation in laminar opposed-flow partially premixed methane/air flames. *Combust. Flame* **127**, 2102–2118.

BARTON, I.E. (1998) Comparison of SIMPLE-and PISO-type algorithms for transient flows. *Int. J. Numer. Meth. Fluids* **26**, 459–483.

BERGMANN, V., MEIER, W., WOLFF, D. AND STRICKER, W. (1998) Application of spontaneous Raman and Rayleigh scattering and 2D LIF for the characterization of a turbulent CH4/H-2/N-2 jet diffusion flame. *Appl. Phys. B* **66**(4), 489–502.

BIAGIOLI, F. (1998) Calculation of laminar flows with second-order schemes and collocated variable arrangement. *Int. J. Numer. Meth. Fluids* **26**, 887–905.

BOOK, D.L. (1981) *Finite Difference Techniques For Vectorized Fluid Dynamic Calculations.* Springer-Verlag.

BOWMAN, C.T., HANSON, R.K., LISSIANSKI, V., FRENKLACH, M., GOLDENBERG, M. AND SMINTH, G.P. (1996) GRI-Mech 2.11: An optimized detailed chemical reaction mechanism for methane combustion and NO formation and reburning. technical report, Gas Research Institute, Chicago.

BRADLEY, D. (2002) Problems of predicting turbulent burning rates. *Combust. Theory Modelling* **6**, 361–382.

BRADLEY, D., EMERSON, D.R., GASKELL, P.H. AND GU, X.J. (2002) Mathematical modeling of turbulent non-premixed piloted-jet flames with local extinctions. In: *Proceedings of the combustion institute* Vol. 29, The Combustion Institute, pp. 2155-2162.

BRADLEY, D., GASKELL, P.H. AND GU, X.J. (1996) Burning velocities, Markstein lengths, and flame quenching for spherical methane-air flames:a computational study. *Combust. Flame* **104**, 176–198.

BRADLEY, D., GASKELL, P.H. AND GU, X.J. (1998*a*) The mathematical modeling of liftoff and blowoff of turbulent non-premixed methane jet flames at high strain rates. In: *Twenty-seventh symposium (international) on combustion* Vol. 1-2, pp. 1199-1206.

BRADLEY, D., GASKELL, P.H. AND GU, X.J. (1998*b*) The modeling of aerodynamic strain rate and flame curvature effects in premixed turbulent combustion. In: *Twenty-seventh symposium (international) on combustion* Vol. 1-2, pp. 849-856.

BRADLEY, D., GASKELL, P.H., GU, X.J., LAWES, M. AND SCOTT, M.J. (1998) Premixed turbulent flame instability and no formation in a lean-burn swirl burner. *Combust. Flame* **115**(4), 515–538.

BRAY, K.N.C. AND PETERS, N. (1994) Laminar flamelets in turbulent flames. In: P.A. Libby and F.A. Williams (eds.), *Turbulent reacting flows*. Academic Press, pp. 63–113.

CANDEL, S.M. AND POINSOT, T.J. (1990) Flame stretch and the balance equation for the flame area. *Combust. Sci. Tech.* **70**(1-3), 1-15.

CHAMPAGNE, F.H., HARRIS, V.G. AND CORRSIN, S. (1970) Experiments on nearly homogeneous shear flow. *Journal of Fluid Mechanics* **41**, 81 139.

CHEN, J.C. AND LIN, C.A. (1999) Computations of strongly swirling flows with second moment closures. *Int. J. Numer. Meth. Fluids* **30**, 493-508.

CHIEN, K-Y. (1982) Prediction of channel and boundary layer flows with a low-Reynolds-number turbulence model. *AIAA J.* **20**, 33-38.

CHOMIAK, J., HAKBERG, B. AND OLSSON, E. (1991) A note on the scalar dissipation rates in turbulent flows. *Comb. Flame* **83**(3), 412-414.

CHOU, P.Y. (1945) On velocity correlations and the solutions of the equations of turbulent fluctuation. *Quart. Appl. Math.* **3**(1), 38-54.

CLAVIN, P. (1985) Dynamic behavior of premixed flame fronts in laminar and turbulent flows. *Prog. Energ. Combust.* **11**(1), 1-59.

CRAFT, T.J. AND LAUNDER, B.E. (2001) Principles and performance of TCL-based second-moment closures. *Flow. Turb. Combust.* **66**, 355 372.

DALY, B.J. AND HARLOW, F.H. (1970) Transport equations of turbulence. *Phys. Fluids* **13**, 2634.

DARWISH, M.S. AND MOUKALLED, F. (2003) TVD schemes for unstructured grids. *Int. J. Heat Mass Tran.* **46**(4), 599 611.

DENG, G.B., PIQUET, J., QUEUTEY, P. AND VISONNEAU, M. (1994) Incompressible flow calculations with a consistent physical interpolation finite volume approach. *Comput. Fluids* **23**(8), 1029 1047.

DIBBLE, R.W., MAAS, U. AND WARNATZ, J. (1999) *Combustion: physical and chemical fundamentals, modeling and simulation, experiments, pollution formation.* 2 edn, Springer-Verlag.

DIXON-LEWIS, G. (1990) In: *23rd Symposium (International) on Combustion* p. 305.

FAVRE, A. (1971) Statistical equations for turbulent fluctuations in compressible flows - rates and temperatures. *C. R. Ac. Sc. Serie A* **273**(22), 1087–1092.

FAWEHINMI, O.B., GASKELL, P.H. AND THOMPSON, H.M. (2002) Finite element analyses of flow in a cavity with internal blockages. *P. I. Mech. Eng. C - J. Mech.* **216**(5), 517–530.

FERZIGER, J.H. AND PERIC, M. (2004) *Computational methods for fluid dynamics.* Springer-Verlag.

FU, S., LAUNDER, B.E. AND LESCHZINER, M.A. (1987) Modelling strongly swirling recirculating jet with Reynolds stress transport closure. In: *Proceedings of the 6th Symposium on Turbulent Shear Flows* pp. 17.6.1–17.6.6.

FU, S., LAUNDER, B.E. AND TSELEPIDAKIS, D.P. (1987) Accommodating the effect of high strain rates in modelling the pressure-strain correlation. Technical Report TFD/87/5, UMIST Mech. Eng. Dept.

GASKELL, P.H. AND LAU, A.K.C. (1988) Curvature-compensated convective transport: SMART, a new boundedness preserving transport algorithm. *Int. J. Numer. Meth. Fluids* **8**, 617–641.

GATSKI, T.B. AND RUMSEY, C.L. (2002) Linear and nonlinear eddy viscosity models. In: N.D. Sandham and B. Launder (eds.), *Closure Strategies for Turbulent and Transitional Flows.* Cambridge University Press, chapter 1, pp. 9–46.

GHIA, U., GHIA, K.N. AND SHIN, C.T. (1982) High-*Re* solutions for incompressible flow using the Navier- Stokes equations and a multigrid method. *J. Comput. Phys.* **48**, 387–441.

GIBSON, M.M. AND LAUNDER, B.E. (1978) Ground effects on pressure fluctuations in the atmospheric boundary layer. *J. Fluid Mech.* **86**, 491–511.

GROSSHANDLER, W.L. (1993) Radcal: A narrow-band model for radiation calculations in a combustion environment. NIST technical note 1402, National Institute of Standards and Technology.

GU, X.J. (1993) A theoretical and computational study of turbulent flames. PhD thesis, Mechanical Engineering, University of Leeds, UK.

GUPTA, A.K., LILLEY, D.G. AND SYRED, N. (1984) *Swirl flows* Abacus Press.

GURSUL, I. (2004) Recent developments in delta wing aerodynamics. *Aeronaut. J.* **108**(1087), 437–452.

HALLBACK, M., GROTH, J. AND JOHANSSON, A.V. (1990) An algebraic model for nonisotropic turbulent dissipation rate in Reynolds-stress closures. *Phys. Fluids A* **2**, 1859–1866.

HANJALIC, K. AND JAKIRLIC, S. (1998) Contribution towards the second-moment closure modelling of separating turbulent flows. *Comput. Fluids* **27**(2), 137–156.

HANJALIC, K. AND JAKIRLIC, S. (2002) Second-moment turbulence closure modelling. In: N.D. Sandham and B. Launder (eds.), *Closure Strategies for Turbulent and Transitional Flows.* Cambridge University Press, chapter 2, pp. 47 101.

HANJALIC, K. AND LAUNDER, B.E. (1972) A Reynolds stress model of turbulence and its application to thin shear flows. *J. Fluid Mech.* **52**, 609.

HARLOW, F.H. AND WELCH, J.E. (1965) Numerical calculation of time-dependent viscous incompressible flow of fluid with free surface. *Phys. Fluids* **8**(12), 2182-2189.

HARTEN, A. (1983) High resolution schemes for hyperbolic conservation laws. *J. Comput. Phys.* **49**(3), 357-393.

HOEKSTRA, A.J., DERKSEN, J.J. AND VAN DEN AKKER, H.E.A. (1999) An experimental and numerical study of turbulent swirling flow in gas cyclones *Chem. Eng. Sci* **54**(13-14), 2055-2065.

HOGG, S. AND LESCHZINER, M.A. (1989) Computation of highly swirling confined flow with a reynolds-stress turbulence model. *AIAA J.* **27**(1), 57-67.

ISSA, R.I. (1985) Solution of the implicitly discretized fluid flow equations by operator splitting. *J. Comp. Phys.* **62**, 40-62.

JAKIRLIC, S. AND HANJALIC, K. (2002) A new approach to modelling near-wall turbulence energy and stress dissipation. **459**, 139 166.

JAKIRLIC, S., HANJALIC, K. AND TROPEA, C. (2002) Modeling rotating and swirling turbulent flows: a perpetual challenge. *AIAA J.* **40**(10), 1984 1996.

JAKIRLIC, S., TROPEA, C., HADZIC, I., PASCAL, H. AND HANJALIC, K. (2001) Computational study of joint effects of shear, compression and swirl on flow and turbulence in a valveless piston-cylinder assembly. SAE technical paper 2001-01-1236, Society of Automotive Engineers.

JAKIRLIC, S., VOLKERT, J., PASCAL, H., HANJALIC, K. AND TROPEA, C. (2000) DNS, experimental and modelling study of axially compressed in-cylinder swirling flow. *J. Heat Fluid Flow* **21**(5), 627-639.

JONES, W.P. (1979) Models for turbulent flows with variable density and combustion. In: W. Kollman (ed.), *Prediction methods for turbulent flows.* Hemisphere, pp. 379-422.

JONES, W.P. AND LAUNDER, B. E. (1972) The prediction of laminarization with a two-equation model of turbulence. *Int. J. Heat Mass Tran.* **15**, 301 314.

JONES, W.P. AND WHITELAW, J.H. (1982) Calculation methods for reacting turbulent flows - a review. *Comb. Flame* **48**(1), 1 26.

JOVANOVIC, J., OTIC, I. AND BRADSHAW, P. (2003) On the anisotropy of axisymmetric strained turbulence in the dissipation range. *J. Fluid. Eng.* **125**, 401 413.

KECK, O., MEIER, W., STRICKER, W. AND AIGNER, M. (2002) Establishment of a confined swirling natural gas/air flame as a standard flame: Temperature and species distributions from laser Raman measurements. *Combust. Sci. Tech.* **174**(8), 117 151.

KEE, R.J., RUPLEY, F.M. AND MILLER, J.A. (1989) Chemkin-ii: A fortran chemical kinetics package for the analysis of gas phase chemical kinetics. Sandia technical report SAND89-8009B, Sandia National Laboratory.

KITOH, O (1991) Experimental study of turbulent swirling flow in a straight pipe. *J. Fluid Mech.* **225**, 445–479.

KLIMENKO, A.Y. AND BILGER, R.W. (1999) Conditional moment closure for turbulent combustion. *Prog. Energ. Combust.* **25**, 595–687.

KOBAYASHI, M.H. AND PEREIRA, J.C.F. (1991) Numerical comparison of momentum interpolation methods and pressure- velocity algorithms using non-staggered grids. *Commun. Appl. Numer. M.* **7**, 173–186.

KOLMOGOROV, A.N. (1941) The local structure of turbulence in an incompressible fluid for very large Reynolds numbers. *C. R. Acad. Sci., USSR* **30**, 301 305.

KOLMOGOROV, A.N. (1942) The equations of turbulent motion in an incompressible fluid. *Izv. Acad. Sci., USSR Phys.* **6**, 56–58.

KUZNETSOV, V.R. AND SABELNIKOV, V.A. (1990) In: P.A. Libby (ed.), *Turbulence and combustion.* Hemisphere.

LANDENFELD, T., KREMER, A., HASSEL, E. P. AND JANICKA, J. (1997) Anstze zur modellierung eingeschlossener drallflammen. In: *TECFLAM-Seminar* Vol. 13, Drallflammen und Industriecodeentwicklung.

LANDENFELD, T., KREMER, A., HASSEL, E. P., JANICKA, J., SCHFER, T., KAZENWADEL, J., SCHULZ, C. AND WOLFRUM, J. (1998) Laser-diagnostic and numerical study of strongly swirling natural gas flames. In: *Twentyseventh Symposium (International) on Combustion* The Combustion Institute.

LAUNDER, B.E., REECE, G.J. AND RODI, W (1975) Progress in the development of a Reynolds-stress turbulence closure. *J. Fluid Mech.* **68**(3), 537 566.

LAUNDER, B.E. AND SHARMA, B.I. (1974) Application of the energy dissipation model of turbulence to the calculation of flow near a spinning disc. *Lett. Heat Mass Trans.* **1**(2), 131–138.

LAUNDER, B.E. AND SPALDING, D.B. (1972) *Lectures in mathematical models of turbulence.* Academic Press.

LAW, C.K. AND SUNG, C.J. (2000) Structure, aerodynamics, and geometry of premixed flamelets. *Prog. Energ. Combust.* **26**, 459–505.

LE, H., MOIN, P. AND KIM, J. (1997) Direct numerical simulation of turbulent flow over a backward-facing step. *J. Fluid Mech.* **330**, 349–374.

LEONARD, B.P. (1979) A stable and accurate convective modelling procedure based on quadratic upstream interopolation. *Comp. Meth. Appl. Mech. Eng.* **19**, 59–98.

LEONARD, B.P. AND DRUMMOND, J.E. (1995) Why you should not use 'Hybrid', 'Power law' or related exponential schemes for convective modelling - there are much better alternatives. *Int. J. Numer. Meth. Fluids* **20**, 421 442.

LI, G, NAUD, B AND ROEKAERTS, D. (2003) Numerical investigation of a bluff-body stabilised nonpremixed flame with differential reynolds-stress models. *Flow. Turbul. Combust.* **70**, 211–240.

LIBBY, P.A. AND BRAY, K.N.C. (1977) Variable density effects in premixed turbulent flames. *AIAA J.* **15**(8), 1186 1193.

LIBBY, P.A. AND BRAY, K.N.C. (1981) Countergradient diffusion in premixed turbulent flames. *AIAA J.* **19**(2), 205 213.

LIBBY, P.A. AND WILLIAMS, F.A. (1990) On the speed of strained laminar flames in premixed systems. *Combust. Sci. Technol.* **72**, 131–136.

LIBBY, P.A. AND WILLIAMS, F.A. (1994) Fundamental aspects and a review. In: P.A. Libby and F.A. Williams (eds.), *Turbulent reacting flows.* Academic Press, pp. 1–61.

LIEN, F.S. AND LESCHZINER, M.A. (1994) A general non-orthogonal collocated finite volume algorithm for turbulent flow at all speeds incorporating second-moment turbulence-transport closure, Part 1: Computational implementation. *Comput. Methods Appl. Mech. Engrg.* **114**, 123–148.

LILEK, Z. AND PERIC, M (1995) A fourth order finite volume method with colocated variable arrangement. *Comput. Fluids* **24**(3), 239–252.

LIU, Y.S., SCHMIDLI, J. AND SMITH, B.L. (1998) Numerical and experimental study of swirling flow in a model combustor. *Int. J. Heat Mass Transfer* **41**(11), 1485–1497.

LU, P. AND SEMIAO, V. (2003) A new second moment closure approach for turbulent swirling confined flows. *Int. J. Numer. Meth. Fluids* **41**, 133–150.

LUMLEY, J.L. (1978) Computational modeling of turbulent flows. *Adv. Appl. Mech.* **18**, 123–176.

MAJUMDAR, S. (1988) Role of underrelaxation in momentum interpolation for calculation of flow with nonstaggered grids. *Numer. Heat Transfer* **13**, 125–132.

MANSOUR, N.N., KIM, J. AND MOIN, P. (1989) Near-wall $k-\epsilon$ turbulence modeling. *AIAA J.* **27**(8), 1068–1073.

MEIER, W., KECK, O., NOLL, B., KUNZ, O. AND STRICKER, W. (2000*a*) Investigations in the TECFLAM swirling diffusion flame: Laser Raman measurements and CFD calculations. *Appl. Phys. B.* **71**(5), 725–731.

MEIER, W., KECK, O., NOLL, B., KUNZ, O. AND STRICKER, W. (2000*b*) Investigations in the TECFLAM swirling diffusion flame: Laser raman measurements and cfd calculations. *Appl. Phys. B* **71**(5), 725–731.

MENTER, F.R. (1994) Eddy viscosity transport models and their relation to the $k-\epsilon$ model. Technical Report TM-108854, NASA.

MURTY, B.S. (2002) Turbulence modeling. In: G. Biswas and V. Eswaran (eds.), *Turbulent Flows* Alpha Science International, chapter 10, pp. 319–338.

O'BRIEN, E.E. AND JIANG, T.L. (1991) The conditional dissipation rate of an initially binary scalar in homogeneous turbulence. *Phys. Fluids A* **3**(12), 3121–3123.

PAPAGEORGAKOPOULOS, J., ARAMPATIZIS, G., ASSIMACOPOULOS, D. AND MARKATOS, N.C. (2000) Enhancement of the momentum interpolation method on non-staggered grids. *Int. J. Numer. Meth. Fluids* **33**, 1–22.

PATANKAR, S.V. (1980) *Numerical Heat Transfer and Fluid Flow* Hemisphere.

PATANKAR, S.V. (1981) A calculation procedure for two-dimensional elliptic situations. *Numer. Heat Transfer* **4**, 409–425.

PATANKAR, S.V. AND SPALDING, D.B. (1972) A calculation procedure for heat, mass and momentum transfer in three- dimensional parabolic flows. *Int. J. Heat Mass Transfer* **15**, 1787–1806.

PIRONEAU, O. (1989) *Finite element methods for fluids.* John Wiley & Sons.

PRANDTL, L. (1925) Über die ausgebildete turbulenz. *ZAMM* **5**, 136–139.

PRESS, W.H., FLANNERY, B.P., TEUKOLSKY, S.A. AND VETTERLING, W.T. (1993) *Numerical recipes in C.* 2nd edn, Cambridge University Press.

REYNOLDS, O. (1895) On the dynamical theory of incompressible viscous fluids and the determination of the criterion. *Phil. Trans. R. Soc. London Ser. A* **186**, 123 164.

RHIE, C.M. AND CHOW, W.L. (1983) Numerical study of the turbulent flow past an airfoil with trailing edge separation. *AIAA J.* **21**, 1525–1532.

RODI, W. (1988) Recent developments in turbulence modeling. In: Y. Iwasa, N. Tamai and A. Wada (eds.), *Proceedings of the 3rd International Symposium on Refined Flow Modeling and Turbulence Measurements.*

ROEKAERTS, D. (2002) Reacting flows and probability density function methods. In: N.D. Sandham and B. Launder (eds.), *Closure Strategies for Turbulent and Transitional Flows.* Cambridge University Press, chapter 10, pp. 328 337.

ROTTA, J.C. (1951) Statistiche theorie nicht-homogener turbulenz. *Z. Phys.* **129**, 547–573.

SAFFMAN, P.G. (1970) A model for inhomogeneous turbulent flow. *Proc. Roy. Soc. London A* **317**, 417–433.

SANDHAM, N.D. (2002) Introduction to direct numerical simulation. In: N.D. Sandham and B. Launder (eds.), *Closure Strategies for Turbulent and Transitional Flows.* Cambridge University Press, chapter 7, pp. 248–266.

SEOK, K.C., HO, Y.N. AND MANN, C. (1995) A comparison of higer-order bounded convection schemes. *Comp. Meth. Appl. Mech. Eng.* **121**, 281 301.

SHARIF, M.A.R. AND WONG, Y.K.E. (1995) Evaluation of the performance of three turbulence closure models in the prediction of confined swirling flows. *Computers and Fluids* **24**(1), 81–100.

SHIH, T-H., ZHU, J., LIOU, W.W., CHEN, K-H. AND LUMLEY, J.L. (1997) Modeling of turbulent swirling flows. In: *Proceedings of the 11th Symposium on Turbulent Shear Flows* pp. 31.1–31.6.

SMITH, A.M.O. AND CEBECI, T. (1967) Numerical solution of the turbulent boundary-layer equations. *Douglas aircraft division report no. DAC 33735* .

SO, R.M.C., AHMED, S.A. AND MONGIA, H.C. (1984) An experimental investigation of gas jets in confined swirling air flow. *NASA CR3832* .

SO, R.M.C., ZHAO, C.Y. AND GATSKI, T.B. (1999) Predicting buoyant shear flows using anisotropic dissipation rate models. *Flow Turb. Comb.* **63**, 193 221.

SONG, B., LIU, G.R., LAM, K.Y. AND AMANO, R.S. (2000) On a higher-order bounded discretisation scheme. *Int. J. Numer. Meth. Fluids* **32**, 881 897.

SPALART, P.R. AND ALLMARAS, S.R. (1992) A one equation turbulence model for aerodynamic flows. *AIAA Paper No. 92-439* .

SPALDING, D.B. (1972) A novel finite difference formulation for differential expressions involving both first and second derivatives. *Int. J. Numer. Meth. Eng.* **4**, 551 559.

SPEZIALE, C.G. (1987) On non-linear $k-l$ and $k-\epsilon$ models of turbulence. *J. Fluid Mech.* **178**, 459–475.

SPEZIALE, C.G. (1996) Modeling of turbulent transport equations. In: T.B. Gatski, Hussaini M.Y. and Lumley J.L. (eds.), *Simulation and modeling of turbulent flows.* Oxford University Press, chapter 5, pp. 185–242.

SPEZIALE, C.G. AND GATSKI, T.B. (1997) Analysis and modelling of anisotropies in the dissipation rate of turbulence. *J. Fluid Mech.* **344**, 155–180.

SPEZIALE, C.G., SARKAR, S. AND T.B., GATSKI (1991) Modelling the pressure-strain correlation of turbulence: an invariant dynamical systems approach. *J. Fluid Mech.* **227**, 245–272.

SPEZIALE, C.G., YOUNIS, B.A. AND BERGER, S.A. (2000) Analysis and modelling of turbulent flow in an axially rotating pipe. *J. Fluid Mech.* **407**, 1–26.

STOKES, G.G. (1845) *Trans. Camb. Phil. Soc.* **8**, 287–305.

STREHLOW, R.A. (1985) *Combustion Fundamentals.* McGraw-Hill.

SWEBY, P.K. (1984) High resolution schemes using flux limiters for hyperbolic conservation laws. *Siam J. Numer. Anal.* **21**(5), 995–1011.

VAN DOORMAAL, J.P. AND RAITHBY, G.D. (1984) Enhancements of the simple method for predicting incompressible fluid flows. *Numer. Heat Transfer* **7**, 147 163.

VAN LEER, B. (1979) Towards the ultimate conservative difference scheme, v. A second -order sequel to Godunov's method. *J. Comput. Phys.* **32**, 101 136.

VERSTEEG, H.K. AND MALALASEKERA, W. (1996) *An introduction to computational fluid dynamics: the finite volume method.* Addison-Wesley.

WALKLEY, M.A., GASKELL, P.H., JIMACK, P.K., KELMANSON, M.A., SUMMERS, J.L. AND WILSON, M.C.T. (2004) On the calculation of normals in free-surface flow problems. *Commun. Numer. Meth. En.* **20**(5), 343 351.

WALL, K.M. AND TAULBEE, D.B. (1995) Application of a nonlinear stress-strain model to axisymmetric turbulent swirling flows. *Int. J. Heat Fluid Flow* **17**, 116 123.

WARMING, R.F. AND BEAM, R.M. (1976) Upwind second-order difference schemes and applications in aerodynamic flows. *AIAA J.* **14**, 1241–1249.

WILCOX, D.C. (1994) *Turbulence modeling for CFD.* 2nd edn, DCW Industries.

WILLIAMS, F.A. (1985) Turbulent combustion In: J.D. Buckmaster (ed.), *The mathematics of combustion* pp. 97–131.

WILLIAMS, F.A. (2000) Progress in knowledge of flamelet structure and extinction. *Prog. Energ. Combust.* **26**, 657–682.

XIA, J.L., YADIGAROGLU, G., LIU, Y.S., SCHMIDLI, J. AND SMITH, B.L. (1997) Numerical and experimental study of swirling flow in a model combustor. *Int. J. Heat Mass Transfer* **41**(11), 1485–1497.

YARAS, M.I. AND GROSVENOR, A.D. (2003) Evaluation of one- and two-equation low-*Re* turbulence models. Part i - axisymmetric separating and swirling flows. *Int. J. Numer. Meth. Fluids* **42**, 1293–1319.

YOUNG, D.L., LIAO, C.B. AND SHEEN, H.J. (1999) Computations of recirculation zones of a confined annular swirling flow. *Int. J. Numer. Meth. Fluids* **29**, 791–810.

YOUNIS, B.A., GATSKI, T.B. AND SPEZIALE, C.G. (1996) Assessment of the SSG pressure-strain model in free turbulent jets with and without swirl. *Trans. ASME: J. Fluids Engng.* **116**, 800–809.

YUAN, S.P. AND SO, R.M.C. (1998) Turbulent rotating flow calculations: an assessment of two-equation anisotropic and Reynolds stress models. *Proc. Instn. Mech. Engrs.* **212**, 193–212.

ZHU, J. (1991) A low-diffusive and oscillation-free convection scheme. *Commun. Appl. Numer. M.* **7**, 225–232.